UNIVERSITY OF SOUTHAMPTON

FACULTY OF PHYSICAL SCIENCES AND ENGINEERING

Optoelectronics Research Centre

Phenomena of Ultrafast Laser Material Modification with Respect to Spatio-Temporal Couplings of the Laser Pulse

by

Aabid Patel

Thesis for the degree of Doctor of Philosophy

September 26, 2016

UNIVERSITY OF SOUTHAMPTON

ABSTRACT

FACULTY OF PHYSICAL SCIENCES AND ENGINEERING

Optoelectronics Research Centre

Thesis for the degree of Doctor of Philosophy

PHENOMENA OF ULTRAFAST LASER MATERIAL MODIFICATION WITH RESPECT TO SPATIO-TEMPORAL COUPLINGS OF THE LASER PULSE

Aabid Patel

The nano-structuring of transparent media with subpicosecond laser pulses has attracted significant interest due to its unique applications. In contrast to nanosecond pulses where the energy introduced to the lattice is absorbed, leading to melting/boiling of the material around the focal volume, femtosecond lasers can alter material properties of the glass at high pressures without excessive production of heat, modifying the structures with sub-micron resolution. Permanent modifications can then be induced without strong collateral damage. Although femtosecond pulses are beneficial for material processing, short pulse durations and broad spectral bandwidths require a novel approach to femtosecond pulse control.

It is well known that laser induced modification depends on fluence, wavelength and polarization. Another dependence of material modification is the spatio-temporal properties of the ultrashort pulse. These spatio-temporal couplings give rise to intrinsic nonlinear optical phenomena, which are well known in experiment but otherwise lack a clear explanation. While the formation mechanisms with respect to the nano-structuring of transparent media is still under debate, a better understanding of the nonlinear optical phenomena that affects the formation would provide insight into the physics of ultrafast light-matter interaction.

In this thesis, the origin and thorough investigation of spatio-temporal induced phenomena are reported. By controlling the spatio-temporal couplings separately, I demonstrate complete control of all of the dependencies with the use of prism compressors and grating compressors and discuss the intricacies behind the control of the spatio-temporal couplings with complete characterization of the pulse. By investigating two of the main phenomena associated with spatio-temporal couplings, which give rise to a directional dependence when writing in the bulk

("quill-writing effect") and a photosensitive anisotropy ("blade effect"), a more thorough understanding of the light-matter interaction is demonstrated and reported.

I demonstrate that spatio-temporal couplings are inherent for all ultrafast laser systems with chirped-pulse amplification and result in a strongly anisotropic light-matter interaction. I identify angular dispersion in the focus as the main cause for the anisotropic photosensitivity coming from the spatially chirped pulse, which shows to yield a 200% increase in modification strength. With tighter focusing (NA ≥ ~0.4), this non-paraxial effect leads to a more apparent manifestation of spatio-temporal couplings in photo-induced modification. I control the anisotropy and exploited it as a new degree of freedom in tailoring laser induced modification in transparent material. A non-paraxial field structure analysis near the focus is conducted, with an elliptical optical beam, to provide insight on the origin of the photosensitive anisotropy.

After a complete identification of the spatio-temporal properties of the electric field, the quill-effect was confirmed to be due to pulse front tilt in the focus with a direct comparison with other major spatio-temporal couplings including wavefront rotation. I reveal that the non-reciprocity during femtosecond laser writing in transparent media induces either an isotropic damage-like structure or a self-assembled nanostructure depending on the movement direction of the beam - known as the "quill-writing effect." I also identify the switching of the modification regime from the formation of isotropic damage-like to anisotropic grating-like structures observed when the translation of the beam is in the direction of the tilt and is qualitatively described in terms of the first-order phase transition in the irradiated volume of a transparent dielectric.

The structural evolution from void modification to self-assembled nanogratings in fused silica for moderate (NA > 0.4) focusing conditions is also discussed in this thesis. Void formation appears before the geometrical focus after the initial few pulses with nanogratings gradually occurring at the top of the induced structures after subsequent irradiation. Nonlinear Schrödinger equation-based simulations are conducted to simulate the laser fluence, intensity and electron concentration in the regions of modification. Comparing the experiment with simulations, the voids form due to cavitation in the regions where electron concentration exceeds 10^{20} cm^{-3} but remains below critical. In this scenario, the energy absorption is insufficient to reach the critical electron concentration that was once assumed to occur in the regime of void formation and nanogratings, shedding light on the potential formation mechanism of nanogratings.

In-situ observations of harmonic generation during the ultrafast laser writing is presented to better understand the underlying physics that occur during the process of nanograting formation. Second and third harmonic generation is observed, with third harmonic distributed as two lobes following the polarization orientation of the electric field, identified as Cherenkov Third Harmonic.

These harmonics are observed and correlated with the different regimes of material modification to understand whether they are part of the nanograting formation or corollary to give insight on the formation mechanisms of the self-assembled nanostructures.

Finally, I discuss the work on the concept of an on-axial simultaneous spatio-temporal focusing with the use of a simple polarization dependent circular grating for the purpose of material modification using the expertise of the group on polarization gratings. The design and theoretical validation of the technique is reported in this thesis with the potential of further work in perfecting it for material modification and chirped-pulse amplification applications.

Table of Contents

List of Tables

List of Figures

DECLARATION OF AUTHORSHIP

I, Aabid Patel, declare that this thesis and the work presented in it are my own and has been generated by me as the result of my own original research.

Phenomena of Ultrafast Laser Material Modification with Respect to Spatio-Temporal Couplings of the Laser Pulse

I confirm that:

1. This work was done wholly or mainly while in candidature for a research degree at this University;
2. Where any part of this thesis has previously been submitted for a degree or any other qualification at this University or any other institution, this has been clearly stated;
3. Where I have consulted the published work of others, this is always clearly attributed;
4. Where I have quoted from the work of others, the source is always given. With the exception of such quotations, this thesis is entirely my own work;
5. I have acknowledged all main sources of help;
6. Where the thesis is based on work done by myself jointly with others, I have made clear exactly what was done by others and what I have contributed myself;
7. Parts of this work have been published as:

    - **A. Patel**, V. T. Tikhonchuk, J. Zhang, M. Beresna, P. G. Kazansky. “Non-Paraxial Polarization Spatio-Temporal Coupling: A New Degree of Freedom in Light Matter Interaction.” Laser and Photonics Reviews. 1600290 (2017)

    - **A. Patel**, Y. Svirko, C. Durfee, M. Beresna, P. G. Kazansky. “Pulse Front Tilt Induced Non-Reciprocity during Ultrafast Laser Direct Writing.” Scientific Reports. (2017)

    - Y. Dai, **A. Patel**, J. Song, M. Beresna, P. G. Kazansky. “Void-Nanograting Transition by Ultrashort Laser Pulse Irradiation in Silica Glass.” Optics Express, Vol. 24 (17), 19344-19353 (2016).

- J. Zhang, A. Čerkauskaitė, R. Drevinskas, **A. Patel**, M. Beresna, P. G. Kazansky. “Eternal 5D Data Storage by Ultrafast Laser Writing in Glass.” SPIE Photonics West: Laser-Based Micro- and Nanoprocessing X, United States. p. 1-16 (13-18 Feb 2016)

Signed:

Date: 09/11/2017

Acknowledgements

First and foremost, this work is dedicated to my family. This is dedicated to them for understanding the choices I have made in order to get this far in my life. The sacrifices that they have made to see me succeed. For their patience and constant love and support for me. To my brother and sisters for putting up with all of my issues and still being there for me in the end. To my beautiful niece, Laila, for always reminding me what's important in life. This is especially dedicated to my mother and father for the risks they took by coming to Canada to provide me and my siblings a better future and the sacrifices they have made to give us the life we have today. Without my family's undying love and support, I would not have been able to complete this PhD.

I want to thank my lab mates Rokas Drevinskas, Ausra Čerkauskaitė, Mindaugas Gecevičius, Jingyu Zhang and Fangteng Zhang who working alongside has been a pleasure. We went through many difficult times together but it was our combined support that got us through the hard times. Your assistance, camaraderie and overall presence has made these past 4 years something to remember. I also want to thank Dr. Martynas Beresna for his tutelage and support during our time together as part of the Physical Optics group. Regardless of the political and social issues that took place during my PhD studies, your mentorship has been beneficial and pivotal towards my overall learning.

I also want to thank those who helped me edit this work. That includes Bojan Miljkovic, Rob Blom, Jiannis Katis, Aly Hubrecht and Martynas Beresna. While you may not have understood it, you definitely helped make it a coherent piece of work.

Being away from home for such a long period made the time during my PhD studies quite difficult. I am blessed to have made so many amazing friends during my time at the ORC that I will cherish them for the rest of my life. To Matt Cino, Pony Boy and Jenn Potter, thank you for providing a bit of Canada in Southampton. To Stan Vassilev, thank you for being able to stand me while living with me for 3 years. To the friends I made outside of the ORC, thank you for making Southampton bearable. To my friends in the ORC, thank you for all the memories and fun times that got our minds off of our work. I want to especially thank my brothers in the portakabin (ΠΚΦ – Stan, Kyle, Jianni, Pete, Rocky, Gregorio, Udara and Chris Nash), for providing an atmosphere that made the time enjoyable. Our random debates and long winded conversations on current events to our random social gatherings and trips to our North American Free Donut Agreement (NAFDA) made my stint at the ORC bearable during stressful times. I also would to thank Chris Nash. To be honest, I don't know how we got along since we are almost completely opposite from one

another. But our misanthropic views definitely allowed us to bond and your support in my times of need has been something I will never forget. You are a true friend.

I also want to thank all my friends back in Canada. It was extremely difficult to move away from home and miss out on so many occasions that left me home sick. I've missed weddings and crucial life changing events that made my time in the UK quite difficult. But it was your support that got me through it all. I want to especially thank Corey Stewart for his help and constant support, Tom and Alyson Hubrecht for their ability to keep me from stressing out, to the Sirs (Goran Vlacic, Chris Lam and Jimmy Murphy) for providing humour in my life and everyone else who I do not have room to list off that came in during periods of my PhD where I did not think I would be able to get through it. You guys are the true MVPs. Except Grant Salton. I owe you nothing.

I also need to thank Monster Energy for providing me with the caffeine necessary to accomplish this work. Without your product, I would not have been able to stay up all those nights in the lab and office and I would not have been able to "Unleash the Beast."

But most importantly, the main thing that gets me through everything on a day to day basis is my faith. My belief and faith has allowed me to stay focused and driven, which has allowed me to experience the success I have in my life. Thank you Allah.

Definitions and Abbreviations

Angular Dispersion	AD
Angular Frequency of Light	ω
Bandgap Energy	E_g
Boltzmann Constant	k_B
Chirped Pulse Amplification	CPA
Coupled Charge Device	CCD
Electric Field	E
Electric Permittivity in Free Space	ε_0
Extraordinary Refractive Index	n_e
Finite-Difference Time-Domain	FDTD
Frequency Chirp	FCH = ϕ_2
Frequency Gradient	FRG = υ
Frequency of Light	v_0
Frequency Resolved Optical Gating	FROG
Grating-Eliminated No-nonsense Observation of Ultrafast Incident Light E-fields	GRENOUILLE
Group Delay Dispersion	GDD = φ_2
Group Velocity Dispersion	GVD
Keldysh Parameter	γ
Laser Intensity	I
Non-Collinear Optical Parametric Amplifier	NOPA
Numerical Aperture	NA
Optical Parametric Amplifier	OPA
Ordinary Refractive Index	n_o
Pulse Duration	τ
Pulse Energy	Ep

Pulse Front Tilt	PFT
Quantitative Phase Microscopy	QPM
Reduced Planck Constant	$\hbar$
Refractive Index of Material	n
Scanning Electron Microscopy	SEM
Second Harmonic Generation	SHG = 2ω
Simultaneous Spatial and Temporal Focusing	SSTF
Spatial Chirp	SC
Spatial Dispersion	SD = ζ
Speed of Light	c
Temporal Chirp	TC
Third Harmonic Generation	3ω
Time vs. Angle	TVA
Two-Plasmon Decay (Three-Half Harmonic)	$3\omega/2$
Wavefront Rotation	WFR
Wavelength	λ
Wavenumber in Vacuum	k_0

Chapter 1: Introduction

1.1 Motivation

The nanostructuring of transparent media with ultrafast laser pulses has attracted significant interest due to its unique applications. The growing interest into femtosecond laser material processing comes from the unique ability of inducing highly nonlinear processes. As opposed to long pulse ($\tau > 10$ ps) or CW lasers where the energy introduced to the lattice is absorbed, leading to melting and boiling of the material around the focal volume, femtosecond-pulsed lasers can alter the material properties of the glass without excessive production of heat, but at high pressures, modifying the structures with sub-micron resolution (Fig. 1.1). Therefore, permanent nanostructure modifications can be induced without damage caused by melting or boiling.

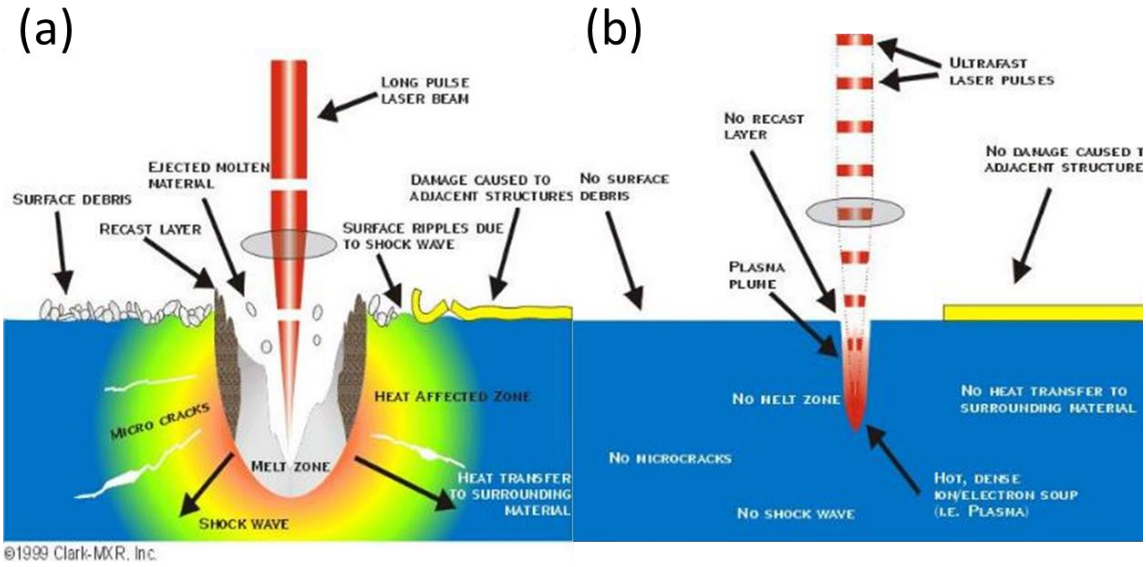

Figure 1.1: Difference between (a) long pulse and (b) short pulse laser material modification. (a) Energy is absorbed directly to the lattice through heat diffusion leading to collateral damage through thermal melting and explosive shock waves. (b) Energy does not have sufficient time to be absorbed by the lattice but excites the electrons, leading to plasma generation and permanent nanostructure modification. Image Source: Bado et al. [1]

While ultrafast laser writing has been utilized in many applications, the interaction of ultrashort pulses with matter is still not fully understood. For example, it was demonstrated that when focusing ultrashort pulses into the bulk of a dielectric above a certain intensity threshold, self-assembled nanogratings can be induced [2,3]. The mechanism that triggers the nanostructure formation is still unclear. Theoretical models which are supposed to explain the self-organization

are solely based on post-mortem observations but no direct evidence of the formation mechanism exists. The understanding of the phenomena observed during ultrafast laser writing would provide vital information towards potential applications that have not been utilized and could further advance existing applications.

In order to experimentally characterize physical processes that occur, a complete understanding of the spatio-temporal properties of the laser is needed to provide a fundamental understanding of the conditions during ultrafast laser writing. Spatio-temporal properties of ultrashort pulses, such as pulse front tilt, have shown to have a direct effect in material modification, providing understanding of which modifications are induced at the time of writing [4–6]. However a lack of control and sufficient characterization of what is seen in the bare laser pulse inhibits a full understanding of any of the associated phenomena that is induced. Therefore, in order to evaluate how spatio-temporal couplings affect laser-matter interactions, thorough control is necessary.

1.2 Thesis overview

Chapter 2: This chapter provides an overview of the basics in ultrafast laser material modification. I provide a background of the main nonlinear propagation and ionization mechanisms governing the light-matter interaction and review the structural modification that can be induced with ultrashort pulses. I also go into detail about current standing theories about how nanostructuring forms in the bulk of a dielectric.

Chapter 3: In this chapter, I review the general background on spatio-temporal couplings. I describe in detail how to define the electric field with spatio-temporal couplings and provide a description of the major couplings involved in ultrafast laser-material interaction. I also review the characterization methods available to measure pulses with spatio-temporal couplings as well as the focusing techniques developed around them. I also summarize some of the main ultrafast laser induced phenomena involving spatio-temporal couplings.

Chapter 4: This chapter describes the experimental set-up used for femtosecond laser material processing. The measurement techniques, which were frequently used (Quantitative Birefringence Measurement and Quantitative Phase Microscopy) in characterizing the irradiated samples, are described as well. The experimental design used to control and characterize spatio-temporal couplings involving pulse compressors (prism and gratings) is discussed extensively in this chapter.

Chapter 5: An *in-situ* measurement technique which measures the harmonics generated during ultrafast laser writing in transparent dielectrics is discussed in this chapter. The technique was developed in hopes of measuring harmonic signatures associated with popular models of nanostructure formation. While the harmonic was never measured, second and third harmonic signals were measured and studied alongside the modification being induced in the bulk of fused silica. The harmonics were studied as a function of pulse energy, laser irradiation and polarization; unique enhancements were observed that associate the harmonics generated with self-assembled nanograting formation. Third harmonic was also observed to manifest itself as two lobes along the polarization direction of the incident light and identified to be generated based on the Cherenkov radiation mechanism.

Chapter 6: This chapter presents the results on the systematic study of polarization anisotropy in material modification due to the mutual orientation of spatio-temporal couplings and the laser light polarization. In contrast to previous work, the spatio-temporal couplings of the laser pulse were controlled and characterized to deduce the origin of the polarization dependence observed - known as the "blade-effect." It was found that angular dispersion in the focus coupling with polarization is the origin of the effect. The phenomenon is shown to be observed in any laser that has chirped pulse amplification or any form of spatio-temporal manipulation and is a non-paraxial multi-pulse effect. The blade-effect is also shown to provide an extra degree of control in tailoring modification by being able to change the strength of modification, simply by rotating the polarization orientation.

Chapter 7: In this chapter, the structural evolution from void modification to self-assembled nanogratings in fused silica is observed, which was originally thought to be a forbidden transition. The evolution of the void to nanograting transition was studied against nonlinear Schrödinger equation-based simulations. Upon single pulse simulations, the voids were found to form in the regions where the electron density exceeds 10^{20} cm^{-3} but remains below the critical electron concentration. This observation has ramifications on the formation mechanism of ultrafast laser induced material modification.

Chapter 8: This chapter is dedicated to the investigation of the non-reciprocal writing behaviour observed in ultrafast laser writing known as the quill-writing effect. Using the same control and characterization used in Chapter 6, a systematic study of the directional dependence was conducted. After comparing it to other evident spatio-temporal couplings that reside in the pulse, it was confirmed that pulse front tilt in the focus is the cause of the non-reciprocal behaviour. Also, an identification of a switching of the modification regime from the formation of isotropic damage-like to anisotropic grating-like structures is observed when translating the beam in the

direction of the tilt. This transition is described in terms of the first-order phase transition in the irradiated volume of a transparent dielectric.

Chapter 9: This chapter discusses the concept of an on-axial pulse compressor and simultaneous spatial and temporal focusing design with the use of a polarization circular grating. The concept is evaluated theoretically and then a proof of concept was shown to demonstrate the potential of the design. The main limitations associated with the design of the circular grating element as well as the intrinsic spatio-temporal behaviour of the design have also been summarized here.

Chapter 10: This chapter concludes the thesis by summarizing the key findings of my research. I also provide a future outlook on research and developments that could greatly benefit the understanding of ultrafast laser-material interactions and ultrafast laser writing.

Chapter 2: Ultrafast Laser Material Modification

In this chapter, I will review the background associated with ultrafast light-matter interactions primarily focusing on permanent modifications in transparent materials. When focusing ultrafast laser pulses into the bulk of a transparent medium, intensities are sufficient to reach nonlinear breakdown. Based upon the laser conditions, different nonlinear light-matter interactions can occur. In particular, three types of modification in bulk dielectrics can be produced depending on the laser fluence used: isotropic refractive index increase (Type I), nanogratings (Type II) and voids (Type III). Type I modification occurs at low pulse energies and leads to smooth positive refractive index changes with very little transmission losses. Type II modification occurs at higher pulse energies where birefringent nanogratings, aligned orthogonally to the polarization of the laser, are formed [2,3,7,8]. At even higher pulse energies, Type III modifications occur due to extremely high pressures, which lead to void structures within the bulk of the volume [9–11]. The use of these modifications has led to applications that can replace complicated optical set-ups such as waveguides [12] and polarization sensitive holograms [13] and has led to new applications such as polarization control [14] and 5D optical memory [15].

Since the objective of this thesis surrounds the understanding of phenomena based upon nanogratings and void formation, I will concentrate on the background of these two types of modifications. While the formation mechanisms for some of the modification states are unknown, there has been considerable discussion on the origin of the ultrafast laser induced phenomena. Below, I will discuss some of the current popular models.

2.1 Permanent Transparent Material Modification

The band gap of dielectrics is typically much larger than the energy of the single photon of an infrared source. For comparison, the band gap of fused silica is approximately 9 eV, while the photon energy at 1030 nm wavelength is 1.2 eV. In the linear interaction regime, a photon with $\hbar\omega$ energy cannot be absorbed because it is much smaller than the band gap of the material. However, if the light intensity is high, nonlinear processes can lead to strong material ionization. There are two classes of such processes: nonlinear photoionization and avalanche ionization [16,17] (Fig. 2.1).

Photoionization refers to the direct electron excitation by an electric laser field. Depending on laser frequency and laser intensity, the ionization can occur in the form of tunneling or

multiphoton absorption. Normally, the character of the nonlinear photoionization is evaluated by calculating the adiabatic parameter, γ, also widely referred as the Keldysh parameter [18]:

$$\gamma = \frac{\omega}{e}\sqrt{\frac{m_e c n_0 \epsilon_0 E_g}{I}} \tag{2.1}$$

where ω is the laser frequency, I is the laser intensity at the focus, m_e and e are the reduced mass and charge of the electron, c is the speed of light, n_0 is the refractive index of the material, E_g is the band gap of the material and ϵ_0 is the permittivity of free space. When $\gamma < 1.5$, the tunnelling process is dominant. When $\gamma > 1.5$, the multi-photon process is dominant. In the intermediate regime, the photoionization process is a mix between the two regimes (Fig. 2.1).

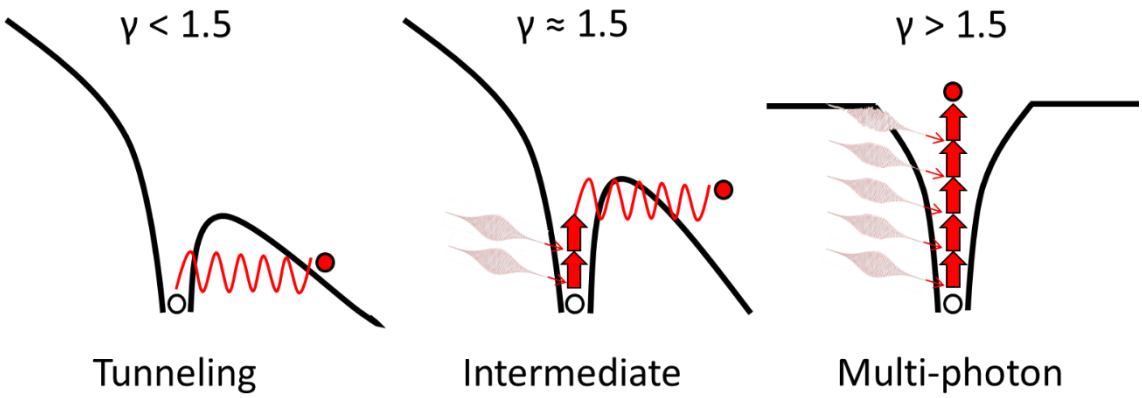

Figure 2.1: Nonlinear Photoionization Processes of an electron in an atomic potential for different Keldysh parameters.

Tunneling ionization involves the electric field of the laser suppressing the Coulomb well that binds a valence electron to its parent atom and typically takes place for strong laser fields and low laser frequency. If the electric field is strong, the Coulomb well can be supressed enough that the bound electron tunnels through the short barrier and becomes free (Fig. 2.1).

Multi-photon absorption is the process of simultaneous absorption of several photons by an electron, typically seen at high laser frequencies but are still below that needed for single photon absorption. In order to promote the electron from the valence to the conduction band, an electron must absorb a sufficient amount of photons so that the product of the number of photons absorbed and the photon energy is equal to or greater than the band gap of the electron. In this regime, the photoionization rate, P_{PI}, greatly depends on the laser intensity:

$$P_{PI}(I) = \sigma_k I^k \tag{2.2}$$

where σ_k is the multi-photon absorption coefficient for absorption of k photons. From here, it can be seen that multi-photon ionization occurs faster for higher intensities. Based on the definition

of multi-photon absorption, the electron will be excited to the conduction band if the following condition is met:

$$\hbar\omega \geq E_g \tag{2.2}$$

In the case when there are electrons already present in the conduction band of a material, avalanche ionization can occur (Fig. 2.2). These "seed electrons" can be the result of photoionization (such as multi-photon or tunneling ionization) or pre-existing defects within the material that are more accessible for ionization. An electron in the conduction band can move to higher energy states within the band by linearly absorbing several photons sequentially, otherwise known as inverse Bremsstrahlung absorption. The energy held by the elevated electron will eventually exceed the bandgap of the material and then ionize another electron from the valence band via collision. This collision results in the two electrons falling to the conduction band minimum, allowing for both electrons to continue the free carrier absorption and impact ionization process as long as the laser field is present. The electron density, n_e, generated through avalanche ionization grows with time as [19]:

$$n_e(t) = n_0 2^{w_{imp}t} = n_0 e^{(\ln 2) w_{imp}t} \tag{2.3}$$

where n_0 is the initial electron density and w_{imp} is the probability for the impact ionization.

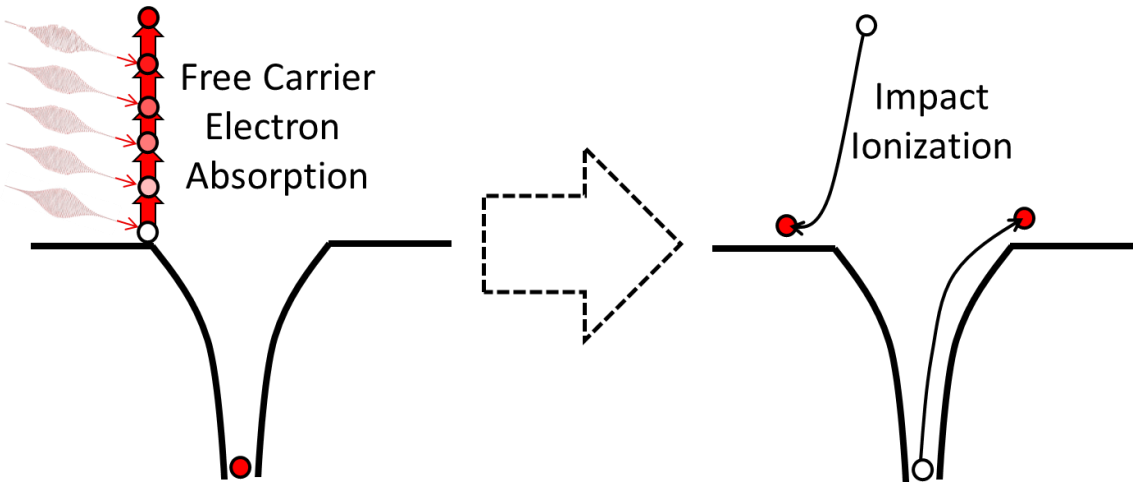

Figure 2.2: Schematic diagram for Avalanche Ionization. Free electron absorbs energy through carrier absorption. This provides sufficient energy to knock-out another electron from the valence to the conduction band.

After sufficient energy is absorbed via the ionization processes described and deposited into the material, permanent damage occurs. However, the permanent damage threshold is typically characterized by post-mortem observations [17,20] of a material, meaning that there is no real definition as to what the permanent damage threshold of a material is. The other issue with the definition is that it is typically thought to be the same for modification on the surface as it is in the

bulk of a medium. In reality, these two situations are drastically different from one another. Focusing on the surface, for example, is not affected by spherical aberration or self-focusing of the pulse as it is for the bulk. Also, the damage threshold of the surface can greatly vary because of its quality and preparation (polishing, impurities, etc.) whereas the bulk is typically pristine.

Ultrafast laser material modification largely depends on the laser pulse duration. During laser irradiation, the energy from the electric field is absorbed by the electrons. These electrons are excited into the conduction band and then distribute energy amongst themselves via scattering. Carrier-carrier scattering leads to a fast energy redistribution among the excited carriers within 10-100 fs, whereas carrier-phonon scattering leads to a transfer of energy to the lattice directly, equalizing the temperature of the electrons and lattice. The latter process has a lifetime of tens of picoseconds (Fig. 2.3).

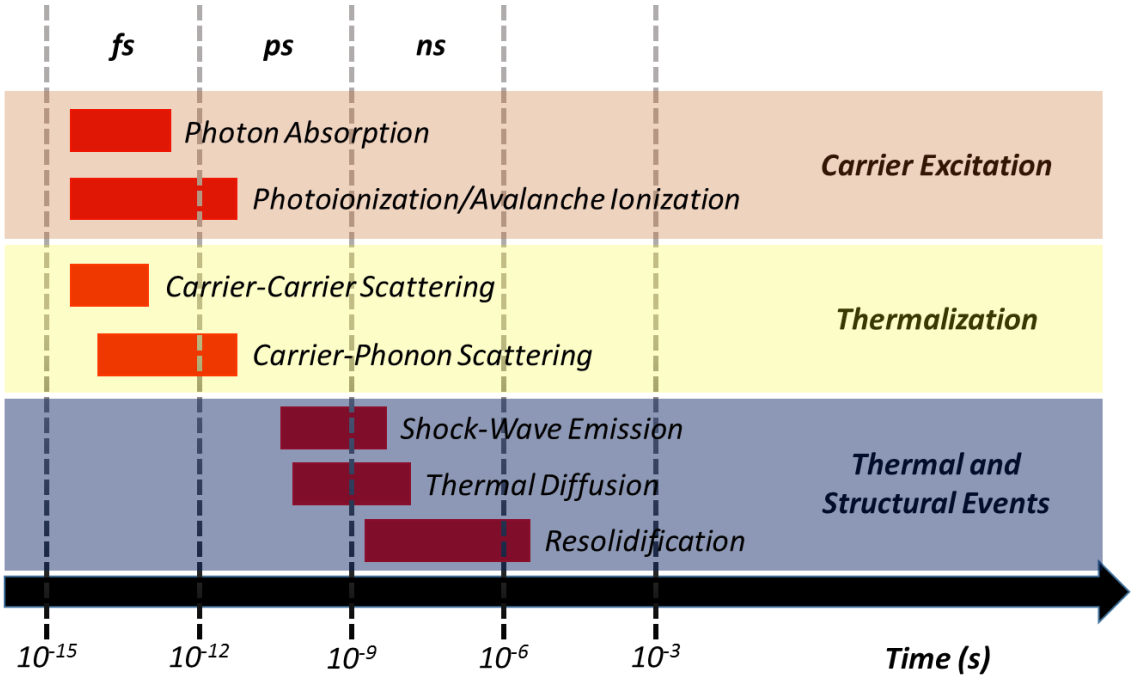

Figure 2.3: Time scales of the physical interactions that occur during light-matter interactions. In the regime of ultrafast lasers (fs and ps), only the non-linear mechanisms such as multi-photon absorption, photoionization and avalanche ionization occurs. At longer time scales, thermal and structural events become dominate resulting in shock-wave, melting and/or boiling through thermal diffusion. Adapted from Gattass and Mazur [16].

Therefore, depending on the laser pulse duration, different processes come into play resulting in different types of modification (Fig. 2.3). If the laser pulse is of the same time scale as carrier-phonon scattering (> 10 ps) a substantial amount of energy will be transferred directly to the lattice during laser irradiation [17]. Energy is transferred directly to the laser focus through

thermal diffusion from the excited lattice phonons resulting in permanent damage, which is indicated through either melting or boiling. The material is then fractured from the strong tension gradient, degrading the quality of the material. In this case, the damage threshold is defined by the relative rate of energy deposition and thermal diffusion. Classically, the damage threshold based upon this (defined as fluence) scales as the square root of the pulse duration (Fig. 2.4). However with the development of ultrafast lasers able to reach sub-picosecond pulse durations, it was found that a deviation from the law was observed for laser pulses that are less than 10 ps. For pulses less than 10 ps, there is not a sufficient amount of time during pulse propagation for energy to be deposited directly to the lattice. Thermal diffusion and electron-ion interaction takes place after the laser pulse, allowing for the electrons to be excited to high temperatures while keeping the lattice in a cold state during pulse propagation. After the pulse, the electrons release energy but remain localised within the irradiated zone. This reduces the heat affected zone and minimizes any collateral damage in the vicinity. The damage in this case is typically related to the critical plasma concentration, when the laser irradiation is strongly absorbed by the excited electron plasma. However, the identification of a critical plasma concentration in these conditions is largely under dispute [21,22]. This will be discussed further in Chapter 7.

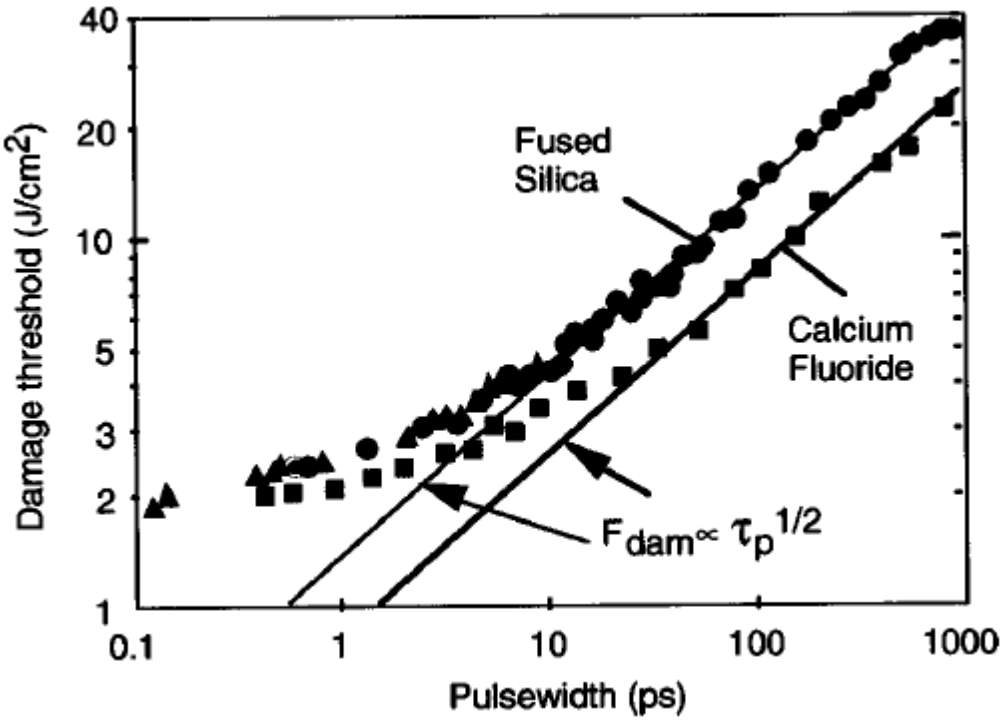

Figure 2.4: The damage thresholds observed for surface modification of calcium fluoride at 1053 nm (black squares) and fused silica at 1053 nm (circles) and 825 nm (triangles). The solid lines are $\tau^{1/2}$ best fits for long pulse durations. However, the deviation from the square root fit for pulse durations less than 10 ps indicates the presence of a different mechanism for permanent damage. Image source: Perry et al. [20].

When working with sub 10 ps pulses, laser irradiation can produce three types of modification depending on the laser parameters such as wavelength, pulse duration and pulse number (Fig. 2.5). But usually for a single laser pulse at 800 nm, the induced structures in the exposure area mainly depend on the level of the laser intensity and therefore have long been classified qualitatively into three types. Type I is a smooth positive refractive index change observed at a low intensity regime (< 10^{12} W/cm^2), which may originate from material densification after structural network reorganization [23,24], formation of agglomerate colour centres or defects [25], or mechanical stress due to pressure wave release [26]. When the incident intensity exceeds 10^{12} W/cm^2, a type II modification (i.e. periodic nanostructure or nanogratings) form under a multi-pulse exposure condition. This structure consists of alternating nanoplanes, oriented perpendicular to the polarization of light, and exhibits optical birefringence [2,3,8] (discussed further in Chapter 2.2). If the laser intensity exceeds 10^{13} W/cm^2, it could potentially lead to the formation of voids (Type III; discussed in Chapter 2.3) or the density of induced plasma at the focus will continue increasing and potentially reach the critical electron density (1.7×10^{21} cm^{-3} for 800 nm in fused silica) above which the plasma becomes opaque and reflective [27]. The subsequent relaxation, in this case, depends on focusing conditions and pulse density.

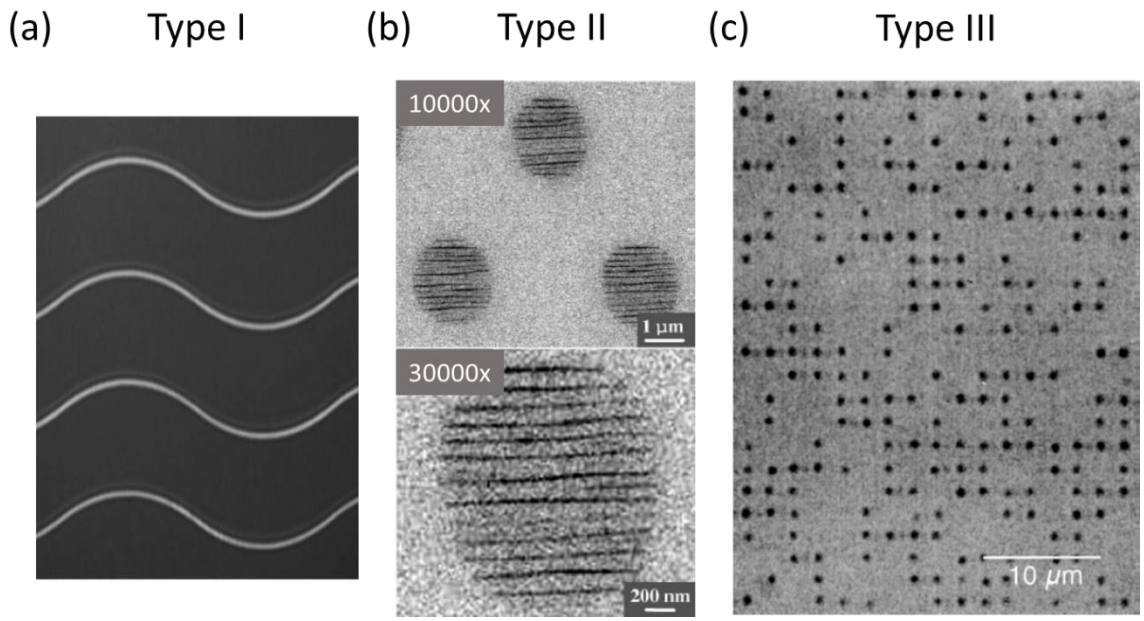

Figure 2.5: The classification of femtosecond laser induced modification in transparent glass: (a) refractive index increase (Type I), (b) self-assembled nanogratings (Type II) and (c) void formation (Type III). Image source: (a) Qiu et al. [28] (b) Shimotsuma et al. [2] (c) Glezer et al. [29].

2.2 Self-Assembled Nanogratings

Under certain experimental conditions, highly ordered self-organized subwavelength structures with features smaller than tens of nanometres can be formed within the bulk of the volume (Fig. 2.5b). The first reported observation of laser induced periodic nanostructuring was in 1965, when ripple formation was observed on the surface of a semiconductor produced by a Ruby Laser [30]. Since then, a wide range of laser sources have been investigated making it apparent that surface ripple formation could be observed with any wavelength, ranging from the mid-infrared to the visible, regardless if the source is CW or nanosecond and femtosecond based. Furthermore, surface ripple formation is relatively independent of the material since it can be formed on dielectrics, metals and polymers [31–36]. The periodic arrangement of surface ripples is observed to be dependent on the electric field, with the period being close to the wavelength of the incident light and oriented perpendicularly to the electric field [37]. If the light is p-polarized (parallel to the plane of incidence), the surface ripple spacing, Λ, is given by [38]:

$$\Lambda = \frac{\lambda}{1 \pm \sin\theta} \tag{2.4}$$

where θ is the angle of incidence with respect to the surface. When the light is s-polarized (perpendicular to the plane of incidence), the spacing remains similar to the wavelength of the light. For femtosecond lasers, surface ripple formation is typically observed at fluences above the ablation threshold with a low number of pulses following the same ripple spacing as seen in Equation (2.4). These ripples are widely considered to be the result of interference between an incident wave and a surface scattered wave [39–41]. However, surface ripple formation has been observed at sub-wavelength spacing when using laser fluences well below the single-pulse ablation threshold [42,43]. The periods for these structures are seen to increase with the number of pulses and fluence, with the formation being only observed after long irradiations and can be both orthogonal and parallel to the polarization direction. While the formation mechanisms for these structures have been proposed to come about from either interference [40], nanoplasmonics [36,44], standing waves [36], second harmonic generation (SHG) [42] and/or self-organization [45], the origin is still under debate.

Evidence of periodic nanostructuring within the bulk of a material was not discovered until the late 90s. Initial evidence of subwavelength nanostructuring within the bulk of glass was found through anisotropic light scattering, which peaks in the plane of light polarization within an isotropic media [46]. The effect observed produced a propeller shape along the polarization direction when focused within the bulk of glass. The luminescence observed was roughly half of the incident laser wavelength and was interpreted based on the angular distribution of

photoelectrons within the bulk of solid state materials. It was suggested that subwavelength structures within the bulk could be responsible for the scattering. Shortly after, it was discovered that permanent birefringent structures, controlled by polarization, could be inscribed within fused silica directly by writing tracks into the bulk by focusing an ultrafast laser while displacing the sample orthogonally to the laser light [47]. However, this experiment reported positive birefringence and explained their observation due to light induced anisotropy (anisotropic bond rearrangement). It was not until 2003 when the discovery of self-organized gratings were made within the bulk of fused silica after being irradiated by a focused femtosecond pulsed laser [2]. Depending on the irradiation conditions, these highly ordered subwavelength structures with features that can be smaller than ~20 nm could be formed in the irradiated volume, giving them the title as the smallest embedded structures ever created by light (Fig. 2.5b). These nanogratings are associated with a negative refractive index change, thus explaining both the form birefringence and anisotropic light scattering [7]. Since the initial observation in fused silica, self-assembled nanogratings have been observed in a handful of transparent materials such as sapphire, tellurium oxide, borosilicate glasses, ULE glass and multi-component glasses [48–53]. However, as opposed to surface ripples, self-assembled nanogratings have only been formed in the bulk of transparent materials even though volume nanogratings have been reported to continuously transform into surface ripples when the laser focus is translated in and out of the sample [54].

The birefringence introduced by nanogratings can be measured by observing the slow-axis orientation and the phase retardance [2]. These parameters can be controlled independently since the retardance is dependent on the laser fluence and the slow-axis orientation is dependent on the polarization of the laser. Once the nanogratings are formed, the retardance can quickly reach a saturation value with weak dependence on the irradiation power. The nanogratings also exhibit two periodicities (Fig. 2.6) [55]. The first grating periodicity runs perpendicular to the polarization and is typically smaller than the wavelength of light depending on experimental conditions. The second period observed runs along the propagation direction of the light, which grows from the beginning of the structure starting with a period relative to the input laser wavelength in the material, λ_0/n. Recent studies suggest that these nanogratings occur in an environment of glass decomposition [56,57]. After examining the interior of the nanogratings by cleaving an irradiated sample with a field emission electron microscope, the formation of nanopores within the nanoplanes are seen with diameters of 10-30 nm. The formation of these nanopores are attributed to SiO_2 decomposition during the laser irradiation.

Beside the polarization dependence and form birefringence, nanogratings possess inherent intrinsic properties. Nanogratings exhibit extraordinary thermal stability and can withstand

temperatures over 1000°C without any significant degradation [8]. At room temperature, nanogratings are estimated to have a lifetime of 300 quintillion years based upon Arrhenius modelling [58,59]. Nanogratings can also be completely overwritten simply by irradiating the pre-written structures with an ultrafast laser with different polarization orientations [15,60]. Also, the structures are self-replicating since they form over distances greater than the spot size of the laser beam [55]. This is suggested to be due to an initial "seeding" from the earlier imprinted structure leading to a self-assembly. However, the physical mechanism responsible for the formation of nanogratings is still currently under debate. Some theories of nanostructure formation attempt to correlate surface ripple and volume nanograting formation [36], after nanogratings induced in the volume were observed to switch into surface ripples continuously [54]. Others have looked at interference based mechanisms from laser induced plasmas with the interference of bulk plasmons [2] to subwavelength formation by nanoplasmas [3]. More recently, interference and self-trapping of exciton-polaritons induced in the bulk was introduced based on observations made in SiO_2 nanostructuring [61]. Each theory is incomplete, with fundamental issues ranging from the explanation of the periodicities observed to electron collision time discrepancies, which is why the mechanism for Type II modification is still unclear. These models will be further described in Chapters 2.2.1, 2.2.2 and 2.2.3.

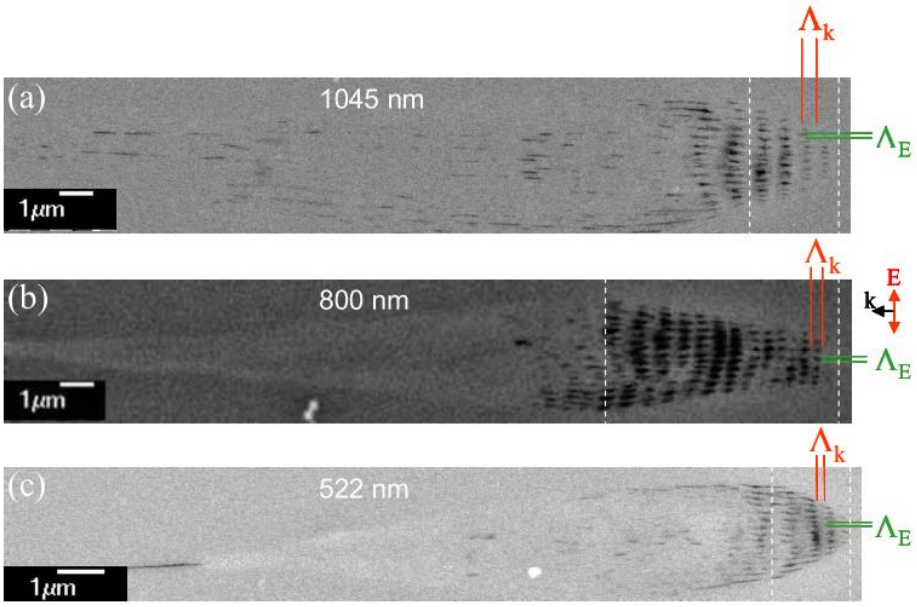

Figure 2.6: SEM images of nanograting cross-sections observed in fused silica after femtosecond laser writing with varying wavelengths: (a) 1045 nm (τ = 520 fs, Ep = 0.9 μJ, 500 kHz, 200 μm/s writing speed), (b) 800 nm (τ = 150 fs, Ep = 0.5 μJ, 250 kHz, 100 μm/s writing speed) and (c) 522 nm (τ = 490 fs, Ep = 0.15 μJ, 200 kHz, 200 μm/s writing speed). E represents the direction of polarization and k is the writing direction. Two periodicities are seen parallel (Λ_k) and perpendicular (Λ_E) to the light propagation. Image source: Yang et al. [55].

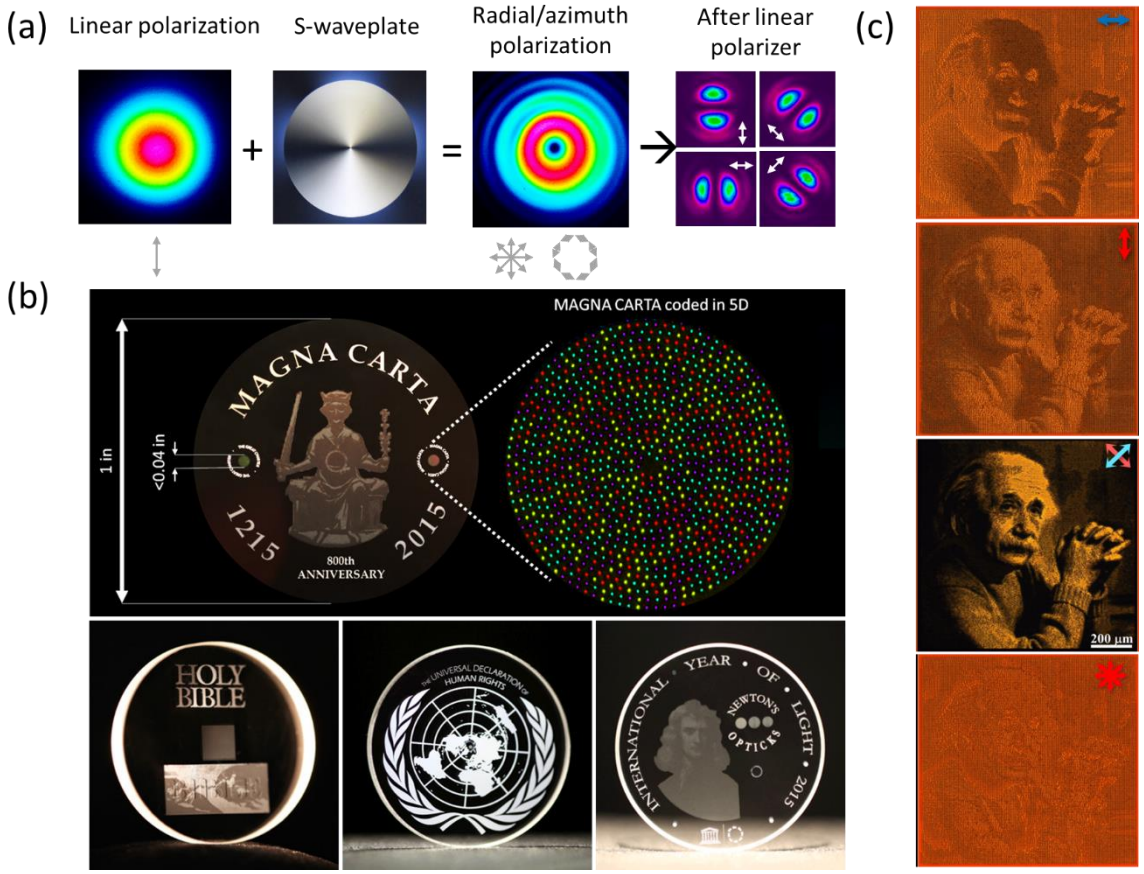

Figure 2.7: Applications of self-assembled nanogratings. (a) Optical converters can be printed to create waveplates that can create space variant polarized and vortex beams. (b) 5D optical memory based on position, slow-axis orientation and retardance provides the ability to store 360 TB of memory with a seemingly unlimited lifetime. (c) Image of Albert Einstein can be hidden from unpolarised light but visible under cross-polarized illumination. This uses the slow-axis orientation of nanogratings for security marking under specific orientations of light. Image sources (a) Beresna et al. [62] (b) Zhang et al. [59] (c) Drevinskas et al. [63]

While the formation mechanism of nanogratings is still under debate, the unique properties of nanogratings have led to the development of a multitude of photonic devices and applications [19,28,64]. Diffractive elements such as Fresnel zone plates [65], Fiber Bragg gratings [66], optical vortex converters (S-Waveplate) [14] and microreflectors [67] have been easily produced and have been utilised in various applications such as polarization imaging [68], optical trapping [69], holograms [13], radially polarized fibre lasers [70] and beam generation [71]. Furthermore, the uniqueness of the birefringence and azimuthal slow-axis direction provides an avenue for 5-dimensional optical data storage [58,59]. By controlling the position within the bulk and the relative retardance and slow-axis orientation, one can easily encode data in the bulk of a transparent material. Due to the small volume necessary for nanogratings, it is possible to encode

hundreds of terabytes of memory into a typical sized data disc made out of a transparent material. With the thermal stability and virtually unlimited lifetime of nanogratings, 5D optical data storage provides an avenue for eternal data archiving (Fig. 2.7).

2.2.1 Interference Based Model

When self-assembled nanogratings were first observed within the bulk of fused silica, the main focus was to explain the subwavelength periodicity observed perpendicular to the polarization of the incoming light. Since surface ripple formation was well understood, the first model proposed was an extension of the traditional interference model [2]. When the light interacts with the glass, multiphoton ionization produces a high density of free electrons creating a plasma. This plasma then begins to absorb the laser light through inverse Bremsstrahlung heating and generates bulk electron plasma waves. These plasma waves run longitudinally and oscillate parallel to the propagation direction of the oncoming irradiation. Therefore, the bulk electron plasma waves interfere with the incident laser light, creating an interference pattern, which initially couples due to inhomogeneities induced by moving electrons in the plane of the light polarization. This subsequently produces a periodic modulation of the electron plasma concentration which creates the structural change in glass. If the medium is able to transfer part of its absorbed energy to the emitted electromagnetic radiation (i.e. positive gain coefficient for the generated plasma waves), an exponential growth of the periodic structure orthogonal to the light polarization is observed and is then set within the material. In order for this model to hold, the longitudinal component of momentum must be conserved similar to the condition in Cherenkov's mechanism of nonlinear wave generation [72].

$$\vec{k}_{pl} = \vec{k}_{gr} + \vec{k}_{ph} \tag{2.5}$$

Here, $\vec{k}_{pl} = \omega_{pl}/v_{pl}$ is the plasma wavevector in the plane of the light polarization, $\vec{k}_{ph} = \omega n/c$ is the photon wavevector and $\vec{k}_{gr} = 2\pi/\Lambda$ is the grating wavevector. The dispersion relation of the electron plasma waves (also known as Langmuir waves) is:

$$\omega_{pl}{}^2 = \omega_p + \frac{3}{2} v_e{}^2 k_{pl}{}^2 \tag{2.6}$$

where $\omega_p = \sqrt{N_e e^2/(\varepsilon_0 m_e)}$ is the plasma frequency, N_e is the electron density, m_e is the electron mass and e is the electron charge, $v_e = \sqrt{2k_B T_e/m_e}$ is the thermal speed of electrons, T_e is the electron temperature and k_B is Boltzmann's constant. Combining the Equations (2.5) and (2.6) and setting $\omega = \omega_{pl}$ for energy conservation, the grating periodicity can be explicitly written as:

$$\Lambda = \frac{2\pi}{\sqrt{\frac{1}{3k_B T_e}\left(m_e\omega^2 - \frac{e^2 N_e}{\varepsilon_0}\right) - {k_{ph}}^2}} \tag{2.7}$$

However, there are a few consequences to this particular model. The model predicts that the period increases with the electron concentration and the temperature. Therefore, when the electron concentration reaches critical, N_{cr}, a steep increase in the period occurs.

$$N_{cr} = \frac{\omega^2 \varepsilon_0 m_e}{e^2} \tag{2.8}$$

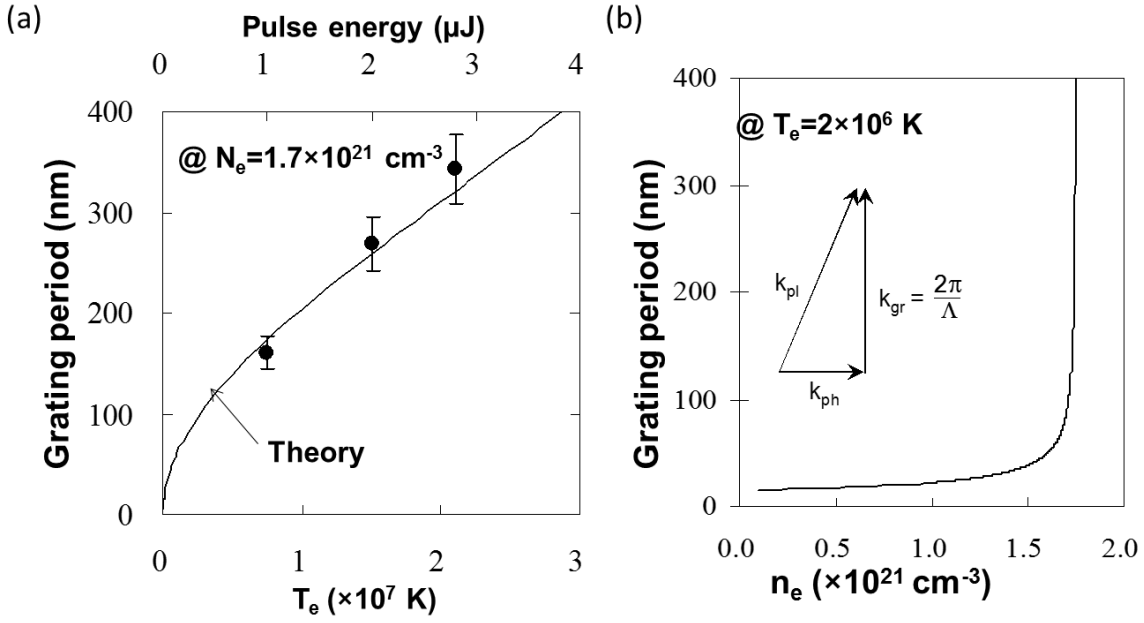

Figure 2.8: Nanograting period evolution predicted by the plasmon interference theory as a function of (a) electron temperature and (b) electron density. The inset image in (b) shows the wave vector matching diagram necessary for the interference model. Image source: Shimotsuma et al. [2]

It also becomes clear the periodicity is dependent on the pulse energy and thus should grow with the pulse energy. Based on the initial observation of 150 nm periodicity from an 800 nm wavelength ultrafast laser, the temperature of electrons and electron density is T_e = 5 X 10^7 K and N_e = 1.75 X 10^{21} cm^{-3} (Fig. 2.8). This would then mean that nanogratings are facilitated in an environment of critical plasma densities and in similar conditions in which microexplosions have been observed [11,73,74], even though nanogratings have been observed in regimes associated with subcritical plasma concentrations (pulse energies as low as 100 nJ [21,75,76]). There is also the issue that the electron temperatures are limited by the bandgap of the material since the heated electrons will dissipate their energy through collisions. In the case of silica glass, electron temperatures cannot exceed 1.04 X 10^5 K. Moreover, the model predicts that nanogratings should

be produced in a single pulse. However, it is well known that nanogratings can only be formed after a sequence of laser pulses. There is also the limitation with respect to the coupling mechanism and how it behaves with further laser irradiation. The plasma lifetime (roughly 150 fs) is too short to explain the influence of subsequent pulses on the interaction during nanograting formation [77].

To overcome the difficulties associated with the critical plasma environment, the interference model was modified using two-plasmon decay. Two-plasmon decay is the parametric process where an incident laser photon splits into two plasmons (two electron plasma waves). The process must fulfil frequency and phase matching conditions for both energy and momentum conservation (ω_0, $\omega_{pl}^{(i)}$ (i = 1, 2) are the frequencies of the incident photon and the respective plasmons) (Fig. 2.9). The major difference from the previous interference model is that this parametric instability develops when the electron concentration reaches a quarter of the critical density ($N_e = N_{cr}/4$) [78–80] so that 2 bulk plasmons are generated with about half of the photon energy ($\omega_{pl}^{(i)} \approx \omega_0/2$). This then makes the energy conservation condition:

$$\omega_0 = \omega_{pl}^{(1)} + \omega_{pl}^{(2)} \approx 2\omega_p \tag{2.9}$$

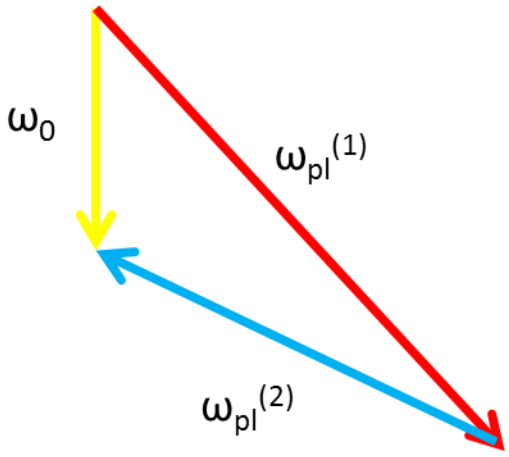

Figure 2.9: Conservation diagram for two-plasmon decay. The plasmon frequencies, $\omega_{pl}^{(1,2)}$, are relatively the same in order for two-plasmon decay to occur.

This introduces an interesting case in which only one plasmon is propagating ($\omega_{pl}^{(1)} = \omega_{pl}$, $k_{pl}^{(1)} = \omega_{pl}/v_{pl} \approx \omega_0/2v_{pl}$) and the second plasmon is the plasma oscillation ($\omega_{pl}^{(2)} = \omega_p$, $k_{pl}^{(2)} = 0$). Instead of the periodic structure being created through interference between the incident electric field and the bulk electron plasma wave, interference between the two plasmons of the same frequency occurs, exciting and propagating in opposite directions in the plane of light polarization (Fig. 2.10). Combining Equation (2.9), (2.5) and (2.6), alongside the dispersion relation for light ($\omega^2 = {\omega_p}^2 + \left(\frac{c}{n}\right)^2 {k_{ph}}^2$), it is possible to obtain an analytical expression for the grating period:

$$\Lambda = \frac{\lambda}{2c\sqrt{\frac{1}{3{v_e}^2}\left(1-2\frac{\omega_p}{\omega}\right)-\left(\frac{n}{c}\right)^2\left(1-\frac{\omega_p}{\omega}\right)}} \tag{2.10}$$

Similar to the previous interference model, the grating period increases with the electron energy and concentration. It is also easy to show from this dependence, assuming $\Lambda >> \lambda$, that the electron energy decreases when the plasma frequency approaches half of the light frequency ($\omega_{pl} = \omega_0/2$) or when the electron concentration approaches quarter of the critical density.

The two-plasmon model can also explain the formation of the periodic structure along the light propagation direction (Fig. 2.10). In this case, it is necessary to suggest interference between two plasma waves of the same frequency ($\omega_{pl} \approx \omega_0/2$) propagating in the opposite direction in the plane of polarization and the plasma oscillation which is not propagating ($\omega_p = \omega_0/2 \approx \omega_{pl}$). This interference will produce a two-dimensional periodic structure (similar to three-wave interference) with one interference term oscillating with a period of the wavelength of light along the propagation direction alongside the other interference term oscillating along the polarization direction:

$$\left|E_{pl}e^{i(k_{pl}^{(1)}{}_x x+k_{pl}^{(1)}{}_y y+\omega_{pl}t)}+E_{pl}e^{i(k_{pl}^{(1)}{}_x x-k_{pl}^{(1)}{}_y y+\omega_{pl}t)}+E_p e^{i\omega_p t}\right|^2 \tag{2.11}$$

A signature of two-plasmon decay is the generation of the 3ω/2 harmonic, which has been observed in experiments on femtosecond direct writing in silica glass [80]. The 3ω/2 is generated through the coupling of an incident laser photon with a plasmon. To satisfy matching conditions within the inhomogeneous plasma, direct coupling only occurs when [81–83]:

$$\beta = 1.41\times10^{14}\frac{{T_{keV}}^2}{I{\lambda_\mu}^2} < 1 \tag{2.13}$$

where T_{keV} is the electron temperature in kiloelectron volts, λ_μ is the laser wavelength in microns and I is the laser intensity (W/cm^2) and:

$$\beta = \frac{9{v_e}^2{k_0}^2}{|v_0|^2{\omega_0}^2} \tag{2.14}$$

where v_e is electron thermal velocity, k_0 is the incident wavenumber and v_0 is the electron quiver velocity (velocity of electron driven by an oscillating laser field). To date, there has not been any observation of the 3ω/2 harmonic during the formation of nanogratings. An apparatus was developed in this thesis to try and measure this harmonic. This will be further discussed in Chapter 5.

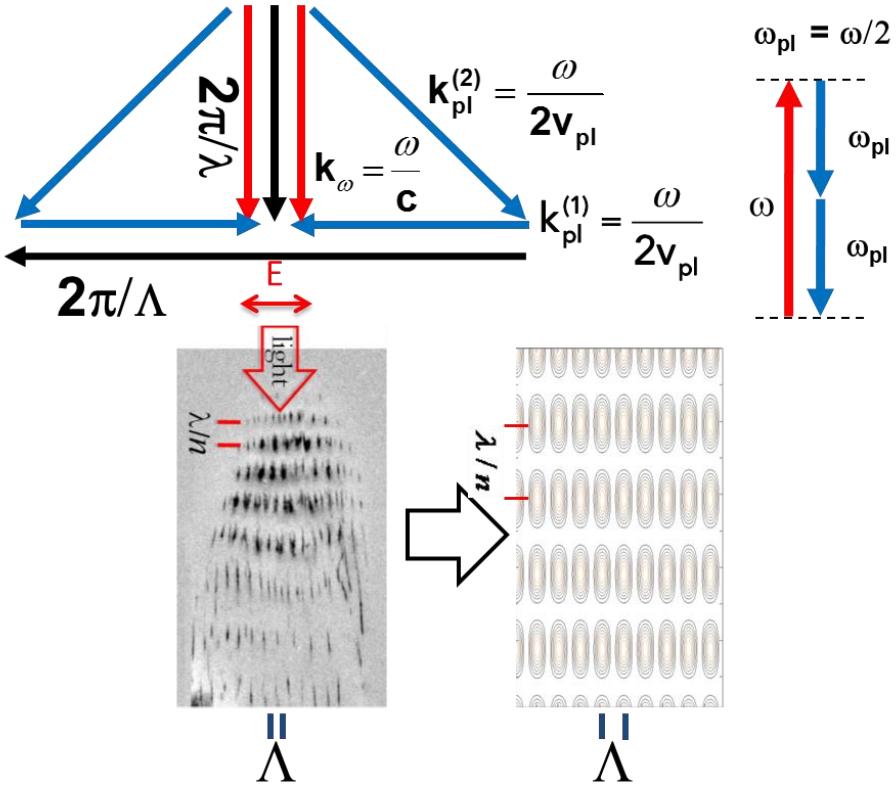

Figure 2.10: Momentum conservation and plasmon interference producing periodic nanostructures via two plasma waves and plasma oscillation interference. The two plasma waves induce the periodicity orthogonally to the electric field direction. Additionally, three-wave interference of the two opposite travelling plasma waves and the incident photon induces the periodicity along the propagation. When Equation (2.11) is modelled, the periodicities match those seen in experiment.

While the two-plasmon decay model shows promise in explaining nanograting formation, there are issues with the model that make it quite unrealistic. The first issue arises in the plasma inhomogeneity. The inhomogeneity threshold of plasma must be less than the ionization threshold. The inhomogeneity threshold, according to the theoretical analysis in a fully ionized plasma, is given by [81,84]:

$$\left(\frac{v_{0Th}}{v_{Te}}\right)^2 = \frac{12}{k_0 L} \tag{2.15}$$

where L is the plasma scale length, v_{Te} is the thermal velocity and v_{0Th} is the quiver velocity at threshold (i.e. $v_{0Th} \sim c$). During experiments described in this thesis, the threshold intensity in units of 10^{14} W/cm^2, I_{14Th}, is given by:

$$I_{14Th} \cong \frac{0.04Te}{\lambda L} \tag{2.16}$$

which is easily satisfied for typical laser parameters, knowing that the temperature to excite an electron is 10 eV in fused silica and the scale length is roughly 10 μm, yielding a threshold of 10^{13} W/cm^2. However, the growth rate for the instability is of the order of 100-200 fs [84]. In order for the two-plasmon decay process to occur, the electron collision time and laser pulse duration needs to be longer than the growth rate. Nanogratings are only thought to be printed for pulse durations greater than 100 fs [16,17] but the electron collision time is between 0.1 - 1 fs [20]. This effectively makes the plasmon decay instability forbidden. One of the methods to circumvent this is to suggest that the environment of the plasma is cold (i.e. electron temperature is smaller than the Fermi energy ~ 1 eV), which is extremely unlikely in ultrafast laser writing.

2.2.2 Nanoplasmonic Model

The other popular model for nanograting formation is based on the enhancement of the electric field due to defects, like colour centres, that are inherently present in transparent glasses during the formation of nanoplasmas (Fig. 2.11) [3,64,85–87]. Transparent glasses typically possess microscopic heterogeneities (such as colour centres) due to either chemical and structural variations, voids, density fluctuations or gas inclusions. When focusing an ultrafast laser pulse into the bulk, it ionizes the microscopic heterogeneities leading to the formation of inhomogeneous plasma (Fig. 2.11a). Electrons and/or holes are trapped at the location of the heterogeneities and their ionization potential is reduced, allowing them to be ionized more easily than other electrons in the atoms through multiphoton ionization. These seed electrons then initiate avalanche ionization and thus having defects make the plasma inhomogeneous. Hot spots generated in the inhomogeneous plasma by the first pulse then evolve into spherically shaped nanoplasmas over several pulses by a memory-based feedback mechanism of the previous nonlinear ionization (Fig. 2.11b) [3]. Each subsequent pulse decreases the ionization threshold and enhances ionization of the material on the following pulse. The under-dense nanoplasmas experience field enhancement at the edges, leading to an asymmetric growth of the initially spherically-shaped plasma, orthogonally to the laser light polarization (Fig. 2.11c). The spherically-shaped nanoplasmas become ellipsoidal where the electric field at the poles, E_{pol}, and the equator, E_{eq}, is (Fig. 2.11e) [3,87]:

$$E_{pol} = \frac{3\varepsilon' E}{\varepsilon' + 2} \tag{2.17}$$

$$E_{eq} = \frac{3E}{\varepsilon' + 2} \tag{2.18}$$

where ε' is the ratio of the real parts of the electric permittivities for the plasma and dielectric medium. The electron concentration is below critical as long as $E_{pol} < E_{eq}$, which would then continue the asymmetric growth of the nanoplasmas. However when $E_{eq} \approx E_{pol}$, the electron concentration of the nanoplasmas approaches critical and the asymmetric growth accelerates, finally evolving the nanoplasmas into plasma disks. Field enhancement at the edges of the disks provides an environment to form nanoplanes. With successive pulses, the nanoplanes continue to coherently grow as new nanoplanes form and link together (Fig. 2.11d). The electron concentration in between planes exceed critical and thus make the planes quasi-metallic in behaviour. This influences the light propagation of the laser pulses and causes interference of scattered and incident light. Quasi-metallic waveguiding emerges and controls the plane distribution to be no less than half of the femtosecond laser wavelength in the medium. Ionization is then suppressed beside each plasma plane and enhanced at distances of $\lambda/2n$, which coincides with the periodicity of nanogratings [86,87].

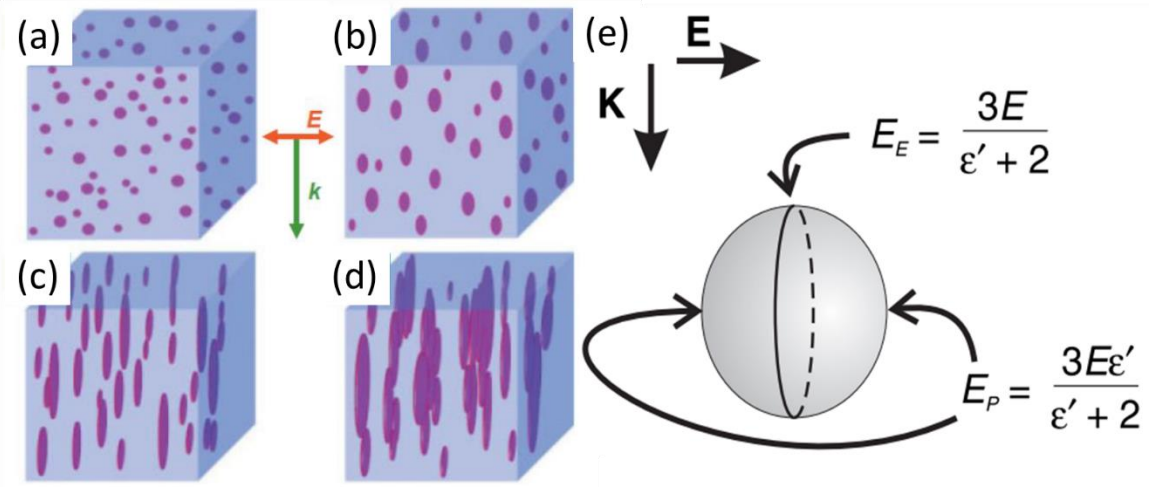

Figure 2.11: The nanoplasmonic theory. (a-d) Evolution of nanoplasma starting from the formation of inhomogeneous nanoplasmas (a) into nanoplanes that form due to field enhancement (d). (e) Schematic diagram showing local field enhancements outside a nanoplasma (k is the propagation direction and E is the electric field direction). Image source: (a-d) R. Taylor et al. [64] (e) Bhardwaj et al. [3]

While this theory helps overcome the issue of nanogratings forming under multiple pulses, it still runs into the issues concerning critical plasma concentrations. The theory also breaks down with the dependency of the periodicity on the number of laser pulses. Nanoplanes are suggested to be set to the smallest possible standing wave cavity in the material [36], making the periodicity independent on subsequent pulses even though experimentally this is not the case. The dependency on the number of pulses also collapses in the model when it comes to the

corresponding changes of the refractive index observed [77]. This theory also does not explain the periodicity observed in the propagation direction.

2.2.3 Exciton-Polariton Model

To overcome the difficulties with electron concentrations, as well as explaining the observed longitudinal periodicity of nanogratings, an exciton-polariton mediated self-organization mechanism was proposed (Fig. 2.12) [61]. Exciton-polaritons are a quasiparticle that arises due to strong couplings between an exciton (an electron hole and bound state of an electron, which are attracted to each other via Coulomb force) and light (photon). The evidence of exciton existence in typical SiO_2 glass is indicated by a strong exciton peak in the absorption spectra at ~10.4 eV. In addition, the binding energy and oscillator strength of excitons in SiO_2 is expected to exceed by orders of magnitude to GaAs where excitonic effects are studied. Also, the appearance of polarization gratings oriented in the direction of the propagation of light due to interference of exciton-polariton modes within GaAs was predicted in previous studies [88], providing the potential of nanograting formation in other glasses that exhibit excitons. The period for the grating in GaAs was found to increase as a function of the distance from the front edge of the sample. This is because of the dependence of the splitting between the two interfering exciton-polariton modes on the group velocity of the exciton-polaritons. In fused silica, the two dispersion branches of exciton-polaritons could be excited via multiphoton absorption, which leads to the formation of nanogratings when the propagating exciton-polaritons interfere (Fig. 2.12a). It should be noted that the exciton-polaritons form a dynamical grating that is dependent on time. However, exciton-polaritons have a lifetime that is limited to fractions of a picosecond (<300 fs), effectively trapping the excitons. Due to exciton self-localization, the polariton gratings are frozen and may then be permanently imprinted by the exciton-polariton interaction with light. When modelling this scenario, the initial period of this grating increases as the square root of the distance from the edge of the sample, with an initial periodicity approximately equivalent to the wavelength of the incident light (Fig. 2.12 b, c). These two periodicities are in excellent agreement with the two periodicities observed in nanograting formation. The critical concentration for the formation of exciton-polariton grating formation is estimated to be 10^{15} cm^{-3} for a laser of 800 nm. If the electron concentration does not exceed this value, nanograting formation cannot occur, potentially explaining the phase transition between Type I and Type II modification. Evidence of this mechanism is in the generation of molecular oxygen through the recombination of self-trapped excitons. Formation of nanopores filled by oxygen have been observed in many experiments investigating volume expansion induced by femtosecond laser irradiation. Clusters of

these nanopores form the nanogratings, making them responsible for the freezing of the polariton-induced grating in silica glass.

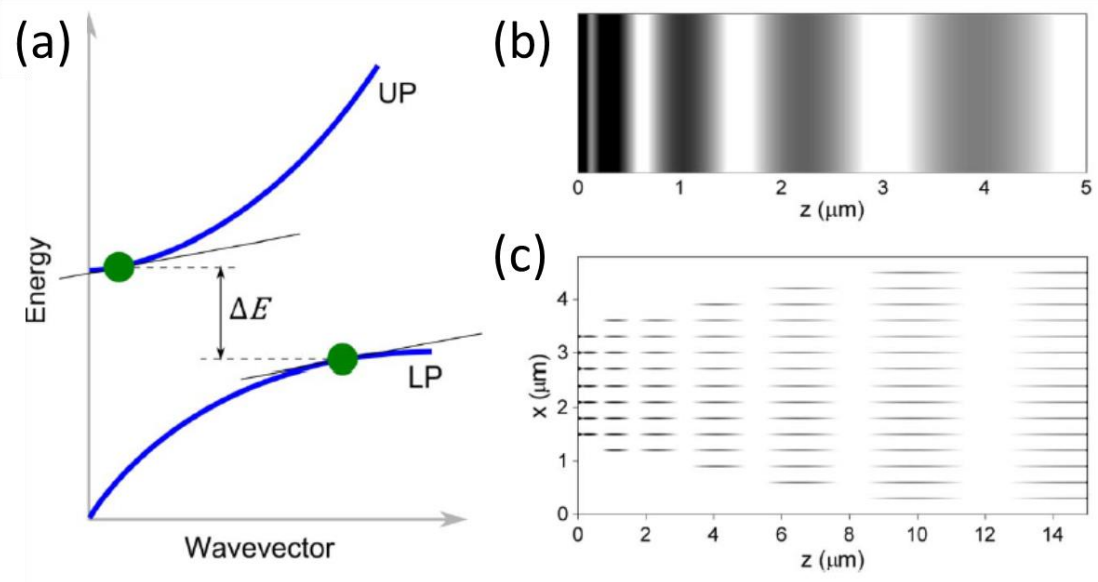

Figure 2.12: Theoretical simulation for the exciton-polariton nanograting formation model. (a) Schematic of the exciton-polariton dispersion. The exact position on the upper polariton branch (UP) and lower polariton branch (DOWN) where the group velocities are the same, to facilitate the interference with an energy split of ΔE. (b) Theoretical simulation of the formation of the grating in the propagation direction, *z* (zoomed in). (c) Theoretical simulation of the grating periodicity in the *x* and *z*. Image source: Beresna et al., [61]

While this formation mechanism overcomes the obstacles associated with critical concentrations as well as fully explaining the observed periodicities, there is an issue with the strong material dependence. This explanation holds valid for SiO_2 glass, which provides an environment for strong excitonic behaviour. However, nanogratings have been observed in a multitude of transparent materials which may or may not share the same sort of exciton potential. There is also the matter with high incident fluences where the exciton-polariton interaction is screened by the absorbing electron plasma, which begins to develop secondary electrons instead.

2.3 Void Formation

Void formation in transparent materials has been an active topic of study with ultrafast lasers due to an abundance of applications in micro-fabrication, including high-density optical storage [29]. Voids are typically spherical volumes of less dense material, or a hole, surrounded by higher density material [29,73], which can be created by single [73] or multiple [89] femtosecond pulses

at high intensities. When tightly focusing a single pulse with energy lower than the critical power ($P_{cr} = 3.77\lambda^2/8\pi n_0 n_2$ [90]) at a shallow depth or using immersion optics, spherical aberrations and self-focusing are negligible. The threshold for multiphoton ionization is then met at the geometrical focus, where the excited electron concentration will dramatically increase due to impact ionization. Since the ionization is confined to a small volume, the energy is quickly transferred to the lattice producing high temperatures and extreme pressures, similar to those seen in the formation of stars and planets [10]. This tight confinement and extreme conditions subsequently results in a shock and/or rarefaction wave and stress that exceeds the Young modulus of the material [10,29,73]. A microexplosion occurs at the focus, ejecting material from the centre and forces it to the surrounding volume that results in the formation of a void as small as 200 nm within a compressed shell [11,73] (Fig. 2.13). The radius of the shock-affected region, r_{sh}, is given by [9]:

$$r_{sh} \cong \sqrt[3]{\frac{E_{abs}}{\frac{4}{3}\pi Y}} \tag{2.17}$$

where E_{abs} is the absorbed energy and Y is the Young modulus of the bulk material. However, this model only considers the actual microexplosion phase and does not consider any post-explosion relaxation of the material.

If the input pulse exceeds the critical power or focuses at a deeper depth in the bulk of a material, the energy is deposited over a larger volume around the focus, instead of converging at a point leading to the formation of void arrays [91,92]. Spherical aberration can further expand the energy deposition region resulting in an elongated plasma channel. After plasma rapidly transfers energy to the lattice, a cylindrical shock wave emerges leading to the rupture of the material behind the wave's crest. The formation of such channels by single pulse irradiation have been previously observed, which were observed to break into chains of voids by subsequent irradiation [92,93] but single pulse imprinting of void arrays have been reported [94]. However, the theory detailing how these chains form is still under debate. When periodic void formation was first observed [91], the femtosecond beam had to focus close to the bottom surface of the transparent glass, with the filament produced reaching the bottom surface. Once the filament reaches the bottom surface, the core of the filament increases in temperature causing it to be highly absorbent, especially near the end of the filament. This then facilitates a microexplosion forming a void at the bottom of the filament. The next pulse interacts with the region around the void formed beforehand, resulting in a new high temperature location facilitating a microexplosion in a chain fashion. However, it is clear that periodic void chains can form in the bulk without approaching the bottom of the glass [92,95]. Other studies suggest void arrays arise

from the interference of ultrafast laser driven electron waves interfering to create a standing electron plasma wave, inducing multiple periodic microexplosions, similar to the interference model of nanograting and surface ripples [96]. Another suggested physical model is based on the interfaces generated by spherical aberration and the nonlinear effects of femtosecond pulses [97]. Using the non-paraxial nonlinear Schrödinger equation alongside the effect of spherical aberration, the model shows that the Gaussian focal point exhibits quasiperiodic alternations in laser fluence. In the locations where the laser fluence is a maximum, more electrons are produced, thus creating periodic microexplosions, subsequently creating a chain of voids, providing evidence that the period of voids can be controlled with spherical aberration. However, in all of these studies, it is unsure that critical electron concentrations are met. There is also the fact that long void arrays can be produced in a material with low critical powers for self-focusing. This provides further evidence that the void shape depends on the heat generated and fluidity of the surrounding area of the structure that has been thermally melted during laser irradiation [98]. Regardless of the mechanism, optical cavitation in glass can lead to Type III modification in the irradiated zone and have been used in a multitude of applications such as waveguides [99], interferometers [98], optical data storage [29] and polarization optics [100].

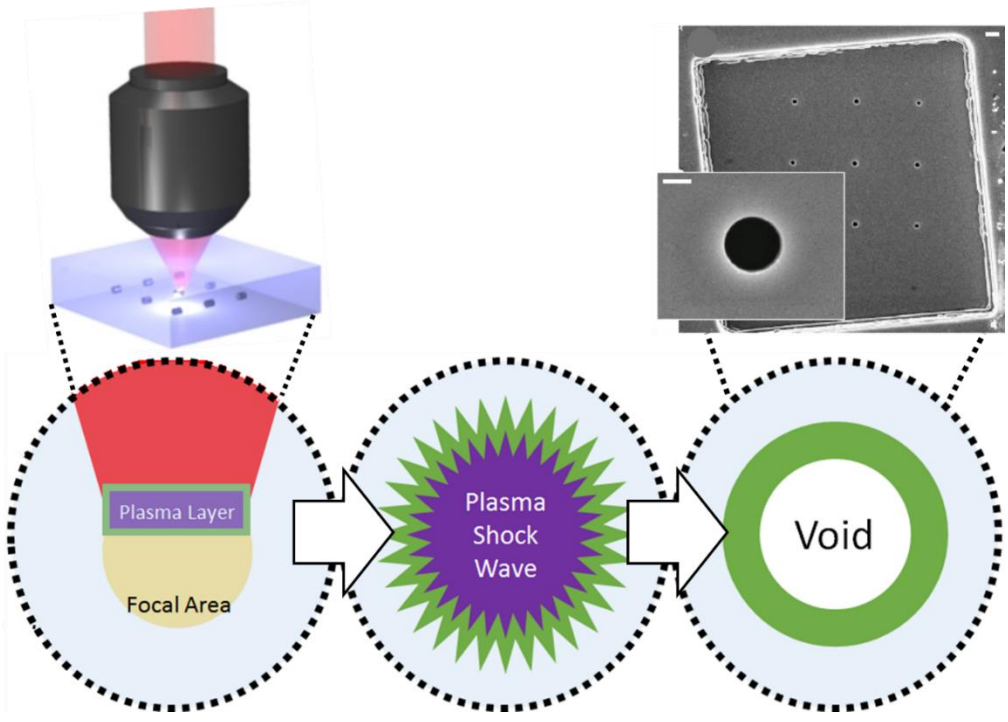

Figure 2.13: Diagram of the laser-induced microexplosion in transparent materials to the formation of voids. Plasma is generated by focusing ultrafast laser pulses into the bulk such that the energy absorbed exceeds the Young's modulus of the bulk, resulting in a shock wave. The end result is the formation of the void within the bulk. Inset image of scanning electron microscope image (SEM) of voids produced in the bulk of sapphire. Image source of SEM: Juodkazis et al. [10].

The above classification of modification regimes has been regarded as a non-reversible path following the laser intensity regimes. However, recently it was observed that under moderate focusing conditions (NA > 0.4) in fused silica, self-assembled nanogratings (Type II) could be developed from void formation (Type III) after the first few pulses [101]. While void formation is not necessary for the formation of nanogratings [101], it is interesting to observe Type II modification after void formation when it was originally theorized that near-critical threshold plasma densities are met when the voids are visible [21,102]. This will be further discussed in Chapter 7.

Chapter 3: Spatio-Temporal Couplings

3.1 Defining the Spatio-Temporal Couplings

Broad spectrum is one of the key requirements for ultrafast laser systems. The invention of effective mechanisms capable of locking spectral components in phase, paved the way towards pulses as short as one optical cycle. Given that these ultrashort pulses have durations on the order of timescales for fundamental molecular and atomic processes, they have found a wide variety of applications, stretching from observing photochemical processes on femtosecond time scales [103], to selectively instigating molecular excitation via adaptive quantum control [104]. Nonlinear processes triggered by ultrafast laser pulses have revolutionized the world of microscopy through targeted nonlinear excitation techniques. In particular, second- and third-harmonic generation microscopy as well as multiphoton microscopy provide the best non-invasive means for biological imaging [105]. Femtosecond lasers have also been successfully applied to non-invasive surgeries in the bulk of human tissue with sub-micrometre resolution without collateral damage [106]. Ultrafast laser pulses are commonly described in terms of their intensity and phases, treating the electric field's dependence on spatial coordinates separately. This is assuming the temporal properties of a pulse are the same across every spatial position of the beam. This assumption is typically incorrect since the broad spectrum comes at the price of taking extra care to control the phase of the pulse, which can be disturbed by dispersive media or self-phase modulation, and lead to a significant decrease of pulse intensity. Therefore, ultrashort pulses exhibit an interdependence of spatial and temporal coordinates, which is better known as spatio-temporal couplings.

Spatio-temporal couplings are common place, particularly from misaligned prisms, gratings or other dispersive mediums. Normally, this is seen as a negative effect. However, a method called chirped-pulse amplification (*CPA)* clearly demonstrates that the manipulation of spectral components could be exploited for the benefit of alleviating the issue of damaging gain mediums by excessive intensities by temporarily stretching out a pulse before the gain medium. The amplified pulse is then recompressed back to the original pulse width in the same manner it was stretched, enabling terawatt to petawatt intensities [107,108]. Recently, simultaneous spatial and temporal focusing (*SSTF*) has shown promise in overcoming nonlinear side-effects when reaching the critical power near the focus, not only in material modification [109–113], but also in microscopy and tissue ablation [114–117] and atmospheric propagation [118]. This is accomplished by separating the spatial components of the incident light pulse. Each portion of the beam then carries a reduced local-bandwidth, resulting in an increased overall pulse duration and

reduced intensity. Upon focusing, the separated components are brought back together recovering the initial bandwidth and duration of the laser pulse. As a result, the maximum light intensity is only observed near the focus. Thus, nonlinear phenomena are localized at the focus as opposed to conventional focusing of a transform limited femtosecond-picosecond laser pulse.

Normally working with temporal and spatial dependencies like those seen within SSTF and CPA, the vectorial nature of the spatio-temporal couplings is overlooked. Spatial chirp (spread of frequency components across the beam front; *SC*) [119], pulse front tilt (inclination of the intensity front with respect to the propagation direction; *PFT*) [120], angular dispersion (angular separation of light rays of differing frequencies; *AD*) [121,122] and wavefront rotation/Time vs. Angle (rotation of wavefront in time - lighthouse effect*; WFR/TVA*) [123,124] have all been discussed individually from a theoretical point of view and thorough experimental techniques have been developed to characterize them [125]. In this chapter, I will go into greater detail of these spatio-temporal couplings and will discuss the general definitions of the spatio-temporal couplings and go into detail about how they are characterized. I will also discuss recent advancements in controlling these parameters and how they've been implemented in various fields. From there, I'll discuss intrinsic phenomena thought to be originating from spatio-temporal couplings with respect to ultrafast laser material modification.

3.1.1 General Definition of the Electric Field with Spatio-Temporal Couplings

Ultrafast laser pulses are typically expressed in terms of their spatial and temporal dependencies of the electric field. As discussed earlier, typically the spatial and temporal dependencies are treated separately from one another. However, because of their interdependence on one another, it is important to correctly state the electric field of an ultrafast laser pulse with the appropriate spatio-temporal couplings. The pulse free of any spatio-temporal couplings after the lens has the following electric field distribution [126]:

$$E(x,t) = E_0 \exp\left\{-\left(\frac{1}{w^2} + \frac{ik}{2R}\right)x^2 - \left(\frac{1}{\tau^2} - i\beta\right)t^2\right\} \tag{3.1}$$

where w is the beam radius, R is the beam front curvature (initially $R = \infty$), k is the wavevector, τ is the temporal width and β is the TC. When this pulse is traversed through a dispersive medium like a grating pair, spatio-temporal couplings like SC or AD can be introduced, which would drastically change the electric field. Then the electric field with a coupling term between time and space is:

$$E(x,t) = E_0 \exp\left\{-\left(\frac{1}{w^2} + \frac{ik}{2R}\right)x^2 - \left(\frac{t - px}{\tau}\right)^2 + i\beta t^2\right\} \tag{3.2}$$

where *p* is the coupling term. It is a complex number with the real part representing the pulse front tilt (PFT) and the imaginary part representing the WFR (or TVA) [126]. To understand how spatio-temporal couplings behave, an identification of the major spatio-temporal coupling that is seen in and out of the focus is needed. Therefore, the electric field in Equation (3.2) can be re-written in a more functional form based upon a well-established matrix formalism known as Kostenbauder matrices [127] (discussed further in Chapter 3.2.1). The electric field represented by complex Q-parameters is [126]:

$$E(x,y,t) = E_0 \exp\{-\tilde{Q}_{xx}x^2 - \tilde{Q}_{yy}y^2 - 2\tilde{Q}_{xt}xct - \tilde{Q}_{tt}c^2t^2\} \tag{3.3}$$

Here complex parameters $\tilde{Q}_{xx}$ and $\tilde{Q}_{tt}$ can be written as:

$$\tilde{Q}_{xx} = \frac{1}{w^2} + i\frac{\pi}{\lambda_0 R} \tag{3.4}$$

$$\tilde{Q}_{tt} = \frac{1}{c^2}\left(\frac{1}{\tau^2} - i\beta\right) \tag{3.5}$$

where $\tilde{Q}_{xx}$ describes the spatial properties of the beam (beam spot size and wave-front curvature) and $\tilde{Q}_{tt}$ describes the temporal properties of the beam (pulse duration and temporal chirp). $\tilde{Q}_{xt}$ represents the interdependence between the spatial and temporal properties of the beam. The real part of $\tilde{Q}_{xt}$ is representative of the PFT and the imaginary party represents the WFR.

Although this formalism of the electric field provides a general method to state the electric field in the (x, t) domain, there are scenarios where it can be beneficial to state the electric field in terms of different domains. For example, the field can be Fourier transformed to the (x,ω) domain [126]:

$$E(x,\omega) = \frac{1}{2\pi}\int E(x,t)e^{-i\omega t}dt \propto \exp\{-R_{xx}x^2 - 2R_{x\omega}xc\omega - R_{\omega\omega}c^2\omega^2\} \tag{3.6}$$

where the R-coefficients can be written in terms for the Q-parameters.

$$R_{xx} = \tilde{Q}_{xx} + \frac{\tilde{Q}_{xt}{}^2}{\tilde{Q}_{tt}} \tag{3.7}$$

$$R_{x\omega} = \frac{-i\tilde{Q}_{xt}}{2\tilde{Q}_{tt}} \tag{3.8}$$

$$R_{x\omega} = \frac{1}{4\tilde{Q}_{tt}} \tag{3.9}$$

Following the same arguments that were used for the (x, t) domain, these complex coefficients each describe a physical component of the beam. R_{xx} is representative of the beam spot size and wavefront curvature. $R_{\omega\omega}$ represents the bandwidth and the frequency chirp (essentially equivalent to the temporal chirp). $R_{x\omega}$ represents the spatial chirp and the wavefront tilt dispersion (the tilt of the wavefront dependent on the frequency). It can then be seen that depending on the measurements made in a lab environment, it may be more beneficial to write the electric field in terms of the observables measured. The electric field can also be written in terms of the (k, ω) and the (k, t) domain simply by Fourier transforming the fields accordingly:

$$E(k,\omega) \propto \exp\{-S_{kk}k^2 - 2S_{k\omega}kc\omega - S_{\omega\omega}c^2\omega^2\} \tag{3.10}$$

$$E(k,t) \propto \exp\{-P_{kk}k^2 - 2P_{kt}kct - P_{tt}c^2t^2\} \tag{3.11}$$

S_{kk} represents the angular divergence and angular phase-front curvature (similar to wavefront curvature but in the spatial-frequency domain). $S_{\omega\omega}$ is the bandwidth and frequency chirp. S_{kw} describes the angular dispersion and the angular spectral chirp. P_{kk} describes the angular divergence and the angular phase-front curvature. P_{tt} describes the temporal pulse width and temporal chirp. P_{kt} represents the time versus angle (similar to WFR) and angular temporal chirp.

Based on this formalism, it is straightforward to derive relations between spatio-temporal couplings from direct observables in the lab. However, depending on what measurements are made, it can be difficult to define the electric field appropriately. In order to properly define the electric field, six independent variables must be measured. In certain cases, it may be easier to measure certain parameters that may not be in the same domain. For example, SC can be measured using a fibre spectrometer in the (x, ω) domain and temporal chirp can be measured with characterization systems such as a FROG measurement system in the (x, t) domain (discussed further in Chapter 3.2.2). Due to the nature of the electric field definitions in the four domains, it is quite simple to calculate the values of any coefficient based upon any measurement made of the spatio-temporal couplings, similar to Equations (3.7 - 3.9). A summary of these relations are written in Table 3-1, making it possible to define the electric field of an ultrafast laser pulse with spatio-temporal couplings [126].

(x, t)	(x, ω)	(k, ω)	(k, t)
$\tilde{Q}_{xt}$	$\frac{iR_{x\omega}}{2R_{\omega\omega}}$	$\frac{S_{k\omega}}{4(S_{kk}S_{\omega\omega} + {S_{k\omega}}^2)}$	$\frac{-iP_{kt}}{2P_{kk}}$
$\frac{-i\tilde{Q}_{xt}}{2\tilde{Q}_{tt}}$	$R_{x\omega}$	$\frac{-iS_{k\omega}}{2S_{kk}}$	$\frac{P_{kt}}{4(P_{kk}P_{tt} + {P_{kt}}^2)}$

$\frac{\tilde{Q}_{xt}}{4(\tilde{Q}_{xx}\tilde{Q}_{tt}+\tilde{Q}_{xt}{}^2)}$	$\frac{iR_{x\omega}}{2R_{xx}}$	$S_{k\omega}$	$\frac{-iP_{kt}}{2P_{tt}}$
$\frac{i\tilde{Q}_{xt}}{2\tilde{Q}_{xx}}$	$\frac{R_{x\omega}}{4(R_{xx}R_{\omega\omega}+R_{x\omega}{}^2)}$	$\frac{iS_{k\omega}}{2S_{\omega\omega}}$	P_{kt}

Table 3-1: Summary of Spatio-Temporal Coupling Relations in All Four Domains

3.1.2 Angular Dispersion and Spatial Chirp

When transmitting an ultrafast laser pulse through a dispersive medium, the broad spectrum is affected, causing different wavelengths in the beam to deviate from one another spatially. The dispersive nature of materials was first observed by Newton in 1704 [128]. He observed that white light propagates a prism caused the different frequency components that made up the white light to leave the prism at different angles. The refractive index of the medium is wavelength dependent, thus making the angles of refraction, governed by Snell's law, change at each interface based on the wavelength. The measure of the angular separation of the different wavelength components of light going through a prism, grating or another dispersive medium, is known as angular dispersion (*AD*). AD is equal to the rate of change of the angle of deviation, with respect to the change in wavelength.

$$AD = \frac{\mathrm{d}\theta_0}{\mathrm{d}\omega} \tag{3.12}$$

AD is most often introduced into the beam with the use of gratings or prisms (Fig. 3.1). When an incident wave with a spectral distribution impinges on one of these dispersive mediums, each frequency component is dispersed in a different direction. As the beam propagates through the dispersive medium, certain components will travel faster than others; known as group velocity dispersion (*GVD*). To quantify the total dispersion of an element based on length, GVD can be represented as a length dependent dispersion known as group delay dispersion (*GDD*). The sign of GDD relates to what portion of the beam is leading (i.e. which group velocity is faster/slower). When GDD is positive, the redder portion of the beam leads ($v_{red} > v_{blue}$). When GDD is negative, it is vice versa ($v_{red} < v_{blue}$). This property makes AD an enabling tool in many areas of optics. Pulse compression and pulse stretching can be accomplished through the use of a series of prisms and gratings (discussed further in Chapter 4.2.2 and 4.2.3). One of the key benefits of this is through CPA. When trying to reach short pulse durations and create high power lasers, there is a potential to damage the gain medium with high peak powers of several gigawatts per square centimetre [107]. To avoid this, it is possible to reduce the peak power of a pulse before entering the gain medium at the amplifying stage of a laser. By introducing angular dispersion to the beam,

one can shape the temporal properties of the pulse. Spectral broadening will shorten the bandwidth which effectively stretches the pulse duration of the pump. The stretched pulse is then sent to the gain medium, which amplifies the signal without damaging the gain medium itself. The angular dispersion is then compensated afterwards with the use of an anti-parallel dispersive element equivalent to what was used to induce the dispersion.

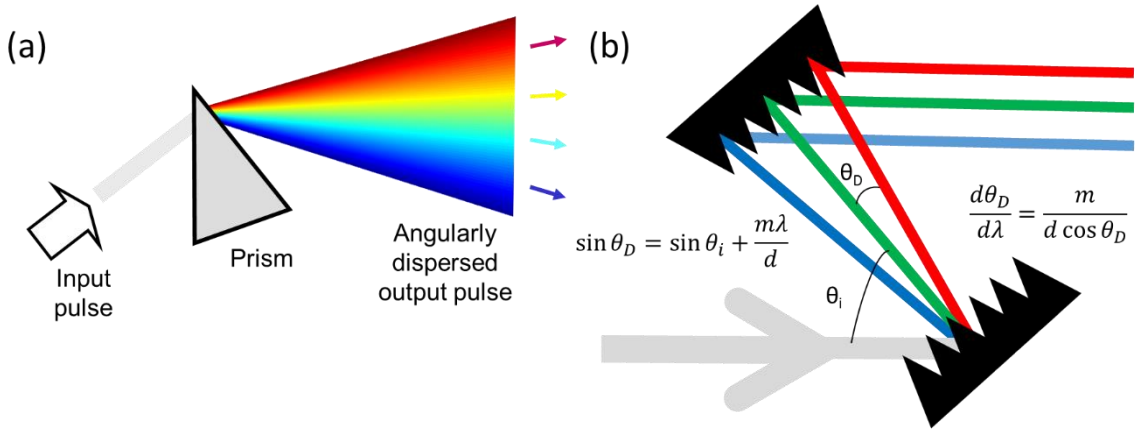

Figure 3.1: AD and SC induced by (a) prism and (b) gratings.

A beam that experiences angular dispersion effectively separates the frequency components in a space transverse to the propagation direction. As the beam propagates, the frequency components naturally separate in space and results in what is known as spatial chirp (*SC*). If a second prism or grating is aligned anti-parallel to the previous optic inducing the original angular dispersion, the angular dispersion is removed but a significant amount of SC remains. While a double pass geometry of a prism/grating pair can effectively remove the SC, minor misalignments of the dispersive elements can result in residual SC, which can often be undesirable in many routine laser laboratories. SC can also be introduced into the path by propagating through a tilted substrate, depending on the spectrum of the pulse and the thickness of the medium.

SC is typically defined in one of two ways. The first is to measure the centre frequency, ω_0, of each spatial slice of the laser pulse. This yields a position dependent frequency function, $\omega_0(x)$. The slope of said function with respect to position is known as frequency gradient (*FRG*) [119,129].

$$FRG = \upsilon = \frac{\mathrm{d}\omega_0}{\mathrm{d}x} \tag{3.13}$$

The other definition would be to find the beam centre position, x_0, of each frequency component, yielding the function $x_0(\omega)$. The slope of this function would provide a valid measure for SC known as spatial dispersion (*SD*) [119,129].

$$SD = \zeta = \frac{\mathrm{d}x_0}{\mathrm{d}\omega} \tag{3.14}$$

SD is often the more fundamental of the two since it can be directly measured through AD. When a beam with AD travels a distance, *L*, the induced change in SD is:

$$\Delta\zeta = L\frac{\mathrm{d}\theta_0}{\mathrm{d}\omega} \tag{3.15}$$

In the absence of SC, both parameters are effectively zero. Also, more importantly, these parameters are not reciprocals of one another. The relationship between FRG and SD depends on the shape of the spectrum and the spatial-mode profiles of all the frequency components in a laser pulse; the bandwidth, *Δω*, and the beam width, *Δx* [119,129].

$$\upsilon = \frac{\zeta}{\zeta^2 + \left(\frac{\Delta x}{\Delta\omega}\right)^2} \tag{3.16}$$

The distinction between the two parameterizations of SC also follows in the same nature as the temporal chirp (*TC*). TC defines the time dependence of its instantaneous frequency. In a more general sense, it is a measure of how much a pulse is stretched with the sign indicating whether the bluer side or redder side of the pulse is leading. Temporal chirp can be in either the time domain or the frequency domain. In the time domain, the frequency chirp (*FCH*) is the derivative of the instantaneous (angular) frequency with respect to time. In the frequency domain, GDD is the derivative of the group delay with respect to frequency. Similar to the definitions of SC, they are two different, yet equivalent parameters, that are not reciprocals of one another [119]:

$$FCH = \phi_2 = -\frac{\mathrm{d}\omega_0}{\mathrm{d}t} \tag{3.17}$$

$$GDD = \varphi_2 = \frac{\mathrm{d}t_0}{\mathrm{d}\omega} \tag{3.18}$$

$$\varphi_2 = \frac{-\phi_2}{\frac{1}{4}{\phi_2}^2 + \left(\frac{1}{\tau}\right)^2} \tag{3.19}$$

While SC is considered to be obtrusive in most laboratory settings, it has been successfully used in many applications. Fourier-synthesis pulse shaping provides a manner to manipulate femtosecond pulse shapes according to specification [130,131]. Using a grating and lens in a telescopic geometry, pulse shaping is achieved by spatially filtering optical frequency components, which has been used extensively in spectroscopy and optical communications [132,133]. Another application of spatial chirp has been in simultaneous spatial and temporal focusing [134,135]. By inducing SC and then recombining the spectral components at the focal plane of a lens, the intensity distribution is confined to the focal plane and supresses unwanted nonlinear side effects. This will be discussed further in Chapter 3.3.2.

3.1.3 Pulse Front Tilt

AD and SC in a laser pulse can lead to a tilt in the intensity front relative to the phase front. This phenomenon is known as pulse front tilt (*PFT*) [5,79,136]. PFT typically arises from the spatio-temporal couplings due to the considerable involvement of spatio-temporal manipulations in ultrafast lasers [129,137]. The most common is AD since it derives from the use of prisms or gratings, which are used in most ultrafast laser experiments (Fig. 3.2). When light travels through a dispersive medium, different frequency components of the beam will propagate at different angles. This can be alleviated with the use of parallel prisms or grating pairs but if any misalignment or beam divergence remains, a residual PFT and AD will remain. It was generally accepted that AD and PFT are one in the same and have even been explained with different ray-tracing methods [121,138] and general proofs based upon the Fourier Transform [139].

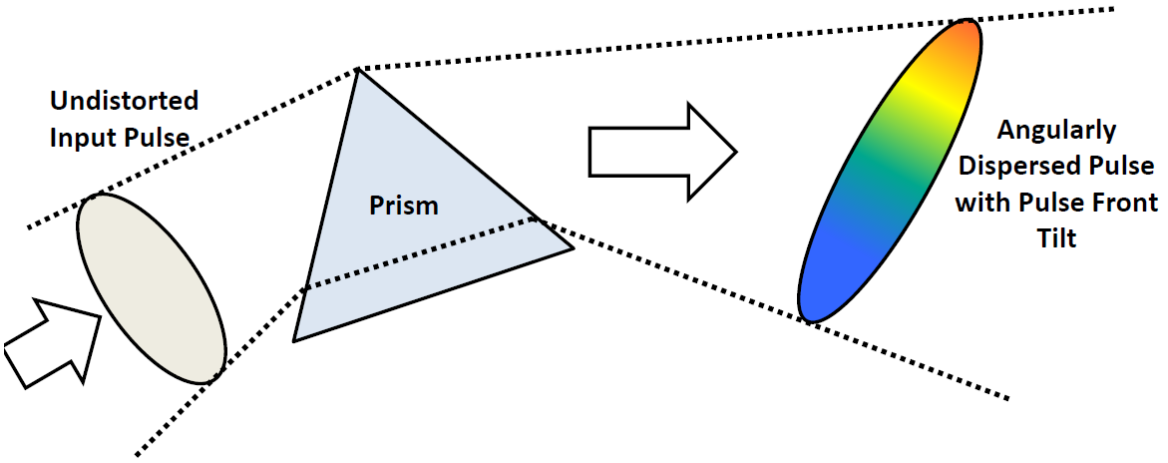

Figure 3.2: Input pulse through a prism introduces angular dispersion, causing pulse front tilt

Akturk et al. [129] demonstrated that this is not typically true and that another form of PFT exists from a beam with spatial chirp (Fig. 3.3). When a spatially chirped pulse, with no AD, enters a dispersive medium, the bluer side of the pulse lags behind its redder counterpart resulting in a titled pulse front, due to the group-velocity dispersion in the medium. This was also demonstrated with a temporal chirped pulse [129]. Therefore, the PFT can be quantified as a sum of the two parts [129]:

$$PFT = PFT_{SC+TC} + PFT_{AD} = (FRG * GDD) + (AD * k_0) \tag{3.20}$$

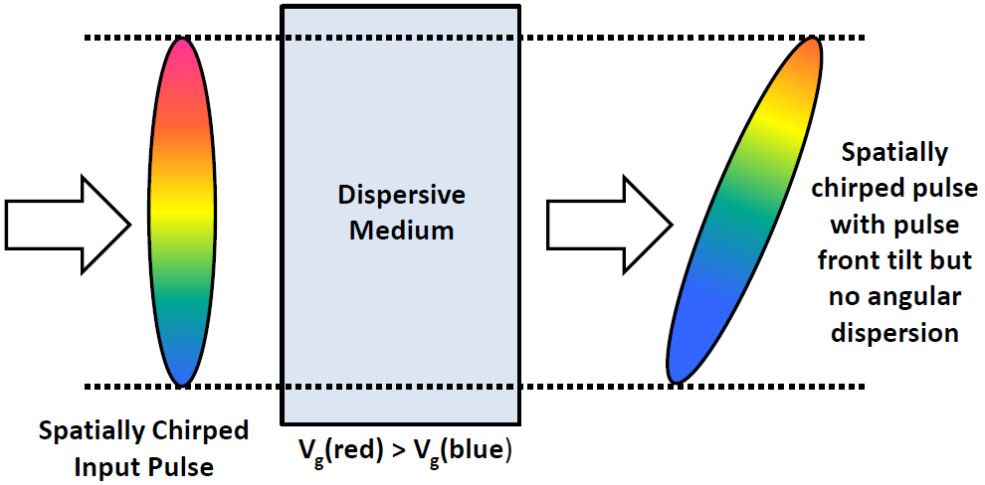

Figure 3.3: Pulse front tilt caused by the combination of spatial and temporal chirp.

Even though PFT is associated with misaligned optical components and can be detrimental for certain experimental settings, it has been used in many applications. Tilted pulse front excitation is used to achieve amplified spontaneous emission in dye solutions by matching the sweep velocity of the pump to the velocity of the generated excitation or to another pulse such as an electron packet. AD (and thus PFT) can also play a key role in achromatic phase matching [140–142]. The presence of PFT in the beam provides higher efficiency in generating harmonics in a birefringent crystal when using large beam sizes. This is especially important for optical designs such as non-collinear optical parametric amplifiers (*NOPA*), where PFT can add an additional level of control in selecting the wavelength desired [142,143]. Another major application of PFT is the generation of THz pulses by optical rectification. For optical rectification, phase matching conditions is necessary to generate high energy THz pulses. By applying PFT to a pulse and pumping a crystal (ex. GaP, GaAS, LN, etc) to generate THz radiation, velocity matching can be achieved to generate high energy THz pulse generation [144–146].

3.1.4 Wavefront Rotation

Alongside PFT, there exists another widely neglected spatio-temporal coupling known as the wavefront rotation *(WFR),* which manifests itself as a lighthouse-like rotation of the beam's wavefront [126]. WFR causes the wavefront of a pulse to effectively rotate in time or, in other words, the direction of propagation of the pulse varies during the pulse duration of a pulse (also known as time vs. angle; *TVA*) (Fig. 3.4). WFR can be thought of in terms of PFT and/or SC. When a beam has PFT and is sent to a focusing optic, the tilted front will have one side of the pulse reach the focusing optic before the other. This results in the initial intersecting portion of the beam to reach the focus before the latter, implying the direction of light sweeps at the focus, resulting in a

rotation in time. With SC, the centre frequency of the laser pulse increases (or decreases) across the beam. This results in the phase to evolve faster (or slower) along the transverse axis causing the wavefronts to rotate as time passes. With this being said, WFR can then be quantified based on the combination of SC and PFT [126]:

$$WFR = \frac{FRG}{2} + (FCH * PFT) \tag{3.21}$$

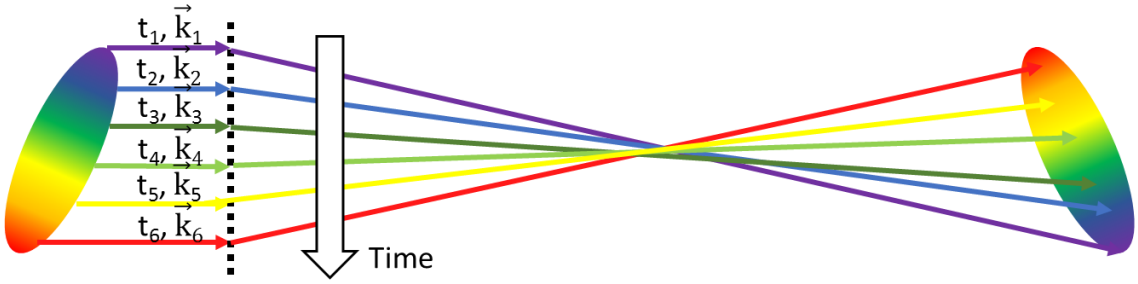

Figure 3.4: Classical interpretation of WFR or TVA. A laser pulse with PFT is focused causing the different components of the beam to arrive at the focus at different points in time. This effectively changes the direction of the pulse at the focus, effectively rotating the wavefront over the pulse duration.

Only recently has WFR been utilized for generating high harmonics and angular separation of the successive attosecond pulses produced in the laser plasma [123,124,147]. When attosecond pulses are generated through the interaction of a high intense laser with a medium, they are emitted around specific phases of the field. They are typically emitted once or twice during a laser cycle and propagate normal to the instantaneous laser wavefront. Therefore, if the wavefront is rotating in time, successive attosecond pulses will change propagation directions as a function of the rotation of the WFR velocity and the number of pulses generated during a cycle. If the propagation directions of each pulse is correlated to an emission time, separate beamlets for each individual attosecond pulse from a train of pulses can be generated at the focus. This has been proven to be an attractive means of temporal gating [124], photonic streaking [148] and phase metrology for carrier envelopes [147]. It should be noted that the effect of the WFR on the light-matter interaction has been visualized for the processes that take place in the attosecond (~10^{-18} s) timescale when the nonlinear optical response of the plasma is formed [147].

3.2 Characterization of Spatio-Temporal Couplings

Due to the ubiquitous nature of spatio-temporal couplings in all laboratory settings, it is important to correctly measure those that exist within a laser beam. This part of the chapter describes the methods used to characterize the pulse throughout the research conducted for this

thesis. However, it should be noted that there are plenty of methods available that are used to characterize and define the spatio-temporal couplings that can provide a complete picture of the properties of a pulse [149–151].

3.2.1 Kostenbauder Matrices

One of the most common ways of describing the beam propagation is through the use of geometric optics. A simple beam can be easily defined by two parameters that define a ray vector: position (x) and slope (x') relative to a defined reference axis. Using these two parameters, optical elements can be represented with the use of matrices. Most commonly, an ABCD matrix can be used to define the position and slope of a beam after an optical element by matrix multiplication of an input ray vector by the ABCD matrix of the element:

$$\begin{bmatrix} x_0 \\ x_0' \end{bmatrix} = \begin{bmatrix} A & B \\ C & D \end{bmatrix} \begin{bmatrix} x_i \\ x_i' \end{bmatrix} \tag{3.22}$$

Consider a beam propagating through a thin lens with a focal length, f. It can be defined by the matrix formalism (Fig. 3.5). Knowing the lens is thin, $x_0 = x_i$, the slope can be determined using the following relations:

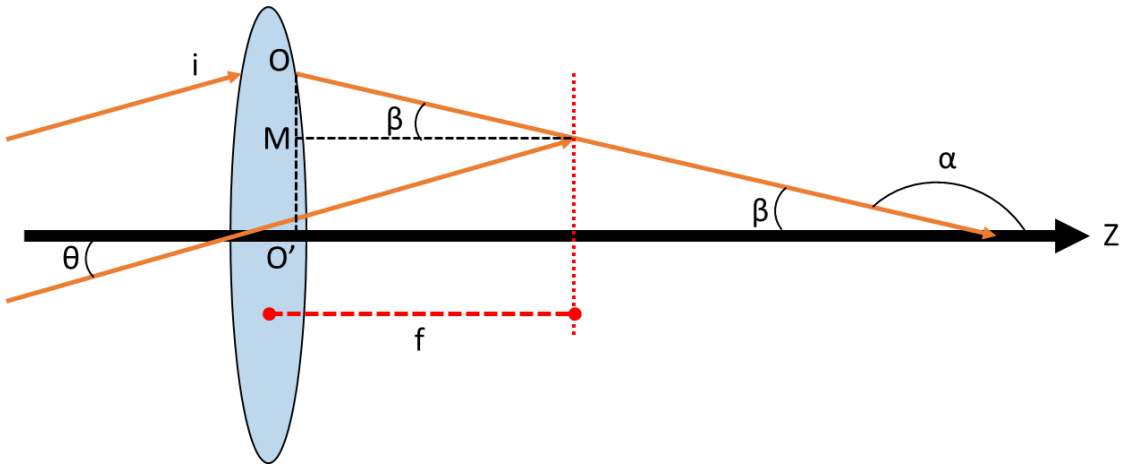

Figure 3.5: Thin Lens Propagation

$$x_0 = x_i \tag{3.23}$$

$$x_0' = \frac{\mathrm{d}x_0}{\mathrm{d}Z} = \tan\alpha = -\tan\beta = -\frac{OM}{f} = -\frac{OO' - MO'}{f} = -\frac{x_0 - f\tan\theta}{f} = -\frac{x_i - f x_i'}{f} \tag{3.24}$$

This results in the following ABCD matrix:

$$\begin{bmatrix} x_0 \\ x_0' \end{bmatrix} = \begin{bmatrix} 1 & 0 \\ -\frac{1}{f} & 1 \end{bmatrix} \begin{bmatrix} x_i \\ x_i' \end{bmatrix} \tag{3.25}$$

In most cases, the angle between the ray and the optical axis is quite small. Therefore the paraxial approximation can be used to describe the slope. This then changes the ABCD matrix formalism:

$$\begin{bmatrix} x_0 \\ \theta_0 \end{bmatrix} = \begin{bmatrix} A & B \\ C & D \end{bmatrix} \begin{bmatrix} x_i \\ \theta_i \end{bmatrix} \tag{3.26}$$

This method is quite easy to use for propagation through multiple optical systems. In order to analyse a system, each matrix in the system must be multiplied in the order in which it is propagated.

The ABCD matrices only take into consideration the spatial components of the beam. To introduce the temporal components of the beam, the matrix formalism was extended to a 3x3 matrix [152]. This was an attempt to explain dispersive elements such as prisms and gratings by introducing a frequency dependent phase shift. It did not take long to perfect this when Kostenbauder introduced a 4x4 formalism, now known as The Kostenbauder Matrix [127]. The formalism extended the ABCD matrix by adding the frequency (ν) and time delay (t) of the pulse alongside the position and slope. Equation (3.26) can then be re-written as:

$$\begin{bmatrix} x \\ \theta \\ t \\ \nu \end{bmatrix}_{\text{out}} = \begin{bmatrix} \frac{\partial x_{out}}{\partial x_{in}} & \frac{\partial x_{out}}{\partial \theta_{in}} & \frac{\partial x_{out}}{\partial t_{in}} & \frac{\partial x_{out}}{\partial \nu_{in}} \\ \frac{\partial \theta_{out}}{\partial x_{in}} & \frac{\partial \theta_{out}}{\partial \theta_{in}} & \frac{\partial \theta_{out}}{\partial t_{in}} & \frac{\partial \theta_{out}}{\partial \nu_{in}} \\ \frac{\partial t_{out}}{\partial x_{in}} & \frac{\partial t_{out}}{\partial \theta_{in}} & \frac{\partial t_{out}}{\partial t_{in}} & \frac{\partial t_{out}}{\partial \nu_{in}} \\ \frac{\partial \nu_{out}}{\partial x_{in}} & \frac{\partial \nu_{out}}{\partial \theta_{in}} & \frac{\partial \nu_{out}}{\partial t_{in}} & \frac{\partial \nu_{out}}{\partial \nu_{in}} \end{bmatrix} \begin{bmatrix} x \\ \theta \\ t \\ \nu \end{bmatrix}_{\text{in}} \tag{3.27}$$

Looking at Equation (3.27), it is easy to see the upper left 2x2 block represents the original ABCD formalism since they determine the changes in the output position and slope. The bottom row is simplified for a time invariant linear system, $\nu_{out} = \nu_{in}$. Therefore the bottom row becomes 0, 0, 0, and 1. The third column becomes 0, 0, 1, and 0 since passive optical components do not change behaviour with time. Therefore, the general Kostenbauder matrix can be re-written as:

$$\begin{bmatrix} x \\ \theta \\ t \\ \nu \end{bmatrix}_{\text{out}} = \begin{bmatrix} A & B & 0 & E \\ C & D & 0 & F \\ G & H & 1 & I \\ 0 & 0 & 0 & 1 \end{bmatrix} \begin{bmatrix} x \\ \theta \\ t \\ \nu \end{bmatrix}_{\text{in}} \tag{3.28}$$

The new derivatives introduced are renamed E, F, G, H and I. However, the physical meaning behind these entries have been discussed in Equations (3.12), (3.14), (3.18), (3.20) and (3.21). For reference, they are:

$$E = \frac{\partial x_{out}}{\partial \nu_{in}} = SD \tag{3.29}$$

$$F = \frac{\partial \theta_{out}}{\partial \nu_{in}} = AD \tag{3.30}$$

$$G = \frac{\partial t_{out}}{\partial x_{in}} = PFT_{AD} \tag{3.31}$$

$$H = \frac{\partial t_{out}}{\partial \theta_{in}} = TVA \tag{3.32}$$

$$I = \frac{\partial t_{out}}{\partial \nu_{in}} = GDD \tag{3.33}$$

To calculate propagation through multiple optical components, the matrices of the successive optical components are multiplied to one another in the order in which the light propagates (i.e. $K_{final} = K_n \cdot K_{n-1} \ldots K_1$). Table 3-2 summarizes the typical Kostenbauder matrices for common optical components [127]. For example, when looking at the matrix for a grating element, it is clear that the grating has a non-zero term for the F and G element. This means that the grating introduces two spatio-temporal couplings, AD and PFT, alongside a spatial and angular magnification as expected. To compute the final Kostenbauder matrix for a single-pass grating compressor, the three matrices are multiplied together. Two of them represent the matrix associated with the two gratings. One would represent the space between the gratings. Your final matrix would then be:

$$K_{final} = K_{Grating_2} K_{FreeSpace} K_{Grating_1} \tag{3.34}$$

Once the matrices have been calculated, it is possible to formulate the electric field of the laser beam in the generalized manner discussed in Chapter 3.1.1. To generate the $\tilde{Q}$-coefficients for the electric field, the output Q-matrix needs to be calculated [127]:

$$Q_{out} = \frac{\begin{bmatrix} A & 0 \\ G & 1 \end{bmatrix} Q_{in} + \begin{bmatrix} B & \frac{E}{\lambda} \\ H & \frac{1}{\lambda} \end{bmatrix}}{\begin{bmatrix} C & 0 \\ 0 & 0 \end{bmatrix} Q_{in} + \begin{bmatrix} D & \frac{F}{\lambda} \\ 0 & 1 \end{bmatrix}} = \frac{i\lambda}{\pi} \begin{bmatrix} \tilde{Q}_{xx} & \tilde{Q}_{xt} \\ -\tilde{Q}_{xt} & \tilde{Q}_{tt} \end{bmatrix}^{-1} \tag{3.35}$$

where Q_{in} for a well-collimated beam is [129]:

$$Q_{in} = \begin{bmatrix} \frac{-i\lambda_0}{\pi w^2} & 0 \\ 0 & -\frac{i\pi\tau^2}{\lambda_0} \end{bmatrix} \tag{3.36}$$

Based on this formalism, one can re-write some of the more common spatio-temporal couplings in terms of the Q-coefficients [126].

$$\frac{1}{\tau^2} = Re\left[\tilde{Q}_{tt}\right] \tag{3.37}$$

$$GDD = \frac{1}{2} Im\left[\frac{1}{\tilde{Q}_{tt}}\right] = \frac{-Im\left[\tilde{Q}_{tt}\right]}{2|\tilde{Q}_{tt}|^2} \tag{3.38}$$

$$AD = \frac{Re\left[\tilde{Q}_{xt} \cdot \tilde{Q}_{tt}^*\right]}{|\tilde{Q}_{tt}|^2} = Re\left[\frac{\tilde{Q}_{xt}}{\tilde{Q}_{tt}}\right] \tag{3.39}$$

$$FRG = \frac{2Im\left[\tilde{Q}_{xt} \cdot \tilde{Q}_{tt}^*\right]}{Re\left[\tilde{Q}_{tt}\right]} \tag{3.40}$$

$$PFT = \frac{Re\left[\tilde{Q}_{xt}\right]}{Re\left[\tilde{Q}_{tt}\right]} \tag{3.41}$$

$$WFR = Im[\tilde{Q}_{xt}] \tag{3.42}$$

Free Space	**Lens/Mirror**
$\begin{bmatrix} 1 & L & 0 & 0 \\ 0 & 1 & 0 & 0 \\ 0 & 0 & 1 & 0 \\ 0 & 0 & 0 & 1 \end{bmatrix}$ $L = Propagation\ Length$	$\begin{bmatrix} 1 & 0 & 0 & 0 \\ -\frac{1}{f} & 1 & 0 & 0 \\ 0 & 0 & 1 & 0 \\ 0 & 0 & 0 & 1 \end{bmatrix}$ $f = Focal\ Length$
Grating	**Brewster Prism**
$\begin{bmatrix} -\frac{\cos\beta}{\cos\alpha} & 0 & 0 & 0 \\ 0 & -\frac{\cos\alpha}{\cos\beta} & 0 & \lambda_0\frac{\sin\beta-\sin\alpha}{\cos\beta} \\ \frac{\sin\alpha-\sin\beta}{c\cos\alpha} & 0 & 1 & 0 \\ 0 & 0 & 0 & 1 \end{bmatrix}$ $\alpha = Incident\ Angle\ to\ the\ Grating$ $\beta = Diffracted\ Angle\ to\ the\ Grating$	$\begin{bmatrix} 1 & 0 & 0 & 0 \\ 0 & 1 & 0 & -2\frac{\partial n}{\partial \nu_0} m\tan\gamma \\ -2\frac{\partial n}{\partial \nu_0}\frac{m\tan\gamma}{\lambda_0} & 0 & 1 & 0 \\ 0 & 0 & 0 & 1 \end{bmatrix}$ $\gamma = Incidence/Exit\ Angle$ $n = Index\ of\ Refraction\ of\ Prism$ $m = \frac{\cos\gamma}{\cos\gamma'}$ $\gamma' = Interior\ Angle$

Table 3-2: Kostenbauder Matrices for Various Optical Components

3.2.2 Frequency Resolved Optical Gating

One of the most direct methods to measure spatio-temporal couplings of a pulse is with the use of a Frequency-Resolved Optical Gating (*FROG*) [153]. It uses the same methods as an autocorrelator but by focusing the delayed pulses in a non-linear medium, a spectrogram of the pulses is measured, which can be used to determine the electric field of the pulse.

In order for the FROG to work effectively for ultrafast laser pulses, the pulse needs to be effectively gated upon itself in a nonlinear medium. But since FROG is a spectrally resolved autocorrelation, every nonlinear-optical process that can be effectively used in an autocorrelator is possible for FROG setup. Three of the most common designs of FROG are based on polarization-gating (*PG*), self-diffraction (*SD*) and second harmonic generation (*SHG*). The PG-FROG splits the pulse into two (probe and gate pulses), with the probe sent through cross-polarizers and the gate sent through a half-wave plate to be ± 45° linearly polarized in comparison to the probe, while having a variable delay (Fig. 3.6). The pulses overlap in a medium of good third-order susceptibility (ex. fused silica) to generate the Kerr-effect. During the overlap, the medium acts as a waveplate, which slightly rotates the probe pulse's polarization allowing it to be transmitted through the analyzer. From here the overlap, which generates an autocorrelation of the two pulses, is spectrally resolved to generate a PG-FROG trace. This trace is best represented by the autocorrelation of the two pulses [151]:

$$I^{PG}{}_{FROG}(\omega,\tau) = \left| \int_{-\infty}^{\infty} E(t)|E(t-\tau)|^2 e^{-i\omega t} dt \right|^2 \tag{3.43}$$

where *E(t)* and *E(t-τ)* represent the signals for the probe and gate pulse respectively, ω is the instantaneous frequency and τ is the variable delay. PG-FROG is the most intuitive FROG setup. The design has no issues with intensity and phase characterization. Also because of the manner of the process of generating a trace, there are no issues with phase-matching in the nonlinear medium. The disadvantage apparent with the design is the need of high-quality polarizers, which typically are expensive and add dispersion to the measurement. The design also needs high power since it is based on a third-order non-linearity. The signal intensity scales as the third power of the input intensity. This is detrimental when dealing with weak, long and/or large signals.

Another set-up that involves third-order nonlinear optical processes is the SD-FROG. This set-up involves crossing two pulses in a third-order nonlinear medium, inducing a material grating, diffracting the beams into different directions (Fig. 3.7). Spectrally resolving one of the beams as a function of the variable delay generates the trace expressed by the autocorrelation [151]:

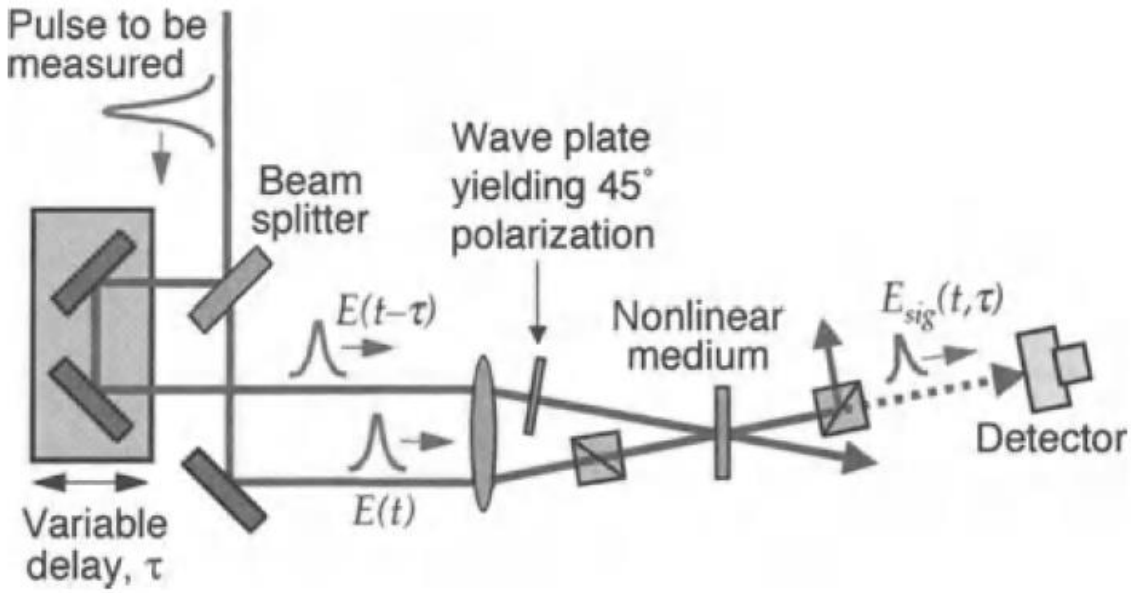

Figure 3.6: PG-FROG Set-up. Image Source: Trebino [151]

$$I^{SD}{}_{FROG}(\omega,\tau) = \left| \int_{-\infty}^{\infty} E(t)^2 |E(t-\tau)| e^{-i\omega t} dt \right|^2 \tag{3.44}$$

While it works similarly to a PG-FROG, the beams can have the same polarizations. SD-FROG traces are more sensitive to odd-order temporal phase distortions and does not require any polarizers. The disadvantage is that it is not a phase-matched process leaving strict restrictions to the thickness of the non-linear medium and the angle between the probe and gate pulses. Wavelength-dependent inefficiencies are introduced for large pulse bandwidths, leading to distortions [151].

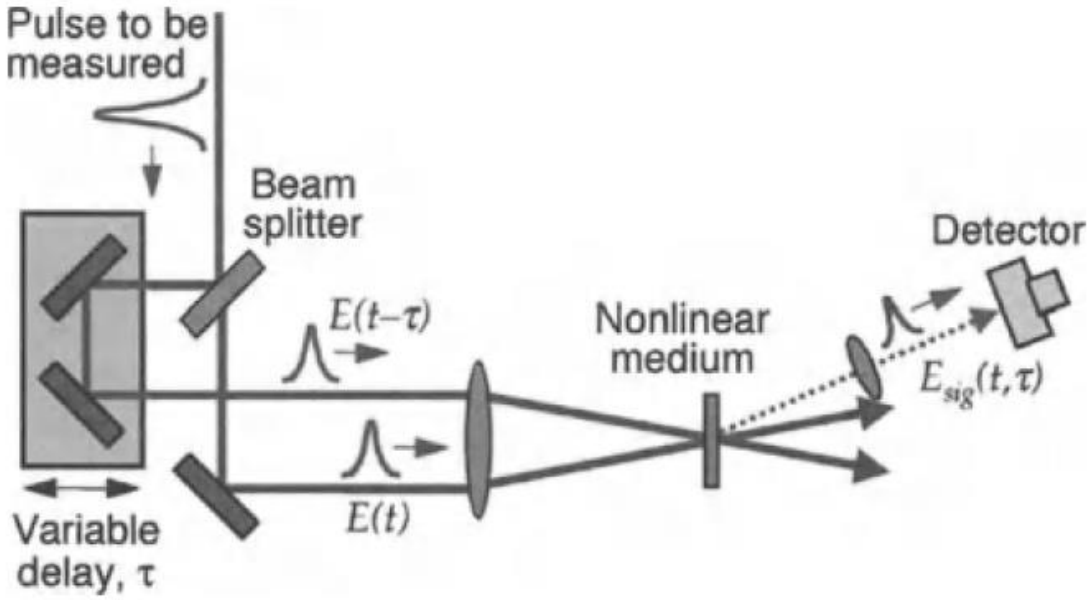

Figure 3.7: SD-FROG Set-up. Image Source: Trebino [151]

One of the more common and sensitive FROG set-ups is the SHG-FROG. The design is similar to the SD-FROG set-up but with the use of second-order nonlinearity, which yields a stronger signal than the previous two designs (Fig. 3.8). It has the ability to discern traces for extremely weak signals since it can achieve the best signal-to-noise ratios. This is because the trace that is measured is the SHG in the second-order nonlinear medium. Since the trace is a different colour from the input wavelength, the background is easily filtered out. The major disadvantage is the symmetrical nature of the trace. As seen in the autocorrelation [151]:

$$I^{SHG}{}_{FROG}(\omega,\tau) = \left| \int_{-\infty}^{\infty} E(t)|E(t-\tau)|e^{-i\omega t}dt \right|^2 \tag{3.45}$$

there is a symmetrical nature with respect to the delay, which yields an ambiguity in the direction of time. For SHG, the pulse amplitude, *E(t)*, is equal to its complex-conjugated time reversed replica, *E*(-t)*. When taking the respective Fourier transforms, it can be shown that the retrieved trace can be a time-reversed version of the actual pulse. This can be alleviated by taking second measurements with some distortion, such as placing a piece of glass before the second-order nonlinear medium to know the result of the initial measurement through comparison.

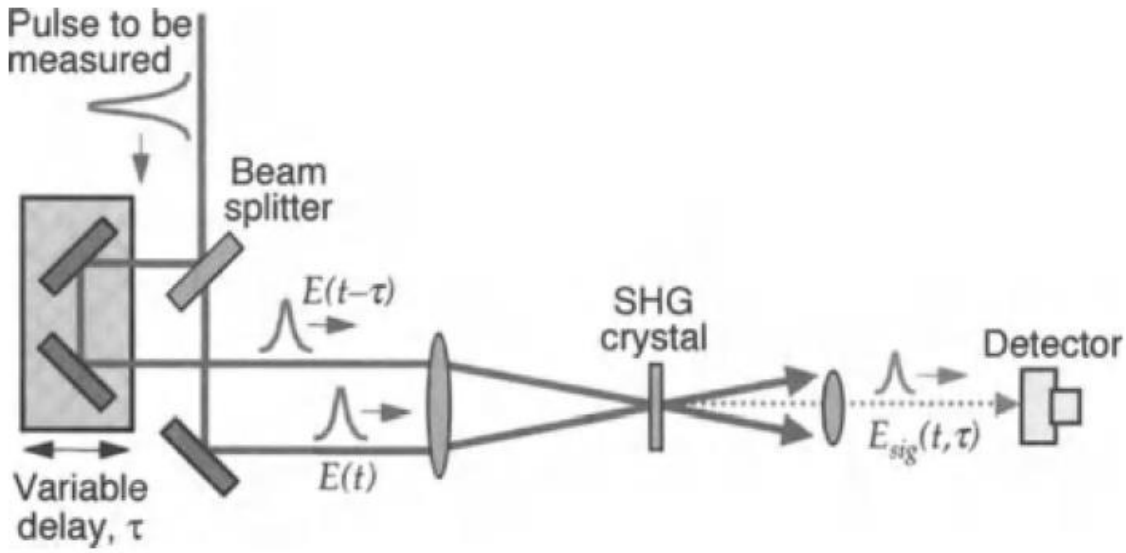

Figure 3.8: SHG-FROG Set-up. Image Source: Trebino [151]

In order to generate the information needed on the ultrafast laser pulse, the complex electric field, *E(t)*, needs to be retrieved for the trace. This involves re-creating the trace using a form of iterative-Fourier transform algorithms. The basis of the algorithms work by taking an initial guess for the electric field based on the geometry of FROG used. The field is then Fourier transformed into the frequency domain, where the measured FROG trace is used to generate an improved

signal field in the frequency domain since the squared magnitude of the frequency domain signal is equivalent to the autocorrelation measured. The new frequency domain signal is then inversely Fourier transformed to the time domain, yielding a new signal field to use as the initial guess for *E(t)*. The process is then repeated until the correct complex electric field is determined (Fig. 3.9). Two of the most common iterative based algorithms used is the "Vanilla" and generalized projections methods. The "Vanilla" method works exactly as outlined (Fig. 3.9), except that the new guess is generated by integrating the new signal field over the delay, which generates a quantity proportional to the signal to be taken as the new guess. The generalized projection method works by taking projections onto a set of constraints that the trace must fulfil until convergence is met. These two methods, used in conjunction, provide a reliable manner of generating a reconstruction of the FROG trace with a high degree of convergence.

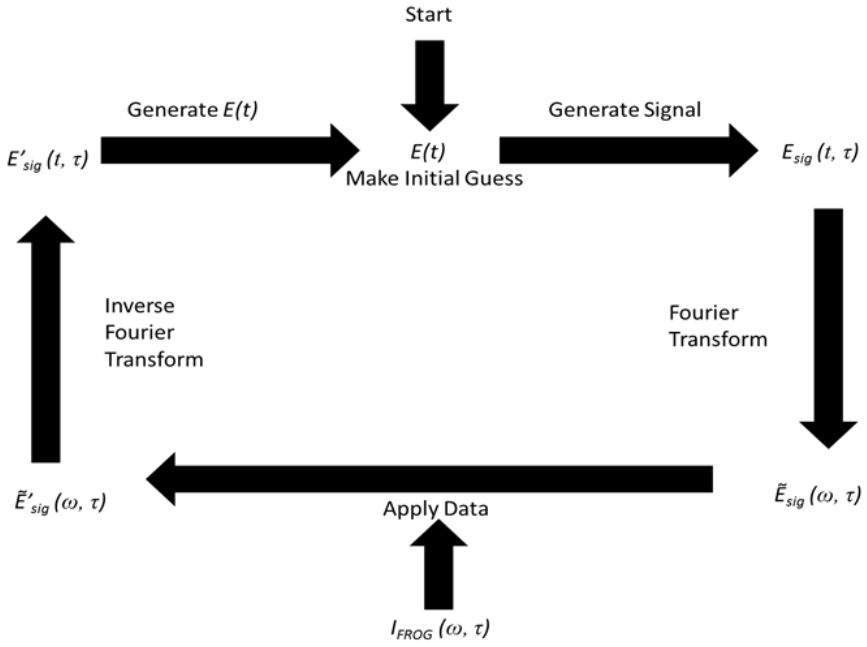

Figure 3.9: Schematic of the generic FROG algorithm used to recreate the trace to retrieve the complex electric field, *E(t)*

One of the important properties of the trace that can be determined is the phase. By fitting the phase across the spectrum and/or autocorrelation and knowing what order fits the phase best, one can determine the couplings in the pulse (Fig. 3.10). A first-order phase relates to a shift in time or frequency, which is essentially the delay in the pulse or some small spectral shift. The second-order phase corresponds to a spatial or temporal chirp in the pulse. This is important because it is directly proportional to PFT. A large second-order term correlates to a large PFT in the pulse, and vice-versa. If there is no second-order phase, there is no PFT. The higher-order phase terms relate to complicated distortions that are seen only in extremely complex pulses. It is

important to remember that when the intensity of the pulse goes to zero, the phase becomes meaningless.

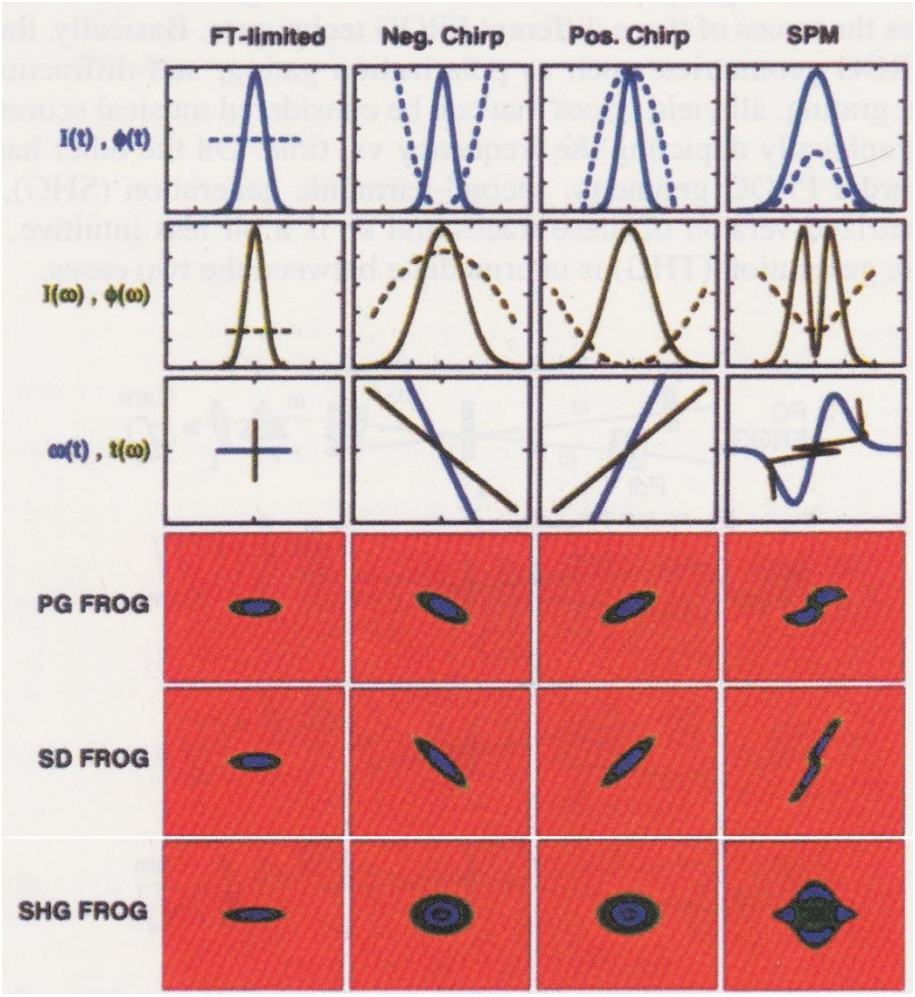

Figure 3.10: Different order phase distortions and FROG traces for different FROG Geometries. It should be noted that for a transform limited pulse (FT-limited), there is no PFT. Image source: Trebino [151].

To measure PFT directly with a SHG-FROG system, certain modifications need to be made. The beam splitter, delay lines and recombination optics can be replaced with a Fresnel biprism. The original SHG crystal is replaced with a thicker SHG crystal to yield more signal. This geometry is known as a Grating-Eliminated No-nonsense Observation of Ultrafast Incident Light E-fields (*GRENOUILLE*) (Fig. 3.11). The Fresnel biprism splits the beam into two beams and crosses them at an angle. They overlap within the thick-SHG crystal, which acts as both the nonlinear-optical time gating element and the spectrometer since the phase-matching bandwidth is dependent on the angle. The relative beam delay is mapped onto the horizontal position of the crystal, which can then be imaged for a direct measurement of SC and/or PFT on a CCD camera [125,154,155]. Two cylindrical lenses are needed to focus and collimate the beam as such. This device has many advantages over its FROG counterparts. The number of elements are few making it a compact

optical device. It also is much more sensitive since the phase measurements are directly measured as a function of position on the crystal. It is also a real-time measurement since the traces are done directly on a camera. The major issue with typical GRENOUILLE systems is that they are black box measurement systems. If any misalignment occurs within the system, it is quite difficult to open the device and re-align it as it was calibrated upon its fabrication. However, if they are in functioning order, they are an integral laser pulse characterization device for any ultrafast laser system.

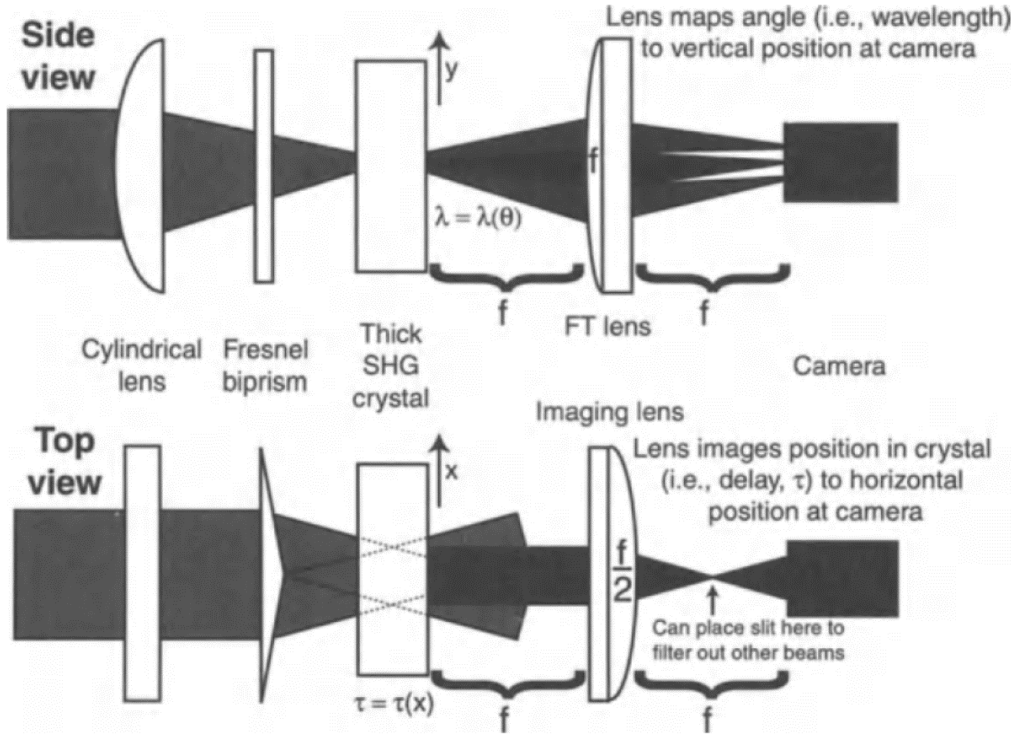

Figure 3.11: Side and top views of a GRENOUILLE system. A Fresnel biprism replaces the beam splitter, delay line and recombination optics. The delay is mapped on the thick SHG crystal as a function of position, providing an avenue of a single-shot SHG-FROG trace on a CCD camera. Image Source: Trebino [151]

3.2.3 Spatial Chirp Measurements with Fibre Spectrometer

When viewing the laser pulse that propagated through a dispersive medium, the different frequencies separate in space and create SC. The most direct method to measure SC is by scanning the beamspot of the pulse with a fiber attached to a spectrometer (Fig. 3.12). A fiber attached to a spectrometer is scanned across the laser beam, measuring the central wavelength as a function of the beam width. The wavelength is then plotted against the position on the beam width where the slope of the best-fit line yields FRG. It is important though to understand that the FRG can change as a function of the propagation after a dispersive element due to AD. To

measure the AD after a dispersive element using the same technique, the FRG should be recorded at different locations along the propagation. From here, the change in FRG can be converted to SD. This can then be easily used to calculate AD. It is also a direct method to ensure that there is no AD in the beam by measuring a constant FRG at different locations along the propagation length. It is also important to measure FRG in orthogonal dimensions of the laser beam (i.e. x- and y-axis of the laser pulse) to ensure uniformity.

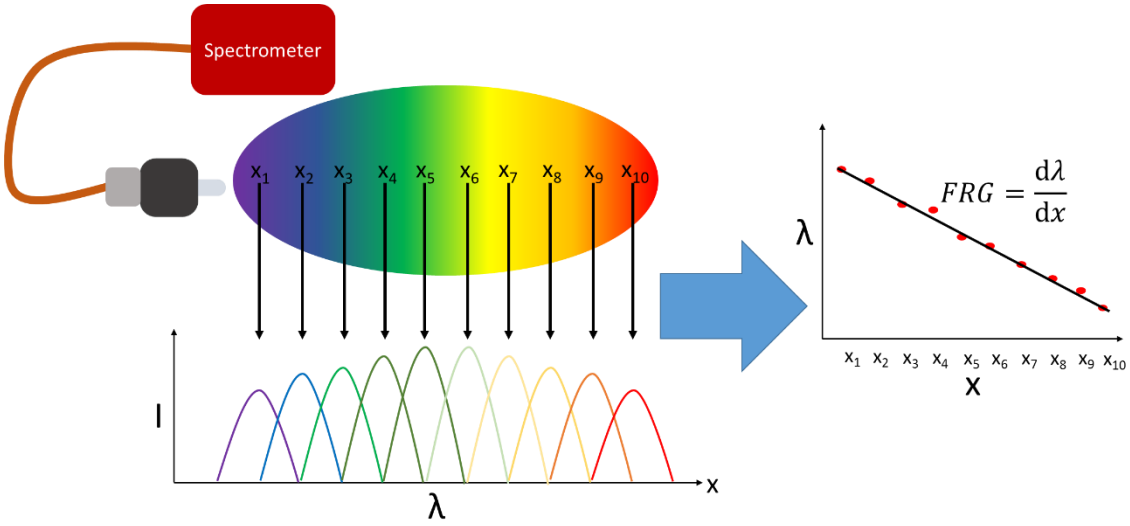

Figure 3.12: Schematic for Measuring FRG with a Fiber Spectrometer.

In the majority of ultrafast laser pulses, the spectrum of the pulse may not be perfectly Gaussian. While most pulses have Gaussian distributions in intensity, the actual spectrum may be irregular making it difficult to accurately measure the central frequency. Therefore, to get a complete picture of the SC in a pulse, three measurements should be plotted against the position on the beamspot: the maximum of the spectral peak, the median of the spectral peak and the weighted average of the spectral peak (*∑(intensity*wavelength)/∑intensity*) (Fig. 3.13). If the spectral peak is not uniform, the maximum of the spectrum may not reside at the centre of the spectral peak. Therefore, either the median and/or the weighted average will compensate for the irregular spectrum. From there, the FRG and/or SD can be calculated and averaged to get a direct representation of the SC.

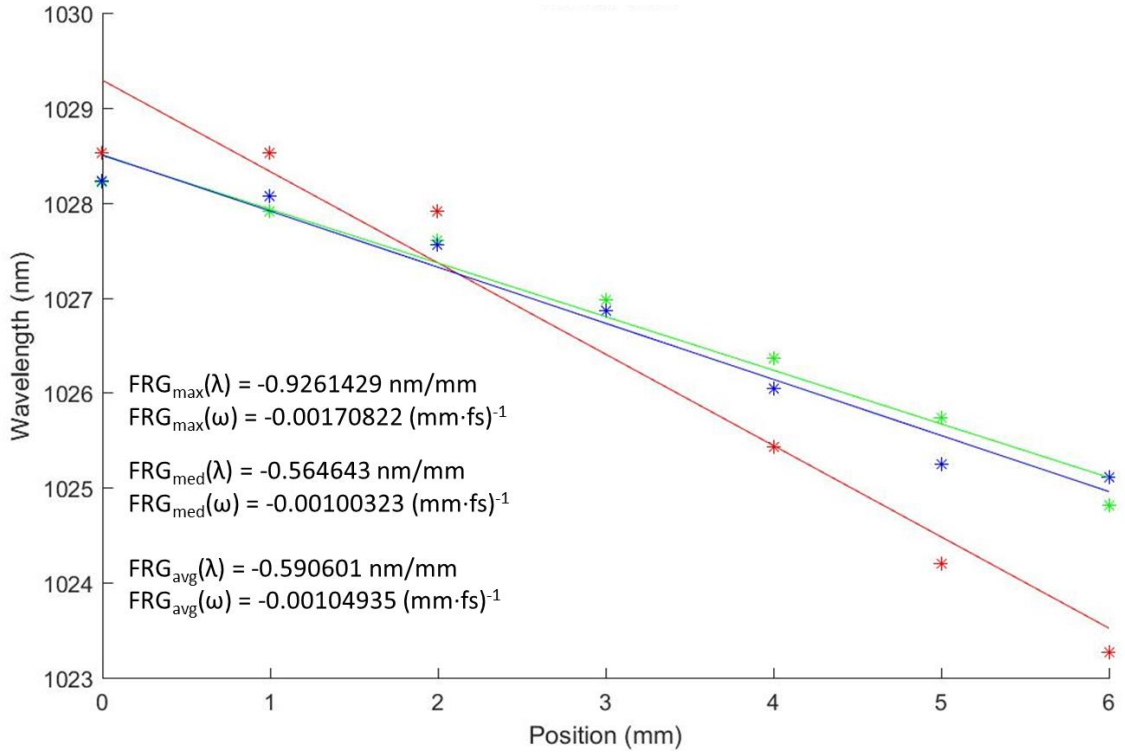

Figure 3.13: SC Measurements Using a Fiber Spectrometer. It can be observed that the maximum of the spectral peak is not uniform and can provide erroneous measurements of FRG. Therefore, it is recommended to measure the median and weighted average of the spectrum to get a more accurate depiction of the SC of a laser pulse.

3.3 Focusing Techniques of Spatio-Temporal Couplings

One of the key parameters for ultrafast laser induced material modification is the focusing conditions. The focusing of a lens is characterized by its numerical aperture (*NA*). With respect to material modification, the focusing conditions can be organized into three categories. The low NA regime (NA < 0.1), ultrafast lasers are weakly focused into the bulk of transparent material and typically produces filament modification, preventing single-pulse permanent structural modification [156]. The spot size is more than 10 µm and, as a result, these lenses are used for surface modification where aberrations such as self-focusing do not take place. For the regime of 0.1 < NA < 0.65, the modification can already be induced within a confined area in the bulk of a material. Due to the mismatch of refractive index between air and the transparent material, spherical aberration can strongly affect the propagation of the laser beam. Typical glasses have much higher refractive index than the air, which leads to non-uniform refraction at the interface. This then results in an extension of the focal spot in the propagation direction since the adjacent part of the pulse is focused deeper than the central portion of the beam. This aberration becomes more apparent as the NA increases. However, the refractive index mismatch can be corrected with the use of objectives that have spherical aberration correction or with the use of immersion

optics [19,157]. The tight focusing regime (NA > 0.65) can typically be achieved with the use of immersion objectives. The immersion objectives tightly focus the laser beam but also can compensate for spherical aberration. This can result in permanent modification in a confined volume near the focus at nanojule pulse energies [17,158].

Depending on the application, it is integral to choose the correct numerical aperture. However, when using low NA or high pulse energies, nonlinear side effects such as self-focusing, filamentation or white light generation can drastically degrade the quality of modification [21,90,159–161]. There is also the need for localising the modification as close as possible to the focus to create confined volumes of modification, like that necessary for polarization multiplexed data storage [58,59]. Yet, when using femtosecond pulses, the intensities met during focusing are sufficient enough to modify the bulk of transparent materials well before the focus. Using high NA objectives can alleviate this issue for material modification but can be extremely detrimental for other applications such as microscopy and laser surgery where collateral damage can occur easily at very low pulse energies.

3.3.1 Simultaneous Spatial and Temporal Focusing

To overcome the undesirable nonlinear effects, a technique known as Simultaneous Spatial and Temporal Focusing (*SSTF*) was introduced [134,135]. Before focusing the laser pulse, the spatial components of the incident laser are separated in space creating a collimated rainbow beam (Fig. 3.14). In doing so, the local bandwidth is reduced, thus increasing the duration of the pulse. Upon focusing, the pulse duration varies along the direction of propagation as the spatial components begin to overlap. Within the focal volume, the entire bandwidth is recovered as all the components overlap, resulting in the initial pulse duration. Consequently, the intensity of the pulse along focusing is reduced because of the change in beam diameter alongside the change in pulse duration. Therefore, the maximum intensity achievable with the pulse is met only at the focus, confining all nonlinear laser-material interaction to the focal volume as opposed to conventional focusing.

While the spatial component separation is the key aspect towards SSTF, the imaging geometry used upon focusing is also crucial to define. There are two forms of SSTF: wide-field scanning and line scanning. Both of these forms are based upon how the beam diameter falls on the focusing optic (Fig. 3.14b, c). In the wide-field scanning, the beam shape is elliptical and spatially chirped along the elliptical axis (Fig. 3.14b). This would mean that in one direction, the beam is a thin line where the different spectral components are spread out and in the other direction the beam is effectively monochromatic. It should be noted that in this geometry, the effective NA of the lens

will be reduced since each monochromatic beam will not focus tightly. This results in a spherically symmetric beamspot at the focus as all the spectral components recombine. In line scanning SSTF, the beam is spatially chirped in one dimension but has a circular beam spot at the lens (Fig. 3.14c). This results in each monochromatic portion of the beam to tightly focus, yielding an elliptical beamspot at the focus.

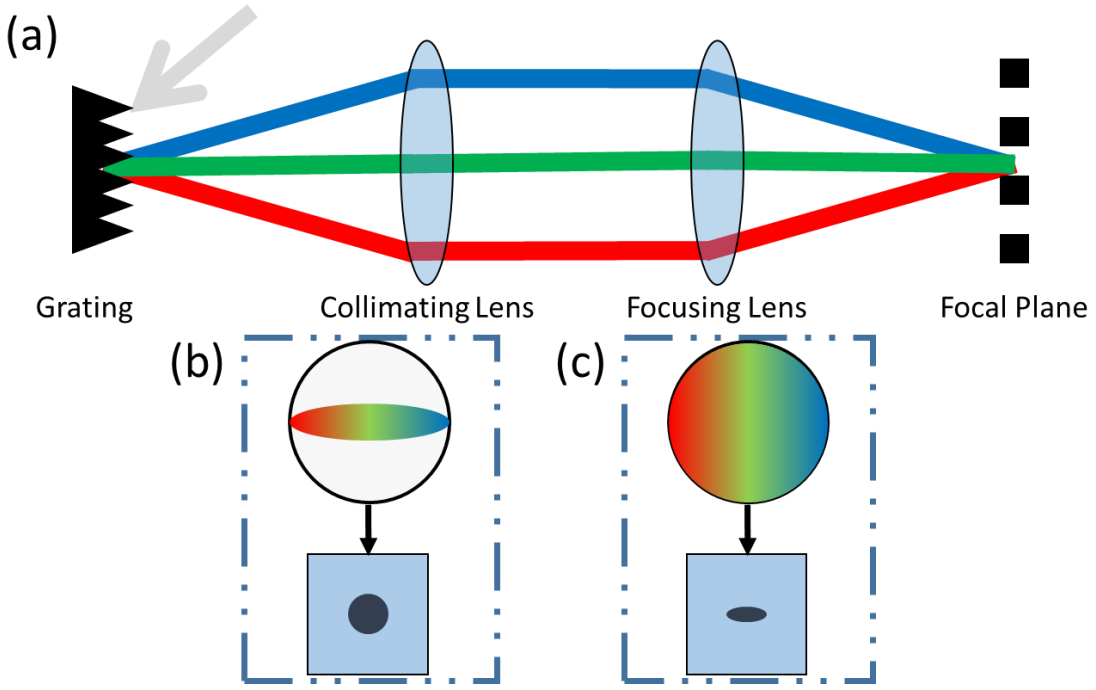

Figure 3.14: (a) Typical SSTF design. (b) Beam profile for wide-field SSTF. The beam is elliptical upon the focusing optic and circularly symmetric at the focus. (c) Beam profile for line scanning SSTF. The beam is circularly symmetric upon the focusing optic which results in an elliptical beam spot at the focus.

The ability to confine the maximum intensity to the focal volume with low NA lenses and overcoming nonlinear side-effects through SSTF has made it an attractive technique for a number of applications. A large field of view is desirable (100 µm to mm) for nonlinear imaging of biological samples. However with conventional focusing, to reach this would entail spanning multiple spatial and temporal scales at sub-µm resolution. A typical imaging system would then take several decades to be able to accomplish this with typical spatial requirements. There is also the need to image the dynamic nature of a sample at sub-ms resolution, thus increasing the acquisition time even further. SSTF can be used to yield a large field-of-view without compromising the axial resolution of the system [135]. It also reduces background excitation observed in multiphoton and fluorescence microscopy when focusing deep in biological samples [114,115,134,162,163]. Adding GDD to a SSTF design also shifts the temporal focus, thus introducing an additional level of control for axial-scanning [115]. SSTF also reduces collateral

damage for applications like laser surgery and tissue ablation where highly localised precision is necessary [111,114,117,164]. SSTF has also shown promise in overcoming nonlinear side-effects when reaching the critical power near the focus in material modification in comparison to conventional focusing [109–113]. Since the intensity sufficient for material modification is localized closer to the focal plane, the modification is confined to the focal volume (Fig. 3.15).

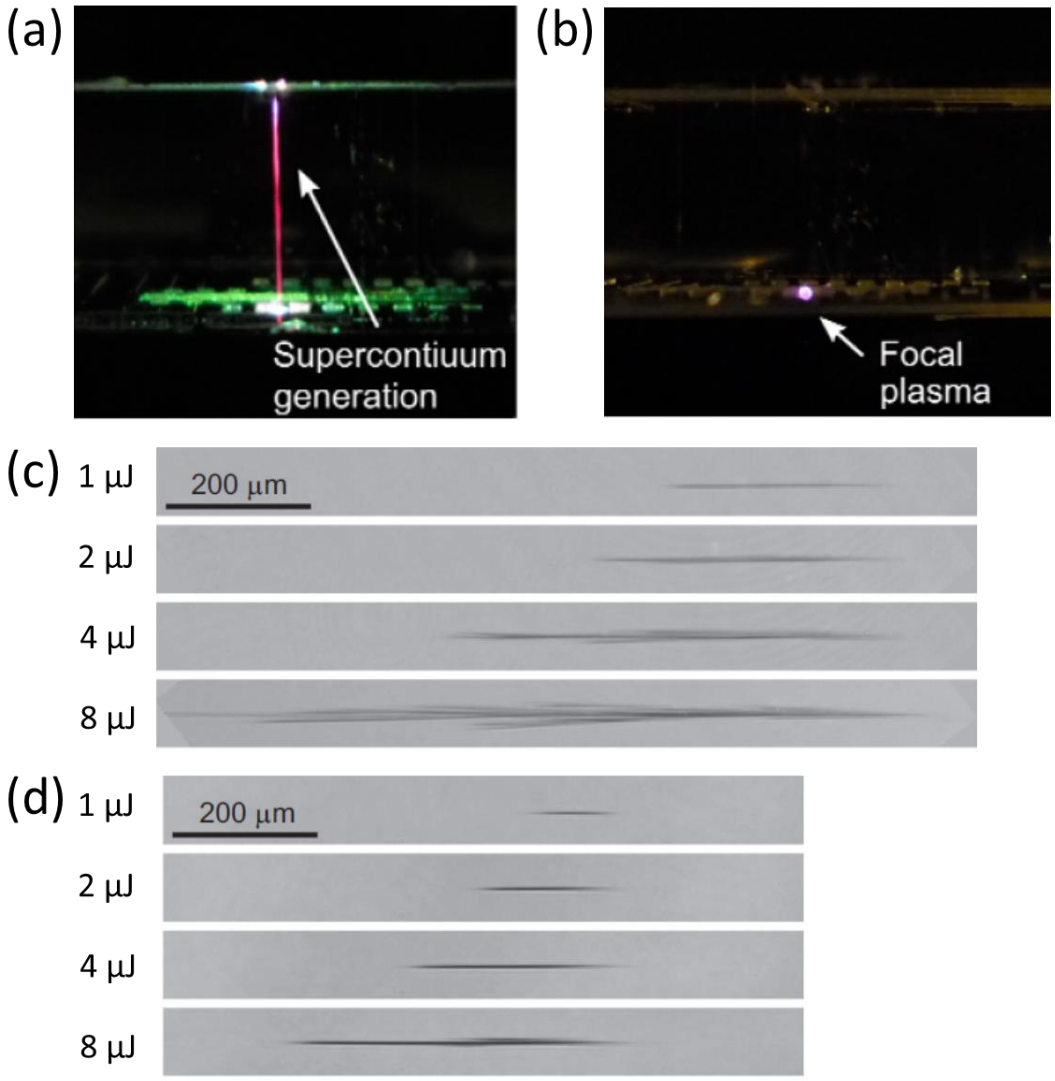

Figure 3.15: (a, b) Focusing on the back surface of a fused silica sample (λ = 800 nm, τ = 60 fs, NA = 0.05, 50 µJ pulses) using (a) conventional focusing and (b) SSTF. Self-focusing and supercontinuum generation is visible, resulting in a loss of intensity at the focus with conventional focusing, yielding a long filament inhibiting ablation of the back surface. With SSTF, all nonlinear distortions are suppressed allowing for the ablation of the back surface of the sample. (c, d) Shadowgraphic images of plasma formation within a water cell (λ = 800 nm, τ = 50 fs, NA ≈ 0.1) for (c) conventional focusing and (d) SSTF. The optical breakdown is strongly confined and filamentation effects are reduced for the SSTF case. Pump is incident from the left. Image source: (a, b) Vitek et al. [136] (c, d) Kammel et al. [111]

3.4 Spatio-Temporal Induced Phenomena

One of the most important aspects of spatio-temporal couplings with respect to ultrafast laser material modification is the underlying phenomena that occurs during laser irradiation. Previous studies have clearly indicated that spatio-temporal couplings can give rise to a strong directional dependence, known as the "quill-effect," and an anisotropic photosensitivity in isotropic homogeneous mediums [4,6,136,165,166], which is thought to depend on the polarization orientation with respect to the azimuth of the PFT and is known as the "*blade effect"* [6]. This section goes into detail about these phenomena.

3.4.1 Non-Reciprocal Writing ("Quill-Effect")

One of the major phenomena observed thought to be due to spatio-temporal couplings in laser machining is the directionality dependence of laser processing of transparent material. When writing with a beam that has PFT, a "quill-effect" is observed in the structures created in the transparent material (Fig. 3.16) [4,5]. In one direction, the nanostructure is smooth, whereas writing in the opposite direction yields a rough texture in the nanostructure. The non-reciprocal behaviour observed is only developed at particular pulse energies where damage is not expected. Since PFT is the tilt of the intensity distribution of the beam front, the intensity gradient is thought to provide a ponderomotive force (nonlinear force on a charged particle within an inhomogeneous oscillating electromagnetic field) to the charges that are present. This then expels electrons from the regions of high intensity, acting as a force on the electron plasma generated during the writing procedure along the direction of the intensity gradient. This ponderomotive force in the front of the pulse then traps and displaces the electrons along the direction of movement in the manner of how a snow-plow works. This effect is known as the *"quill-effect."* This "quill-effect" affects the electron plasma waves, which are potentially responsible for the formation of nanogratings and self-assembled form birefringence. The movement of the beam will then affect the interference of the electron plasma waves and the related form birefringence.

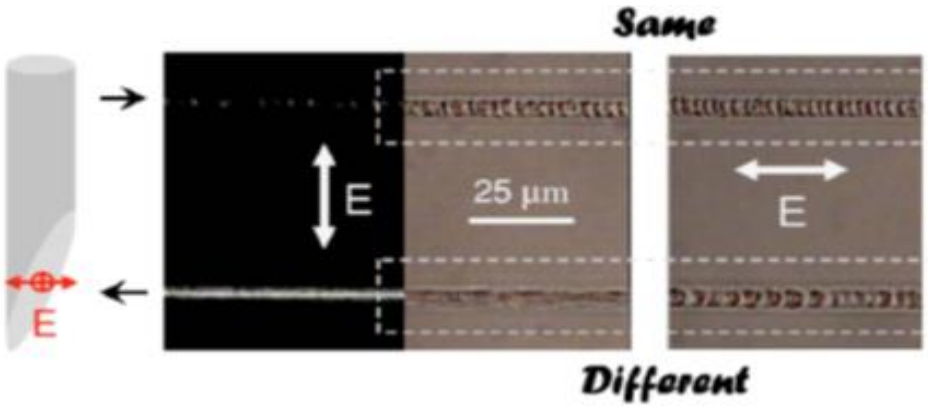

Figure 3.16: Laser writing is done in both directions showing the effect on the modification with respect to PFT direction. Difference in texture is observed in one direction by simply changing the polarization by 90°. Image source: Kazansky et al. (2007) [4].

A more systematic approach to characterizing the quill-effect has shown that the quill-writing effect depends strongly on the focusing depth [5]. A change of depth by only 10% was sufficient enough to remove the quill-effect. It was also observed that by simply switching the writing direction, not only can there be a difference in texture but the modification for both directions can be different. Smooth line structures in one direction correspond to Type II modification and Type III modification can be observed in the opposite direction [5]. Evidence of a regime where the induced modification can transition from void formation to nanogratings abruptly was also observed, which corroborated with other studies [167,168]. The study also showed that the directionality can be flipped by either placing a mirror along the laser propagation to flip the PFT before the lens or by tuning the pulse compressor value of the laser to flip the PFT (Fig. 3.17) [5]. Later it was reported that PFT before the lens can be precisely controlled using a simple two-grating SSTF set-up [136]. With better control of the PFT, they were able to increase the depth at which the phenomena is observed. This was then further strengthened when similar experiments were conducted by a more controlled dynamic SSTF design involving a spatial light modulator (SLM) [166]. However in this study, the non-reciprocal behaviour was observed when asymmetry was introduced to the beam by illuminating the focusing lens asymmetrically.

While the ponderomotive force explanation has never been validated through experiment, a difference in modified plasma distributions is observed through *in-situ* plasma emission microscopy, resulting in a difference in modified index distribution [169]. The intensities necessary for the ponderomotive force to occur are thought to be unreachable due to a laser intensity clamping effect [170]. There is also the issue with how PFT was characterized and controlled in all previous studies. The origin of the PFT, whether it was due to SC and/or AD, was never quantified and is mainly due to residual spatio-temporal couplings from the laser and/or dispersive elements along the laser propagation. This has major ramifications as to what the PFT

actually is in the focus. It was originally thought upon focusing, PFT would proportionally increase as the beam diameter shrinks [165]. However, depending on the actual cause of the PFT at the lens, the evolution of PFT can be drastically different upon focusing [171,172]. There is also the issue when reviewing the original quill-effect experiments and noticing crucial errors in the measurements taken. Upon reviewing the Yang et al. study [5], it is clear that the GRENOUILLE measurements yield incorrect values. While PFT flipped sign, the magnitude is different while the pulse duration remained the same. Therefore, the PFT is not due to SC and TC alone in this study but a combination of effects. Also, the measurement of SC yields an unrealistic value, thus adding more hesitation to the credibility of the origin of the non-reciprocal behaviour.

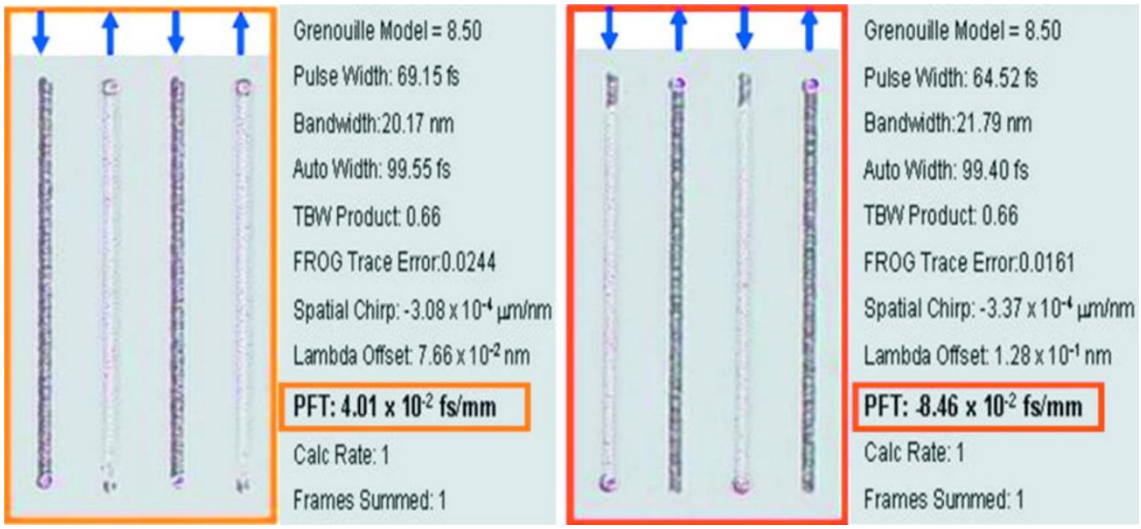

Figure 3.17: Microscope images of the quill-writing effect showing smooth modification one direction and rough in the other. The directional dependence was flipped with a flip in the PFT. The PFT is believed to be flipped by tuning the temporal chirp of the compressor set-up. Image source: Yang et al. [5]

3.4.2 Photosensitive Anisotropy ("Blade Effect")

Alongside spatio-temporal couplings, it is important to consider its mutual orientation with respect to the beam polarization. Kazansky et al. [6] discovered an anisotropic sensitivity of an isotropic homogeneous medium under uniform illumination. This phenomenon was interpreted based on the intrinsic anisotropy of light-matter interactions with ultrashort pulses that exhibit PFT. In multiple experiments in alumosilicate glass, the PFT of the pulse was maintained while rotating the orientation of the polarization. When the polarization was set at 90° to the supposed direction of PFT, more white light emission was observed during stationary ultrafast laser irradiation. This was also coupled with a strong coloration at the irradiated regions with asymmetrical distributed bubbles (Fig. 3.18). The bubbles were thought to correlate with the direction of the PFT.

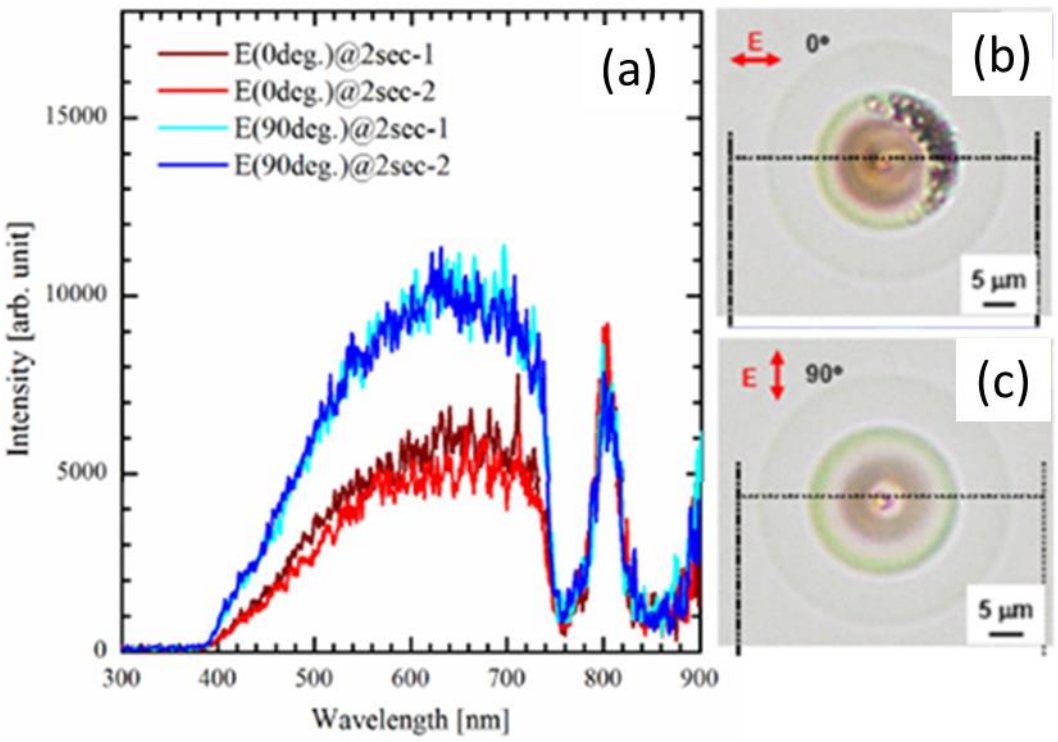

Figure 3.18: (a) Spectra of transmitted light during laser exposure with two orthogonal polarizations, with 90° polarization providing more light. b, (c) Optical microscope images of modified regions for both orthogonal polarizations, showing differences in void formation with a defined direction thought to be due to PFT. Image source: Kazansky et al., [6].

Also, by observing the cross-sections along the beam propagation, the modification structure is dramatically different for when the beam is polarized parallel or perpendicular to the PFT (Fig. 3.19). When the beam is polarized in the direction of the PFT, strong colouration is observed in the head and tail of the imprinted structure. A bubble belt is also observed in the middle of the structure. When the beam is perpendicular to the PFT, a beautiful coloured flower-shaped structure is observed. This polarization dependence is explained with the ponderomotive force. The ponderomotive force that is induced from the anisotropic intensity gradients of PFT removes any defects in the material in the region before the focus, for light that is polarized in the direction of the PFT. This then means the intensity of the beam will be higher at the focus, producing stronger modification to the material.

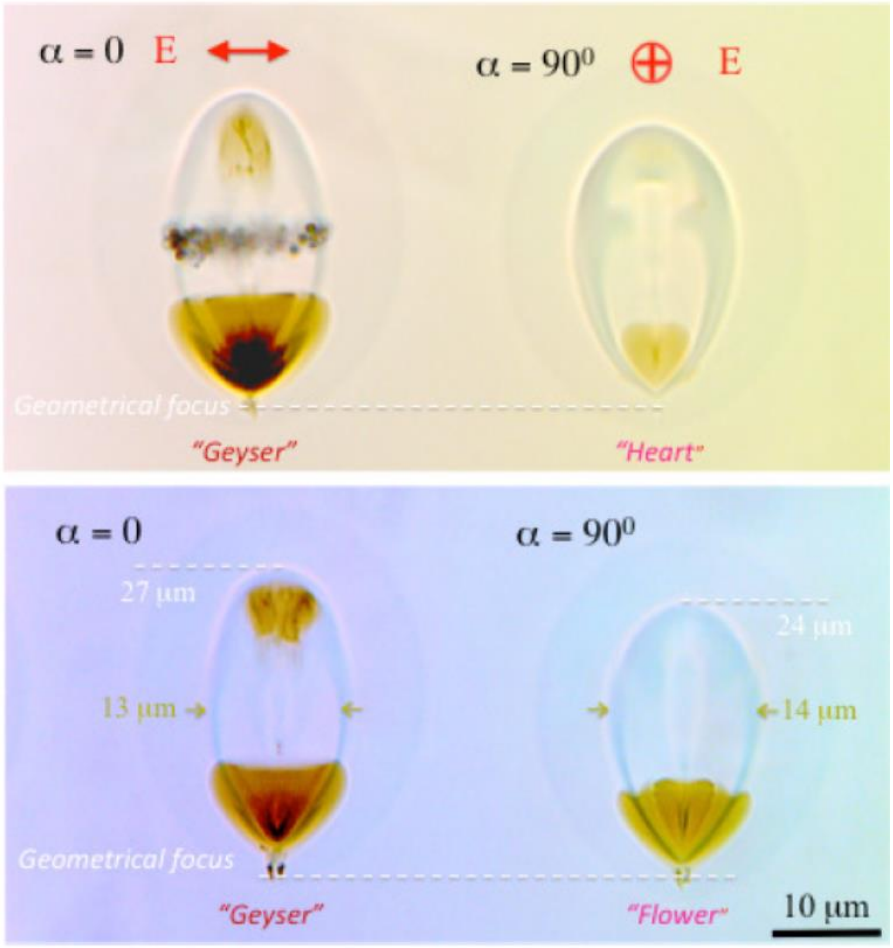

Figure 3.19: Optical microscope images of the modified morphologies observed along the beam propagation direction for light polarized along (α=0°) and perpendicular (α=90°) to the pulse intensity front. Image source: Kazansky et al. [6].

Further studies also observed similar behaviour but with respect to other forms of modification and in different materials [165,168,173–175]. With respect to the formation of nanogratings, when looking at SEM cross-sections of nanograting lines written in the bulk of fused silica, the orientation of the nanograting periodicity along the propagation direction of the laser was observed to rotate (Fig. 3.20) [173,174]. This was also explained using the same PFT-ponderomotive force argument used to explain the blade-effect. Ponderomotive force orthogonal to the PFT direction would potentially push the plasma towards the tilt and thus result in a forced rotation of the nanograting periodicity along the laser propagation. The gap separation, d, and forced angle of rotation of the periodicity, $\beta_{grating}$, between the subsequent gratings is dependent on the polarization orientation, θ, and PFT angle, φ_{PFT}:

$$d = \frac{\lambda}{2n}\left[\frac{1}{\sqrt{1-\cos^2\theta\cos^2\varphi_{PFT}}}\right] \tag{3.44}$$

$$\beta_{grating} = \frac{\pi}{2} + \tan^{-1}\left(-\frac{\sin\varphi}{\tan\theta}\right) \tag{3.45}$$

Even though the phenomena has been observed, the same issues with beam characterization and spatio-temporal control that existed with the quill-writing experiments reside within the aforementioned studies. One of the main issues is the broad spectrum of the ultrafast lasers used in the studies. Any form of dispersive material can cause spatio-temporal distortions to the beam. In many of these studies, the numerical apertures pertain to tight focusing. With the use of large objective lenses, there is a considerable amount of glass that can distort the beam. This can result in any form of PFT and/or other spatio-temporal couplings. Therefore, it is hard to associate the existence of PFT with a mutual orientation to polarization in these experiments, raising questions as to what the phenomenological explanation to the observed polarization dependence is.

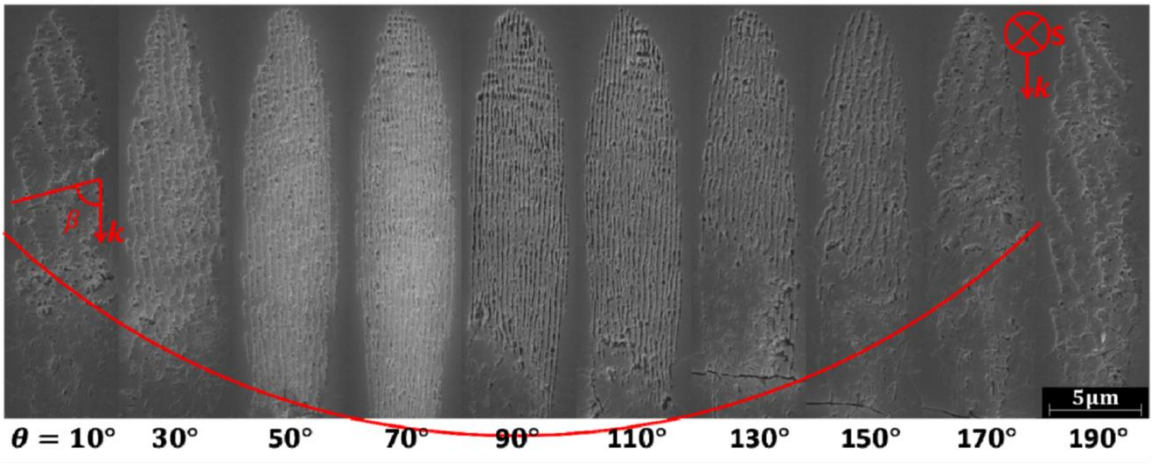

Figure 3.20: SEM images of the periodicity of nanogratings forced rotation due to the mutual orientation of PFT and polarization. The red line indicates the varying trend of the longitudinal length of nanogratings. Image source: Dai et al. [174]

Chapter 4: Experimental Setups

Throughout this thesis, the experimental work presented involves the modification of optically transparent media with femtosecond laser pulses. This chapter discusses the experimental apparatus employed for ultrafast laser writing as well as some of the routine characterization set-ups used.

4.1 Direct-Writing Setup

Experiments were carried out with an ytterbium doped potassium-gadolinium tungstate (Yb:KGW) based mode-locked regenerative amplified femtosecond laser system PHAROS (Light Conversion Ltd.) (Fig. 4.1). This system emits trains of femtosecond pulses at 1030 nm with repetition rates varying from 10-200 kHz. The transform-limited pulse duration of the system is 270 fs, which can be stretched to 10 ps by a built in grating compressor. The maximum average power of the source is 6 W.

Figure 4.1: Yb:KGW (Yb-Doped Potassium Gadolinium Tungstate) Femtosecond Laser System (Pharos, Light Conversion). The laser operates at 1030 nm with a minimum pulse duration of 270 fs over a range of repetition rates from 10 kHz to 500 kHz.

The main femtosecond writing set-up involves the collimated laser beam passing through a power control system consisting of a half-wave plate mounted in a motorized stage and linear Glan polarizer with the use of dielectric mirrors to direct the path of the light (Fig. 4.2). Another half-wave plate and Glan polarizer combination is used at the beginning to ensure the power does not exceed 2 W to make sure sensitive optics in the lab are not damaged. The beam is then sent to the main laser writing set-up. Just before the beam is sent to the focusing optics, the beam traverses another rotation stage, mounted with a wave plate depending on the polarization orientation required. The laser beam is then focused with objective or aspheric lenses. The sample being irradiated by the femtosecond pulses is mounted onto a XYZ linear air-bearing position stage (Aerotech Ltd.). The modification experiments are monitored with a Retiga 2000 QImaging CCD camera that is illuminated from the back side of the sample with a fiber light source. Depending on the focusing optic used, a telescope is needed before the CCD to correctly image the sample during laser writing. The entire system is controlled by a SCA (Workshop of Photonics) writing system, which allows a user friendly interface to program the necessary writing parameters and designs. In order to characterize the duration of the pulse, a sample of the beam is sent to a single shot autocorrelator (APE Pulsecheck). Other methods of characterization and beam manipulation were implemented for the experiments conducted in this thesis, which will be discussed later in this chapter.

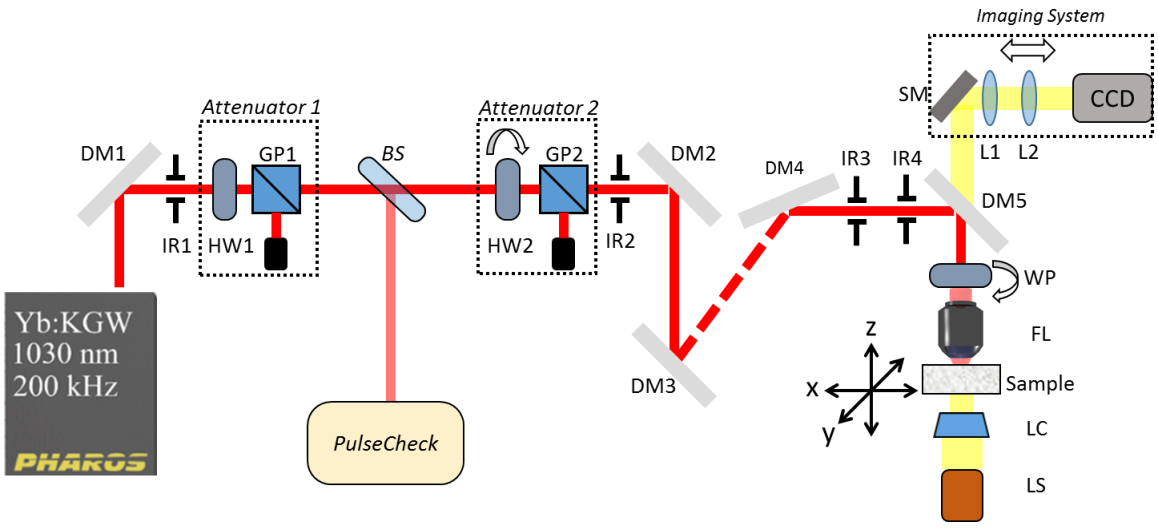

Figure 4.2: The main femtosecond laser writing set-up. DM1-5: dielectric mirrors, SM: silver mirror, IR1-4: irises for alignment, HW1-2: half-wave plate, BS: beam sampler, GP1-2: linear Glan polarizers, L1-2: lenses, LC: condenser, LS: light Source, WP: rotation stage for either half-wave or quarter-wave plate, FL: focusing lens.

4.2 Design for Controlling Spatio-Temporal Couplings

In order to know what state the laser is in during ultrafast laser modification, a multi-shot SHG-FROG was set-up and established as a means of measuring the dispersion seen in the pulse. The control of the dispersion, and thus PFT, is also established and discussed. A discussion about the rotation of a simple dove prism that is shown to rotate the SC of the beam, effectively allowing one to control the direction of the tilt, is also provided.

4.2.1 Pulse Front Tilt Characterization

To have control of the spatio-temporal couplings in each laser pulse, a proper characterization method needs to be introduced. An IR-GRENOUILLE (Swamp Optics) designed for wavelengths from 900 to 1100 nm was available in the lab and was initially tested to see if it could correctly measure the spatio-temporal couplings of the pulse. Before testing, there was an issue with the algorithm associated with the GRENOUILLE, where a specific value in the algorithm had to be multiplied by a constant factor. This then meant that the data had to be extracted from the raw measurement. A simple experiment was conducted to benchmark the accuracy of the GRENOUILE by comparing pulse duration measurements with the autocorrelator. The pulse duration of the main laser set-up was varied from positive to negative dispersion and vice versa and the pulse duration was measured with both systems. The autocorrelator was used as the basis of accuracy since the instrument is known to be correct. While the GRENOUILE system was able to measure increasing and decreasing pulse duration, it was not accurate in the actual values. Even after attempting to re-align the system, the GRENOUILLE was not accurate enough to correctly measure the spatio-temporal couplings of the pulse (Table 4-1).

Autocorrelator (fs)	**GRENOUILLE (+GDD to –GDD) (fs)**	**GRENOUILLE (-GDD to +GDD) (fs)**
1000	505	500
880	475	495
800	425	435
700	346	450
600	325	423
500	297	380
400	277	290

322	280	260
330	264	280
410	318	296
500	360	320
600	422	350
700	449	410
820	482	430
900	520	490
1000	520	535

Table 4-1: Pulse Duration Benchmark Test of GRENOUILLE

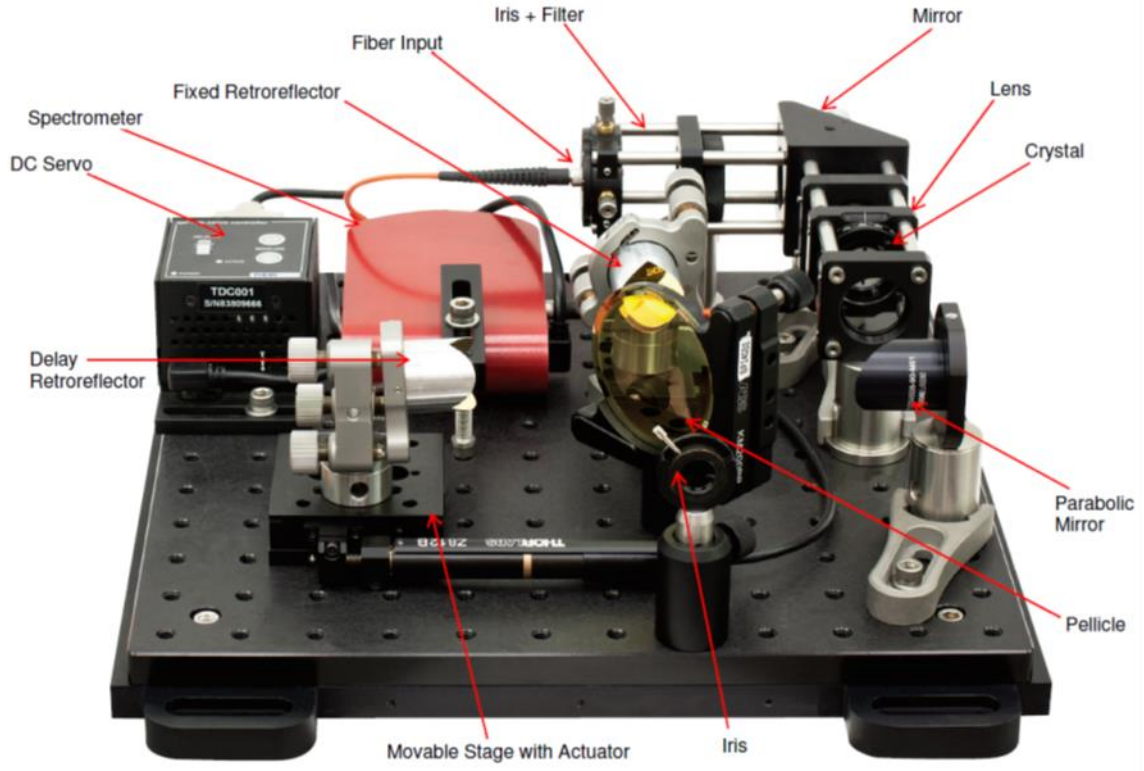

Figure 4.3: Set-up of the multi-shot SHG-FROG used for pulse characterization. Image source: ThorLabs Manual [176]

A multi-shot SHG-FROG set-up was then purchased from Thor Labs and placed into the beam path to provide a method of measurement of the temporal chirp. The set-up (Fig. 4.3) involves splitting the incoming beam into two beams with the use of a pellicle. It is important to note that the pellicle is a few microns thick, thus the original pulse experiences only minimal dispersion before

the measurement. The beam is split into two copies of the same beam, with one travelling in a delayed line via a moveable retroreflector. An off-axis parabolic mirror focuses the laser pulses onto a Barium Borate crystal (*BBO*). SHG is generated in the crystal when both pulses experience a temporal and spatial overlap in the crystal. The resulting SHG is directed to a spectrometer after passing through an iris and filter to ensure a background-free measurement. The measurement involves scanning the delayed line, with the use of a step motor, across the entire overlap of the two copies to generate a FROG trace (Fig. 4.4). The system was designed to measure laser pulses at 650 nm - 950 nm but the appropriate optics can be changed so that the FROG could also measure laser pulses ranging from 950 nm – 1150 nm. This ability to transform the system for different wavelengths and to change the optics for re-alignment and repair, instead of relying on a black box system, is the reason why the SHG-FROG system was used.

A software interface involving a three step process is used to re-create the trace to generate the final FROG trace measurement; acquisition, pre-processing and reconstruction. The acquisition portion involves performing the measurement. Pre-processing converts the raw measurement into something suitable for the FROG algorithm as needed. This involves smoothing to remove any noise or laser fluctuations, thresholding to set pixels with an intensity below a certain level to defining the frequency axis, if it cannot be inferred from the raw trace. Reconstruction uses two different iterative methods, vanilla and generalized projection, to establish satisfactory convergence. Depending on the order of the phase from the reconstruction, the dispersion can be inferred (Fig. 4.4), which directly correlates to the GDD of the pulse. Due to the symmetry of the SHG-FROG trace, the sign of the phase and dispersion (positive or negative) cannot be discerned. This can be alleviated by placing a piece of transparent glass in front of the FROG system to add positive dispersion and phase to determine the resulting properties of the pulse. When used in conjunction with a fiber spectrometer measuring the spatial chirp (Chapter 3.2.3), the PFT can be quantified.

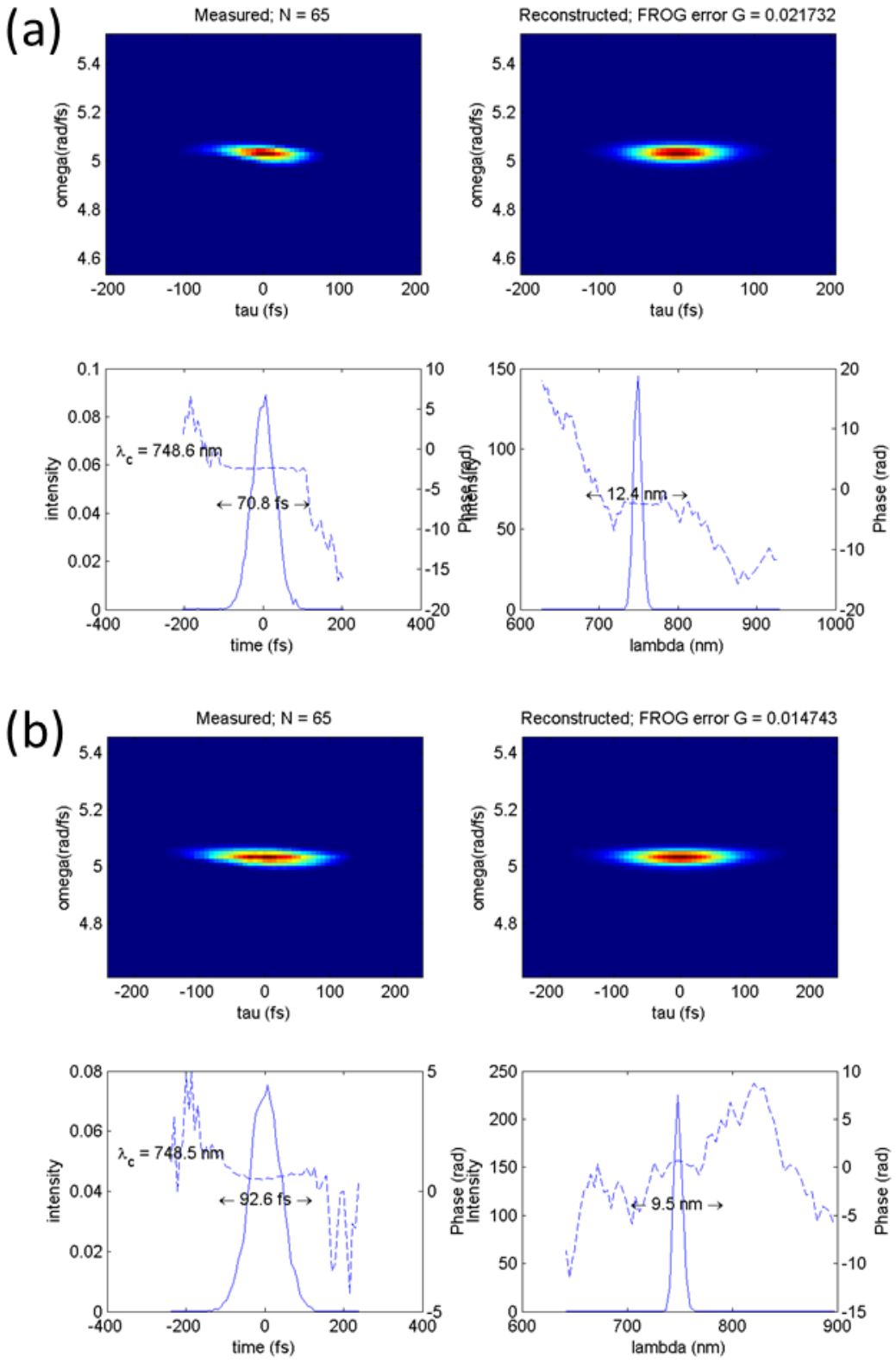

Figure 4.4: Sample FROG traces from the user interface. Both traces are a comparison of what is seen when a pulse has no temporal chirp (a) and a pulse with temporal chiro (b). A flat phase curve across the autocorrelation and spectrum, as seen on the left, means dispersion is zero; no temporal chirp. A second-order curve seen across the

autocorrelation and spectrum, as seen on the right, means strong dispersion is evident in the laser pulse; temporal chirp.

4.2.2 Prism Compressor Control

In the initial stages of research, PFT was introduced into the pulse with the use of prism pairs. Initially, the laser source was used in conjunction with a NOPA (TOPAS, Light Conversion) to obtain a tuneable laser source in a spectral region from 600 nm to 900 nm at pulse durations as low as 30 fs. The concept of a typical optical parametric amplifier (*OPA*) is based on difference frequency generation where a strong pump wave (ω_P) and a weaker signal wave (ω_s) are incident on a nonlinear crystal. At the output, the signal wave is amplified and a new idler wave (ω_i) is generated. An important application of OPA systems is seeding with a large bandwidth pulse in the visible or near-infrared, which allows for high tunability of the output pulse. OPA systems have the capability of generating pulses significantly shorter than the pump pulses by exploiting the broad gain bandwidths observed during the parametric interaction in nonlinear crystals [177]. Typical OPA systems involve the generation of a seed pulse either through parametric superfluoresence or white light generation (Fig. 4.5a). From there, the seed pulse and the pump are combined in a nonlinear crystal to pre-amplify the signal. In order to achieve the correct temporal overlap for a particular wavelength, a delay line is placed in the path of the pump. The signal beam is then sent to another nonlinear crystal to be amplified. From here, the signal beam is sent out to a compressor to obtain a transform-limited pulse. However, when using a collinear geometry as seen in typical OPA systems, the propagation direction is chosen for the phase matching of a particular signal wavelength and can limit the effective broadband range of the system. This can be alleviated by using a noncollinear geometry such that the signal and pump wave vectors are set at an angle from one another, resulting in a projection-based phase matching criteria that increases the broadband frequency range of the system (Fig. 4.5b).

To control the spatio-temporal couplings, two prism pairs were put into the design to control each of the major couplings separately (Fig. 4.6). The initial prism splits the respective wavelength components of the pulse, introducing AD. The second prism is then used to collimate the propagating beam, thus negating the AD and introducing a SC alongside TC. It is then reversed in path by a mirror, propagating through the prism pair again negating the spatial chirp and doubling the temporal dispersion. The temporal dispersion is controlled by controlling the distance between prisms as well as increasing the amount of glass propagated through in the second prism. A second prism pair was put into the laser propagation after this first pair in a single-pass geometry to control the SC. Therefore, the SC and TC can be controlled independently from one

another. Ensuring that there is no AD evident in the beam by monitoring the SC along the propagation of the laser beam means that this system completely controls the PFT.

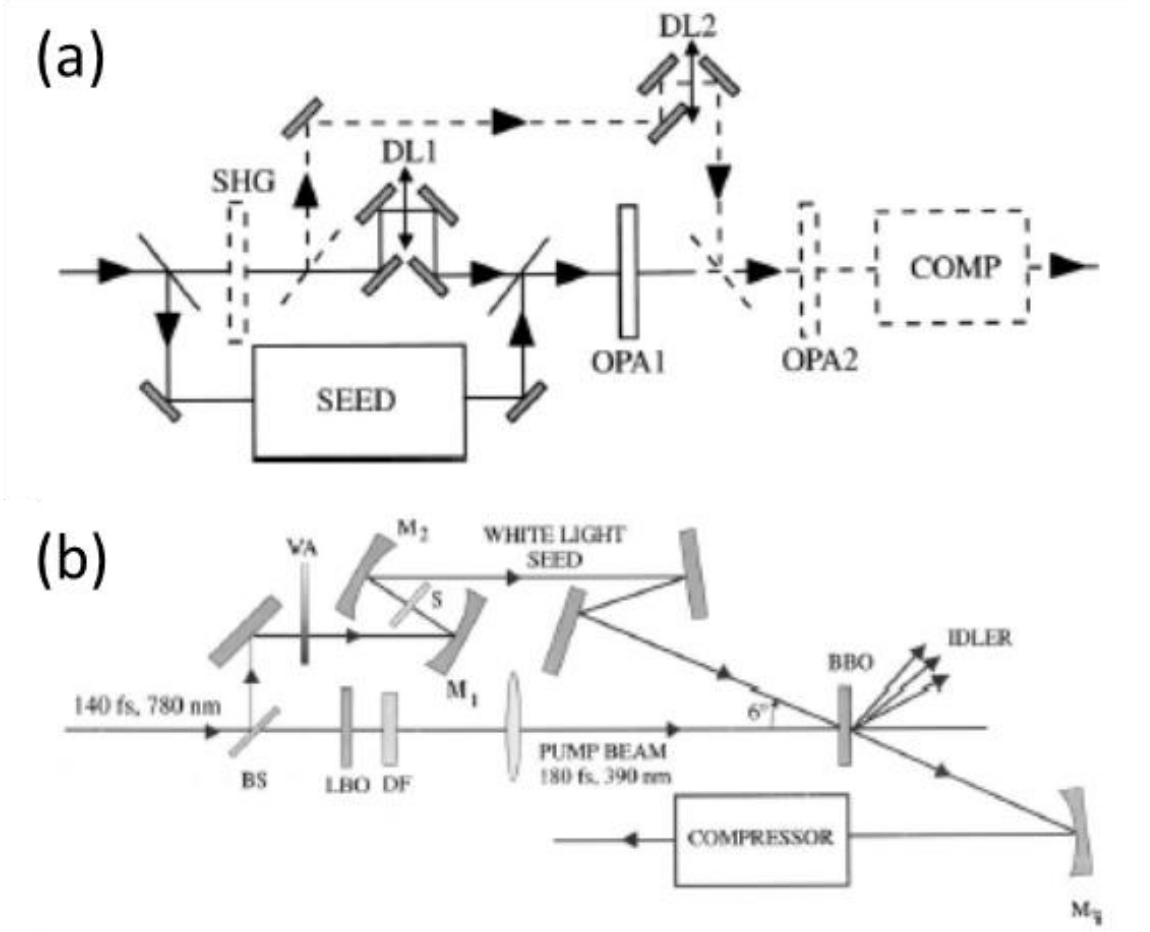

Figure 4.5: (a) Design of a typical OPA. SEED: seed generator, DL1 and DL2: delay lines, OPA1, OPA2: parametric amplification stages, COMP: compressor. (b) Design of a NOPA. BS: beam splitter, VA: variable attenuator, S: sapphire plate, DF: dichroic filter, $M_{1\text{-}3}$: spherical mirrors. Image Source: Cerullo and De Silvestri [177]

When setting up prism pairs, it is imperative that each prism is placed at the angle of minimum deviation (i.e. angle between incident and emerging ray needs to be minimum). This is observed simply by rotating the prism whilst the light is propagating through the prism and finding the exact point where the beam stops deviating. The prisms used in the experiment were all UV-fused silica prisms with apex angles of 60°. The temporal properties of the beam were monitored by the FROG system discussed in Chapter 4.2.1. The TC was controlled with the position of the second prism in the first prism pair. The presence of SC was confirmed by measurements with a fiber coupled spectrometer (Avantes) (discussed in Chapter 3.2.3).

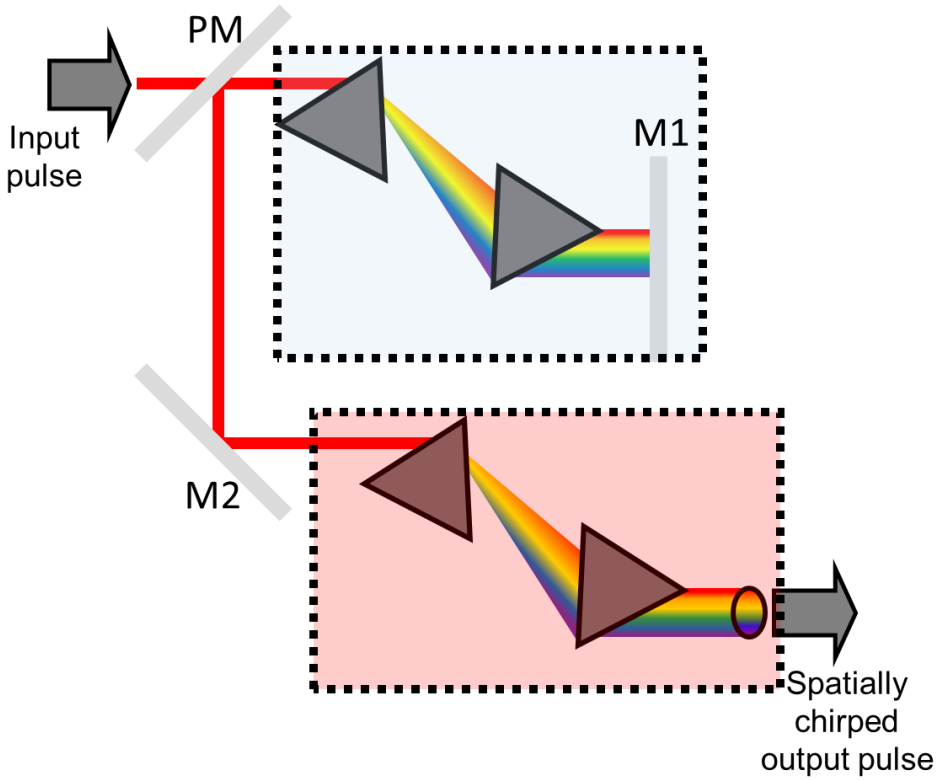

Figure 4.6: Prism compressor setup to control SC and TC independently. The input pulse coming from a source propagates through the first pair of prisms in a double-pass geometry using a mirror, M1 (blue shaded region), removing SC and doubling TC. The distance between the two prisms controls the TC alongside the amount of glass travelled through in the second prism. The beam is picked off from its original path (PM) and propagates through a second set of prisms in a single-pass geometry (red shaded region). The separation distance controls SC while inducing TC, which can be compensated with the first prism set.

While the preliminary work done in controlling spatio-temporal couplings were done with NOPA and the prism pairs, there were many issues with the design. The time that passed between the NOPA system being set-up in the lab and used for this research was long and thus the system was severely misaligned. A lot of time was spent aligning the NOPA set-up but it became abundantly clear that there were several problems with the design. Wavelength registration in the system was incorrect and therefore, the maximum gain achievable for the broad wavelength range based upon the original specifications were never met, even after re-alignment (Fig. 4.7). There was also the issue that the quality of the beamspot coming out of NOPA was not Gaussian and/or symmetric at the highest power achievable for a chosen wavelength. This made it difficult to do experiments where the observed phenomena being investigated could be observed with spatio-temporal couplings and asymmetry in the beam [166]. Therefore, the beam within NOPA was tuned for the highest beamspot quality, instead of maximum power. This greatly reduced the

maximum pulse energy available for experiments, especially considering that power losses were observed as the laser propagated through each prism due to reflections. Since the NOPA system was not completely closed from the laboratory setting, the efficiency of NOPA was affected by the humidity of the room. This meant that day to day the system would have to be tuned to achieve the maximum power and beam quality at a designated wavelength.

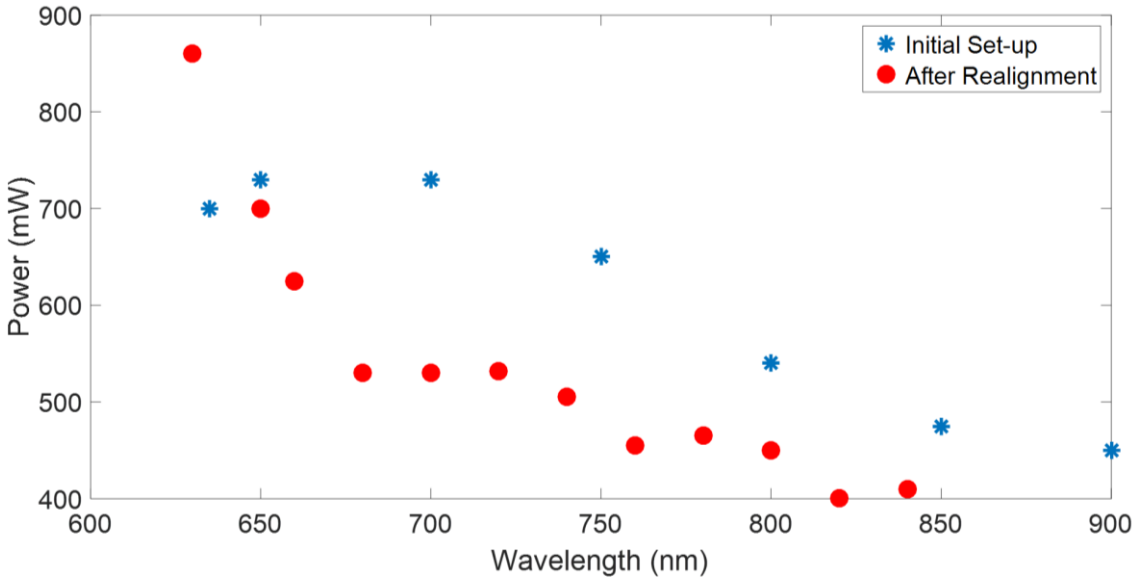

Figure 4.7: Output power vs. output wavelength of NOPA during the initial set-up of the system (blue stars) and after realignment (red circles).

Once the NOPA system was realigned and tuned for maximum efficiency, the first issue involved the residual spatio-temporal couplings from the NOPA design. If the pump or signal had any residual SC or AD, it becomes magnified within the NOPA design [178,179]. There is also the issue of pump and signal beams misalignment, which may introduce several degrees of PFT caused by AD introduced by the angular dependent amplifier in NOPA [178,179]. If the residual spatio-temporal couplings after NOPA are quite complicated, it makes it difficult to compensate and control. For NOPA at λ = 0.75 μm, the bare beam coming out had a GDD magnitude of 3305.286 fs^2. To compensate for this, the initial prism pair controlling TC needs a large separation distance, *L*. The GDD of a single-pass geometry is calculated by [180]:

$$GDD = \frac{\lambda^3}{2\pi c^2}\left\{4L\cos\vartheta\left(\frac{dn}{d\lambda}\right)^2 - 2L\sin\vartheta\left[\frac{d^2n}{d\lambda^2} + \left(2n - \frac{1}{n^3}\right)\left(\frac{dn}{d\lambda}\right)^2\right]\right\} \tag{4.1}$$

where θ is the angle separation of the propagating wavevectors of the laser pulse and the derivatives of the refractive index are based on the Sellmeier Equation [180]:

$$n(\lambda) = 1 + \frac{B_1\lambda^2}{\lambda^2 - C_1} + \frac{B_2\lambda^2}{\lambda^2 - C_2} + \frac{B_1\lambda^2}{\lambda^2 - C_3} \tag{4.2}$$

where the coefficients $B_{1\text{-}3}$ and $C_{1\text{-}3}$ are Sellmeier coefficients that are experimentally determined. If λ = 0.75 μm, $\theta \approx 4°$, and the prisms were made of fused silica (B_1 = 0.69617, B_2 = 0.40794, B_3 = 0.897479, C_1 = 4.67915 x 10^{-3} μm^2, C_2 = 1.35121 x 10^{-2} μm^2, C_3 = 97.934 μm^2), L would have to be roughly 1.3 m. Therefore, the separation distance in a double pass-geometry, where the beam is propagating apex-to-apex of the prisms, only needs to be 65 cm (Fig. 4.8). To control the residual SC and/or AD in the beam, the single pass prism geometry would need to be used, which also induces TC that needs to be compensated for.

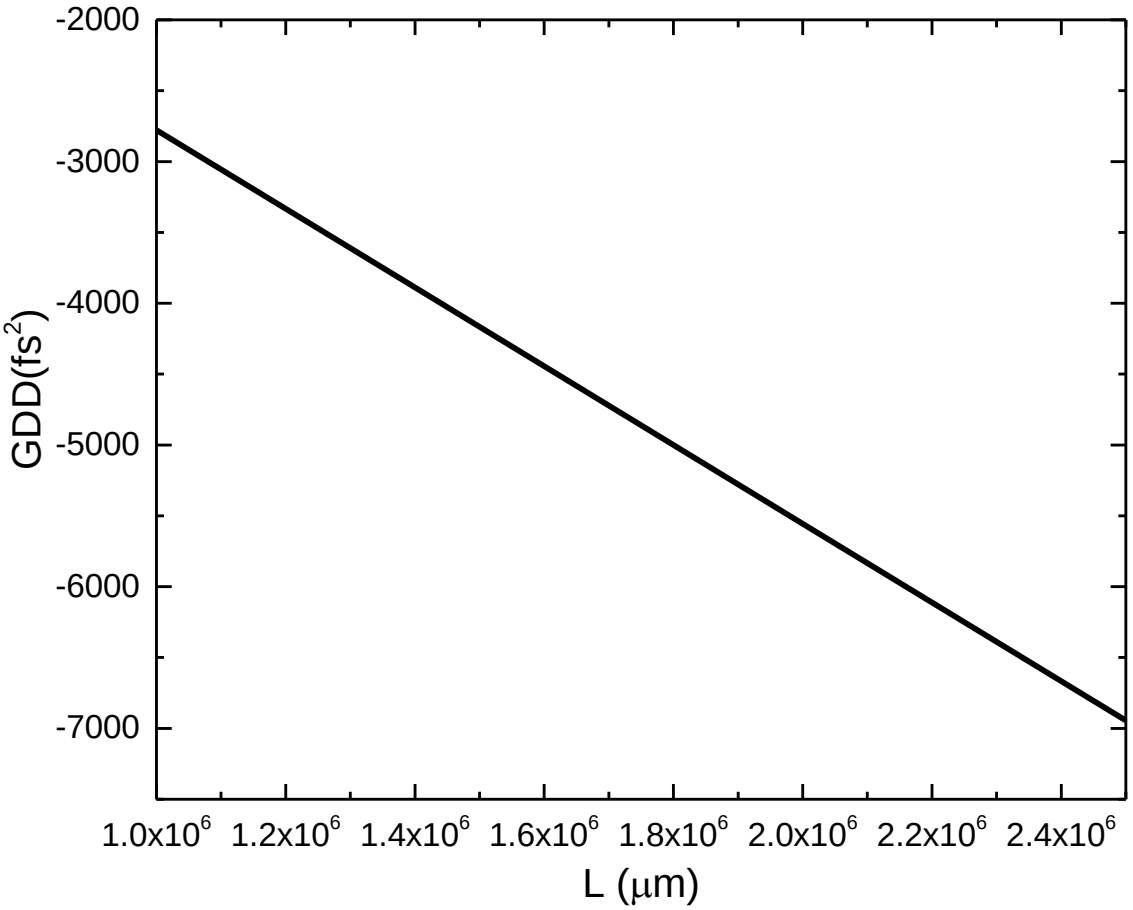

Figure 4.8: GDD induced by single-pass prism compressor. To compensate for the GDD from the bare pulse, the separation distance (*L*) between the 2 prisms needs to be roughly 1.3 m in a single pass geometry - 65 cm in a double pass geometry. (λ = 0.75 μm)

There is also the issue of dispersion induced by large glass elements such as objective lenses. Objective lenses are actually known to have detrimental effects in focusing with spatio-temporal couplings of a large bandwidth pulse, like those generated from NOPA [181]. For example, a NA = 0.55 objective lens was characterized using the SHG-FROG (Fig. 4.9). With the objective lens in place, the pulse is stretched, with a GDD of roughly 2500 fs^2. This alongside the bare beam coming out of NOPA at λ = 0.75 μm would need a prism separation of roughly 2 m in a single pass geometry to compensate for the total residual dispersion alone. When working with such large

propagation distances, the quality of the beam worsens. The NOPA design used in the experiment utilises telescopes to attain the highest possible gain without causing optical damage to any of the nonlinear crystals or inducing unwanted nonlinear effects, such as self-focusing, in order to limit beam distortions or breakups. However, these telescopes typically have a particular range where the beam remains collimated, after which the beam expands due to diffraction. Using long propagation distances to compensate all the residual spatio-temporal couplings ruins the quality of the beam, making it nearly impossible to control the spatio-temporal couplings after the fact. The lack of stability of the beam generated with NOPA, alongside the difficulty of compensating spatio-temporal couplings whilst controlling them, made this design not ideal for experiments where the underlying causes of ultrafast laser-material interaction phenomena are under investigation.

To characterize the spatio-temporal couplings of the prism pairs, Kostenbauder matrices were used. For a double pass geometry (please refer to Appendix A for derivation):

$$K_{prismcomp} = \begin{bmatrix} 1 & L1 + L2 + L3 & 0 & -4\pi \frac{\partial n}{\partial \omega} \frac{\cos\gamma}{\cos\gamma'} \tan\gamma \, (L1 - L3) \\ 0 & 1 & 0 & 0 \\ 0 & \frac{4\pi \frac{\partial n}{\partial \omega} \frac{\cos\gamma}{\cos\gamma'} \tan\gamma}{\lambda} (L1 - L3) & 1 & \frac{-\left(4\pi \frac{\partial n}{\partial \omega} \frac{\cos\gamma}{\cos\gamma'} \tan\gamma\right)^2}{\lambda} (L1 + L3) \\ 0 & 0 & 0 & 1 \end{bmatrix} \quad (4.3)$$

where L1 - L3 are the separation lengths between prisms and γ and γ’ are the incident and interior angles of light on the prism. Looking at the GDD term of the matrix, it becomes clear that prism compressors induce negative GDD. This can be tuned simply by changing the amount of extra glass in the beam with the second prism.

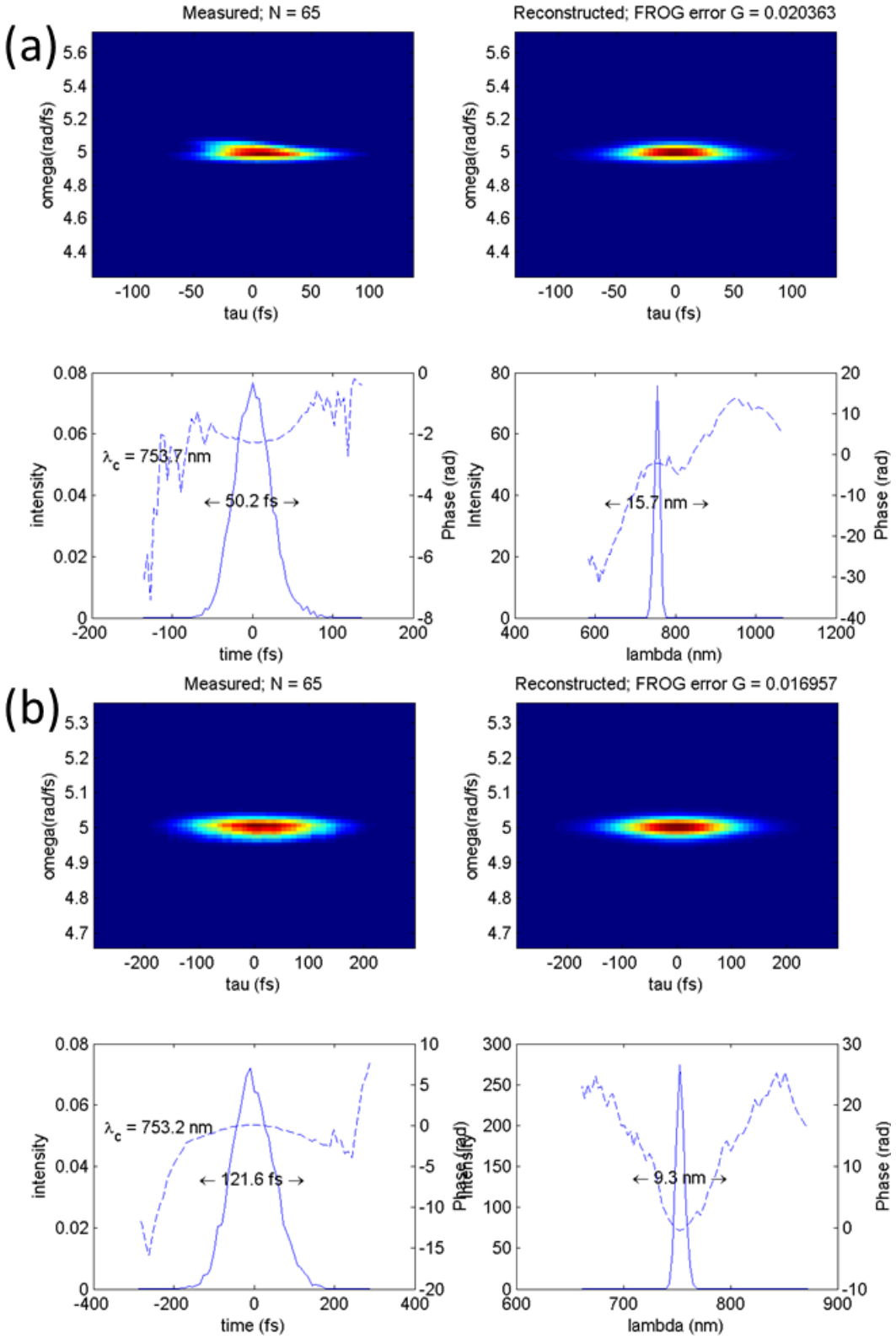

Figure 4.9: FROG trace measurements of the (a) bare beam after prism compressor and (b) with the NA = 0.55 objective lens (below). The significant amount of glass in the objective lens disperses the bare beam, stretching the pulse by ~70 fs.

4.2.3 Diffraction Grating Compressor Control

In order to overcome the issues associated with the spatio-temporal control seen with the original prism compressor set-up, a design was created to control spatio-temporal couplings with the Pharos system. The benefit of NOPA was the large bandwidth available to disperse with prisms. However, the sensitivity to dispersion in these laser pulses also made it extremely difficult to compensate and control. With the main Pharos laser, the bandwidth is quite narrow (~ 8 nm), making it difficult to disperse by simply going through glass volumes, making it advantageous to control. There is also the weak dispersion observed for the near-IR compared to the visible spectrum in typical transparent glasses (Fig. 4.10). Prisms are then not dispersive enough for such narrow bandwidth, near-IR laser pulses. Therefore, dispersion was introduced and controlled with the use of grating compressors.

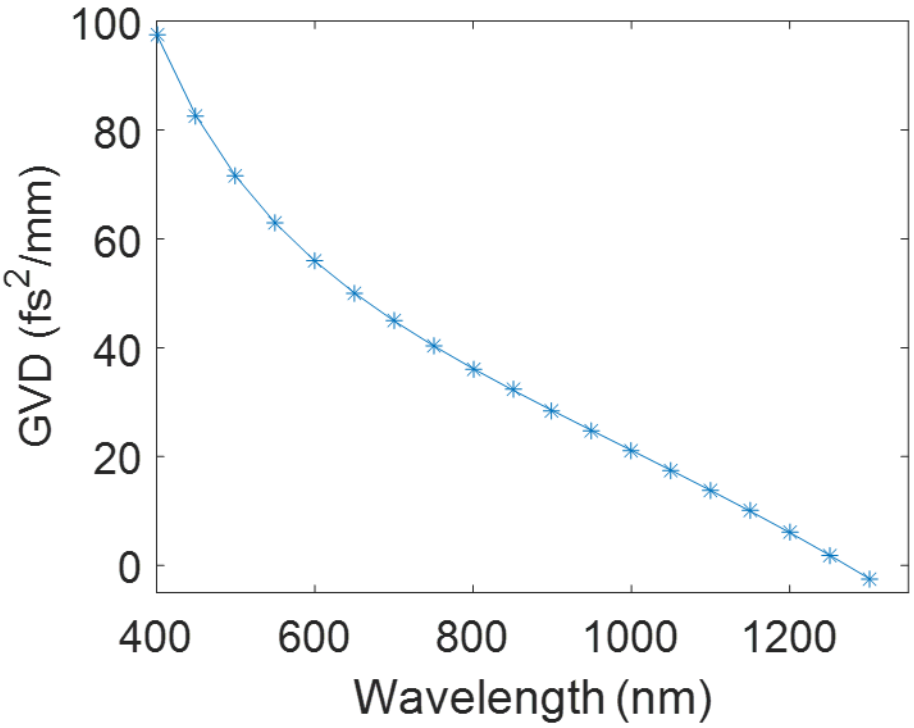

Figure 4.10: Material dispersion of fused silica with respect to wavelength. The group velocity dispersion (GVD) decreases as the wavelength goes from the visible spectrum to the near-IR, indicating weak dispersion for near-IR laser sources.

Grating compressors work similarly to prisms in that an input beam incident on a grating immediately gets diffracted at an angle as a function of frequency, with a front that becomes tilted. It then needs to be collimated effectively by reflecting off a second equivalent grating yielding SC, ensuring there is no AD or residual PFT. This SC and induced TC is dependent on the separation between the two gratings. To remove the SC, a double-pass geometry of gratings is used similarly to the double-pass prism design.

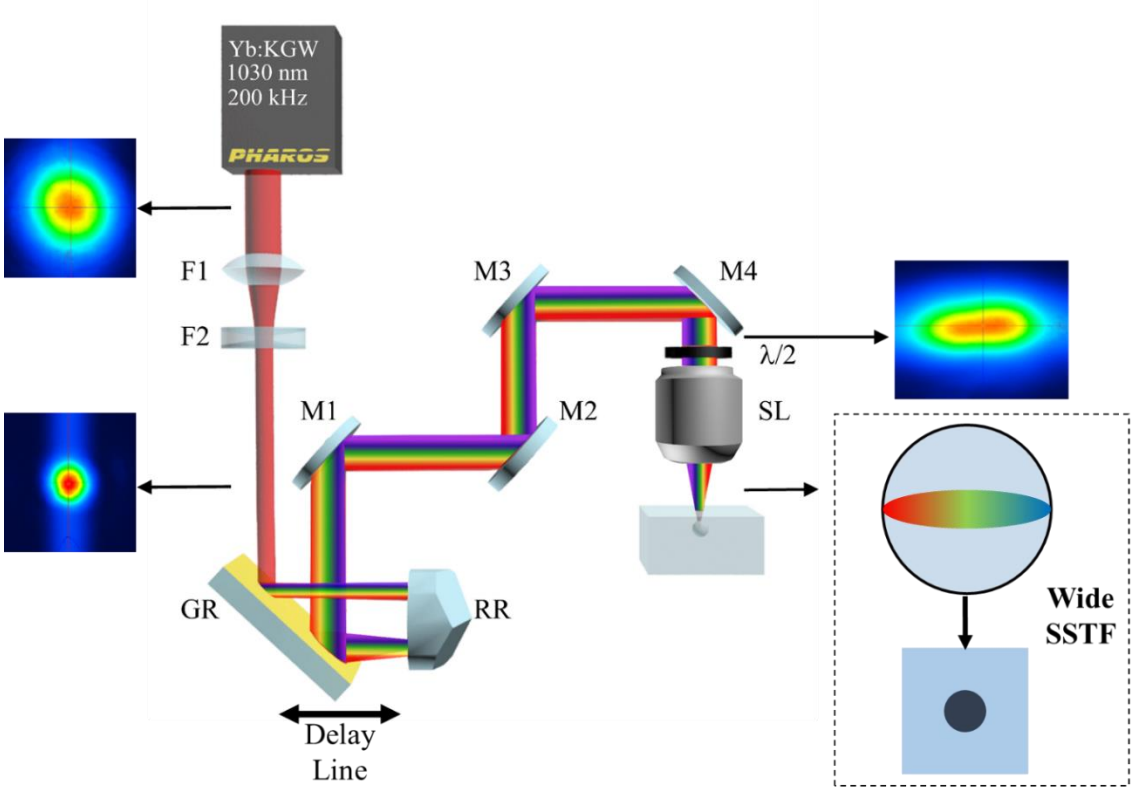

Figure 4.11: Double Grating Set-up for Full Spatio-Temporal Control. The first diffraction grating is integrated in the laser system and controls TC. The second grating in combination with a retroreflector enables tailoring of SC by simply varying the distance between these elements. A Galilean telescope ensures that the laser beam is not clipped by the focusing lens rear aperture. The addition of SC introduces ellipticity into the laser beam. However, a wide SSTF focusing geometry ensures that the beam spot near the focus, where light-matter interaction takes place, is circularly symmetric. (F1 = 200 mm, F2 = -100 mm, GR = Grating, RR = Retroreflector, M1-4 = Mirrors, λ/2 = Half-Waveplate, SL = Focusing lens).

TC and SC were separately controlled with the two grating compressors, allowing one to precisely tailor the spatio-temporal properties of the beam (Fig. 4.11). The first compressor was already incorporated into the laser cavity to control the temporal chirp by adjusting the GDD. SC was controlled by the second pulse compressor, by varying the distance between a single grating and a retro-reflector, in a single pass geometry. The use of the retro-reflector provided an easy manner of aligning the beam for the second reflection to collimate the SC, due to its unique design of being able to reflect light along the same path through which it came. The SC was controlled through a delay line by moving the retroreflector accordingly.

When designing the second grating compressor, third-order dispersion needs to be taken into account. Third-order dispersion arises from a frequency dependence of the GDD, which can

drastically affect the spatio-temporal structure of the pulse [180]. This can occur if multiple grating elements are used in pulse compression techniques but the gratings used are different in periodicity [182]. Even if the groove densities of the gratings are the same, the incident angle of the laser pulses on the gratings need be the same as well. However, it needs to be taken into account that third-order dispersion becomes a major factor for pulse durations less than 50 fs. Regardless, the gratings used in the experiment were identical in periodicity and were designed specifically for a 1 μm wavelength with a suitable blaze angle to maximize the efficiency upon reflection (600 lines/mm, 17°27’ blaze angle).

Additionally a Galilean telescope was placed before the second grating compressor to match the beam with the back aperture of the focusing lens. It should be noted that due to the amount of power loss experienced with grating compressors, due to multiple order diffraction reflections, a large amount of power needs to be used. Careful consideration needs to be taken when focusing large power beams to ensure there is no self-focusing in air or laser-induced breakdown in air, which would greatly distort the beam quality. Therefore, a negative focal length lens is used to ensure no beam distortions are introduced by the telescope.

The beam is then focused in a wide-field SSTF configuration, which yields a circularly symmetric focus despite ellipticity at the focusing lens caused by SC [181]. In the experiments, angular dispersion is not present, thus spatial and temporal chirp can be independently controlled. The SC of the pulse is measured by scanning a fibre attached to a spectrometer across the pulse where the slope of the wavelength vs. position is measured to provide the SC. The TC is controlled with the first compressor and is measured with an APE pulseCheck multi-shot autocorrelator. The GDD is then calculated by the following equation:

$$GDD = \frac{1}{4(\ln 2)} \sqrt{\left(\frac{c_B \Delta t_{out}}{\Delta v}\right)^2 - \left(\frac{c_B}{\Delta v}\right)^4} \tag{4.4}$$

where Δt_{out} is the measured pulse duration, Δv is the pulse bandwidth and c_B is the function of the pulse profile for the time-bandwidth product ($c_B \leq \Delta t_{out} \Delta v$, c_B = 0.44 for a Gaussian pulse). This value is confirmed with the use of the SHG-FROG alongside Kostenbauder matrix formalisms to ensure the experimental measurements match theoretical predictions [127] (Appendix B). With both measurements, PFT is calculated by multiplying the frequency gradient measured with the GDD of the characterized pulse.

This system was then used for all major spatio-temporal coupling experiments discussed in this thesis. To state the electric field of the beam at the focusing lens for all experiments, to discern

the spatio-temporal couplings upon focusing, the Q-matrix formalism was used. The program used can be seen in Appendix B but the Q-coefficient calculation is [129]:

$$\frac{i\lambda}{\pi}\begin{bmatrix}\tilde{Q}_{xx} & \tilde{Q}_{xt}\\ -\tilde{Q}_{xt} & \tilde{Q}_{tt}\end{bmatrix}=\begin{bmatrix}\frac{\lambda_0}{\pi}\frac{2\varphi_2-i\tau^2}{4\zeta^2+w^2\tau^2+i2\varphi_2w^2} & -\frac{2\lambda_0}{\pi}\frac{\zeta}{4\zeta^2+w^2\tau^2+i2\varphi_2w^2}\\ -\frac{2\lambda_0}{\pi}\frac{\zeta}{4\zeta^2+w^2\tau^2+i2\varphi_2w^2} & \frac{i\lambda_0}{\pi}\frac{w^2}{4\zeta^2+w^2\tau^2+i2\varphi_2w^2}\end{bmatrix} \tag{4.5}$$

where w is the beam spot, φ_2 is the GDD (Equation (3.18)), ζ is the SD (Equation (3.14)) and τ is transform-limited pulse duration. Equation (4.5) is a general matrix that can be used for any system that introduces both spatial and temporal chirp [129].

4.2.4 Dove Prism Rotation

One of the most prevalent ways that PFT affects ultrafast laser modification is its orientation with respect to polarization of the laser. The anisotropic sensitivity observed in 2011 [6] shows the direction sensitivity with PFT and to independently move PFT while observing ultrafast laser modification would shed light on its role and importance in modification. One of the ideas was to rotate PFT independently of other parameters to really gauge its mutual dependence. Dove prisms are truncated right-angle prisms that are typically used to invert or rotate an image without dispersion (Fig. 4.12) [183,184]. This is beneficial to experiments involving PFT in order to rotate the PFT orientation without adding any additional effects to the beam before modification, which could be seen in other optical elements [183]. To observe whether or not the PFT is effectively rotated, a spectrometer was scanned across the beam in both directional axes to take accurate measurements of the spatial chirp. The dove prism was then rotated 45° through a full 360° rotation. The spatial chirp is observed to rotate as a sinusoidal function (Fig. 4.13) through the angular rotation, illustrating the rotation of the PFT with the dove prism.

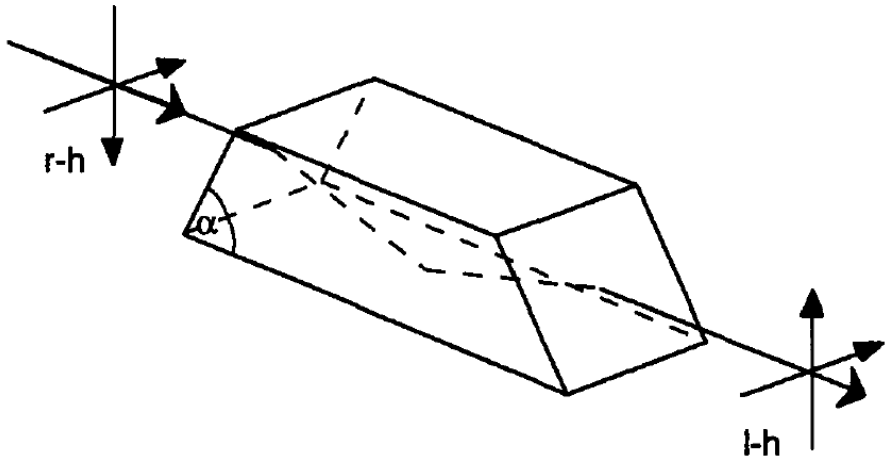

Figure 4.12: How a dove prism rotates images. Image source: Padgett and Lesso [183].

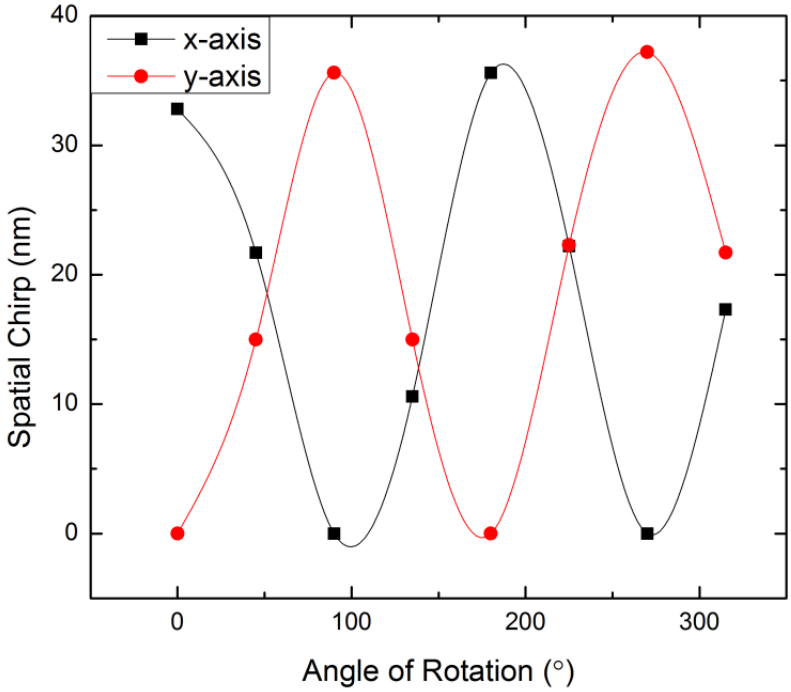

Figure 4.13: Rotation of spatial chirp across the laser pulse transmitted through a rotating dove prism. Measuring the spatial chirp in the x- and y-axis shows the rotation of the spatial chirp through a 360° rotation of a dove prism.

One of the inherent issues with the dove prism is that the polarization state of the light behaves as a polarizer with a poor extinction rate rather than a half-wave plate as expected. The end result of the polarization is a slightly elliptical beam in the angle direction of rotation. To alleviate this issue, a combination of a half-wave plate alongside with the dove prism can be used to ensure the polarization state rotates with the PFT rotation [183,184]. While initial experiments were conducted using the dove prism alongside the original NOPA design, further experimentation with the dove prism was not conducted. However, it does show to be an effective manner in rotating spatio-temporal couplings.

4.3 Quantitative Birefringence Measurement

Birefringence is the optical property of a material that has a polarization dependent refractive index. The form birefringence that results from nanograting formation is the result of an alignment of sub-microscopic platelets [7,8]. When light is polarized parallel to the interfaces from the alignment, the light experiences a larger refractive index. As a result, a phase difference for two orthogonal polarization states is observed. For the ordinary (perpendicular to the optical axis), n_o, and extraordinary (along the optical axis) waves, n_e, the refractive indices of refraction are [7,8]:

$$n_e = \sqrt{\frac{n_1^2 n_2^2}{f_f n_2^2 + (1 - f_f) n_1^2}} \tag{4.6}$$

$$n_o = \sqrt{f_f n_1^2 + (1 - f_f) n_2^2} \tag{4.7}$$

where n_1 and n_2 are the local refractive indices of the nanograting (i.e. the platelets) and $f_f = t_1/\Lambda$ is form filling factor ($\Lambda = t_1 + t_2$, t_1 and t_2 are the thicknesses of the n_1 and n_2 regions) (Fig. 4.14). In comparison to uniaxial crystals, it is easy to discern whether or not nanogratings have a slow or fast optical axis:

$$n_e^2 - n_o^2 = \frac{f_f (1 - f_f)(n_1^2 - n_2^2)^2}{f_f n_2^2 + (1 - f_f) n_1^2} \leq 0 \tag{4.8}$$

Therefore, nanogratings behave as a negative uniaxial crystal (i.e. extraordinary axis (optic axis) is the fast axis). In comparison to a typical quartz crystal where the refractive index difference is n_e-n_o = 9 x 10^{-3}, nanogratings typically possess a difference of -2 x 10^{-3} to -4 x 10^{-3} [7].

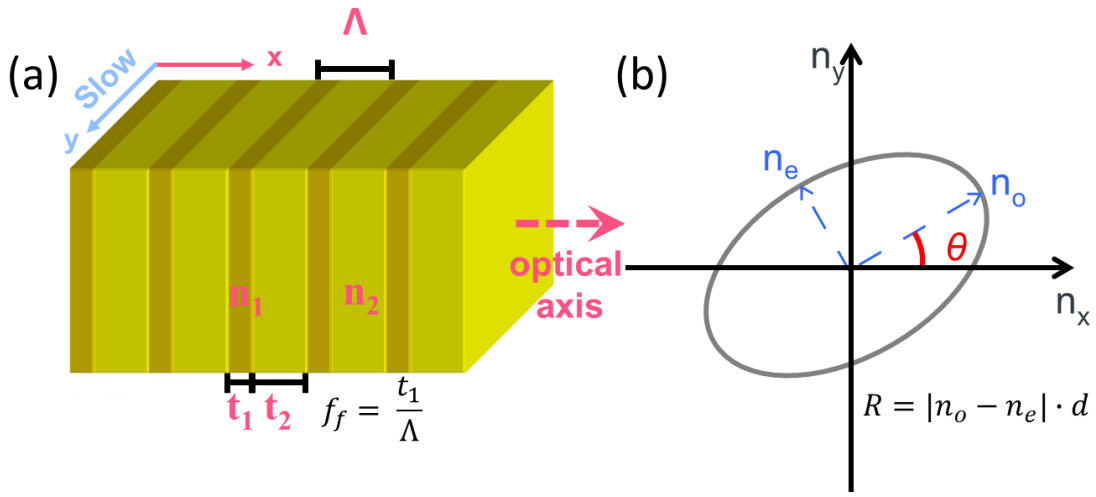

Figure 4.14: Form birefringence due to self-assembled nanogratings. (a) Parallel planes of alternating refractive indices cause form birefringence where t_1 and t_2 are the plane thicknesses of alternating refractive indices n_1 and n_2. (b) Form birefringence is characterized by two parameters: the slow axis orientation, ϑ, and the retardance, R, which is dependent on the thickness of the birefringent structures, d.

The form birefringence of the nanogratings is quantified by the retardance of the fabricated structures. The most direct method to characterize nanogratings is by analysing the structure under a scanning electron microscope. The issues with this method come from the post-processing efforts necessary to expose the underlying structure of the nanogratings through sample polishing and acid etching. There is also the issue that the method restricts the

characterization only to the measurement of the nanograting periodicity. The birefringence can be visibly observed through cross-polarized illumination under a microscope, providing a non-invasive method of observing the birefringence (Fig. 4.15a). However, this is mainly a qualitative measurement and cannot provide a quantitative measure of retardance.

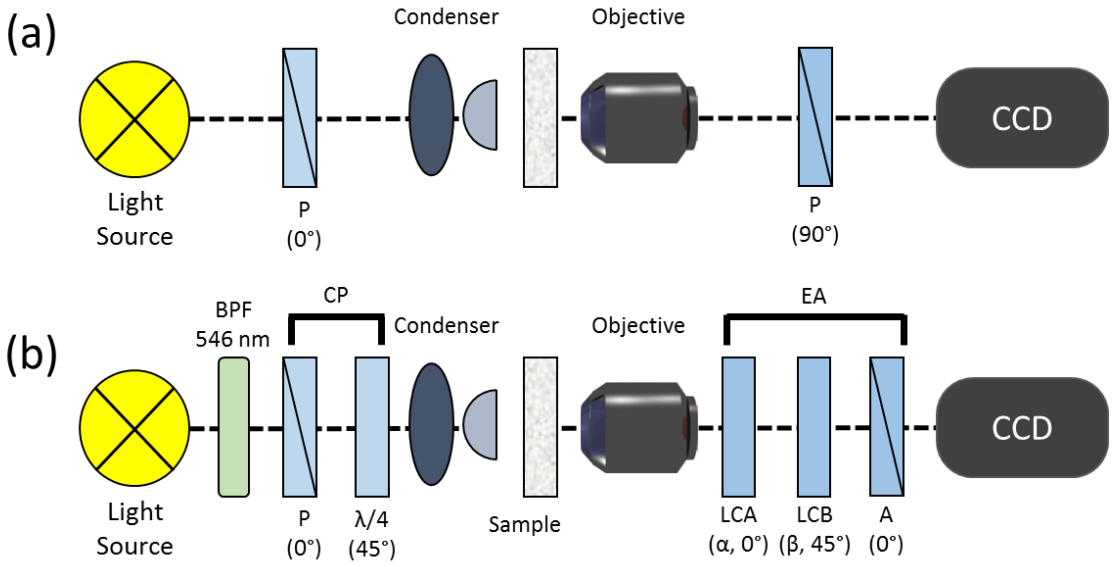

Figure 4.15: Comparison of the two methods of observing form birefringence: (a) cross-polarized illumination and (b) polarized light microscope (PolScope/Abrio). (a) The sample is observed in between crossed polarizers (P) illuminating only the birefringent portions of the sample. (b) The light emitted passes through a bandpass filter (BPF) and is circularly polarized (CP) before being projected onto the sample. The light is collected by the objective and is transmitted through an elliptical analyser (EA) consisting of two liquid crystals (LCA, LCB) of different retardance (α, β) and a linear polarizer (A).

To get a quantitative measurement of the laser induced birefringence, a similar technique to cross-polarized illumination is used. This involves a different combination of polarizers as well as a series of intensity measurements of varying positions of cross-polarization, known as a PolScope microscope [185] (Fig. 4.15b). In the typical polarization microscope design, the sample to be analysed is put in between two linear polarizers. The first one is to make the microscope light source linearly polarized and the second is mounted on a manual rotation stage to control the transmission angle (known as the analyser). Crossing the two linear polarizers would illuminate the birefringent parts of the sample. In the PolScope microscope, the first linear polarizer is replaced with a circular one consisting of a linear polarizer and a quarter wave plate. The design also needs to use monochromatic light, so a bandpass filter is inserted before the circular polarizer (for our design, the bandpass filter is set for 546 nm). The analyser is replaced with an elliptical analyser consisting of two liquid crystal retarder plates (LCA and LCB) and a linear

polarizer. The two liquid crystal plates are controlled by a DC field and are set to be 45° to one another so that it behaves as a linear polarizer with a variable azimuthal, allowing the elliptical analyzer to measure any polarization.

To measure the retardance, R(x, y) and the slow axis orientation, ϕ(x, y), of the birefringent sample, the intensity measured/recorded by the detector (typically a CCD camera) is [185]:

$$I(\alpha,\beta,x,y) = \frac{1}{2}\tau(x,y)I_{max}(x,y)[1 + \cos\alpha\sin\beta\cos R(x,y) - \sin\alpha\sin\beta\cos 2\phi(x,y)\sin R(x,y) + \cos\beta\sin 2\phi(x,y)\sin R(x,y)] + I_{min}(x,y). \quad (4.9)$$

where $I_{max}(x, y)$ represents the illumination intensity on the sample, $\tau(x, y)$ is the isotropic sample transparency, $I_{min}(x, y)$ is the distribution of the depolarized background due to polarizer imperfections and α and β are the retardance values for LCA and LCB, respectively. To attain the measurements of R(x, y) and ϕ(x, y), a series of intensity measurements for different values of α and β are needed. This is done by adding a swing value, χ, to the nominal values of α and β:

$$I_1 = I(\alpha = \frac{\lambda}{2}; \beta = \frac{\lambda}{4}) \quad (4.10)$$

$$I_2 = I(\alpha = \frac{\lambda}{2}; \beta = \frac{\lambda}{4} - \chi) \quad (4.11)$$

$$I_3 = I(\alpha = \frac{\lambda}{2}; \beta = \frac{\lambda}{4} + \chi) \quad (4.12)$$

$$I_4 = I(\alpha = \frac{\lambda}{2} - \chi; \beta = \frac{\lambda}{4}) \quad (4.13)$$

$$I_5 = I(\alpha = \frac{\lambda}{2} + \chi; \beta = \frac{\lambda}{4}) \quad (4.14)$$

where λ is the wavelength set by the monochromatic light source at which the birefringence is measured at (i.e. λ = 546 nm). From here, the measured intensities are used to calculate two parameters, A and B:

$$A = \frac{I_2 - I_3}{I_2 + I_3 - 2I_1}\tan(\frac{\chi}{2}) = \sin(2\phi)\tan R \quad (4.15)$$

$$B = \frac{I_5 - I_4}{I_5 + I_4 - 2I_1}\tan(\frac{\chi}{2}) = \cos(2\phi)\tan R \quad (4.16)$$

Using Equations (4.15) and (4.16), the retardance and the slow-axis azimuth can be calculated.

$$R = \frac{\lambda}{2\pi} \arctan\sqrt{A^2 + B^2}, when\ I_2 + I_3 - 2I_1 \geq 0 \tag{4.17}$$

$$R = \frac{\lambda}{2\pi}\left(\pi - \arctan\sqrt{A^2 + B^2}\right), when\ I_2 + I_3 - 2I_1 < 0 \tag{4.18}$$

$$\phi = -\frac{1}{2}\text{arccot}\left(\frac{A}{B}\right) + 45°, when\ I_2 - I_3 \geq 0 \tag{4.19}$$

$$\phi = -\frac{1}{2}\text{arccot}\left(\frac{A}{B}\right) + 135°, when\ I_2 - I_3 < 0 \tag{4.20}$$

The birefringence measurements taken in this thesis are undertaken with the commercial Cri Abrio Imaging System integrated into an Olympus BX51 optical microscope. This system allows a measurement of retardance up to λ/2 (273 nm) and a slow-axis azimuth from 0° to 180°. When measuring retardance values higher than λ/2, the measured retardance can be ambiguously deduced by $R = \lambda - R_{sample}$ where R_{sample} is the true retardance and the slow axis azimuth is rotated by 90°.

4.4 Quantitative Phase Microscopy

The method utilized in qualitatively analyzing the refractive index profile after modification is through Quantitative Phase Microscopy (*QPM*) [186]. The concept provides a manner to gain a measurement of phase without the use of phase unwrapping or intensity information. In general, to obtain a quantitative phase image, three images need to be taken. The first image is in-focus on the structure being analysed. The other two images need to be very slightly positively and negatively focused from the plane of the structure. These three images are then used to estimate the differential with respect to the defocus of the image. The set-up of QPM is using an Olympus BX51 optical microscope in a typical transmission mode. The objective lens imaging the sample is mounted in a piezo-electric motorized stage (Physik Intrumente) and is imaged with a Pixelink CCD camera. The image acquisition and the algorithm for phase mapping are provided by IATIA Ltd. The piezo-electric stage is controlled through the image acquisition software and automatically takes the three images for QPM (Fig. 4.16).

The images are taken and then converted into intensity data via the software. To attain the phase, φ, the propagation of a light field along the microscope needs to be taken into account. This is governed by the transport of intensity equation [186]:

$$k\frac{\partial I_{image}(\vec{r})}{\partial z} = -\nabla \cdot \left(I_{image}(\vec{r})\nabla\varphi\left(\frac{\vec{r}}{M}\right)\right) \tag{4.21}$$

where I_{image} is the intensity distribution of the image and M is the image magnification and $\vec{r} = (x, y)$. The left-hand side of Equation (4.21) can be obtained from the two positively and negatively focused images, $I_{positive}$ and $I_{negative}$:

$$\frac{\partial I_{image}(\vec{r})}{\partial z} = \frac{I_{positive} - I_{negative}}{2\Delta z} \tag{4.22}$$

where Δz is the distance between the image plane and the defocus planes. Therefore, with the appropriate Fourier transform based algorithm [187], Equation (4.21) can be solved. It should be noted that the images taken with the QPM system are under Köhler illumination to ensure that the illumination on the sample is completely even. This might mean that typical microscopes may not have completely coherent illumination, which is what the formalism in Equations (4.21) and (4.22) are based on. However if the irradiance distribution of the illumination source shows inversion symmetry, the result is identical [186,187]. Once the phase difference is calculated, the refractive index change of the modified region, Δn, can be calculated:

$$\Delta n = \frac{\nabla \varphi \lambda}{2\pi d} \tag{4.23}$$

where d is the thickness of the modified region and λ is the wavelength of the illumination source.

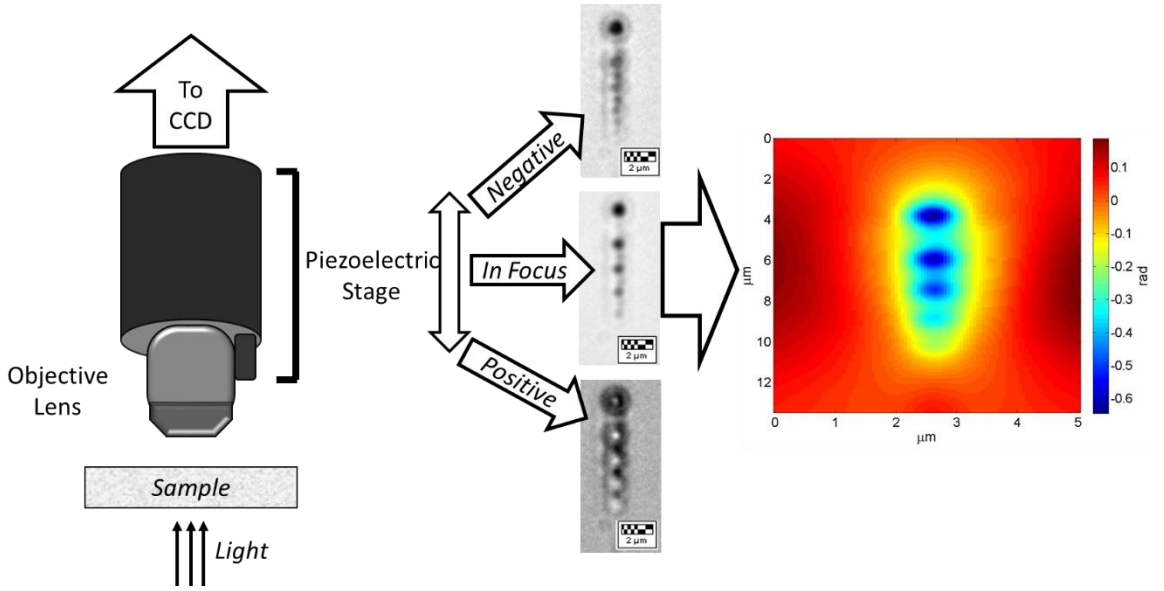

Figure 4.16: Schematic of quantitative phase microscopy. Three bright field images are taken at three locations: negatively focused, in focus and positively focused. The three images then build the phase map of the object being analysed, showing the change in phase.

Chapter 5: *In-Situ* Harmonic Generation during the Ultrafast Laser Writing

5.1 Introduction

The nanostructuring of transparent media with ultrafast laser pulses has attracted significant interest due to its unique applications. It was demonstrated that above a certain threshold, self-assembled nanogratings in silica glass can be induced [2,3]. The mechanism that triggers the nanostructure is still unclear. Up until now, most observations conducted for ultrafast laser material modification are post-mortem. However, for most models, there are signatures that are expected to be observed if the model holds true. The two-plasmon decay interference model predicts the generation of a 3ω/2 signal, which previously was reported at 9x the damage threshold for silica [80]. To provide strength to any theory of ultrafast nanostructure formation, the generation and characterization of the processes that occur during laser irradiation is necessary to provide insight on the physical dynamics that occur during laser writing. It is also important to be able to observe the dynamics during other laser-matter phenomena and observe and understand the physical processes that occur at the time of laser writing. The following chapter summarizes the experimental measurement apparatus developed and the observations made on different dependencies with the harmonics generated within the bulk of transparent materials, with the intention of observing the signal for 3ω/2. This work was conducted during the beginning of my PhD studies in an attempt to better understand the underlying mechanics involved in ultrafast laser writing. While the observation was not successfully made, the other harmonics generated are observed to have dependences on the different ultrafast laser writing modification regimes. In this chapter, I will discuss the results of harmonic generation in fused silica during ultrafast laser writing experiments. I highlight the evidence of Cherenkov third harmonic generation and discuss how harmonic generation could provide insight on the formation mechanisms of self-assembled nanogratings.

5.2 Methods

The experimental set-up used for harmonic generation measurement (Fig. 5.1) was composed of a mode-locked regenerative amplified Yb:KGW based femtosecond PHAROS laser system (Light Conversion Ltd.) operating at λ = 1030 nm and delivering pulses of 300 fs and 600 fs at 200 kHz repetition rate. The laser beam was focused into the bulk of transparent glass samples via a ×10 (NA = 0.16) aspheric lens. The experiments were performed with fused silica, borosilicate and

soda lime glasses and sapphire. The signal was collected into a fibre by collimating the transmitted light along the line of incidence with a ×20 (NA = 0.50) aspheric lens with an antireflection coating for the visible and focusing with an UV fused silica f = 25.0 mm lens. Before the sample, a longpass filter was inserted to cut all light induced from the optical elements placed before the sample, excluding the desired light from the PHAROS laser. The collected signal was analysed with an Andor Shamrock SR-303i imaging spectrometer, where two gratings were used to vary the spectral range of the measurement (150 and 1200 lines/mm).

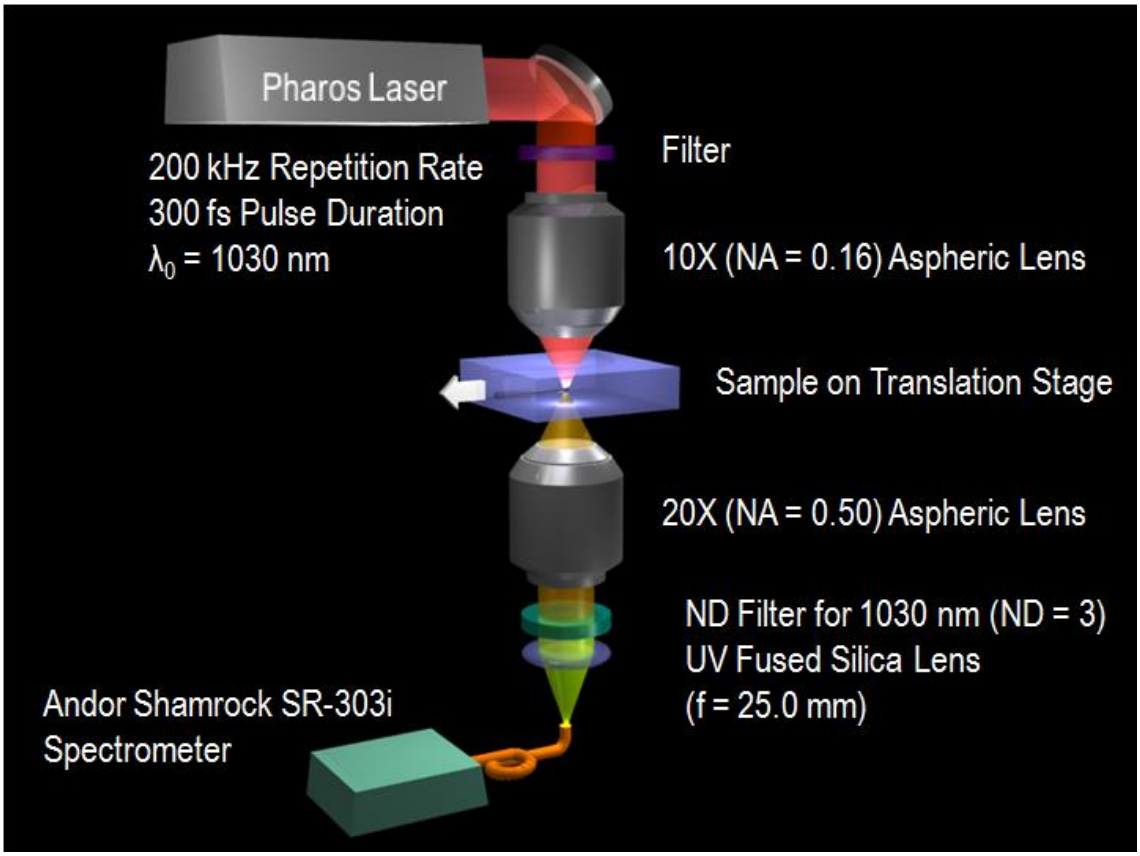

Figure 5.1: Experimental design for harmonic generation observation in the bulk of transparent materials

5.3 Results

Analysing the light collected after the sample in the visible region during laser writing, a spectral characterization revealed the presence of the second harmonic (2ω - addition of two photons through a non-linear medium), third harmonic (3ω - addition of three photons through a non-linear medium) and white light emission (Fig. 5.2). It was originally thought the signal at 687 nm was 3ω/2 but was later found to be a ghost image of 3ω caused by higher order diffraction within the spectrometer. It was observed that by changing the position of the collimation lens with respect to the focusing lens underneath the sample, the signal for a specific

harmonic could be maximized. The maximum of the second harmonic occurred at a different position than 3ω. The difference in the positions of focus was independent of the material used to generate the harmonics and was relatively large. This means the harmonics do not generate in at different depths but potentially the beam profiles of the harmonics show a maximum in intensity at different positions. However, since the lenses used to collimate the light are aspheric, chromatic aberrations could become a factor leading to the collimation for different wavelengths to reside in different positions. For each respective harmonic, measurements were taken at the position where the harmonic's emission was maximized.

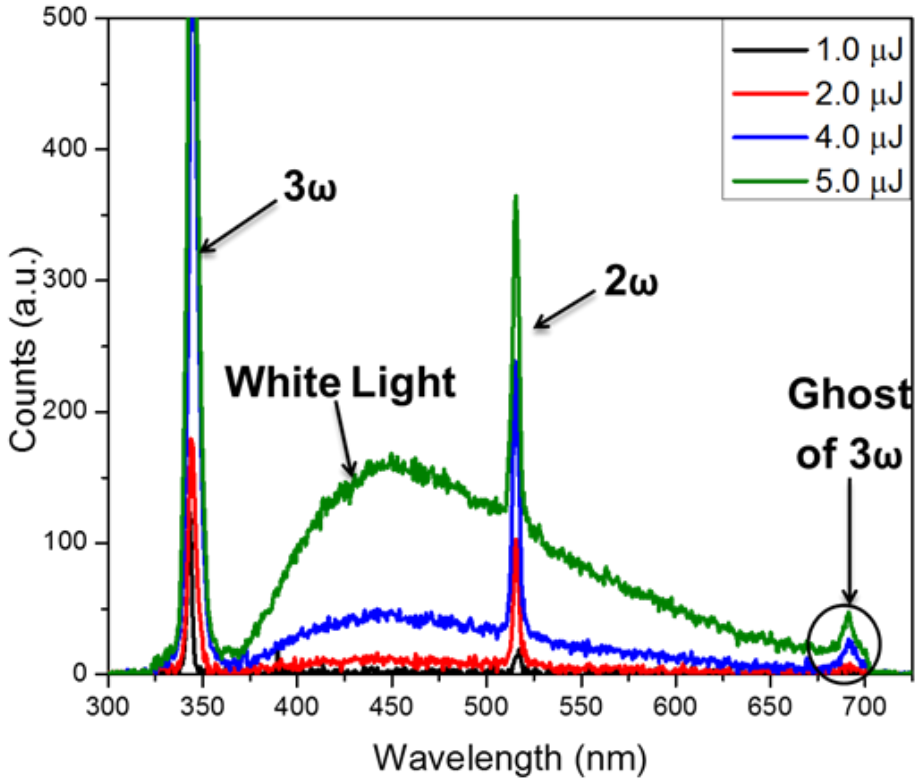

Figure 5.2: Spectrum of harmonics for different pulse energies (200 kHz repetition rate, 150 lines/mm grating), while stationary. White light emission and the peak structure for the harmonics is more evident as pulse energy increases.

When looking at SEM images of nanograting periodicity, it is argued that the mechanism must include a wave-like excitation in the medium to generate an interference–like pattern. The interesting result of the extremely large 3ω signal raised questions on whether or not harmonic generation could be related to the formation of nanogratings. In fact, the amount of 3ω generated during laser writing is visible to the naked eye and upon placing a screen underneath the sample, a propeller-like distribution of the harmonic is observed (Fig. 5.3). Two lobes are generated and aligned along the polarization direction of the incident light, independent of the writing direction. Thus, the 3ω generated is not dependent on the interface of writing but

dependent on the nanostructuring inside the glass during laser irradiation. The propeller-like distribution is similar to the original propeller scattering observed initially before the discovery of nanogratings [46]. However in the previous study, 2ω was generated in the propeller shape due to Ge-doped glass, whereas in this study, a 3ω propeller in pure fused silica is observed.

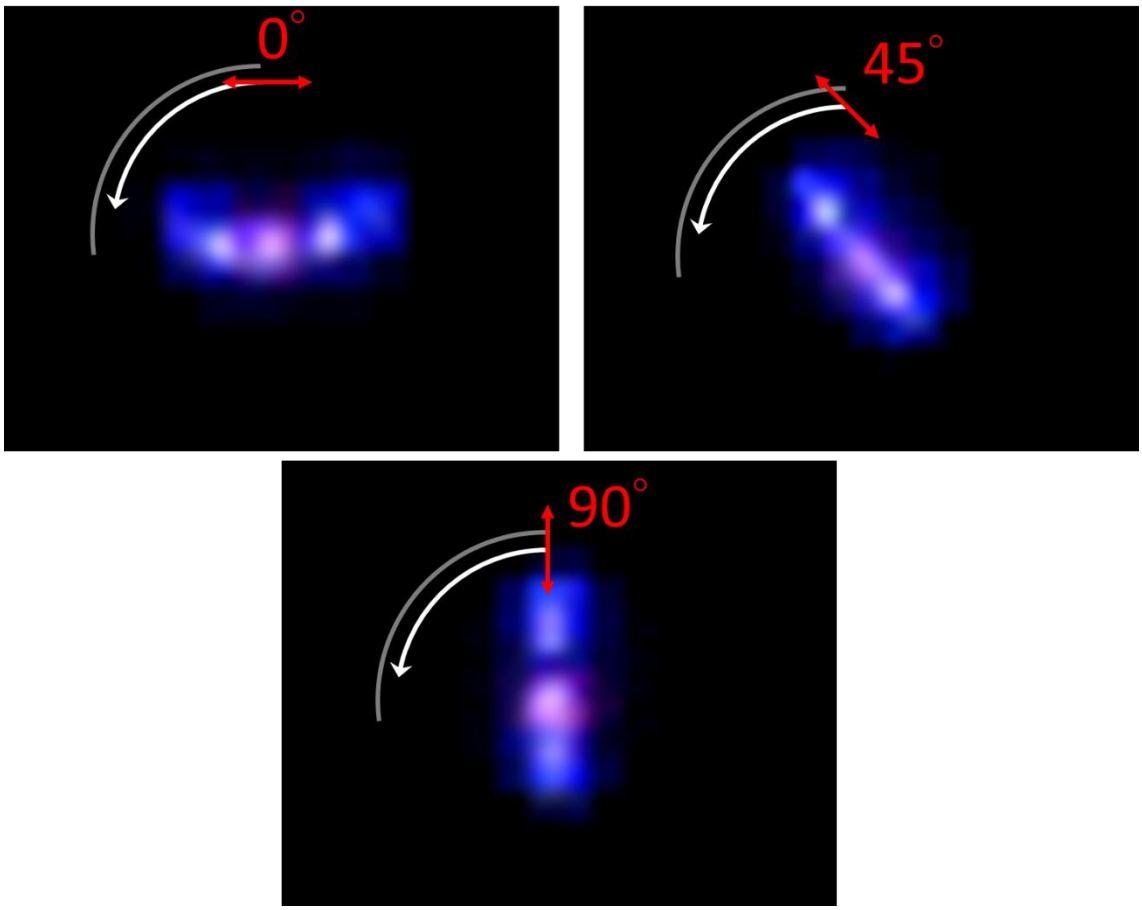

Figure 5.3: 3ω distribution after the bulk during laser irradiation. 3ω is oriented as two lobes aligned along the polarization state of the incident light. As polarization rotates, the distribution rotates. The lobes propagate at roughly 16.81°, similar to the expected angle associated with Cherenkov emission (~16.67°).

To measure the propagation angle of the 3ω signal, a screen was placed under the sample during laser writing in the bulk of fused silica and the lobe distribution was recorded at different distances away from the sample. Measurements were taken at multiple distances and for different polarization orientations. The propagation angle was measured to be 16.81°± 0.2°.

A similar generation of 3ω involving two crescent-liked lobes along the direction of polarization has been observed when focusing on the back surface of the sample [188]. This distribution would disappear as soon as the laser was no longer focused on the back surface and would last up to 10 seconds. In our experiment, the 3ω signal could last for even longer time periods (Chapter 5.3.1) but the propeller-like distribution would be distorted. In that study [188], it was suggested the 3ω

was generated due to Cherenkov radiation. Typically 3ω can be generated in any centrosymmetric media (i.e. isotropic mediums such as glass). In terms of wavevectors, a collimated non-linear polarization wavevector $k'_{3\omega} = 3\omega/c' = 3\omega n_{3\omega}/c$ is generated where n_ω is the refractive index for the incident laser frequency. The polarization emits coherent radiation with a wavevector $k_{3\omega} = 3\omega/c = 3\omega n_{3\omega}/c$ in the direction of $k'_{3\omega}$ that conserves transverse momentum, maximizing the radiation when phase matching is fulfilled and total momentum is conserved (i.e. $k_{3\omega} = k'_{3\omega}$), where $n_{3\omega}$ is the refractive index for third harmonic. However, when this symmetry is broken by an interface or boundary parallel to the light propagation, phase matching and conservation of momentum is no longer satisfied. Cherenkov radiation can then be possible in this environment where the polarization phase velocity, c', exceeds the speed of light in the medium [72,189]. The longitudinal component of the momentum is conserved, making the two wavevectors non-collinear and produces a Cherenkov cone. This cone would have a half-angle in the medium, ϑ'_{cone}, given by [19]:

$$\vartheta'_{cone} = \cos^{-1}\left(\frac{k'}{k}\right) = \cos^{-1}\left(\frac{c}{c'}\right) = \cos^{-1}\left(\frac{n_\omega}{n_{3\omega}}\right) \tag{5.1}$$

Outside of the medium, the angle between the incident light propagation and the 3ω, generated by Cherenkov radiation, ϑ_{cone}, is given by [19]:

$$\vartheta_{cone} = \sin^{-1}\left(n_{3\omega}\left[\sqrt{1-\left(\frac{n_\omega}{n_{3\omega}}\right)^2}\right]\right) \tag{5.2}$$

For fused silica, $n_{1030\ nm} = 1.45$ and $n_{515\ nm} = 1.4781$ yielding $\vartheta_{cone} = 16.67°$. This value is consistent with the measured angle confirming that the 3ω generated is based upon a Cherenkov mechanism.

5.3.1 Temporal Evolution of the Harmonics

Time dependence measurements were performed in stationary conditions, to measure the evolution of the generated harmonics over time. Temporal evolution of the harmonic signal in fused silica was observed by taking accumulated signal measurements every 5 seconds over a 5 minute period. Measurements were taken at pulse energies in the range from 1 μJ to 4 μJ while the pump remained stationary with respect to the sample. 2ω stays relatively constant over time and then after some period, it increases in signal (Fig. 5.4a). The increase can be attributed to a collection of negative charges at the point of focus [14]. The higher the pulse energy, the more rapidly the increase occurs. At 1 μJ, the pulse energy is insufficient for the increase due to charge build up. For 1 μJ < pulse energy < 4 μJ, the emission increases after some time and then relaxes. At 4 μJ, the pulse energy is sufficiently high, not allowing the emission to relax in amplitude.

In the energy range from 1 µJ to 2 µJ, the 3ω signal increased steadily within the first minute and then asymptotically relaxed to a certain level (Fig. 5.4b). This energy range coincides with the uniform nanograting formation regime in these experimental conditions. At high pulse energies above this energy range, the emission of the harmonics became erratic and did not relax smoothly to an asymptotic level. This shows a distinction in behaviour when comparing the laser modification regimes pertaining to uniform nanograting formation and damage in silica.

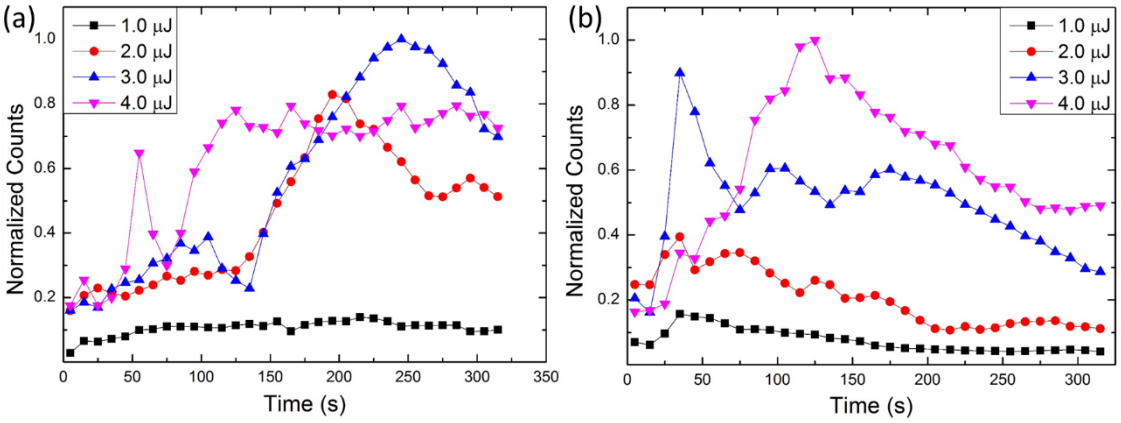

Figure 5.4: Temporal dependence of a) 2ω and b) 3ω. a) 2ω stays constant in emission until sufficient time passes where it increases in emission. b) 3ω emission peaks quickly over time and then asymptotically relaxes

5.3.2 Pulse Energy Dependence of the Harmonics

It becomes apparent that the harmonic generation observed may be dependent on the modification being induced during ultrafast laser-material interactions. Therefore, the pulse energy dependence of the harmonics were measured by translating the sample during laser inscription (100 µm/s writing speed) at 300 fs and 600 fs (Fig. 5.5-5.8) and taking multiple measurements at 2 s accumulations. The writing experiments were conducted in two directions (left and right; $\pm x$) with both parallel and orthogonal polarizations, due to the writing direction dependence in material modification with polarization [165,190]. Pulse energy was varied from 0.125 µJ to 5 µJ from 1.0 µJ to 5 µJ at a step of 0.125 µJ to determine the response of the harmonics over the different modification regimes and is compared to the retardance of the modification being recorded. The fabricated structures were classified with the Abrio birefringence measurement system (CRI In(c). This experiment best reproduces typical writing conditions used during typical ultrafast laser glass writing.

Energy dependence measurements confirmed that the generated emission for both harmonics grows monotonously with pulse energy but at unexpected polynomial orders. 2ω and 3ω should increase with quadratic and cubic dependencies respectively. However when plotting the

measured harmonic counts as a function of pulse energy, the distribution varies randomly, depending on the writing direction orientation with polarization. Moreover, the harmonic counts seem to fluctuate at points when nanograting retardance fluctuates. Nanograting retardance increases until a saturation point is met. At this point, nanograting formation can become non-uniform as pulse energy increases. Depending on the electric field orientation, the harmonics generated could scatter off the interfaces written into the glass. Although, in certain cases, the harmonic counts are enhanced at these particular points, following the retardance dependence with pulse energy, instead of decreasing due to scattering. This raises the question of whether or not the harmonics are the origin of nanograting formation and/or are associated with the process.

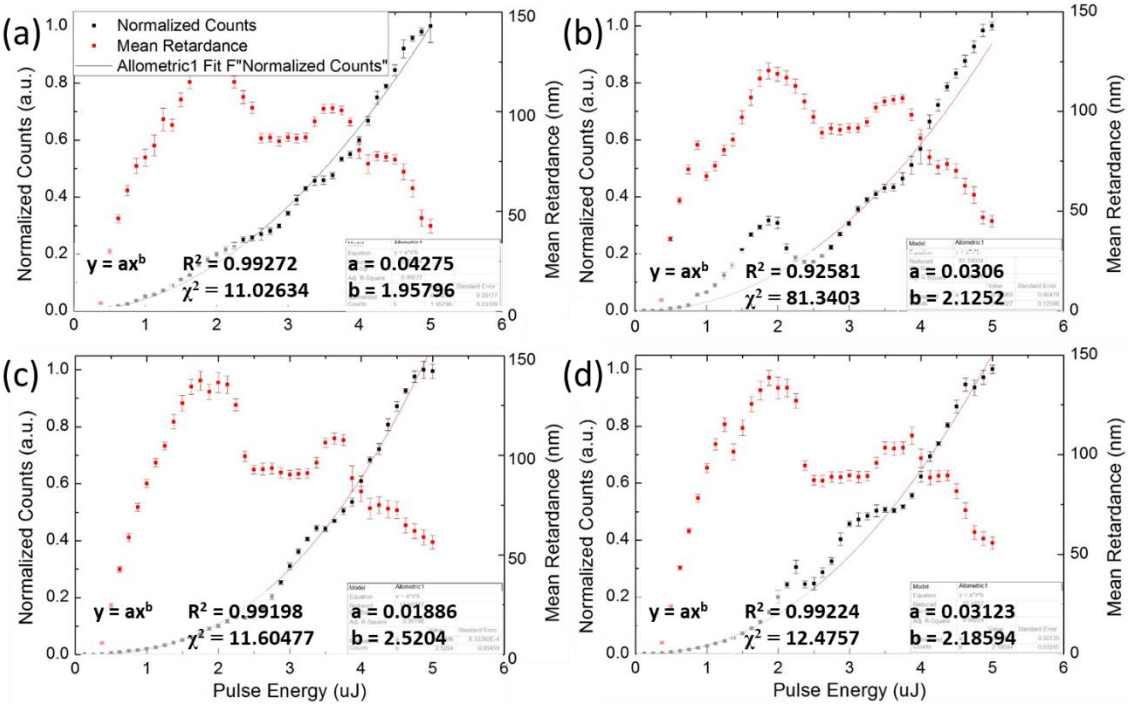

Figure 5.5: 3ω emission at 300 fs for (a) 0°, Right (b) 0°, Left (c) 90°, Right (d) 90°, Left (Black - Normalized Counts, Red – Mean Retardance). Polynomial order for fits of harmonic counts: (a) 1.95796, (b) 2.1252, (c) 2.5204, (d) 2.18594.

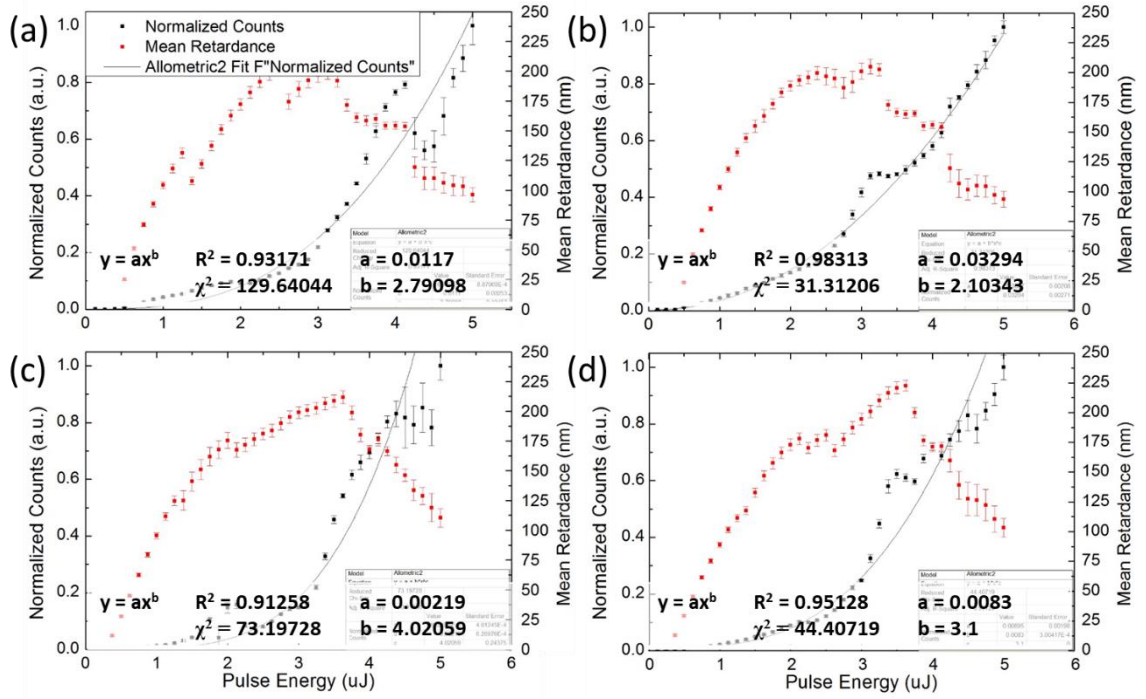

Figure 5.6: 3ω emission at 600 fs for (a) 0°, Right (b) 0°, Left (c) 90°, Right (d) 90°, Left (Black - Normalized Counts, Red – Mean Retardance). Polynomial order for fits of harmonic counts: (a) 2.79098, (b) 2.10343, (c) 4.02059, (d) 3.1.

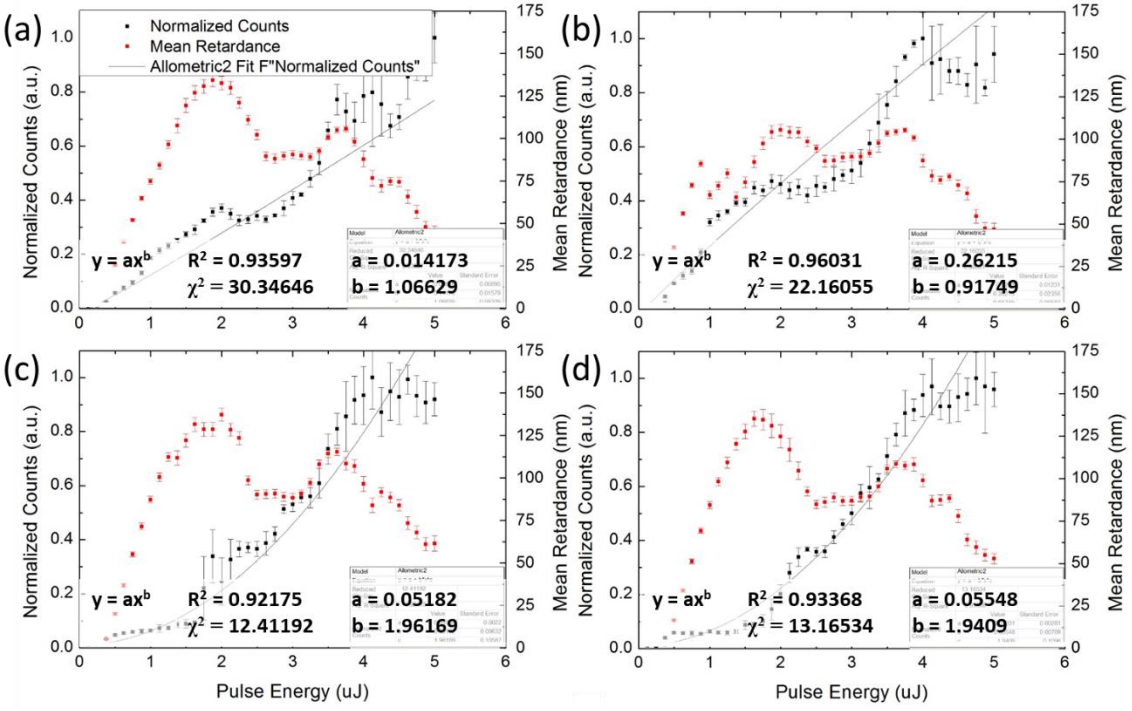

Figure 5.7: 2ω emission at 300 fs for (a) 0°, Right (b) 0°, Left (c) 90°, Right (d) 90°, Left (Black - Normalized Counts, Red – Mean Retardance). Polynomial order for fits of harmonic counts: (a) 1.06629, (b) 0.91749, (c) 1.96169, (d) 1.9409.

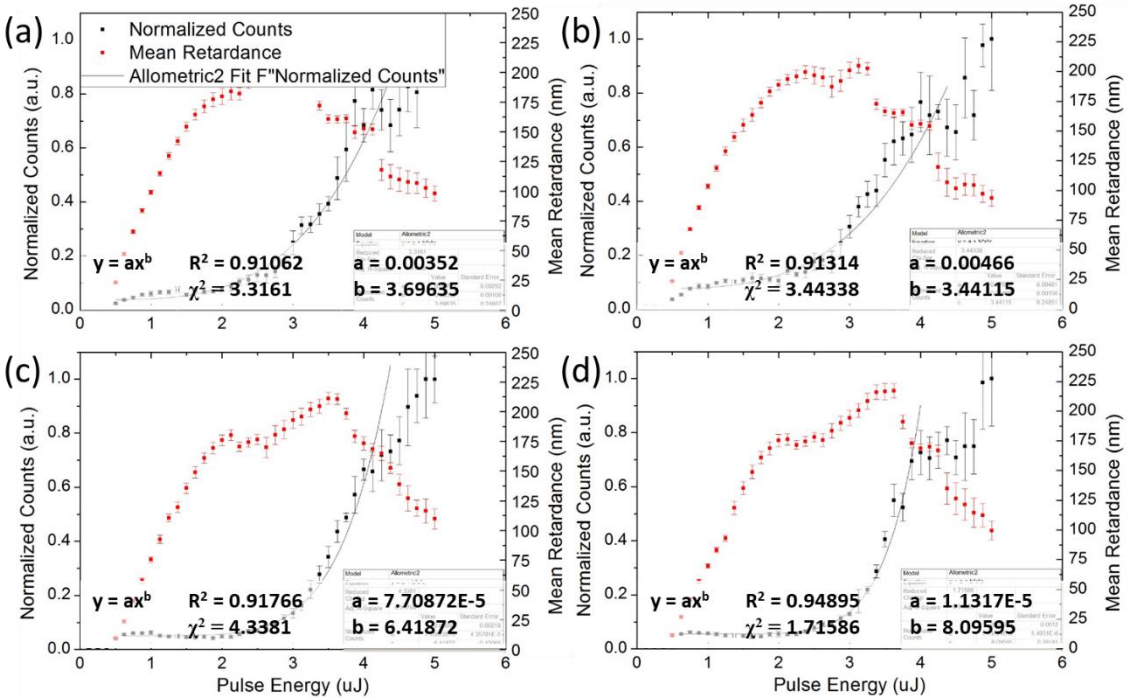

Figure 5.8: 2ω emission at 600 fs for (a) 0°, Right (b) 0°, Left (c) 90°, Right (d) 90°, Left (Black - Normalized Counts, Red – Mean Retardance). Polynomial order for fits of harmonic counts: (a) 3.69635, (b) 3.44115, (c) 6.41872, (d) 8.09595.

5.3.3 Polarization Dependence of the Harmonics

One of the key aspects of nanograting formation is the dependence of the slow-axis orientation of the gratings with the incident laser polarization. The electric field needs to have a well-defined direction for nanogratings to be imprinted into the bulk of a transparent material. If the polarization of the incident light is circular, there is no defined direction of the electric field and thus nanogratings cannot form. Therefore, harmonic generation measurements with linearly and circularly polarized laser light during ultrafast laser writing in fused silica was conducted. Before the experiment was conducted, the polarization of the emitted harmonics were analysed with a linear polarizer. All observed harmonics were co-polarized with the input laser beam while the white light emission was unpolarised. The identity of the white light emission is currently unknown but has been discussed as either supercontinuum generation, recombination of electrons and/or Bremsstrahlung radiation [5,191]. Supercontinuum generation is dependent on the polarization state of the incident laser and its polarization state is the same as the incident laser polarization [192]. This provides evidence that the white light emission generated during ultrafast laser writing in glass is not supercontinuum generation and is most likely emitted due to either a recombination of electrons and/or Bremsstrahlung radiation. This is discussed further in Chapter 10.

A system of dual quarter-wave plates was placed in the input laser beam and rotated to continuously change the laser's polarization from linear to circular to measure the effect of pump polarization on the overall emission of the harmonics. This change in polarization is measured as a degree of linear polarization (1 representing linear polarization and 0 representing circular polarization) by measuring maximum and minimum intensities (I_{max} and I_{min}) for different rotation angles on the λ/4 waveplates, with a linear polarizer.

$$Degree\ of\ Linear\ Polarization = \frac{I_{max} - I_{min}}{I_{max} + I_{min}} \tag{5.3}$$

The experiment was conducted with a stationary pump beam as well as a moving average (0.1 mm/s) in typical ultrafast laser writing conditions (Fig. 5.9, 5.10). For typical writing conditions, i.e. translating the sample with respect to the laser beam, a linearly polarized pump provides the strongest emission for 3ω (Fig. 5.9a). For a stationary beam, a peculiar signature is seen for slightly elliptically polarized beams (Fig. 5.9b). Linearly polarized light still provides sufficient harmonic emission, but linear polarization light in conjunction with a circular component provides a larger excitation based on the emission observed for both harmonics. The dependence on polarization with ionization in dielectrics has been an area of research for quite some time. Multi-photon ionization has been found to be dominated by linear polarization versus circular polarization in bulk dielectrics [193]. However, circular polarization has been observed to improve the spatial distribution of the plasma and minimizes effects caused by beam-filamentation, leading to a better quality in laser-written structures [194]. While different regimes of ionization have been discussed with respect to linear and circular polarization [195–197], it is difficult to deduce how elliptically polarized light in femtosecond pulses behave in bulk dielectrics because it is difficult to derive the multiphoton ionization cross-sections for it. When considering the linear polarization case, the light is focused into the bulk and generates plasma at the focus, at a higher concentration of ionized electrons, yielding a large cross-section. For circular polarization, the light is focused more radially in the bulk, which means that the energy absorbed is diffuse, providing a smaller amount of the plasma to reach the effective density. This is observed in the case when the laser beam is moving across the sample. The same observations are made in the stationary case, but with elliptically polarized light, the light is focused into the bulk near the focus but is also radially spread out around the focus. This orientation would provide a larger effective cross-section and is suspected to develop more plasma, near a quarter of the critical density, then the other two polarization cases, while stationary, thus generating more harmonic emission. More theoretical studies need to be conducted in the case of high order multi-photon ionization in bulk dielectrics for elliptically polarized light.

For 2ω, there is no observable dependence on the polarization whether stationary or moving (Fig. 5.10). This then means that 2ω does not depend on nanograting formation (and vice versa) and is mainly a by-product due to plasma gradients being created during ultrafast laser-material interaction. However, 3ω counts are effectively zero at circular polarization whilst moving and maximizes for linear polarization. The evidence of 3ω being more efficient in the environment where nanograting formation occurs alongside the Cherenkov mechanism for 3ω, indicates that the 3ω process is associated with nanograting formation. What still remains unresolved is whether nanograting formation is dependent on 3ω. This will be discussed further in Chapter 10.

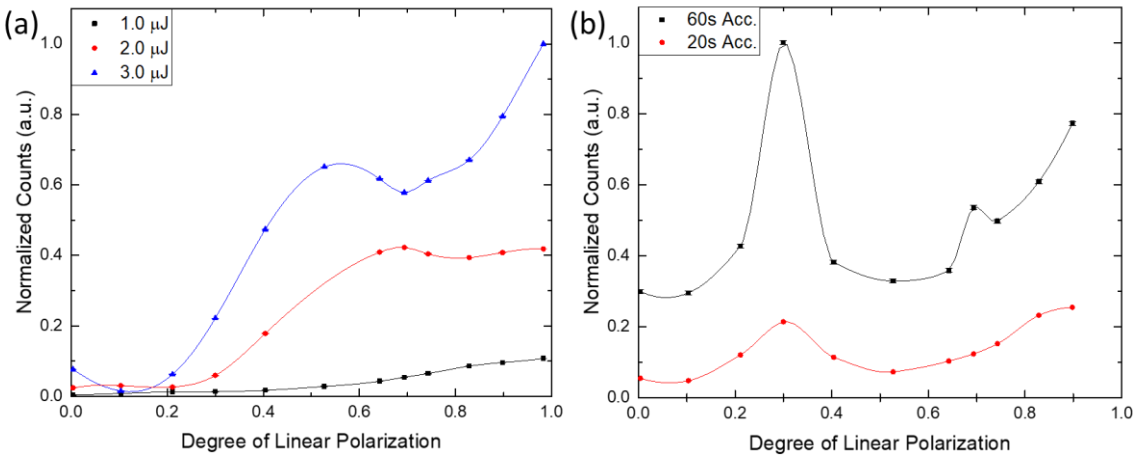

Figure 5.9: (a) 3ω dependence on the degree of linear polarization of the pump beam, while translating across the pump in a typical ultrafast laser writing set-up (0.1 mm/s, 2s accumulation). Linear polarization provides the best emission for 3ω. (b) 3ω dependence on the degree of linear polarization of the laser beam while stationary for 20s and 60s at 1μJ. 3ω emission is at a maximum when the beam becomes elliptical. The strength of the emission grows with time.

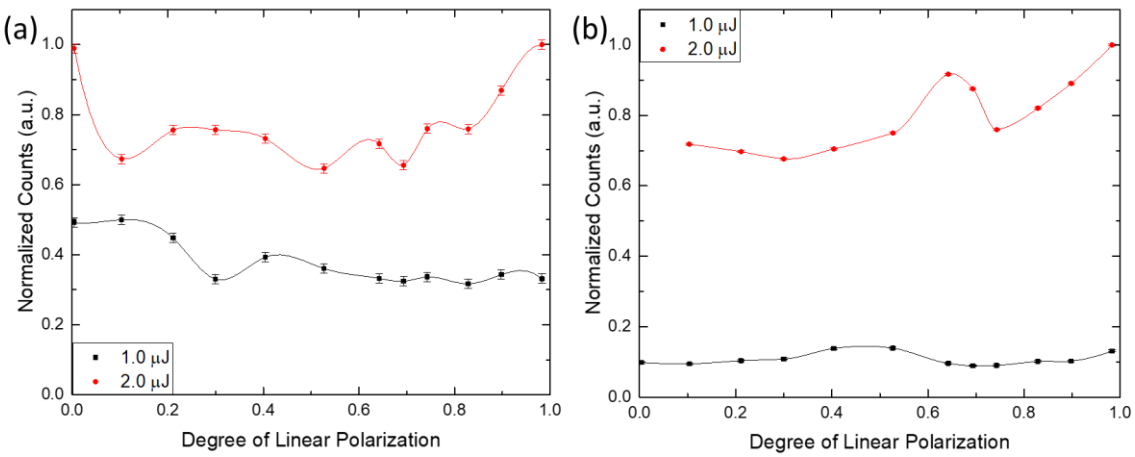

Figure 5.10: (a) 2ω dependence on the degree of linear polarization of the pump beam, while translating across the pump in a typical ultrafast laser writing set-up (0.1 mm/s,

2s accumulation). (b) 2ω dependence on the degree of linear polarization of the laser beam while stationary for 20s and 60s at 1μJ. There is no observable dependence on polarization with respect to 2ω, providing evidence that 2ω does not depend on nanograting formation and is a corollary process due to plasma gradients.

5.4 Conclusions

In summary, I present a simple optical apparatus that is able to measure the physical dynamics that occur during ultrafast laser writing in transparent *in-situ* instead of relying on post-mortem observations. This was done in an attempt to better understand the physical dynamics left unexplained in ultrafast laser-matter interactions. An identification of 2ω and 3ω during laser irradiation is made with the discovery of a Cherenkov mechanism for 3ω due to the laser nanostructuring imprinted into the bulk of fused silica. The dependencies of the harmonics with pulse energy, polarization and laser irradiation times were measured, showing that while the 2ω is not dependent on the laser nanostructuring imprinted in the glass, the 3ω is dependent on the nanograting formation. 3ω can then be potentially used to monitor nanograting formation during the fabrication of S-waveplates or fiber Bragg gratings. *In-situ* monitoring of fiber Bragg gratings have been conducted on a large grating [198] but monitoring 3ω can validate the formation of nanogratings and could be used to indirectly characterize the grating during the writing process. While the intent of the experiment was to measure the 3ω/2 signal in hopes of validating the two-plasmon decay interference model, the results show peculiar enhancements in 3ω that may provide clues in the formation mechanism of self-assembled nanogratings.

Chapter 6: Photosensitive Anisotropy Due to Non-Paraxial Polarization Spatio-Temporal Coupling

6.1 Introduction

As discussed in Chapter 3, broad spectrum is one of the key requirements for ultrafast laser systems. This has led to the invention of effective mechanisms capable of locking spectral components in phase, paving the way towards pulses as short as several femtoseconds. However, the identification of the phase of the pulse is crucial, as it can lead to unwanted decreases in pulse intensity of an ultrafast laser. Through techniques like CPA and SSTF, the phase of the pulse can be exploited to overcome issues originating from nonlinear laser-material interactions. While the separation of spatial components in the laser beam, like that seen in CPA and SSTF, are proven to be beneficial, the ramifications associated with their spatio-temporal counterparts, such as PFT and WFR, are not well understood. This is prevalent especially in ultrafast material modification where previous studies have clearly indicated that spatio-temporal couplings can give rise to an anisotropic photosensitivity in isotropic homogeneous mediums [6,165], which is thought to depend on the polarization orientation with respect to the azimuth of the PFT and is known as the "*blade effect"* [6]. With no effective control of the vectorial dependences, the benefits of the phenomenon cannot be exploited. As a result, this anisotropic behaviour is normally seen as detrimental for applications where precision of the process is essential. The potential effect of PFT in ultrafast laser writing became clear in Chapter 5.3.2 when both polarization and writing direction played a role in the polynomial orders associated with the generation of 2ω and 3ω (Fig. 5.5-5.8). In order to understand what is happening during the light-matter interaction, it became necessary to understand the complete spatio-temporal identity of an ultrafast laser pulse.

Here with the spatio-temporal control set-up discussed in Chapter 4.2, I demonstrate that spatial and temporal components can be separately controlled, allowing one to investigate spatio-temporal dependences on ultrafast laser induced material modification. I first investigate how residual spatio-temporal couplings, which reside in the bare beam of a typical ultrafast laser, influence spot modification. With this, I demonstrate that anisotropic photosensitivity is an inherent property of transparent media in the femtosecond domain and it can be observed in a range of materials. Preliminary modelling of the conditions were conducted alongside Dr. Vladmir Tikhonchuk. Dr. Vladmir Tikhonchuk also provided the mathematical analysis of non-paraxial corrections to the electric field so that the identification of the spatio-temporal couplings at the

focus could be observed. Analysis of the linear behaviour of spatio-temporal couplings in and out of the focus was conducted using linear propagation simulations, allowing one to understand different mechanisms evolved in the focal volume. From here, the spatio-temporal coupling, which plays a dominant role, in the anisotropic photosensitivity, is determined.

6.2 Methods

Experiments were carried out with the mode-locked regenerative amplified ytterbium doped potassium-gadolinium tungstate (Yb:KGW) based femtosecond laser system PHAROS (Light Conversion Ltd.) emitting a train of femtosecond pulses at 1030 nm with 200 kHz repetition rate. A set of grating compressors are used to induce TC and SC separately to have direct control on the PFT and thus, the spatio-temporal couplings (Fig. 4.11). Prism compressors were used originally in the initial stages of the experiments (Fig. 4.6). The laser beam is then sent to a translation stage and focused into the bulk of fused silica with a 0.55 NA aspheric singlet lens or 1.4 NA oil immersion objective. The polarization state is controlled with a $\lambda/2$ waveplate to change the polarization orientation to be either parallel with the direction of SC (0°) or perpendicular to SC (90°).

In this experiment, the second grating compressor remains stationary over a fixed separation length. Thus, the SC is held constant at ~1 nm/mm. The amount of residual SC from the first grating set-up is ten times smaller in comparison to the amount of the frequency gradient from the second grating set-up. This alongside the compressor control for TC provides a complete method for control of spatio-temporal coupling in the laser pulses.

As substantial spatial chirp is added to the beam, it becomes elliptical. Thus, it is important to ensure that the spectral components of the beam are not clipped by the aperture of the focusing lens to reconstruct the initial bandwidth of the pulse correctly near the focus. To ensure this, a Galilean telescope is used to fit the elliptical beam into the back aperture of the focusing lens. As a result, the aperture of the lens is under-filled, reducing the effective numerical aperture. Considering this, all numerical apertures are quoted in this chapter in their effective values.

One of the issues that needs to be taken into consideration is the effect the focusing optics have on the overall PFT of the beam. Most objective lenses have a considerable amount of glass, which is known to stretch the pulse and increase the GDD of the pulse depending on the bandwidth of the pulse. This can drastically change the PFT of the pulse and cause other unwanted aberrations [181]. In the experiment, the bandwidth of the laser is relatively small (~ 8 nm); the effect of glass is negligible so all spatio-temporal couplings are controlled by the grating set-ups.

Here I discuss two cases of spatio-temporal couplings. In the first case, the laser pulse is transform limited before the second grating set-up (*With PFT*). In the second case, the GDD induced by the second grating set-up is compensated with the internal grating compressor in the laser, making PFT = 0 before the focusing lens (*No PFT*). In the first case, the pulse is stretched by the second grating set-up to ~4 ps from the 300 fs bare beam. The PFT measured at the focusing optics in this case is 0.64 fs/μm. In the second case, the PFT is minimized to zero with the first grating set-up so that the pulse is transform limited with SC (~400 fs locally). The beam is then focused in a wide SSTF configuration, which yields a circularly symmetric focus, despite ellipticity at the focusing lens caused by spatial chirp [181].

6.3 Observations

To demonstrate the importance of the residual spatio-temporal couplings evident in typical ultrafast lasers, the beam emitted by the laser was directly focused into the bulk of fused silica (Fig. 6.1). Characterization of the spatio-temporal couplings in the beam emitted by the laser system clearly indicated that both AD and SC are present. In the horizontal direction of the beam, the SC is changing along propagation meaning AD is present. In the vertical direction, SC remains somewhat constant along propagation. At the focusing lens, $SC_x = 0.1$ nm/mm and $SC_y = 0.08$ nm/mm. This laser beam was focused with NA = 0.55 lens and ten 300 fs, 0.5 μJ pulses were shot into the bulk with varying polarization with respect to the SC direction. Inspecting the cross-sections under an optical microscope, a clear difference was observed for the polarization parallel to SC (0°), where a long chain of voids stretching to the focus is seen, as opposed to the polarization perpendicular to SC (90°), where only a single void is seen at the top of the structure (Fig. 6.1b). The observed difference of structures is corroborated with initial experiments performed in fused silica with a typical titanium-sapphire laser (Coherent RegA 9000) (Fig. 6.1a). However the polarization dependence becomes more apparent after longer irradiation. When the polarization is parallel to the SC (0°), long chain of voids stretching to the focus is observed with the void at the head of the structure remaining spherical. When the polarization is orthogonal to the SC (90°), the single void remains at the top of the structure and become elongated after long irradiation.

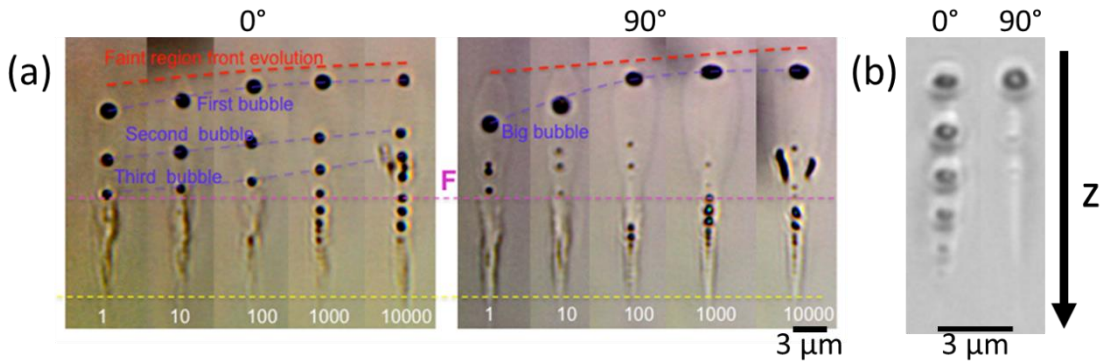

Figure 6.1: Optical Images of Fused Silica Regions Modified by Transform Limited Ultrafast Pulses (a) Ep = 2.4 µJ, NA = 0.65, τp = 70 fs, f = 250 kHz, λ = 800 nm; (b) 10 pulses, Ep = 0.5 µJ, NA= 0.55, τp = 300 fs, f = 200 kHz, λ = 1030 nm. When polarization is parallel to SC (0°), long chains of nano-voids are observed across the structure. Whereas, for perpendicular arrangement, only a single, enlarged void is seen at the top of the structure.

With respect to polarization multiplexed data storage [58], precise spot modification in the bulk of transparent media with tailored birefringence is needed for encoding of information. The laser-induced birefringence was characterized with the quantitative birefringence measurement system (CRi Abrio; Olympus BX51) operating at l = 546 nm. Focusing into the bulk of fused silica with NA = 0.75, a strong sinusoidal modulation in birefringence is observed with respect to the resulting slow-axis orientation of the structures (Fig. 6.2). The modulation is apparent for different pulse energies and shifts when changing the repetition rate from 200 kHz (Fig. 6.2a) to 500 kHz (Fig. 6.2b). This proves that spatio-temporal couplings that exist in typical ultrafast laser systems are extremely complex and may cause drastic effects on the overall modification induced in glass. The inability to control modification reliably and to understand where the discrepancies arise from can be extremely penalizing for writing and reading data encoded in the glass.

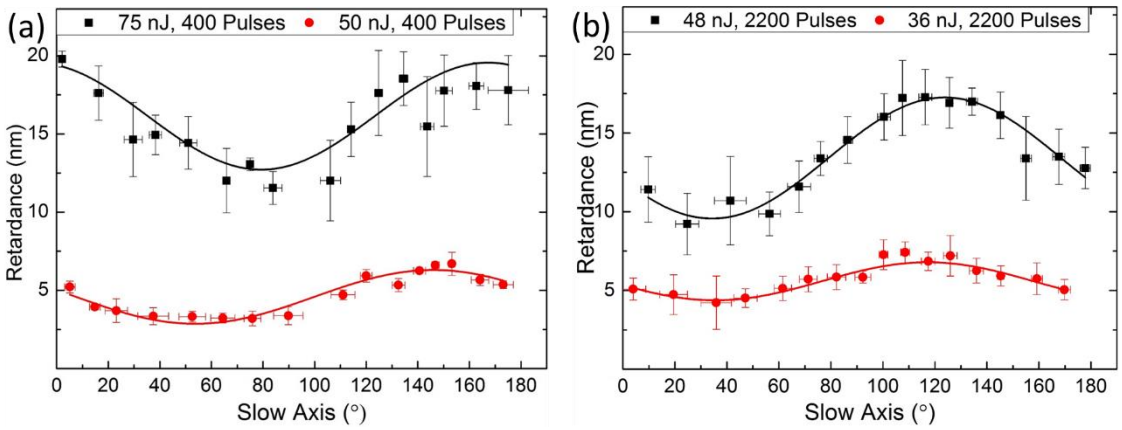

Figure 6.2: Retardance Measurements of Fused Silica Regions Modified by Tightly Focused (NA = 0.75) Femtosecond Pulses with Varying Polarization and Pulse Energy. (a) f = 200 kHz and (b) f = 500 kHz. The retardance value exhibits a sinusoidal modulation when varying the azimuth of the polarization plane. This modulation shifts when changing repetition rate making it difficult to understand the origin of the modulation and control strength of birefringence for digital information encoding.

To determine what causes this polarization dependence in modification, the SSTF set-up was put into the experimental design (Chapter 4.2.2/4.2.3). With the initial prism compressor design, PFT was introduced to the beam along the vertical direction of the beam coming out of NOPA. Using the characterization methods discussed in Chapter 4.2, PFT was measured to be 13.5 fs/mm before the objective lens. Due to the large amount of glass in the objective used for that experiment, NA = 0.65, the PFT increased to 43.94 fs/mm. When rotating the polarization state parallel (0°) or orthogonal (90°) to the PFT direction, a clear difference in void formation is observed when viewing the cross-section (Fig. 6.3). When the polarization is parallel to the PFT, a chain of voids is spread along the structure. When the polarization is perpendicular to the PFT, there is a unique elongated void at the top of the structure with a clear separation between the head to the voids in the tail, very similar to the initial modification observed (Fig. 6.1). The difference in structure confirms the anisotropy of light-matter interaction produced by the mutual orientation of polarization and spatio-temporal couplings; however it does not fully confirm it is due to PFT, based on the issues with the design (refer to Chapter 4.2.2).

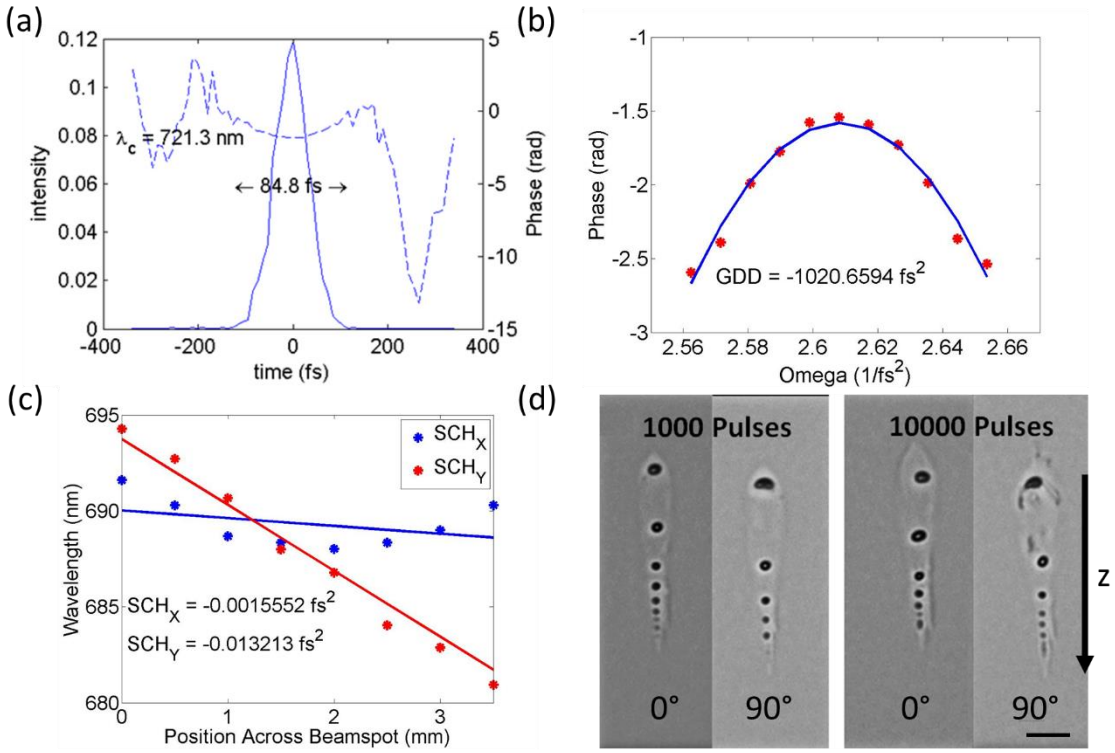

Figure 6.3: (a) FROG measurement yields the electric field and pulse duration (b) GDD measurement from the retrieved phase and (c) Spatial chirp measurement in the X (blue) and Y (red), showing control of direction and orientation of PFT (d) Resulting blade effect in fused silica for 1000 and 10000 pulses when polarization is parallel (0°) and perpendicular (90°) to PFT (Ep = 1.2 µJ, NA = 0.65, PFT = 13.5 fs/mm). The scale bar is 4 µm.

To investigate further, the more stable grating compressor design was used. The AD was removed in the horizontal direction with the second grating compressor and an additional SC was induced. A series of dots were then printed into the bulk of a fused silica sample with NA = 0.43 using the SSTF set-up. The qualitative analysis of the laser induced structures was performed by inspecting them under a Olympus BX51 optical microscope and with quantitative phase microscopy [186] (QPM). When varying the polarization state of the writing laser beam from 0° to 90° with respect to SC, a clear difference in the morphology of the structure was observed from the top and the cross-section (Fig. 6.4).

When polarization is parallel to the direction of SC (E = 0°), the structures exhibit spherical symmetry with and without PFT. The modification is localized slightly above the focal region, being ~1 – 2 µm in diameter (Fig. 6.4, E = 0°).

When polarization is perpendicular (E = 90°) to the SC direction, the modification is observed to be stronger. Stress is induced along the SC direction and the modified region is elongated in that direction to ~3-5 µm. From the cross-section, the laser-induced structure is larger and more

dispersed in stark contrast to a circularly symmetric structure for 0°. The area around the structure shows a larger phase difference, due to larger stress in the modification-induced region (Fig. 6.4, E = 90°).

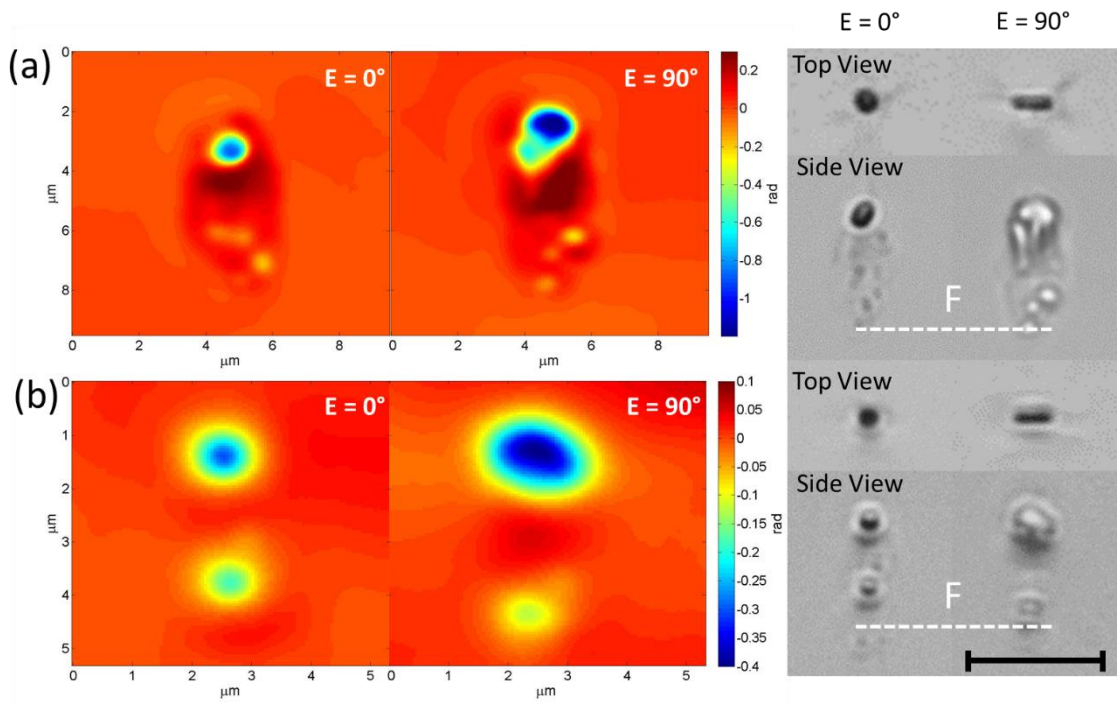

Figure 6.4: Optical and Phase Contrast Images of Modified Region after Irradiation with 10 Pulses. (a) With PFT, Ep = 0.5 µJ, NA = 0.43 and (b) No PFT, Ep = 0.35 µJ, NA = 0.43. Clear difference is observed when polarization rotates from parallel to SC (E = 0^o) to perpendicular to SC (E = 90^o). The cross-section of the structure is circularly symmetric if E = 0°. However, if E = 90^o, it becomes strongly elongated. The modification is more dispersed and exhibits larger phase variation when E = 90^o, indicating stronger structural change. The white dashed line in the optical images indicates the geometrical focal point. The scale bar is 4 µm.

When investigating how the anisotropic photosensitivity evolves within the first 10 pulses, it becomes clear that the effect increases with longer pulse irradiation when observed from the top (Fig. 6.5). No observable differences can be seen with the first pulse, however the void modification becomes larger with subsequent pulses. The anisotropic photosensitivity between orthogonal polarization states becomes more apparent after a few pulses, exhibiting elongation in void structure when polarization is perpendicular to SC (Fig. 6.5, E = 90°) and circularly symmetric voids when polarization is parallel (Fig. 6.5, E = 0°). After 5-6 pulses, the elongation increases while the parallel polarization based structures remain circularly symmetric, further separating the modification induced by the two polarization states. The evolution in void structure

emphasizes how the effect becomes stronger for further pulse irradiation, similar to what is observed in the bare beam case (Fig. 6.1a).

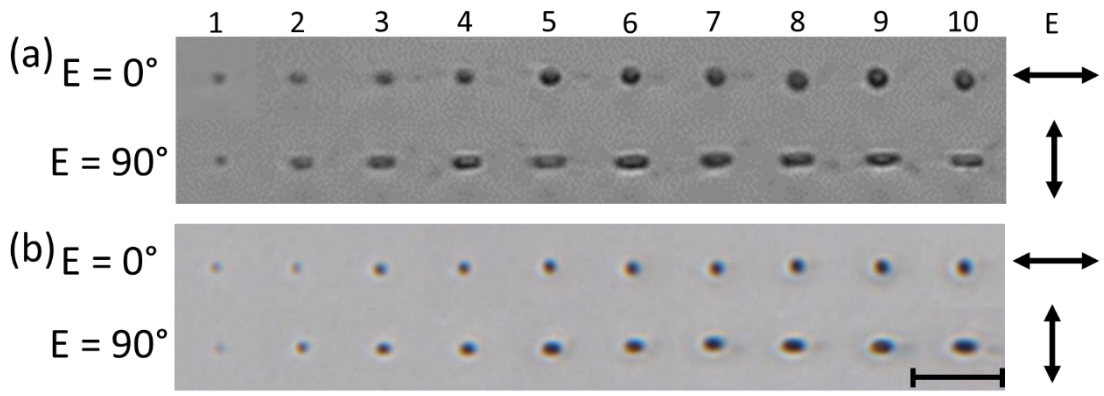

Figure 6.5: Evolution of Anisotropic Photosensitivity over First 10 Pulses, Top View. (a) With PFT, Ep = 0.5 μJ, NA = 0.43 and (b) No PFT, Ep = 0.5 μJ, NA = 0.43. After the first pulse, the modification for the two polarization states are identical. Upon further pulse irradiation, the differences between the two polarization states emerge showing circularly symmetric structures when the polarization is parallel to the SC (E = 0°) and elongated along the SC direction when perpendicular to the SC (E = 90°). The difference continues to increase and becomes stronger with longer irradiation. The scale bar is 5 μm.

One of the benefits of SSTF is to overcome nonlinear distortions, such as spherical aberration, which can drastically distort the localization of modification at deeper depths in transparent materials. To see whether the SSTF design worked, dots (10 pulses/dot) were printed at varying depths within the bulk of fused silica (Fig. 6.6). For both cases discussed, the polarization dependence in modification remains relatively the same regardless of the focusing depth. As the focusing conditions get deeper within the bulk of the material, other parameters such as spherical aberration begins to play a role which may alter the void formation which explains the slight differences between focusing depths for the same conditions (Fig. 6.6, 0° vs. 90°). Moreover, the modification does not distort at varying lengths and remains localised to the focal plane, emphasizing the SSTF technique.

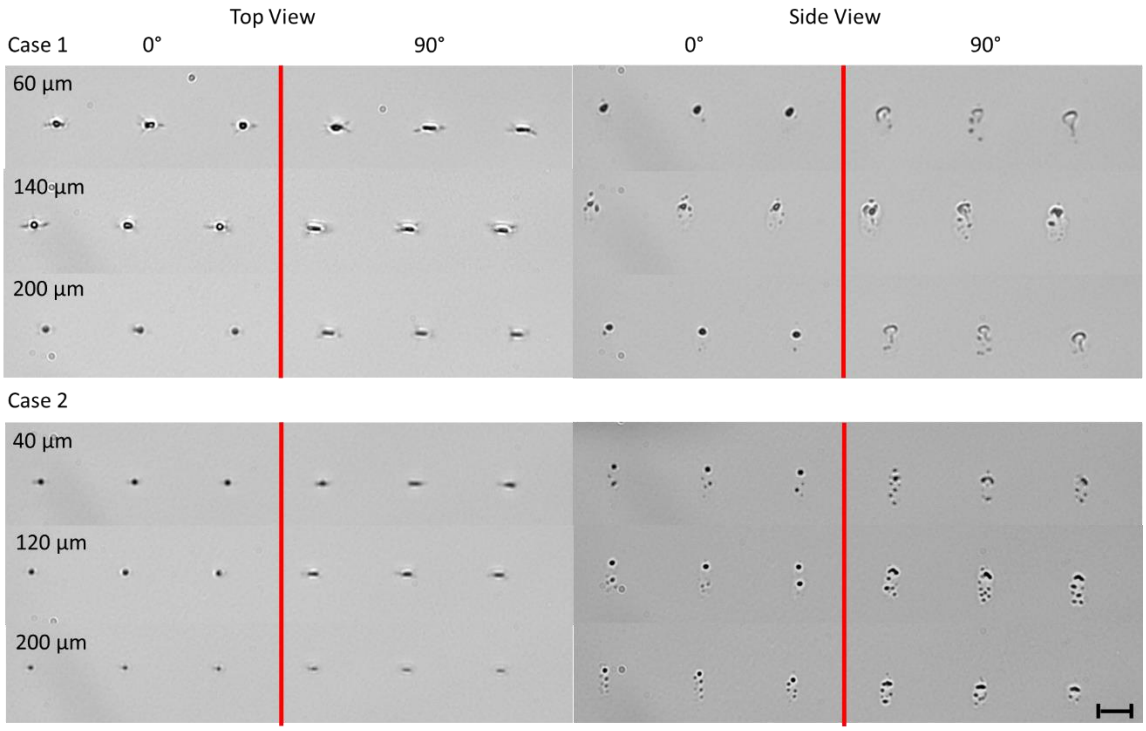

Figure 6.6: Varying depth for both PFT cases. The anisotropic photosensitivity is independent on focusing depth, proving that the anisotropy is a nonlinear phenomenon as well as emphasizing the benefits of SSTF. The scale bar is 5 µm.

When increasing the number of pulses overlapping in one spot even further, the void formation turns into nanograting revealed via birefringence (Type II modification) [101] and with NA = 0.43, the difference between the orthogonal orientations becomes less apparent (Fig. 6.7). In both cases, the greatest difference in measured retardance is seen within the first 100 pulses with nanograting formation being initiated earlier when polarization is orthogonal to SC (Fig. 6.7, red line = 90°, black line = 0°). But as the number of pulses increased past 100, the ratio of retardance between 90° and 0° drops from 0.6 - 0.8 to 0. The photosensitive anisotropy is also less apparent at higher pulse energies for NA = 0.43, even though slight differences reside in the structure closer to the geometric focus when observed from the cross-section (Fig. 6.8, Plane A vs. Plane B). This indicates that the anisotropic photosensitivity is dependent on the location where the nonlinear effects are initiated. Sufficient superposition of the spectral components is needed to maximize the benefits seen by SSTF. Therefore, depending on the location of the nonlinear interaction or if the focusing is not tight enough, the benefits of SSTF are minimized, as well as the anisotropic photosensitivity.

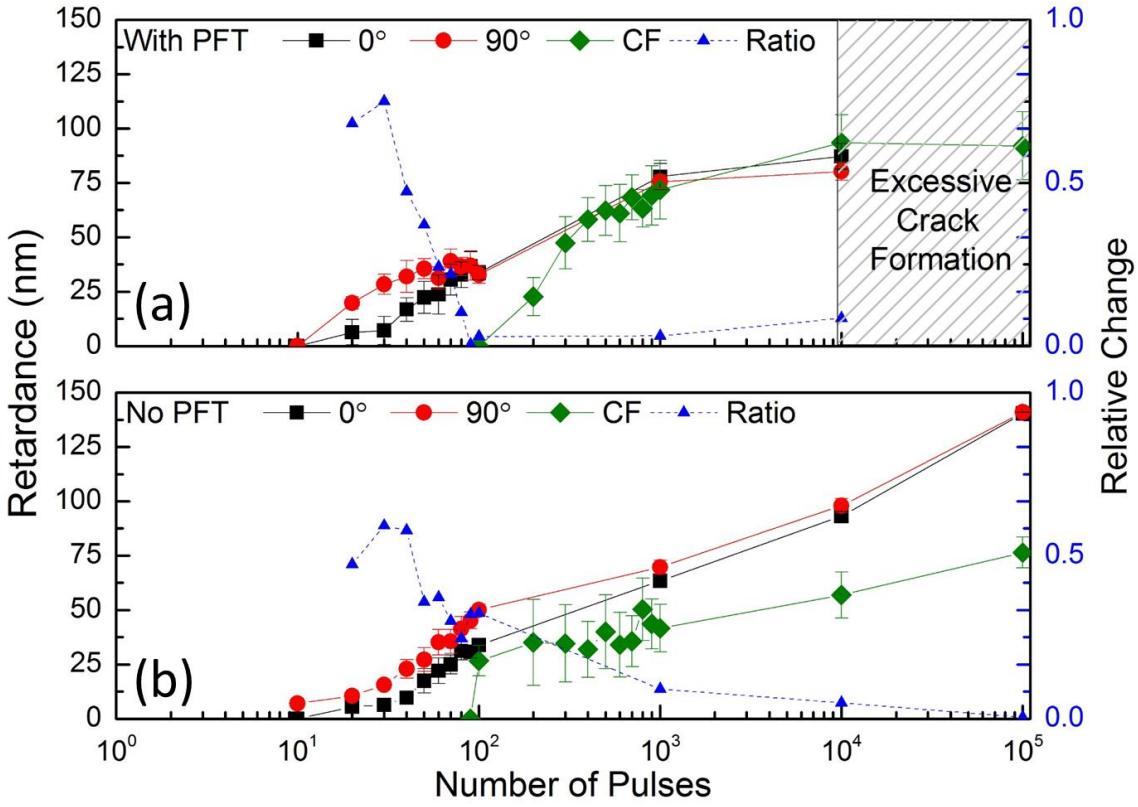

Figure 6.7: Retardance of Regions Modified with Femtosecond Pulses Focused with NA = 0.43 as a Function of Pulse Density. (a) With PFT, Ep = 0.5 μJ (b) No PFT, Ep = 0.35 μJ. Within the first 100 pulses, the structures printed with polarization orthogonal to SC (red circles) have larger retardance than those parallel (black squares). The relative change measured between 90° and 0° (blue triangles, $|Ret(90^o) - Ret(0^o)|/Ret(90^o)$) is 0.6-0.8 within the first 30 pulses and then begins to drop to zero as the pulse density increases. For the two cases discussed, the transition to nanograting occurs within the first tens of pulses, whereas in equivalent conditions under conventional focusing (CF, green diamonds), the transition does not occur until after 10^2 pulses. The retardance achieved under SSTF conditions is larger, especially in the No PFT case where the total retardance after 10^5 pulses is roughly twice that achieved under CF, providing an avenue to attain stronger modification in a smaller focal volume under shorter irradiation times.

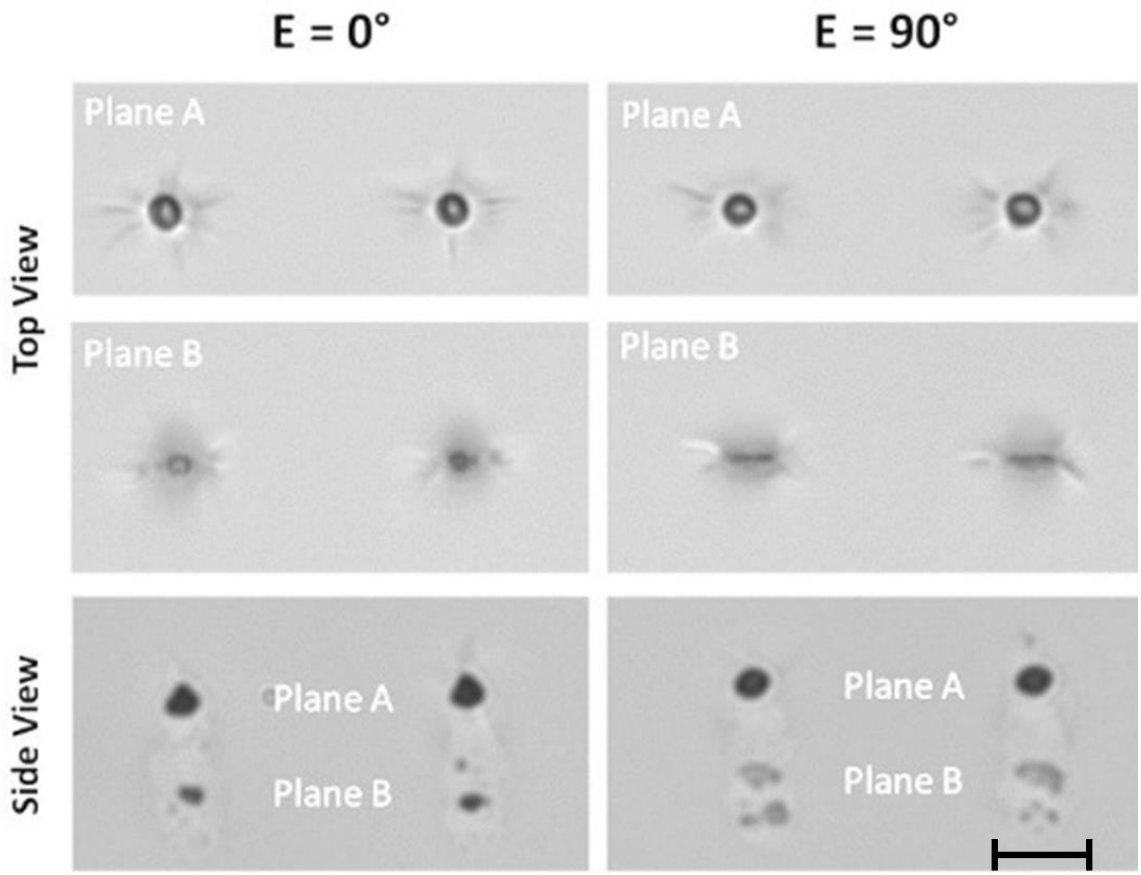

Figure 6.8: Photosensitive Anisotropy for 1.5 μJ. The differences are not at the top of the structure but slight differences exist at the bottom of the structure. This emphasizes the importance of localizing SSTF to the focal plane to see the benefits as well as the location of where the photosensitive anisotropy exists. The scale bar is 5 μm.

In comparison to modification under conventional focusing (*CF*) conditions, the transition to nanograting occurs much earlier (Fig. 6.7, CF = Green Line). With SSTF, the transition occurs within the first tens of pulses whereas with CF, nanograting formation appears around 100 pulses for the equivalent pulse parameters of the two cases discussed. It should also be noted that the maximum retardance achieved within 100,000 pulses in the No PFT case is roughly twice the retardance achieved under CF conditions. The ability to minimize the nonlinear interaction in the bulk with SSTF to a smaller volume near the focal plane provides an avenue to have stronger modification than what would be observed with CF, allowing one to attain stronger modification in a shorter period of exposure.

To check this hypothesis about the location of nonlinear interaction with respect to the polarization dependence, a series of structures were written with tighter focusing. When focusing into the bulk of fused silica using a NA = 0.9 oil immersion objective, the modification is localized closer to the focus and the more apparent manifestation of the anisotropic photosensitivity is observed (Fig. 6.9). In this case, Type II modification is induced and a clear sinusoidal dependence

is observed in the retardance of the structures with highest values measured for the polarization perpendicular to the direction of SC. The sinusoidal dependence is observed through a range of pulse densities but the ratio of the strength of retardance between 0° and 90° lowers from roughly 3:1 to 1.5:1 when increasing pulse density. This can be explained by a combination of thermal effects with the lateral growth of the structures, when regions further from the focus are modified [15]. These two factors will contribute to diminishing the effect of spatio-temporal couplings. Moreover, the shape of the structures are indicating similar behaviour observed at weaker focusing conditions (Fig. 6.9, inset at top). The structures written with parallel polarization were circularly symmetric (Fig. 6.9, inset at top, bluer voids), whereas structures induced with perpendicular polarization were elongated in the SC direction (Fig. 6.9, inset at top, redder voids).

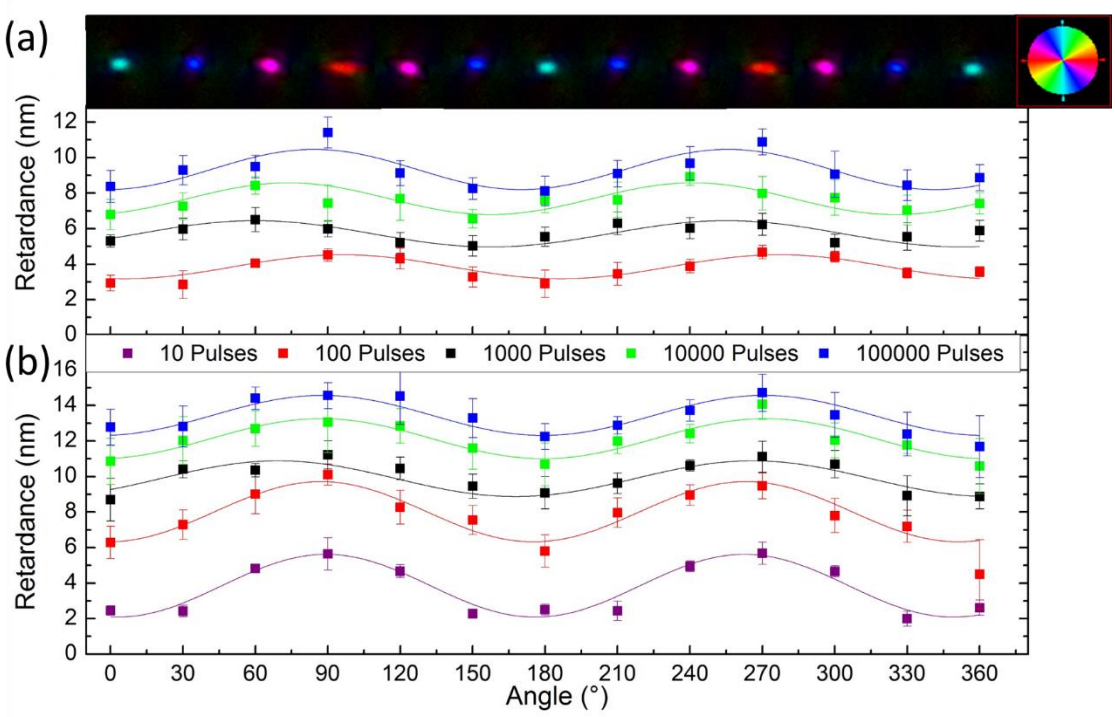

Figure 6.9: Retardance of Regions Modified with 100 nJ Femtosecond Pulses as a Function of Exposure Time and Polarization. (a) With PFT and (b) No PFT. Sinusoidal dependence of retardance is observed for perpendicular polarization yielding strongest birefringence. Ratio of birefringence strength diminishes with larger exposure times as a result of thermal effects but modulation in retardance is still evident. Structures (inset in figure) are circularly symmetric for 0° (light blue structure) and elliptically elongated for 90° (red structure) similarly to what is observed in NA = 0.43 case. The colour of the structures represent the slow axis orientation, illustrated by the inset colour wheel.

6.4 Discussion

It is quite evident that spatio-temporal couplings play a significant role with respect to material modification. What is not well understood is how these couplings change and react when focusing. Recently, simulations and experiments have been developed to evaluate the effect optical aberrations would play in SSTF experiments [181], while others have shown how spatio-temporal couplings behave at the focus in air and in glass for particular situations [110,199,200], demonstrating how important these couplings are to the focusing propagation.

6.4.1 Finite Difference Time-Domain Simulations

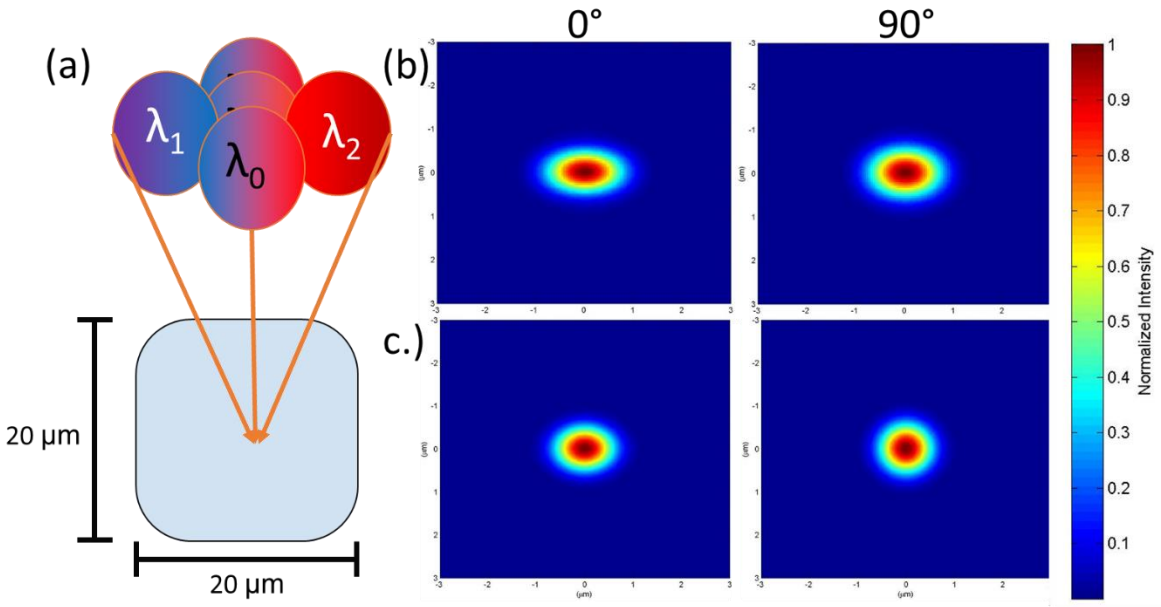

Figure 6.10: FDTD simulations of the polarization dependent modification. (a) Scheme of set-up. SC was simulated by varying wavelength across 5 Gaussian beams overlapping in the focus in a 20 x 20 m fused silica bulk (40 nm mesh resolution size) (b) With PFT (c) No PFT. In both cases, no polarization dependence is seen in the laser fluence.

Initial theoretical analysis used the corresponding total near-field distribution by simulating a propagating beam with SC into the bulk of a fused silica sample (Fig. 6.10). A finite-difference time-domain (FDTD) method was used to perform the calculations (Lumerical). Five Gaussian sources of varying wavelength, similar to the induced SC seen in experiment, were focused together into the bulk of a simulated fused silica environment (Fig. 6.10a). The beams overlap at the focus and the difference in laser fluence is observed for varying polarization states with respect to the SC. The bulk is a 20 x 20 µm environment (mesh resolution = 40 nm) to ensure that there is no polarization issues with the boundary of the cell [201]. In the case with PFT

(Fig. 6.10b), there is no difference in the laser fluence distribution. The equivalent is observed in the case with No PFT (Fig. 6.10c). An elongation is observed in the With PFT case but not in the No PFT case, which suggests there may be a discrepancy involved with the method in how the beam was defined. However, this result corresponds to the observation that the polarization dependence is a multi-pulse effect.

6.4.2 Paraxial Propagation Simulation

For the two cases discussed in this study, further propagation simulations were conducted to demonstrate how the spatio-temporal couplings change when going from the lens to the focus. This sheds light on the origin of the anisotropy induced by polarization.

The pulse free of any spatio-temporal couplings after the lens has the following electric field distribution [126]:

$$E(x,t) = E_0 \exp\left\{-\left(\frac{1}{w^2} + \frac{ik}{2R}\right)x^2 - \left(\frac{1}{\tau^2} - i\beta\right)t^2\right\} \tag{6.1}$$

where w is the beam radius, R is the beam front curvature (initially $R = \infty$), k is the wavevector, τ is the temporal width and β is the TC. When this pulse is traversed through a grating pair, SC is introduced, which is necessary for SSTF. Then the electric field with a coupling term between time and space is:

$$\vec{E}(x,y,t) = \vec{E}_0 \exp\left\{-\frac{x^2}{d_x^2} - \frac{y^2}{d_y^2} - 2pxct - \left(\frac{1}{\tau^2} - i\beta\right)t^2 - i\omega_0 t\right\} \tag{6.2}$$

where d_x^2 and d_y^2 are the beam widths along the x and y axes in the plane perpendicular to the beam propagation axis z, τ is the temporal width, β is the TC, ω_0 is the laser frequency and p is the space-time coupling term. It is a complex number with the real part representing the PFT and the imaginary part representing the WFR (or TVA) [126]. Its value is controlled by the grating pair introduced between the laser and the focusing lens. To understand what causes the anisotropic photosensitivity, an identification of the major spatio-temporal coupling that is seen in and out of the focus is needed. Equation (6.2) can be re-written in a more functional form represented by complex Q-parameters for simplicity for the pulse before the lens (Fig. 6.11) [126].

$$E(x,y,t) = E_0 \exp\{-\tilde{Q}_{xx}x^2 - \tilde{Q}_{yy}y^2 - 2\tilde{Q}_{xt}xct - \tilde{Q}_{tt}c^2t^2\} \tag{6.3}$$

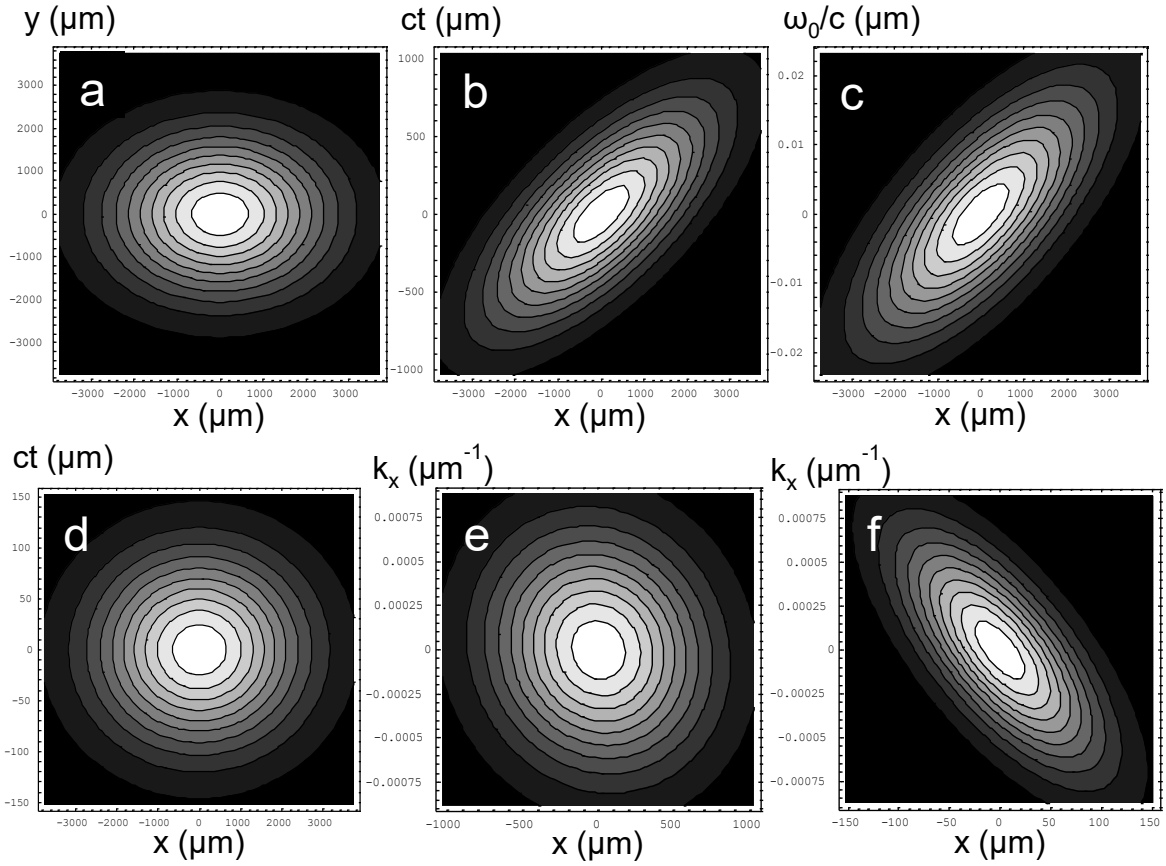

Figure 6.11: Distribution of the Laser Beam at the Lens for the Two Cases Conducted in Experiment. (a) Laser beam fluence for both cases at the lens. (b) & (d) The laser beam intensity distribution in the plane y = 0 for the cases (With PFT) and (No PFT), respectively. (c) The frequency distribution across the laser beam for both cases (i.e. SC). (e) & (f) The WFR of the beam at the lens in the plane y = 0 for the cases (With PFT) and (No PFT), respectively.

Based on the two cases discussed in this publication, the induced SC is the same (Fig. 6.11c), introducing ellipticity into the fluence distribution at the focusing lens with the aspect ratio a = 1.3 (Fig. 6.11a) while AD is zero. However, the TC is different for both cases. In the first case (With PFT), the SC alongside the TC leads to PFT before the lens (Fig. 6.11b) with a negligible WFR (Fig. 6.11e). In contrast, in the second case (No PFT), SC is the same as the previous case but with no TC present by the grating set-up, effectively making PFT zero (Fig. 6.11d) while introducing WFR (Fig. 6.11f).

6.4.3 Non-Paraxial Explanation

To explain quantitatively how the coupling between polarization and spatio-temporal couplings in the focus operates, an analysis of the field structure near the focus is conducted. Since the

polarization dependence increases for tighter focusing conditions, it becomes clear that the anisotropic photosensitivity is a non-paraxial effect. When focusing a spatially chirped laser pulse with a high-NA lens [202,203], the spectral components propagate at angles up to $\varepsilon_y = 1/F\sqrt{Re[\tilde{Q}_{yy}]}$ relative to the original propagation direction, where *F* is the focal length, resulting from the focusing lens characterized by the numerical aperture $NA = n\sin(\arctan\varepsilon_y)$ where *n* is the refractive index of the glass. In the paraxial limit, ε_y is small. It also characterizes the ratio between the beam waist in the focal plane $w_y = 2/(k_0\varepsilon_y)$ to the Rayleigh length $z_{Ry} = \frac{w_y}{\varepsilon_y}$. Also, in this limit, the beam structure in the focus does not depend on the polarization. However, for the numerical apertures used in the experiment, the non-paraxial corrections need to be taken into account. They are responsible for the polarization dependence of the beam intensity distribution in the focus.

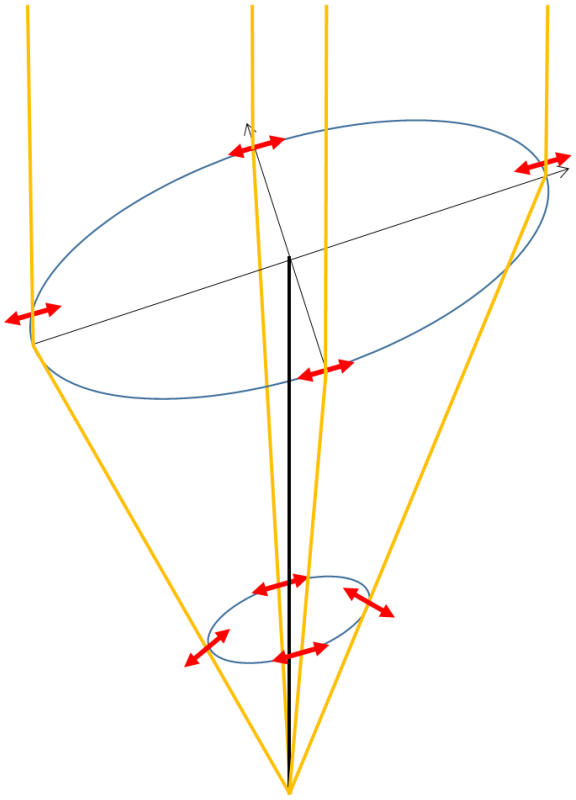

Figure 6.12: Schematic representation of the electric fields in a focused beam. The electric field (red arrows) remains perpendicular to the propagating rays (orange lines) upon focusing, resulting in a component of the electric field in the focus parallel to the propagation direction (black line).

To understand how the polarization dependence arises in the non-paraxial case, the propagation of a focused laser beam under these conditions needs to be discussed and an identification of the major spatio-temporal coupling that is seen in and out of the focus is needed. The non-paraxial

effects in a simplified manner can be considered due to obliquely propagating light rays (Fig. 6.12). As the electric field in the electromagnetic wave should be perpendicular to the ray, the electric field in the p-polarized rays is turned, thus creating a component of the electric field parallel to the beam axis. However, this simple interpretation is only valid for the first-order approximation in the paraxial parameter whereas higher order terms do not have simple geometric representations.

The propagation of a converging laser beam is described by the wave equation for the envelope of the vector potential amplitude, $\vec{A} = \vec{A}(x, y, z, t' = t - \frac{nz}{c})e^{(-i\omega_0 t + ik_0 z)}$:

$$2ik_0\partial_z\vec{A} + \vec{\nabla}_\perp{}^2\vec{A} = -\partial_z{}^2\vec{A} \tag{6.4}$$

where $t' = t - \frac{nz}{c}$ is the retarded time, *n*, is the refractive index and $k_0 = n\omega_0/c$ is the laser wave number. In the paraxial approximation, the second derivative of the amplitude along the propagation direction is small and neglected. In this case, the electric field is defined by the time derivative of the potential, $\vec{E} = i\omega_0\vec{A}$. Beyond the paraxial approximation, the right-hand side of Equation (6.4) needs to be accounted for since it becomes of the order of NA^2 [204,205]. Furthermore, a beam convergence leads to the appearance of the scalar potential, Φ, which arises from the Lorentz gauge $i\omega_0 n^2\Phi = c^2\nabla\cdot\vec{A}$ and maintains the zero divergence of the laser electric field. Expanding to the second order changes the wave equation to:

$$2ik_0\partial_z A^{(2)} + \vec{\nabla}_\perp{}^2 A^{(2)} = -\partial_z{}^2 A^{(0)} \tag{6.5}$$

Following a similar approach for an optical beam with a circular cross-section [204,205], an expression for the vector potential in the case of an elliptical beam can be found. The solution for Equation (6.5) for the vector potential polarized in the x-direction in the second order development on the paraxial parameters $\varepsilon_x = d_x/F$ and $\varepsilon_y = d_y/F$ reads as:

$$A^{(2)} = A^{(0)}(\varepsilon_x^2 g_x + \varepsilon_y^2 g_y) + 1 \tag{6.6}$$

where F is the focal length, $A^{(0)}$ is the paraxial solution and the correction functions $g_{x,y}$ are defined as:

$$g_x(x, y, z, t') = \frac{1}{4}f_x\left(\frac{3}{4} + \frac{1}{2}f_y\frac{y^2}{w_y^2} - f_x^2\frac{(x+\gamma ct')^4}{w_x^4} - f_xf_y\frac{(x+\gamma ct')^2y^2}{w_x^2w_y^2}\right) \tag{6.7}$$

$$g_y(x, y, z, t') = \frac{1}{4}f_y\left(\frac{3}{4} + \frac{1}{2}f_x\frac{(x+\gamma ct')^2}{w_x^2} - f_y^2\frac{y^4}{w_y^4} - f_xf_y\frac{(x+\gamma ct')^2y^2}{w_x^2w_y^2}\right) \tag{6.8}$$

where $f_{x,y}(z) = 1/1(1 + i(z - F)z_{Rx,y})$ are scaling functions, $w_{x,y} = 2/k_0\varepsilon_{x,y}$ are the beam widths, $z_{Rx,y} = w_{x,y}/\varepsilon_{x,y}$ are the corresponding Rayleigh lengths and $\gamma = -2i\,pF/k_0$ characterizes the SC. The development of the wave propagation equation in the series on the paraxial parameters is asymptotic and only valid at the distances of the order of a few Rayleigh lengths from the focal plane. Consequently, the corrections to the longitudinal electric and magnetic fields (E_z and B_z) are of the order of ε and the corrections to the transverse fields are of the second order ε^2. Knowing the expressions for the vector and scalar potentials, one can readily obtain the electric and magnetic fields and the distributions of the laser intensity and fluence near the focus.

The electric field expressions can then be calculated from the electrostatic potential and assuming that the vector potentials are polarized in the (*x, y*) plane at the angle ϑ with respect to the x-direction:

$$E_x = E^{(0)}\cos\theta\left(1 + \varepsilon_x^2 g_x + \varepsilon_y^2 g_y - \varepsilon_x^2 g_{\phi x}\right) + E^{(0)}\sin\theta\,\varepsilon_x\varepsilon_y g_w \tag{6.9}$$

$$E_y = E^{(0)}\sin\theta\left(1 + \varepsilon_x^2 g_x + \varepsilon_y^2 g_y - \varepsilon_y^2 g_{\phi y}\right) + E^{(0)}\cos\theta\,\varepsilon_x\varepsilon_y g_w \tag{6.10}$$

$$E_z = -iE^{(0)}\left(\cos\theta\,\varepsilon_x f_x\frac{x + \gamma t'}{w_x} + \sin\theta\,\varepsilon_y f_y\frac{y}{w_y}\right) \tag{6.11}$$

where *E(0)* is the zeroth order electric field, which can be found by making the right hand side of Equation (6.6) zero,

$$E^{(0)} = E_f\sqrt{f_x f_y}\exp\left[-q_t(ct')^2 - \frac{f_y y^2}{w_y^2} - \frac{f_x(x + \gamma ct')^2}{w_x^2}\right] \tag{6.12}$$

$q_t = \tilde{Q}_{tt} - \tilde{Q}_{xt}{}^2/(\tilde{Q}_{xx} + ik_0/2F)$, E_f is the maximum field amplitude in the centre of the focal spot and:

$$g_{\phi x}(x, y, z, t') = \frac{1}{2}f_x\left(1 - 2f_x\frac{(x + \gamma t')^2}{w_x^2}\right) \tag{6.13}$$

$$g_{\phi y}(x, y, z, t') = \frac{1}{2}f_y\left(1 - 2f_y\frac{y^2}{w_y^2}\right) \tag{6.14}$$

$$g_w(x, y, z, t') = f_x f_y\frac{y(x + \gamma t')}{w_x w_y} \tag{6.15}$$

Here, the corrections to the longitudinal electric field, E_z, are of the order of ε and the corrections to the transverse fields are of the second order ε^2.

The nonlinear effects observed during the experiment are defined by the local strength of the electric field. The nonlocal effects depend on the laser polarization with respect to the spatio-temporal couplings and thus introduce an anisotropy in the electric field distribution. Therefore, the fluence in the focal plane and the distribution along the propagation axis of the beam is the origin of the polarization dependence in modification. According to the experimental observations, the polarization dependence is a multi-pulse irradiation effect. This is in agreement with the theoretical analysis, showing a very small polarization effect in the second-order on the paraxial parameter ε (Fig. 6.13). When compared against a case similar to the No PFT case but without spatio-temporal coupling (*no SC*; $\gamma = 0$), the SC leads to broadening of the focal spot in the chirp direction, thus producing an almost circular symmetric shape of the fluence (Fig. 6.13a)

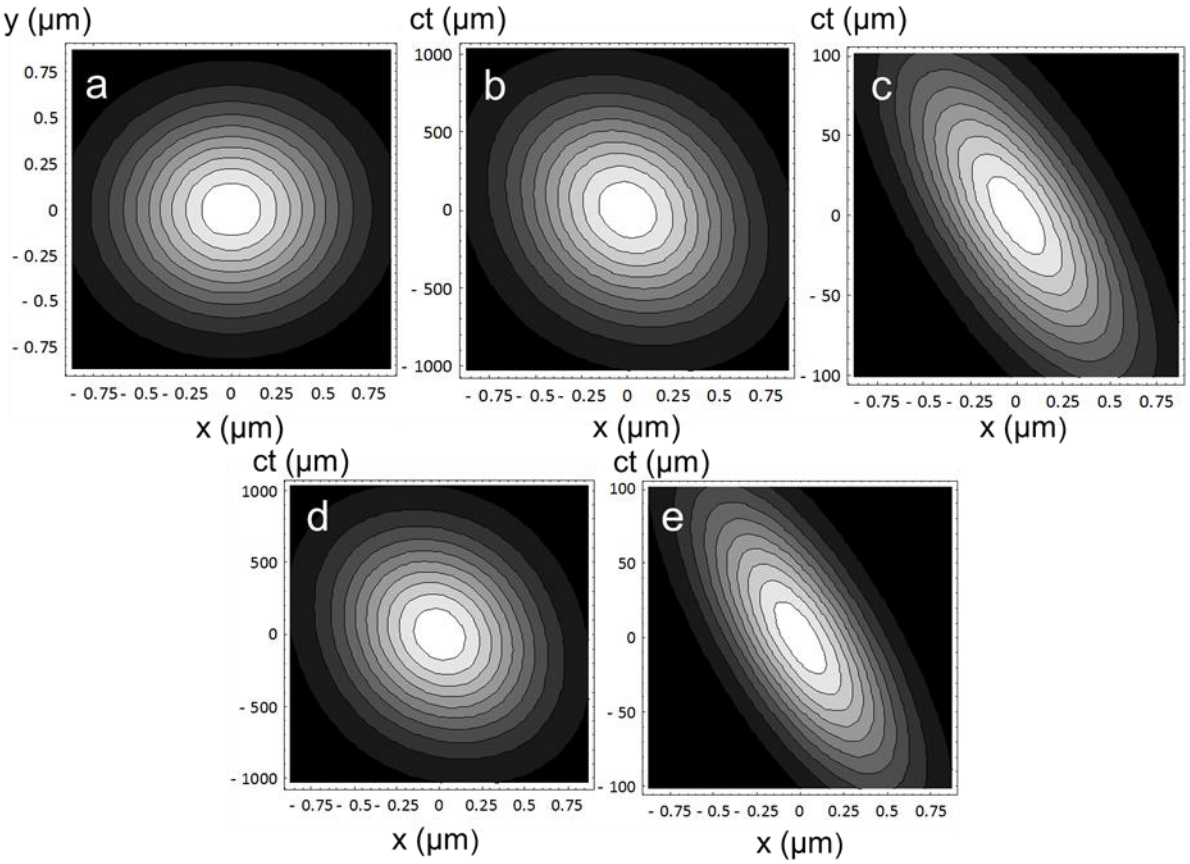

Figure 6.13**:** Distribution of (a) the Laser Fluence and (b-e) Laser Intensity in the Focal Plane z = F for polarization 0° (b, c) and 90° (d, e). (b, d) With PFT, (c, e) No PFT. The fluence distribution is the same in both cases regardless of the polarization state. When looking in the focal plane, the PFT observed is opposite of what is observed before the lens for both cases even with non-paraxial corrections. This furthers the conclusion that PFT is not the origin of the polarization dependence, as originally theorized, and that the polarization dependence is a multi-pulse phenomena as observed in experiment.

It should be noted that non-paraxiality in itself affects the polarization contributions at the focus, introducing anisotropic effects in light-matter interactions.[47] Therefore, the electric field contributions at the focus need to be taken into consideration (Fig. 6.14, 6.15). The transverse electric field components at the focus for both With PFT and No PFT cases are very similar to the laser intensity distributions observed at the focus (Fig. 6.13 b-e). In opposite, the axial component for both With PFT (Fig. 6.14a, c) and No PFT (Fig. 6.15a, c) are quite different. However, the axial components contribute about 2% to the overall electric field at the focus (Fig. 6.14b, d, Fig. 6.15b, d). While anisotropic effects from the non-paraxial focusing are indeed present, the anisotropic and non-paraxial terms are relatively small making them difficult to observe in single-pulse irradiation. The contribution could be quite important with further irradiation of 100 or more pulses but would not become noticeable within the first few pulses. Therefore, the anisotropic photosensitivity observed in this study between the parallel and perpendicular polarizations is primarily due to the AD.

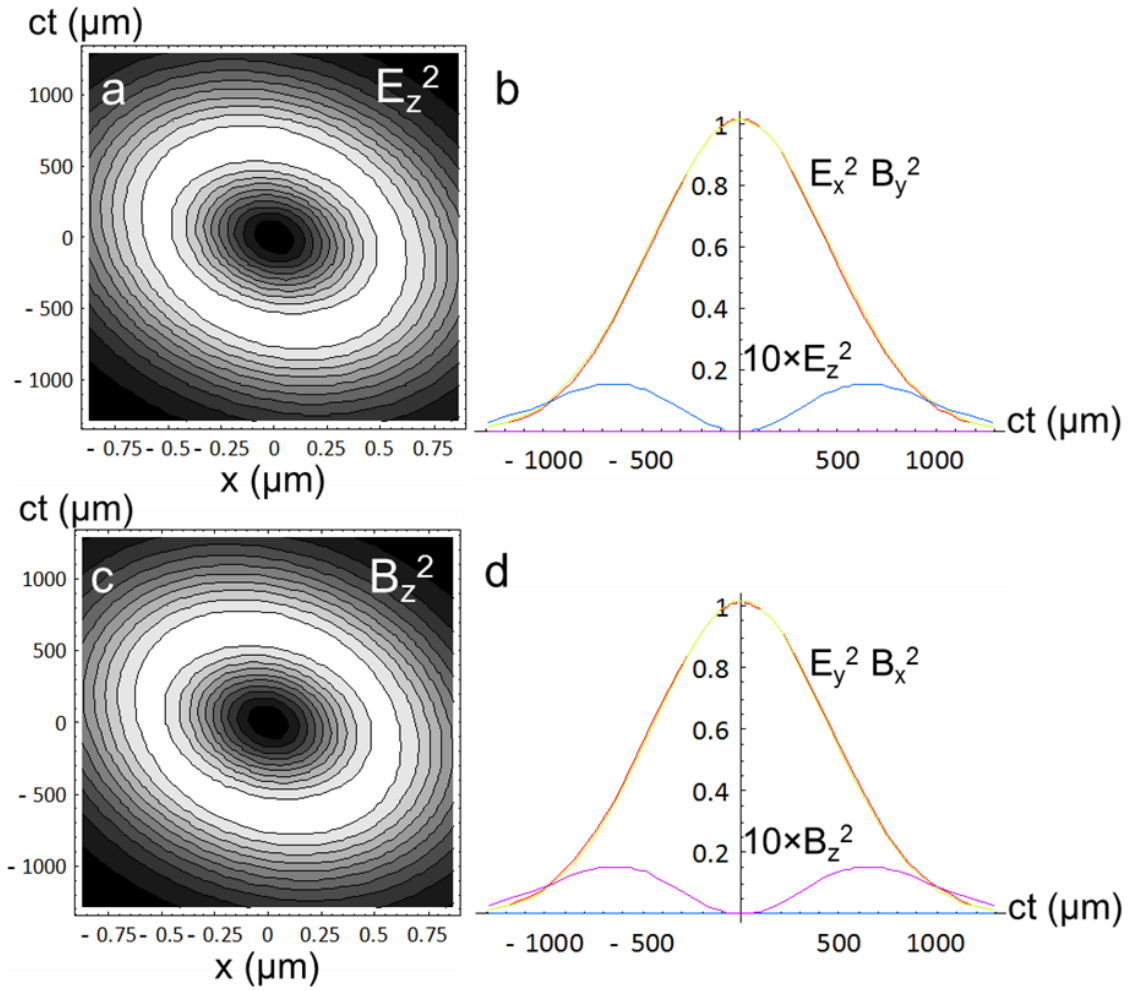

Figure 6.14. Axial Electric Field Contribution for the With PFT case at the focus z = F for polarization 0° (a, b) and 90° (c, d). (b, d) Relative amplitudes of components as a function of time. While the axial contribution is evident and different from its

transverse counterparts, it results in roughly 2% of the overall electric field at the focus.

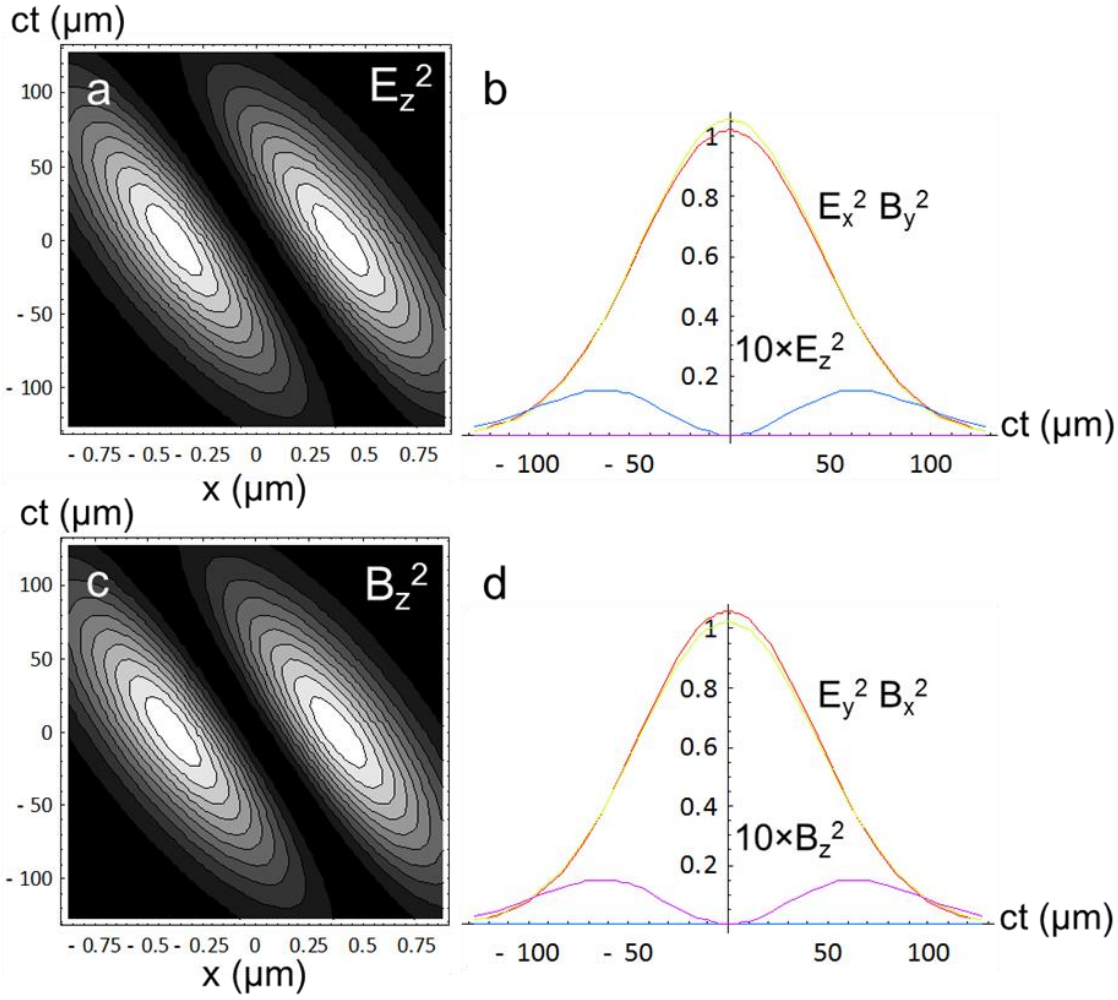

Figure 6.15. Axial Electric Field Contribution for the No PFT case at the focus z = F for polarization 0° (a, b) and 90° (c, d). (b, d) Relative amplitudes of components as a function of time. While the axial contribution is evident and different from its transverse counterparts, it results in roughly 2% of the overall electric field at the focus."

Interestingly, the observed damage is anisotropic (Fig. 6.5) even though the fluence shape in the focus is round (Fig. 6.13a). At the moment, there is no complete explanation for this fact. In experiment, the phenomena is observed to occur after multiple pulses. The effect of the subsequent pulse scattering on the material modifications induced by the previous pulse could be an origin of this effect. The scattering takes place in the plane perpendicular to the laser polarization and may lead to spreading damage in that plane. However, the multi-pulse simulations, accounting for material modification effects, are extremely difficult to model because of complicated physics intervening the non-paraxial propagation and sub-wavelength material inhomogeneities in the focal zone alongside the incubation effects. Once some macroscopic

modification is induced, it behaves as a scattering center for longer irradiation and changes the distribution. The difference in structure for the orthogonal polarization states can scatter the incoming light differently, altering the modification for longer irradiation and changes the distribution of the modification. The contrast in modification between the orthogonal polarization states would then increase with longer exposure. With the initial modification after the first pulse, the observed anisotropic behavior would emerge with further pulse irradiation. The concept of the initial pulse developing a "seed" in the glass, which eventually introduces polarization dependences for further pulse irradiation have been discussed before. [206,207] But these studies do not involve spatio-temporal couplings or non-paraxial effects. A multi-pulse model is currently under development to see how the polarization coupling with SC evolves with further pulse irradiation.

Ensuring that AD before the lens is zero and that the wide-field SSTF geometry used in the experiment leads to a circularly symmetric focus [181], the only spatio-temporal coupling that can cause the observed polarization dependence is the induced SC. It becomes apparent that when using typical ultrafast laser systems with chirp amplification set-ups, the anisotropic photosensitivity will be present, affecting the material nanostructuring. In some cases, polarization dependence in modification can be minimized by overlapping adjacent tracks [165]. However, this is not always possible and for applications like waveguide manufacturing and polarization multiplexed data storage, the polarization dependence plays a major role. This motivates a discussion of how to deal with this issue when modifying glass in a singular position. One possibility is to add a dynamic compensation mechanism, such as using a spatial light modulator *(SLM)* [166]. This is inherently difficult for many reasons. One is power limitations due to the damage threshold of typical SLMs. Another is the difficulty in producing holograms on the SLM to compensate for the spatio-temporal couplings across the entire beam spot of the laser pulse. This can be overcome by using traditional dispersive element techniques like grating or prism compressors. However, depending on the quantity and type of spatio-temporal coupling inherent in the laser beam, large propagation distances may be required, which can be detrimental to the beam spot and overall beam quality factor. One also needs to take into consideration the correction of aberrations from the focusing optics, especially when working with lasers of higher bandwidths.

Instead of correcting for the polarization dependence in modification, one might harness it for an extra degree of control for modification. Once understanding what spatio-temporal couplings lie within the laser beam being used and how they behave in modification, utilization of the polarization dependence allows tailoring of the relative strength of the modification. Depending on the application, different polarization orientations with respect to the SC will appear more

beneficial. For overall larger retardance and stronger modification outside of the focal plane, polarization should be oriented perpendicular to the SC direction. Yet in this regime, the modification is elongated along the chirp direction which could hinder applications where symmetrical modification is needed. Conversely, symmetrical modification is attained by setting the polarization to be parallel to the SC. In this regime, the modification reaches closer to the focal plane but is observably weaker than the orthogonal case, with longer exposures needed to reach the same modification thresholds. By simply rotating the polarization state with respect to the orientation of SC, the relative strength of modification in a spot can be controlled, potentially reducing the manufacturing time for larger scale applications. Another method one may use alongside the spatio-temporal couplings is to rotate the spatio-temporal couplings with rotational optics, such as a dove prism [184], with the polarization to ensure modification is symmetric and of the same strength.

A balance between SC and the effective NA of the focusing optic needs to be determined depending on the laser source used to ensure tight focusing for the effect to be dominant. Moreover, it is clear that SSTF is beneficial in inducing stronger modification under shorter irradiation times (Fig. 6.7). By simply adding SC to the beam, the nonlinear interaction is localized closer to the focal plane as opposed to CF, similar to what has been discussed in previous studies [109,111,208]. Providing an avenue to attain stronger modification with up to 10x less the amount of pulses can again potentially reduce the manufacturing time for larger scale applications or improve the writing speed associated with polarization multiplexed data storage.

6.5 Conclusions

The spatio-temporal couplings play a pivotal role in ultrafast laser material modification dynamics. They are present in all ultrafast laser systems and cause unpredictable results in laser nanostructuring. To alleviate this issue, I have successfully untangled SC and TC with the use of grating compressors and illustrated an additional level of control on the strength of modification. In doing so, an anisotropic photosensitivity is observed in fused silica making it an inherent physical phenomenon in ultrafast laser nanostructuring. This effect arises from AD in the focus that originates from a frequency gradient in the laser pulse and not PFT as originally thought. Modification can be tailored by changing the polarization state of the laser pulse with respect to the direction of SC. This effect is stronger for tighter focusing and is apparent for longer exposures when the modification takes place close to the focal plane. As SSTF becomes more attractive in ultrafast laser nanostructuring, the ability to control the strength of modification with the polarization state can benefit not only tailoring the strength of modification but also the

manufacturing time for time-consuming-based applications to deliver stronger modification in a shorter time.

Chapter 7: Transition from the Void-Like Structure to Self-Assembled Nanogratings

7.1 Introduction

As discussed earlier, ultrafast lasers have become a powerful tool in material microprocessing over the years, which has proven to be pivotal in the development of a growing number of fabricated micro/nano-components for a wide range of applications [16]. In particular, as the interaction process between femtosecond laser pulses and condensed matter originates mainly from nonlinear effects, which occur locally near the focus, volumetric space-selective structural modification can be achieved in the bulk of transparent dielectrics [209]. Previous studies have shown that the damage threshold of a material depends on multiple parameters of incident laser pulse, such as the wavelength, pulse duration and number. But usually for single femtosecond laser pulses at 800 nm, the induced structures in the exposure area mainly depends on the level of the laser intensity and therefore have long been classified qualitatively into three types (refer to Chapter 2).

As discussed in Chapter 2.3, if a single pulse with energy lower than the critical power ($P_{cr} = 3.77\lambda^2/8\pi n_0 n_2$ [90]) is tightly focused at a shallow depth or using immersion optics, spherical aberrations and self-focusing are negligible. The threshold for multiphoton ionization is then met at the geometrical focus, where the excited electron density will dramatically increase due to impact ionization. Since the ionization is confined to a small volume, the energy is quickly transferred to the lattice producing a pressure which subsequently drives a shock wave and stress that exceeds the Young modulus of the material. A microexplosion occurs at the focus and results in the formation of a void as small as 200 nm within a compressed shell [11,73].

If the input pulse exceeds the critical power or focuses at a deeper depth in the bulk of a material, the energy is deposited over a larger volume around the focus instead of converging at a point, leading to the formation of void arrays [91]. Spherical aberration can further expand the energy deposition region resulting in an elongated plasma channel. After plasma rapidly transfers energy to the lattice, a cylindrical shock wave emerges leading to the rupture of the material behind the wave's crest. The formation of such channels by single pulse irradiation have been previously observed, which were seen to break into chains of voids by subsequent irradiation [92,93], while single pulse imprinting of void arrays have been reported [94]. Other studies suggest void arrays arise from the interference of ultrafast laser driven electron waves interfering to create a standing electron plasma wave, inducing multiple periodic microexplosions [96]. However, in all of these

studies, it is uncertain whether critical electron densities are met. Regardless of the mechanism, optical cavitation in glass can lead to Type III modification in the irradiated zone [19]. The above classification of modification regimes has been regarded as a non-reversible path following the laser intensity regimes.

Currently, the formation mechanism for self-assembled nanogratings is still under debate. Therefore, an understanding of the environment during laser irradiation that facilitates nanograting formation is pivotal in understanding. While many different models have been proposed [2,3,36,44,57,61,64,210–214], there exists several mainstream theories on the formation mechanism (Chapter 2.2). When nanograting formation was first discovered, the periodicities were thought to be due to an interference of generated Langmuir waves from a critical plasma [2]. The other popular view describes the evolution of nanoplasma hot spots, which form inhomogeneously around defects and/or colour centres [3,64]. This theory is also explained to be in an environment of high to critical plasma densities. To overcome the issue of critical plasma densities, an exciton-polariton model was introduced which also explained the longitudinal periodicity of nanogratings based on the interference of short-living exciton polaritons [61,210]. Only recently have studies tried to combine the different theories in order to use the same interference models to explain the periodicities. The nanoplasmonic model was further expressed on as an excitation of standing plasma waves at the interfaces of modified-unmodified regions [57]. This excitation at the interface leads to areas of critical plasma densities, promoting the generation of interfering Langmuir waves, resulting in periodic nanogratings similar to the original interpretation as well as the mechanism thought to be responsible for surface ripples formation [57]. This theory was taken further, suggesting the mechanism is based on the interference between incident waves from the laser source and scattered waves from random inhomogeneities [207]. This interference results into the organization of nanoplanes with wavelength-based periodicity, dependent on the density of the inhomogeneities and resulting in a dependence on the electron density. However, within each of these theories, there are issues that invalidate the models such as dependencies on number of laser pulses and/or pulse energies with respect to periodicities, material dependencies and limitations on intensities and electron density. Therefore, the identification of the electron density during laser irradiation is crucial for the fundamental understanding of the formation mechanism.

In the initial experiments involving the blade-effect (Chapter 6), void formation taking place before nanograting formation was directly observed when writing into the bulk of fused silica (Fig. 6.7, Fig. 7.1). Voids would form at the top of the structure and then eventually transition to nanograting formation, as seen in Chapter 6. This transition was observed in other studies showing that under moderate focusing conditions (NA > 0.4) in fused silica self-assembled

nanogratings (Type II) could be developed from void formation (Type III) after the first few pulses [101]. While void formation is not necessary for the formation of nanogratings [101], it is interesting to observe Type II modification after void formation when it was originally theorized that near-critical threshold plasma densities are met when the voids are visible [21,102]. In this chapter, the characteristics and evolution of femtosecond laser-induced structures in fused silica in a multi-pulse regime under tight focusing are discussed. The transition from voids to nanogratings was observed and compared against numerical simulations of the distribution of the laser fluence, incident intensity, and electron density of a single femtosecond pulse by solving the nonlinear Schrödinger equation, conducted by Dr. Ye Dai and our colleagues from Shanghai and Jiangsu University [97]. Here I discuss the possible role of pulse incubation effects in the structural modification. Understanding the role of energy absorption in the regimes of the void to nanograting transition can shed light on the dynamics for laser induced nanostructuring.

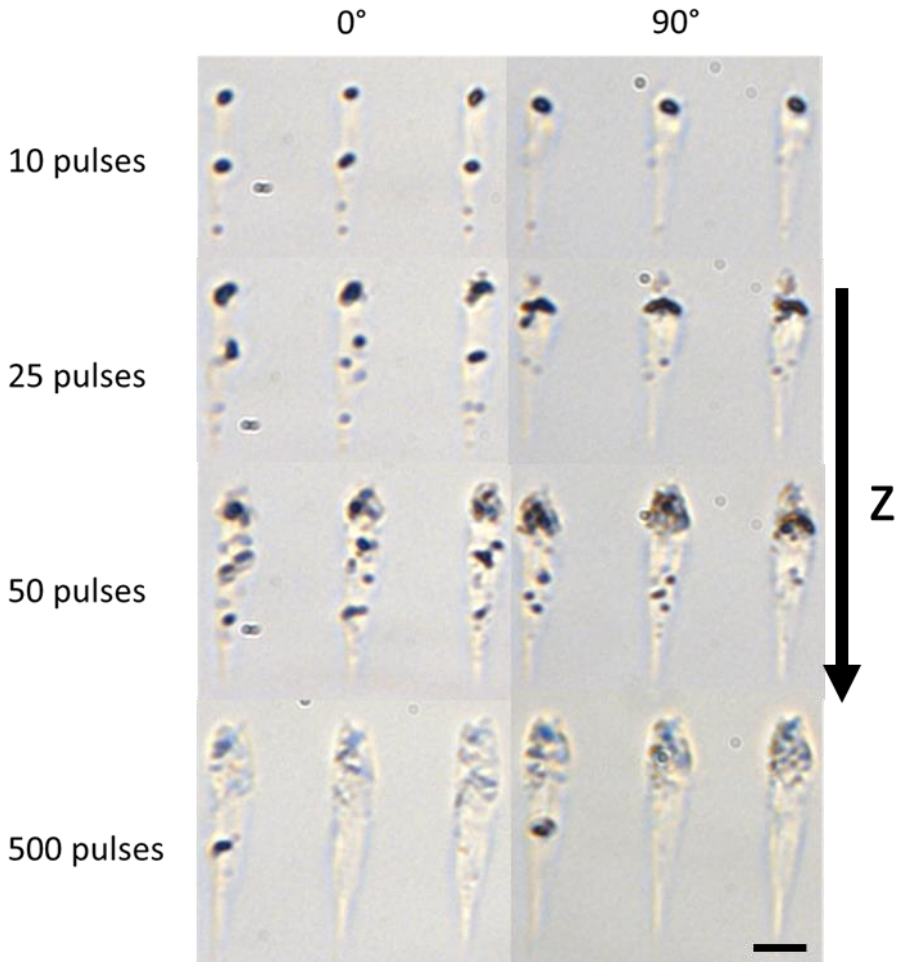

Figure 7.1: Initial experiments of polarization dependent modification in the bulk of fused silica. While the polarization dependence is observed, it is clear that after further irradiation the modification transitions from void to nanograting. (λ = 750 nm, 20 kHz repetition rate, 60 fs, Ep = 1.5 μJ). The scale bar is 5 μm.

7.2 Experimental Set-Up

A mode-locked, regenerative amplified Ti-sapphire laser system (Spitfire, Spectral Physics Ltd.) delivered 120 fs (FWHM) laser pulses with a repetition rate of 1 kHz at a centre wavelength of 800 nm (photon energy 1.55 eV). A Glan polarizer and a λ/2 waveplate were used to adjust the pulse energy and polarization azimuth angle, respectively. The laser beam was focused with a 50× objective (LU Plan, Nikon) (NA=0.55) into the bulk of commercial grade silica glass mounted onto a computer-controlled XYZ translation stage (H101A ProScan model, PSI). The beam waist at the focus was estimated to be 0.8 μm. The geometric focus was fixed at a depth of 150 μm with respect to the surface of the sample throughout all the experiments.

7.3 Results

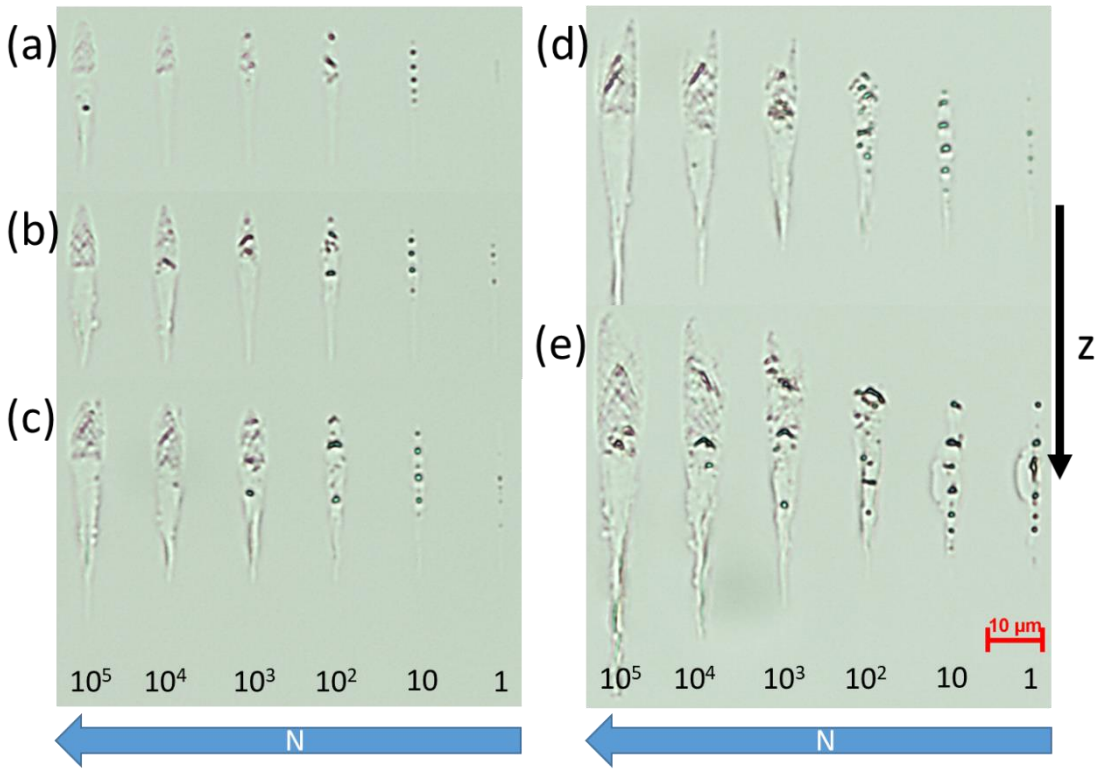

Figure 7.2: Optical images of the dependence of femtosecond laser-induced structures on the input pulse numbers. (a) Ep = 0.5 μJ (b) Ep = 1 μJ (c) Ep = 1.5 μJ (d) Ep = 2 μJ (e) Ep = 3 μJ. As the pulse density increases, the voids formed after the first few pulses transition to birefringence located at the top of the structure, as indicated under cross-polarizers. The red bar is 10 μm.

A series of dots with increasing pulse number were imprinted in the bulk of fused silica (Fig. 7.2). The dependence of the induced structures on number of pulses was analysed with an optical

microscope under two optical illumination modes, i.e., standard and cross-polarized (Fig. 7.3). An elongated trace was observed stretching along the beam propagation direction and structural modification emerges before the geometrical focus. Alongside the observed contour changes of the induced structures, their evolution with respect to pulse number is also important. A chain of voids appears in the exposed area within the first 10 pulses. However, as the pulse density increases, the voids multiply and develop in both directions (towards top and bottom) and disperse in a wide region. Finally, this leads to the emergence of an observable optical birefringence at the top of the induced structure as shown in Figs. 7.3(b) and 7.3(d). This transition indicates that voids, which occur after a few initial pulses, gradually evolve into nanogratings. Evidence of nanograting formation is further expressed through SEM of the 2 μJ case with clear evidence of the nanograting periodicity (Fig. 7.4).

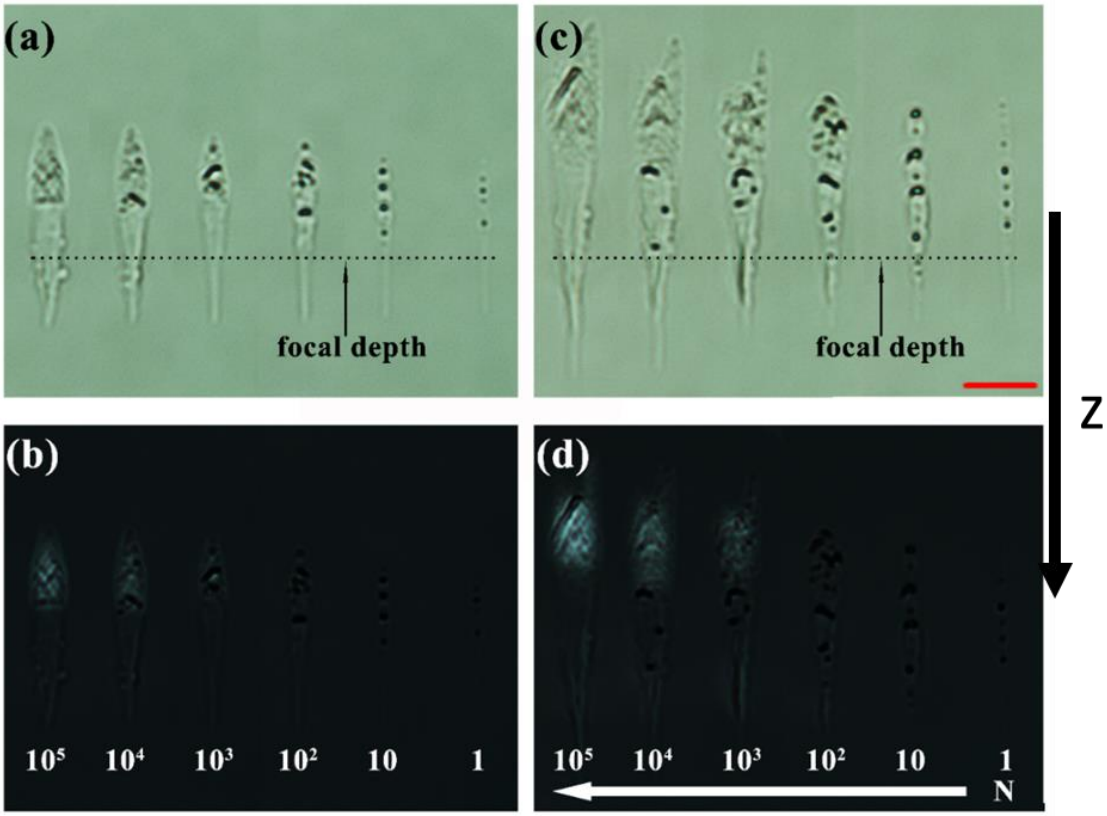

Figure 7.3: (a) and (c) Optical images of the dependence of femtosecond laser-induced structures on the input pulse numbers. (b) and (d) Birefringence of the induced structures under cross-polarization illumination. The red bar is 10 μm.

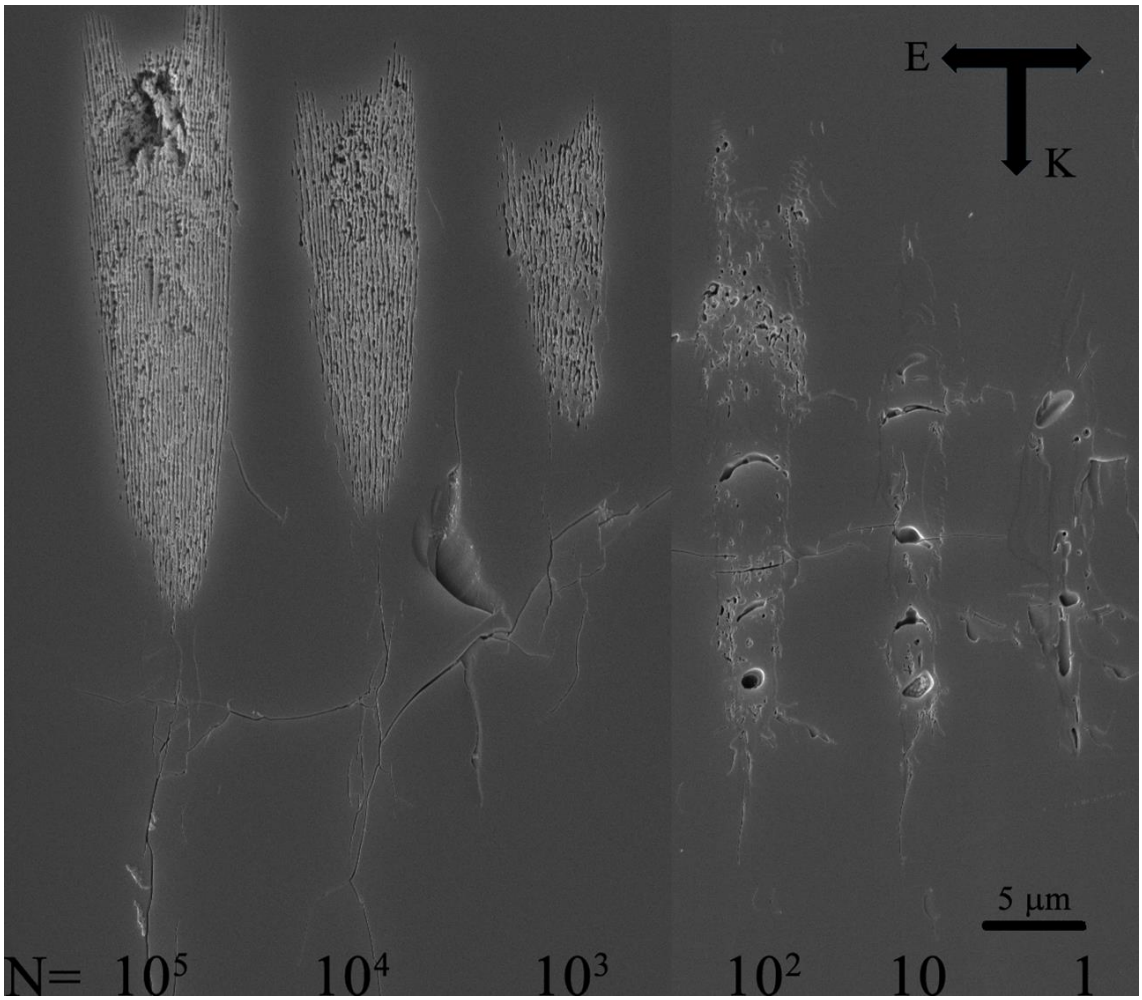

Figure 7.4: Structural transition from voids to nanogratings as a function of number of pulses when viewed under SEM. The pulse energy is 2 μJ.

7.4 Discussion

The nanograting formation has been previously theorized as an accumulative process, which is sensitive to the density of defects from silica decomposition [56,215]. During multi-pulse irradiation, the presence of defects in the exposed area creates energy levels within the material band gap of silica and facilitates the production of free electrons that seed the impact ionization; the electron density is enhanced by the successive input pulses. Consequently, distribution of induced defects or excited plasma depends not only on the number of pulses, but also on a series of factors associated with the spatial distribution of the incident energy. Therefore, a theoretical study on the laser fluence, incident intensity and electron concentration around the focus is performed.

For simulations, the nonlinear Schrödinger equation is used for tightly focused femtosecond pulse propagation. The basis of the model is similar to a previous study in [97]:

$$\frac{\partial E}{\partial z} = \frac{i}{2k}\nabla_{\perp}E - \frac{ik''}{2}\frac{\partial^2 E}{\partial^2 \zeta^2} - \frac{\sigma}{2}(1 + i\omega\tau_c)\rho E - \frac{1}{2}\beta^{(m)}|E|^{2m-2}E + ik_0 n_2|E|^2 E \quad (7.1)$$

where ζ refers to the retarded time variable $t\text{-}z/v_g$. The terms on the right-hand side of Equation (7.1) respectively stands for the diffraction, group velocity dispersion (with coefficient $k'' = 361\ fs^2/cm$) [21], absorption and light defocusing of electron plasma, six-photon absorption (with coefficient $\beta^{(m)} = 2.7\ x\ 10^{-65}\ cm^2/W^5$) [216]), as well as Kerr self-focusing ($n_2 = 2.5 \times 10^{-16} cm^2/W$) [217].

The electron density involved in Equation (7.1) can be further quantified by the following rate equation:

$$\frac{\partial \rho}{\partial t} = \frac{1}{n_0^2}\frac{\sigma}{E_g}\rho|E|^2 + \frac{\beta^{(m)}}{m\hbar\omega}|E|^{2m} - \frac{\rho}{\tau_r} \quad (7.2)$$

For fused silica at 800 nm, the linear refractive index is n_0 = 1.45, the six-photon absorption coefficient is $\beta^{(6)} = 2.7 \times 10^{-65}\mathrm{cm}^9/\mathrm{W}^5$ [216] and the absorption cross-section of inverse bremsstrahlung is $\sigma = k\omega_0\tau_c/n_0^2\rho_c(1 + \omega_0^2\tau_c^2) = 1.55 \times 10^{-18} cm^2$ [218]. Here the electron recombination time is $\tau_r = 150$ fs and electron collision time is $\tau_c = 23.3$ fs [17,21,218].

Since the refractive index mismatch between air and silica glass potentially plays a role in the laser intensity distribution near the focus of a high NA objective [157], the effect of spherical aberration is incorporated into the present model. For example, a relatively complete set of the equations for the electric field distribution has been expressed by Török et al. [219]. In our simulation, the light field distribution in fused silica glass in the proximity of the interface, computed from Equation (7.2), was chosen as the initial condition of the coupled Equations (7.1) and (7.2). The radial range of the simulation was chosen to be 20 times the waist of the incident light at the interface, to ensure that no reflection comes from the boundary of the computational domain. Also, it has been noted that spherical aberration could be ignored if a laser pulse is focused by a lens with ~mm sized focal lengths, even though a similar NLSE approach is used to simulate the fluence and plasma distribution in transparent materials [220]. Alternately, Couairon et al. also numerically simulated the intensity distribution at the focal point by using a pair of parabolic mirrors to overcome spherical aberration arising from the focusing geometry [221]. This approach offers an optional route to avoid the effect of spherical aberration on the induced microstructures.

Looking at the laser fluence and maximum intensity distribution for a single pulse during the pulse duration (Fig. 7.5), it is easy to see that the modification will take a tear-like shape structural distribution. The laser fluence sufficient to induce plasma can be seen well before the geometrical

focus. As the input energy increases, the ionization onset is shifting farther from the geometrical focus.

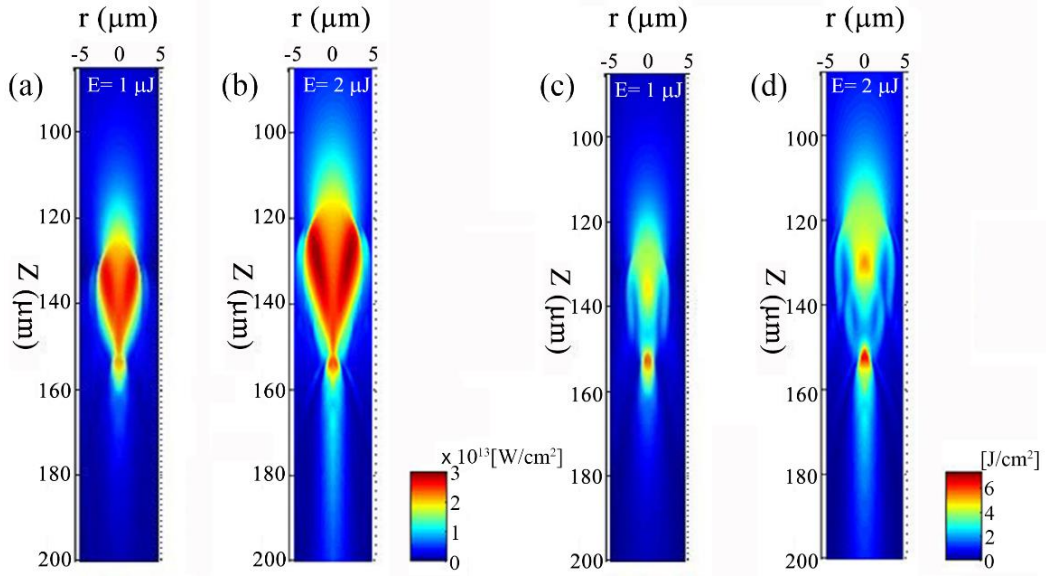

Figure 7.5: (a) and (b) Incident intensity and (c) and (d) Laser fluence simulations for a single pulse at 1 and 2 μJ, respectively. Large tear-like distributions with modification occurring before the focus is seen, as observed in experiment. The laser-induced breakdown reaches as high as ~2.5x10^{13} W/cm2 and the laser fluence is larger than the threshold for fused silica of 2-3 J/cm^2 (4.45 and 5.35 J/cm^2).

Another notable feature of the simulated profile is the on-axial spread of the generated field distribution along the beam propagation direction. This is due to the redistribution of the laser energy caused by the mismatch of the refractive indices between air and glass, resulting in spherical aberration. Compared to the previous models without consideration of spherical aberration [21,218], a secondary focus emerges at the end of the profile because in a paraxial situation, the light at the laser beam edge can converge to a deeper depth. It is also worth noting that the local intensity and electronic excitation in other areas are relatively weak in contrast to what is observed before the geometrical focus. This implies that areas with less intensity, such as the long filament at the end of the entire structure, play a minimal role in structural change even under multi-pulse exposure.

The intensity threshold for femtosecond laser-induced breakdown and damage in fused silica is presumed to be 3.2×10^{13} W/cm^2 [17], which correlates with our simulations in which the peak intensities before the geometrical focus are respectively 2.4 and 2.49×10^{13} W/cm^2 for 1 and 2 μJ. In addition, fused silica breakdown threshold has been suggested at 3 J/cm^2 at 800 nm for a pulse duration of 10~100 fs [102] or at 1.87 J/cm^2 by an 800 nm laser pulse for 160 fs [74]. The two thresholds are below the maximum values of 4.45 and 5.35 J/cm^2 in our two cases.

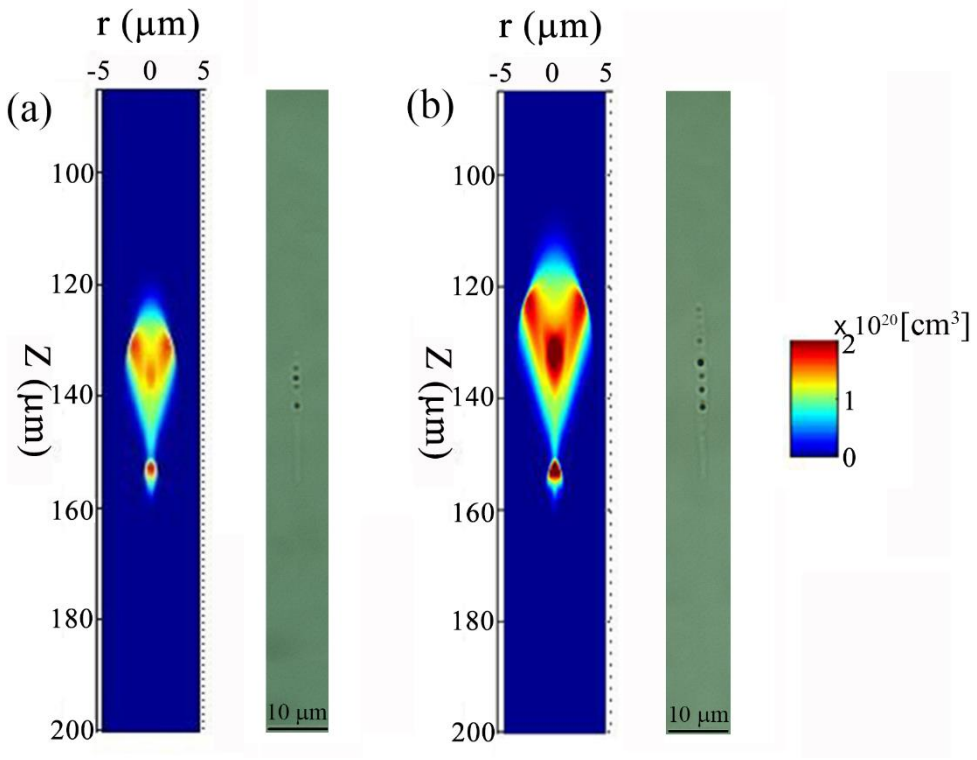

Figure 7.6: Electron density simulation for single pulse irradiation for (a) 1 μJ and (b) 2 μJ alongside optical images of the experimental observation. In the regions where the electron concentration reaches above 10^{20} cm^{-3}, void formation is observed in the structures printed.

The shape of permanent modification is mapped by calculating the electron concentration profile after single pulse exposure (Fig. 7.6). It is clear from the experimental results that a single pulse can result in a chain of voids. In that region where the voids are observed in the experiment, the electron density ranges from 1.07 to 1.49×10^{20} cm^{-3} inside the 11 μm-long void formation area in the 1 μJ case, and 1.14 to 2.55×10^{20} cm^{-3} inside the 13 μm-long area in the 2 μJ case. Integrating over the entire structure approximated as an ellipsoid, it is calculated that 10-20% of the pulse energy is absorbed. The simulation indicates that the electron concentration before the geometrical focus is ~ 10^{20} cm^{-3}, which is one order of magnitude lower than the critical threshold of 1.7×10^{21} cm^{-3} in fused silica. The above simulation result alongside our experimental observations indicate that at sufficient femtosecond pulse energies, the relatively large ionized area within an electron concentration >10^{20} cm^{-3} can facilitate void formation. For void formation to occur, optical cavitation must occur in the glass. Optical cavitation can only occur if the energy deposited during irradiation exceeds the Young's Modulus of the material, regardless of the electron concentration present. For fused silica, the elastic modulus is roughly 73 GPa. Therefore, for a 1 $μm^3$ void, the energy deposited to induce the void is 0.073 μJ. Based on the total volume of the voids formed in a single pulse (~1.362 $μm^3$ for 1 μJ and ~2.18 $μm^3$ for 2 μJ), roughly 8-10% of the pulse energy is deposited into the bulk for the formation of the voids, which agrees well with

the calculated absorption from the electron concentration simulations. The incident intensity, laser fluence and electron density for all pulse energies done in experiment are shown in Fig. 7.7.

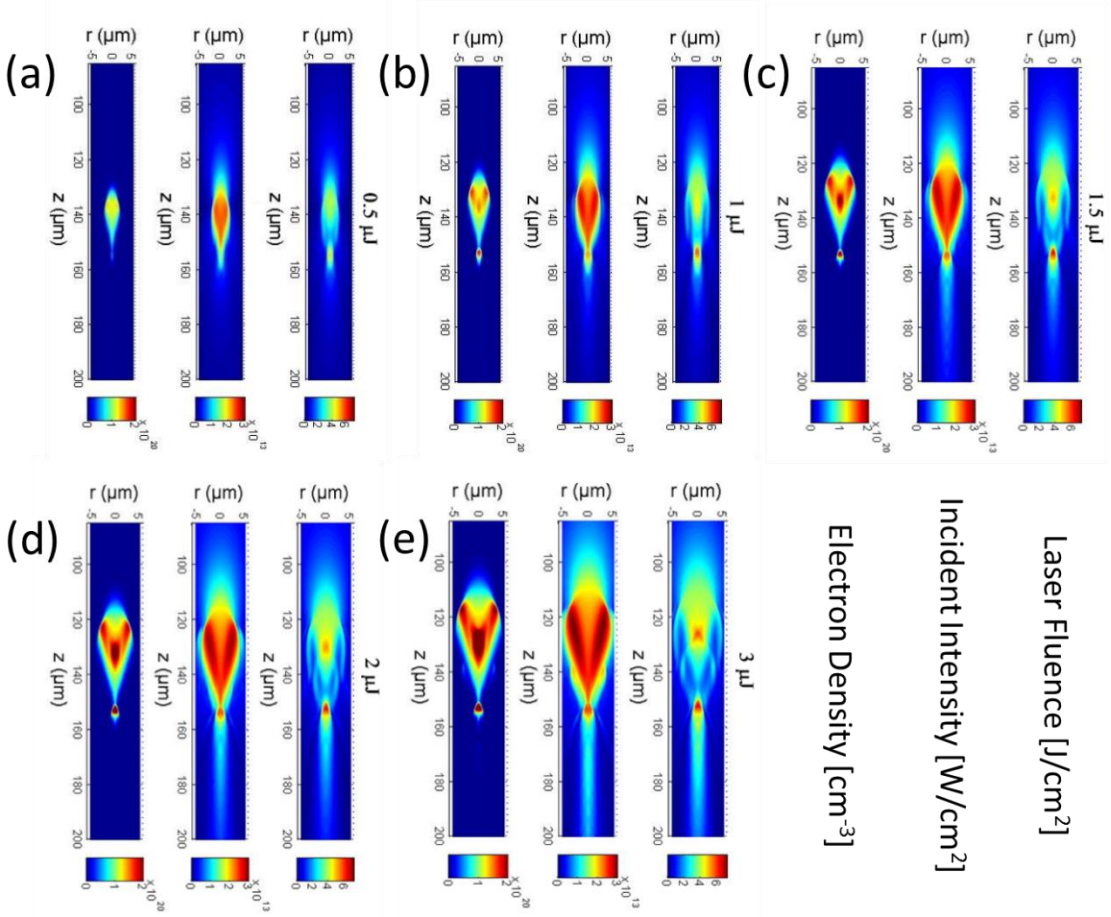

Figure 7.7: Laser fluence, incident intensity and electron density for single pulse irradiation for (a) 0.5 µJ, (b) 1 µJ, (c) 1.5 µJ, (d) 2 µJ, (e) 3 µJ.

The pre-formed voids appearing in the exposed area act as additional scattering centres of light [92,101]. This scattering distorts the intensity distribution of the incident light, leading to a spatial redistribution of the femtosecond pulse energy. As a result, the formed voids multiply, merge and move towards the incident surface within tens of pulses in the areas of lower density or viscosity phase [92]. As more pulses arrive to the area of interaction, the incoming light can be scattered simultaneously with the expansion of the emerging plasma, by an increase in local centres distributing in larger areas. Therefore, the deposited energy will introduce local defects in the glass and accelerate the structural transition and rearrangement before the geometrical focus after further irradiation [222].

Meanwhile, the relatively strong electron-phonon coupling in fused silica leads to the formation of excitons. The excitons become self-trapped, driving local atomic deformations and displacements. Subsequently, the self-trapped excitons decay into E' centres together with non-bridging oxygen hole centres (*NBOHC*) on a time scale of 250 fs [223]. The NBOHC can react

with E' centres when some critical density is reached forming oxygen deficiency centres (*ODC(II)*), which is observed simultaneously with the occurrence of nanogratings [56,215]. These defects lower the threshold for photon-ionization compared to that of pristine glass. Following several studies, it is estimated that electrons excited from defect states account for roughly 1-2% of the total electron concentration [223]. This introduces a circumstance for pulse incubation effects to bridge the time gap between two successive pulses in a continuous exposure no matter how long the pulse interval is [56,210].

With respect to the electron density, to reach the critical threshold, the glass needs to absorb 10 times more energy. Even assuming that 50% of the pulse is absorbed [218], it is insufficient to reach the critical electron concentration in the excited regions where void formation is seen. A growing number of evidence suggests that structural changes may take place in a phase of under-dense plasma [21,218]. Pump probe experiments show that initial electron concentrations as low as 10^{19} cm^{-3} is enough for inducing permanent restructuring in fused silica [22,224]. Low-spatial-frequency periodic structures on the surface of fused silica glass and nanogratings formed in high-silicate nanoporous glass have been reported to form at low degrees of material excitation (N_e~5×10^{20} cm^{-3}) based upon Drude formalisms used to simulate and confirm what is seen in experiment [57,211,225]. Since self-assembled nanogratings are observed after the void state at lower than critical threshold plasma densities, it is then concluded to be near impossible to reach the critical concentration threshold even with further irradiation.

The idea of lower than critical concentrations has consequences with interference-based models where the spacing between the nanoplanes is dependent solely on the plasma temperature and electron concentration [2,61]. It also provides difficulty in explaining the electron densities needed for standing plasma waves to be produced in the bulk from the interfaces of a nanoplasma when trying to unify the theories on in-volume nanogratings based on surface ripples with the nanoplasmonic model [57]. While local field enhancements in under-dense nanoplasmas are known to be stronger than the incident field in an under-dense plasma [87], it is still difficult to explain the order of magnitude increase in electron concentration to reach critical concentrations, as well as any sort of physical process taking place in such an environment. Therefore, the formation mechanism of self-assembled nanogratings should take into account low electron concentrations in future studies.

7.5 Conclusions

In summary, the structural transition from Type III to Type II in fused silica via a femtosecond laser pulse incubation effect is studied. The void formation appears before the geometrical focus after

the initial few pulses and nanograting gradually forms at the top of the induced structure with subsequent irradiation. For comparison, a nonlinear Schrödinger equation considering the effect of spherical aberration is used to simulate the distribution of laser fluence, incident intensity and electron density in the pulse beam propagation. The simulations show that optical breakdown occurs before the geometrical focus. This process leads to the formation of voids due to cavitation in the area where the electron density exceeds 10^{20} cm^{-3}. However, estimates based on energy absorption show that the exited electron density is insufficient to reach the critical threshold that was once assumed to occur in the regime of void formation and nanogratings. This study provides evidence to support the transition from the induced voids to nanograting and states the limitations, which may be useful to explore the potential formation mechanism of nanogratings.

Chapter 8: Spatio-Temporal Coupling Induced Non-Reciprocity during Ultrafast Laser Direct Writing

8.1 Introduction

With the recent observations of the origin of the blade effect discussed in Chapter 6 and how it is always present for a laser pulse with SC before the lens, it introduces a legitimate concern for the origin of the well-known quill-effect [4,5]. Alongside the recent advancements in SSTF and CPA technology, which uses spatial separation of the spectral components, it becomes apparent that the spatio-temporal induced phenomena is prevalent in all ultrafast laser-material interactions. While PFT is thought to be the origin for both the blade effect and quill-effect, there exists another widely neglected spatio-temporal coupling known as the wavefront rotation (*WFR*), which manifests itself as a lighthouse-like rotation of the beam's wavefront [126]. Only recently has WFR been utilized for generating high harmonics and angular separation of the successive attosecond pulses produced in the laser plasma [123,124]. Up until now, the effect of the WFR on the light-matter interaction has been visualized for the processes that take place in the attosecond (~10^{-18} s) timescale when the nonlinear optical response of the plasma is formed [147].

In this chapter, I demonstrate that the quill-effect is in fact due to PFT by analyzing all spatio-temporal couplings that exist during focusing in different conditions. I demonstrate the exact conditions in which the quill-effect can be observed, showing that it is easier to manifest itself on the much longer, sub-picosecond timescale associated with the femtosecond micromachining of transparent dielectrics. I quickly review past experiments discussing quill-effect and introduce concerns in the original experiments that discuss the phenomena. An evolution of spatio-temporal couplings in focusing is presented for the experimental conditions, which determines that PFT is the origin of the quill-effect. In addition, evidence of a PFT-triggered switching between two regimes of the material modification (damage-like and self-assembled nanogratings) is presented. This work was conducted in collaboration with Dr. Yuri Svirko and Dr. Charles Durfee. Dr. Durfee and myself worked alongside one another to provide the calculations for the propagation in focus calculations and Dr. Svirko provided the understanding behind the phase transition discussion. All other parts of experimental design, experiment and data analysis was conducted by myself.

8.2 Methods

The grating compressor SSTF design discussed in Chapter 4 is used to control the spatio-temporal couplings directly. TC and SC were separately controlled with two grating compressors, allowing one to precisely tailor the spatio-temporal properties of the beam (Fig. 8.1).

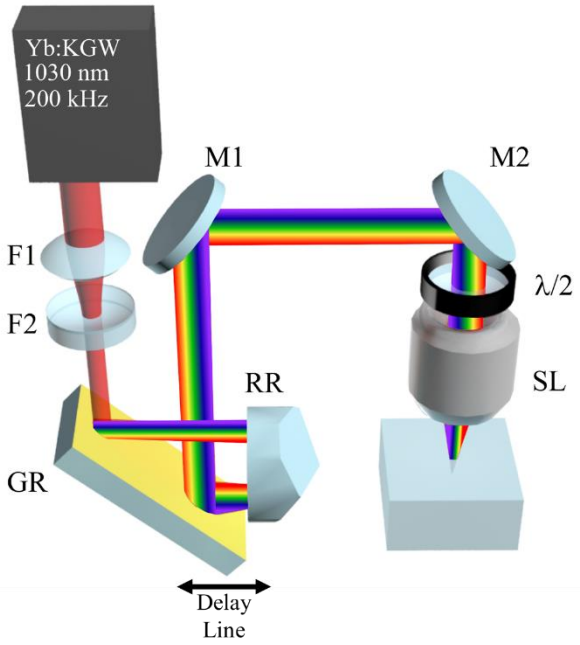

Figure 8.1: Sketch of the spatio-temporal control set-up. The first grating compressor that controls temporal chirp is integrated with the Yb:KGW laser system. The second compressor enables control of spatial chirp by changing the distance between the grating (GR) and a retroreflector (RR). A Galilean telescope made of two lenses of focal distances F1 = 200 mm and F2 = -100 mm is placed before grating GR to ensure that the laser beam is not clipped by the focusing lens rear aperture. A wide-field SSTF focusing geometry ensures a circular beam spot near the focus, despite spatial chirp introduced by the second compressor. In the sketch of the setup, the M1 and M2 are dielectric mirrors, λ/2 is the half-waveplate and SL is the focusing lens.

The second grating compressor was set to maintain a SC of ~1 nm/mm, resulting in a beam aspect ratio [171] of ~1.9 before focusing. Owing to refraction entering the sample, the effective beam aspect ratio is reduced inside to 1.52. The amount of residual spatial chirp introduced by the first compressor was negligible, being roughly ten times smaller.. The amount of residual spatial chirp introduced by the first compressor was negligible, being roughly ten times smaller. Angular dispersion was experimentally removed, thus achieving complete control of the spatio-temporal couplings in the beam. Additionally, a Galilean telescope was placed before the second grating

compressor to match the beam with the back aperture of the focusing lens. The SC value was chosen in order to maximize the SC but still be able to fit into the back aperture of the focusing lens without clipping the beam due to the ellipticity induced. The beam coming from the laser was reduced by a factor of two to a 1/e2 diameter of ~4 mm.

The laser beam was focused with a 0.55 NA aspheric singlet lens 60 μm below the surface of a fused silica substrate, which was mounted onto a XYZ linear air-bearing translation stage (Aerotech Ltd.). The stage was computer controlled via SCA software (Altechna Ltd.) to translate the sample at uniform speeds. The polarization orientation was set to be either parallel or perpendicular to spatial chirp with a λ/2 waveplate.

The spatial chirp was characterized by measuring the FRG with an optical fibre coupled spectrometer. The temporal chirp was monitored with an APE pulseCheck multi-shot autocorrelator. Measured values were confirmed by the Kostenbauder matrix formalism [127].

I studied the effect of the spatio-temporal couplings on micromachining for pulses with positive, negative and zero PFT. As stated previously, the FRG was held constant at ~1 nm/mm with the second grating compressor. In order to achieve PFT of the same magnitude and different sign, the pulse is stretched to ~3 ps yielding PFT at the focusing optics with a magnitude of ~ ±0.6 fs/μm by switching the sign of β ($\beta \sim \pm 1.1\times10^{-6}$ fs^{-2}). To achieve zero PFT, the first (built-in) grating compressor was set to get transform limited, spatially chirped ~400 fs long pulses ($\beta = 0$). In the cases with non-zero β, the WFR over the beamspot is approximately 0.05 mrad/ps (7.85×10^7 revolutions per second). When $\beta = 0$, the WFR is approximately 0.3 mrad/ps (4.7×10^8 revolutions per second). These values are a few orders lower than the WFR being utilized in attosecond generation and streaking [123,124,148], by exploiting the lighthouse-based movement in plasma. It should be noted that the experimental design controls WFR differently from previous studies where the WFR was induced due to angular dispersion of a large bandwidth source, resulting in the direction and large magnitude of WFR to be only dependent on angular dispersion [124].

The beam is then focused in a wide-field SSTF configuration, which yields a circularly symmetric focus despite ellipticity at the end pupil of the focusing lens caused by spatial chirp [181]. The pulse energies used in experiment were 3.5 μJ (3.7×10^{13} W/cm^2) and 2.5 μJ (2.7×10^{14} W/cm^2) for the beam with PFT = ±0.6 fs/μm and PFT = 0, respectively.

8.3 Results

A set of 100 μm long lines were written in the subsurface layer of the fused silica substrate by moving the sample at various speeds from 0.3 mm/s to 1 mm/s at PFT = 0.6 fs/μm (Fig. 8.2, 8.3).

Laser inscription was carried out aligning the direction of the light polarization both orthogonal and parallel to the writing direction. The experiments revealed that the writing process is “non-reciprocal” in a sense that the silica glass was modified differently when the writing direction was reversed. Specifically when the translation stage moved the substrate in one direction, an isotropic damage-like modification with evidence of melting and crack formation abruptly changed to the formation of the birefringent nanograting structure after travelling a certain distance. However, no such change took place when the substrate was moving in the opposite direction. A drop in white-light emission is also observed at the point of transition during laser writing, indicating that the damage-like modification is associated with stronger white-light emission.

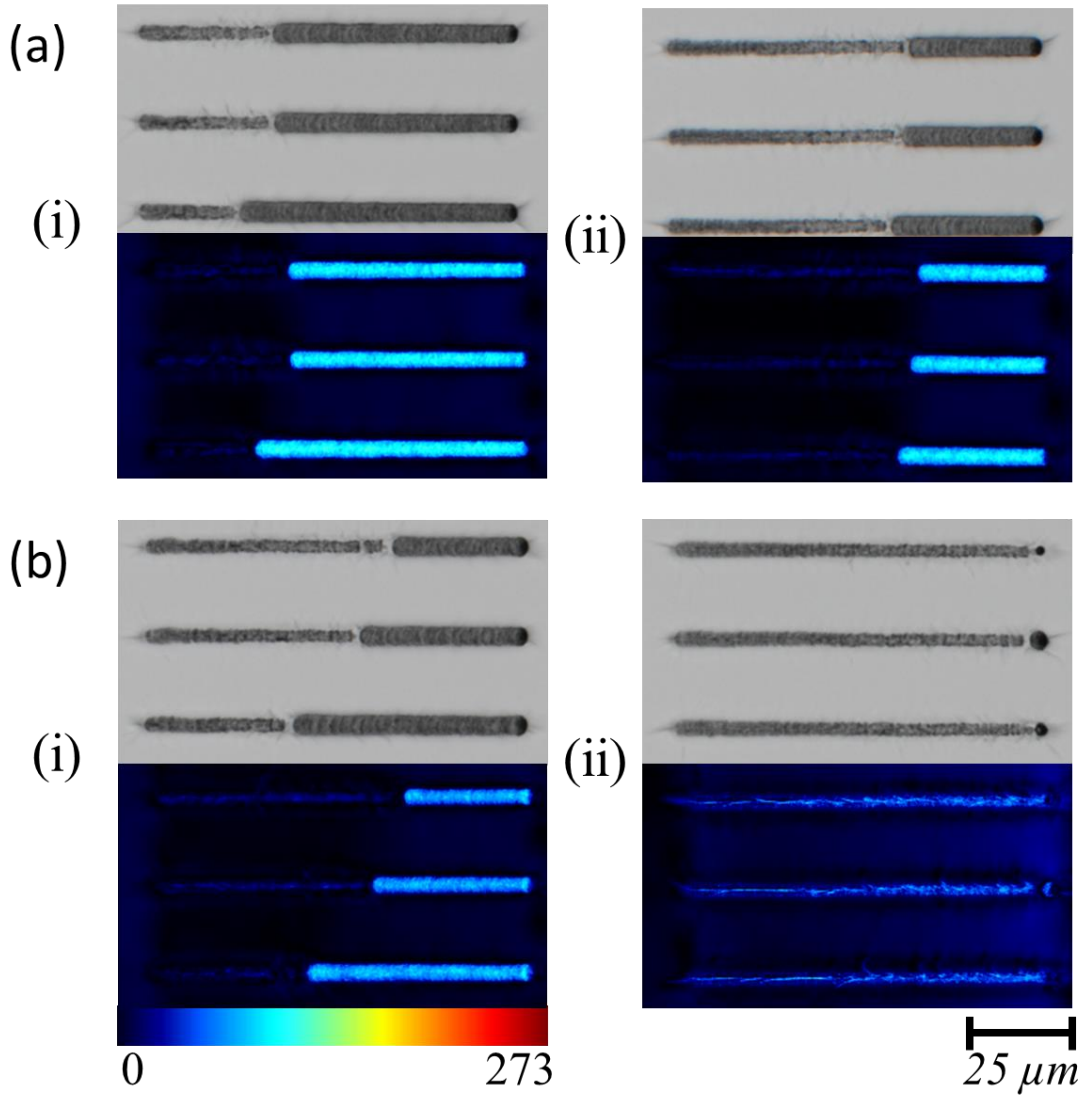

Figure 8.2: Comparison of transition (i) with and (ii) without stage jitter (writing speed = (a) 0.5 mm/s (b) 1 mm/s). The regime transition occurs unpredictably in the vicinity of fluctuations during the writing process. When the fluctuations are removed, the transitions occur at the same point based upon writing speed and beam parameters.

The induced birefringence is seen in the illuminated sections of the lines in the birefringence measurement images (colour bar scale for retardance in nm). Polarization is parallel to the writing direction in all cases.

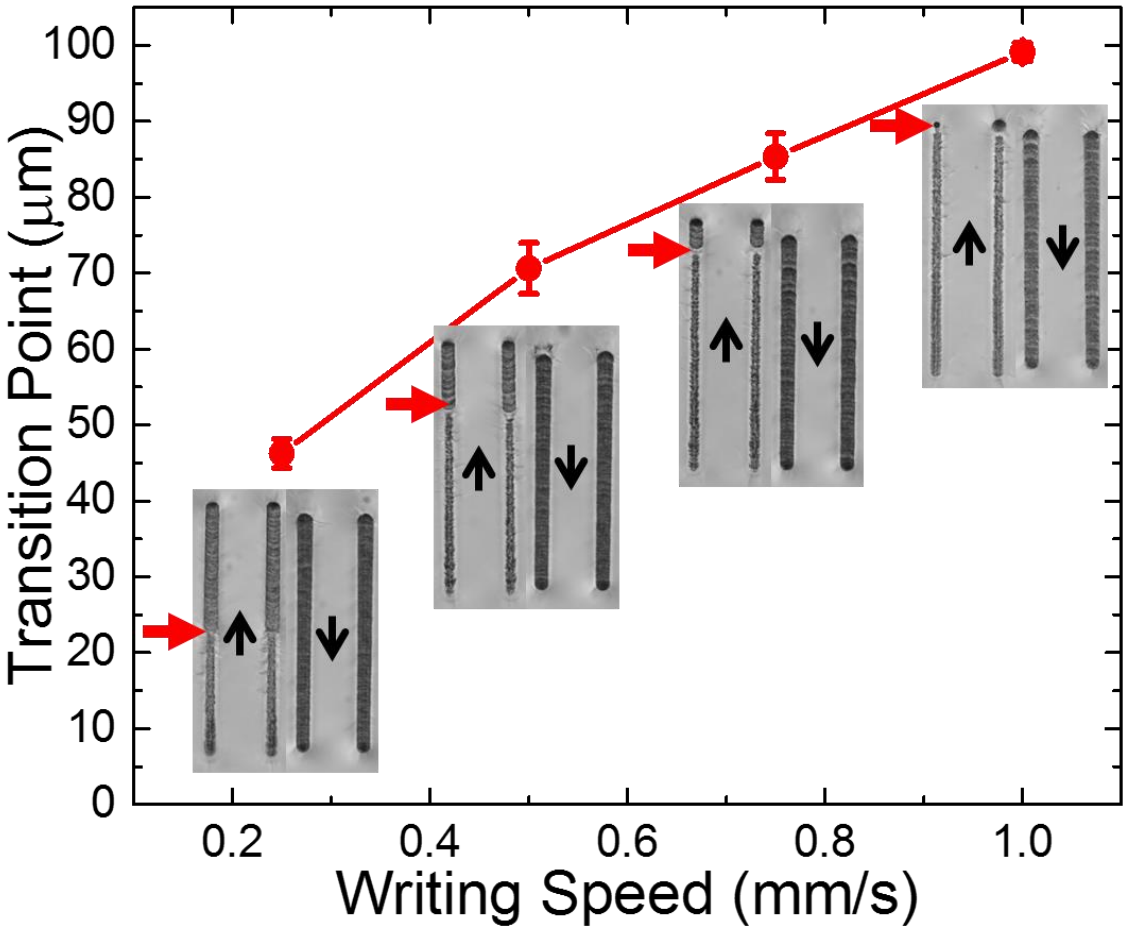

Figure 8.3: The transition point dependence on writing speed. The transition between the damage-like modification and form birefringence (red arrows) occurs at a later distance and scales linearly with the writing speed. Nanograting formation is seen across the entire line when writing in the opposite direction.

The change from one modification regime to another is more apparent when the inscribed line is imaged with the quantitative birefringence measurement system (CRi Abrio; Olympus BX51), with the bright areas of the line representing the nanograting formation (Fig. 8.2a, b). The transition between the two regimes is initiated by fluctuations during the laser writing process. In the experiments, these fluctuations arise in the jitter of the writing stages when insufficient time is given for the stage to stabilize after moving from one line to another. During laser writing, the laser turns on once the stages reaches the set writing speed. This entails particular acceleration and deceleration ramps, alongside the appropriate stops when changing from line to line. If the deceleration ramps and full stops are not set correctly, the stage does not have sufficient time to settle resulting in a stage jitter. As more lines are written, the jitter becomes more substantial resulting in the transition to occur earlier. Even with the appropriate acceleration ramps and

stops, the transition can be initiated by vibrating the writing stage manuallyIt is worth noting that at the same writing speed, suppression of the fluctuations leads to the delay in the modification regime change (Fig. 8.2a(ii), b(ii)).

After sufficient time to minimize the jitter is provided, the moment of the modification regime change is determined only by the beam parameters (laser fluence, intensity, etc.) and writing speed (Fig. 8.3). The modification regime change occurs earlier at slower writing speeds when the beam moves in one direction (up arrow in Fig. 8.3). On the contrary, for lines written by the beam moving in the opposite direction (down arrow in Fig. 8.3), no regime change is observed (i.e. nanograting forms from the start to the end of all the lines).

To demonstrate that fluctuations instigate the change of the modification regime, “seed” tracks were written orthogonal to the writing direction. The scattering of the writing beam results in a sudden drop of fluence when the writing beam crosses the track (Fig. 8.4). When the seed track is not present, the modification regime transition does not occur or happens near the end of the line, depending on the beam polarization (Fig. 8.4, transition point denoted by red arrow). When the seed is present, the transition occurs exactly where the beam crosses the track, regardless of the difference in depth between the seed line and written track or electric field orientation. This indicates that a fluctuation in fluence caused by the scattering on the track is sufficient to instigate the change of the modification regime.

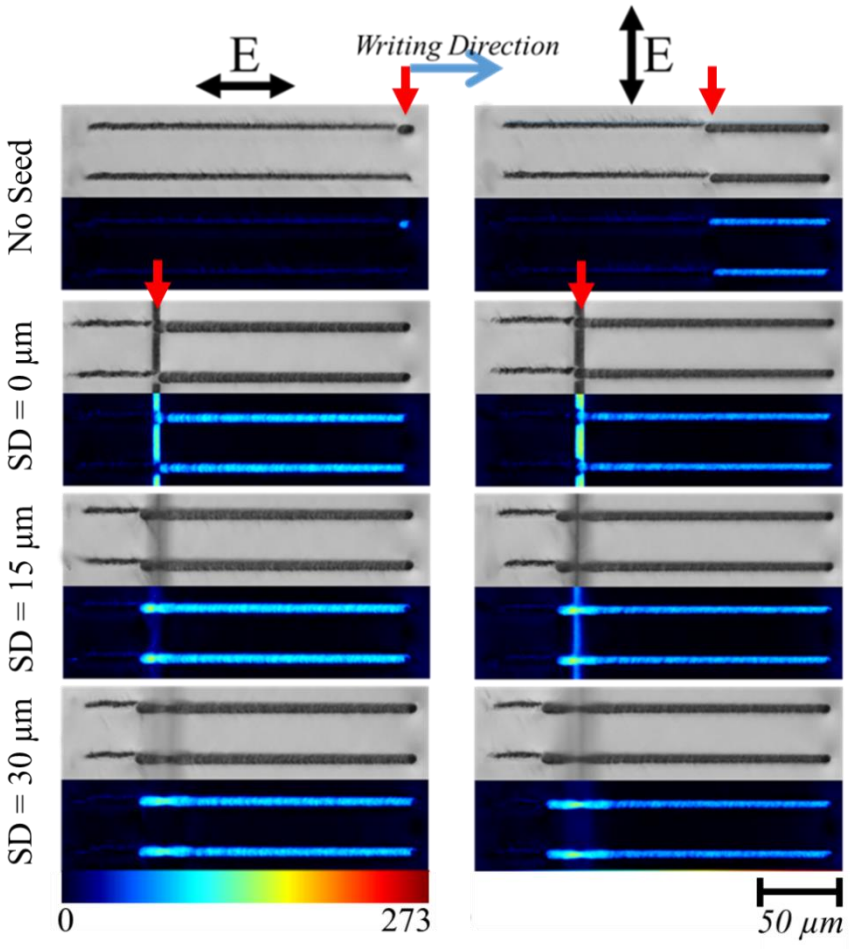

Figure 8.4: Instigating the damage-like modification to self-assembled nanograting transition with seed lines at different seed depths (SD). 200 µm length lines written at 1 mm/s with 3.5 µJ pulses. Regardless of the SD, the transition (red arrows) occurs when the laser line hits the pre-written seed, instigating the transition earlier than when there is no seed present. As the laser light interacts with the pre-written seed, the light is scattered effectively acting as a drop in pulse energy during laser writing. The drop in pulse energy experienced illustrates how minor fluctuations instigate the process.

The dependence of the quill-effect on the spatio-temporal coupling was studied by comparing optical microscope images of the lines inscribed in the bulk of the fused silica as positive, negative and zero temporal chirp, by writing along and against the tilt direction (Fig. 8.5a). Directional dependence is clearly observed when temporal chirp is negative (i.e. PFT > 0 before the lens). Nanograting formation is observed when writing along the tilt direction, with strong polarization dependence (Fig. 8.5b). Damage-like modification is observed when the writing is against the tilt direction (Fig. 8.5b). At zero temporal chirp (i.e. PFT = 0 before the lens), no discernible directional dependence is evident, confirming previous studies [166] (Fig. 8.5c). When temporal chirp is positive (i.e. PFT < 0 before the lens), the directional dependence re-emerges but does not flip with the PFT (Fig. 8.5d). Isotropic damage-like modification occurs when moving along the tilt and

nanograting formation is seen when moving against the tilt, contradicting the original interpretation of the quill-effect.

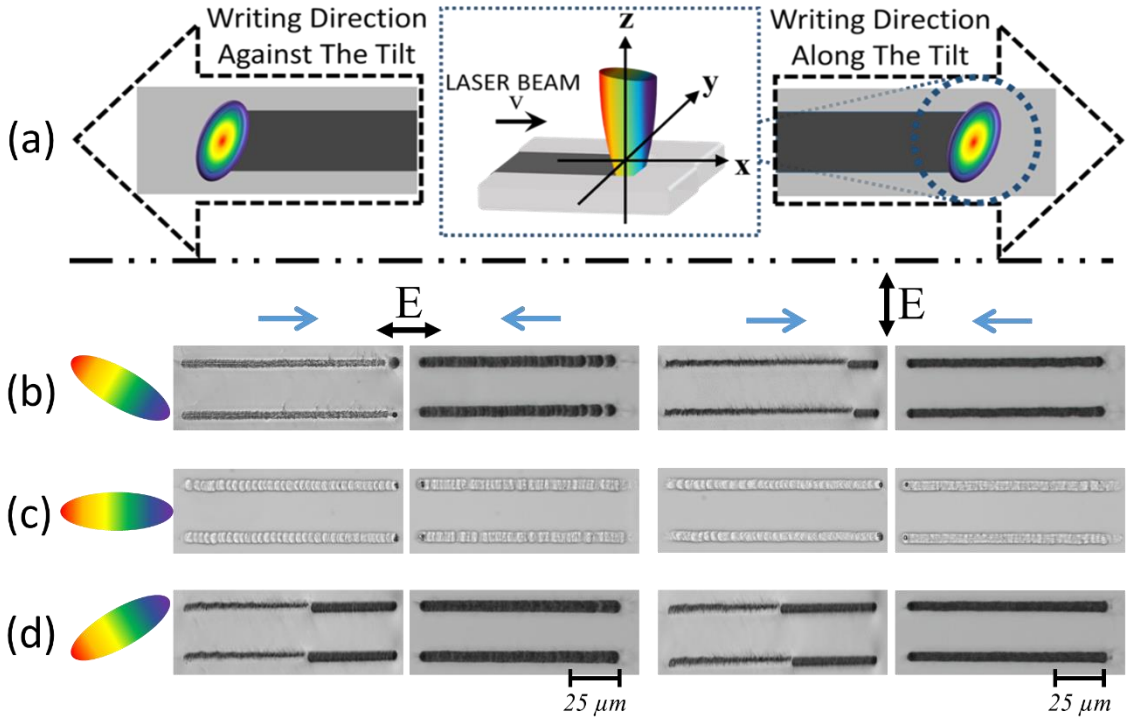

Figure 8.5: Directional dependence on writing for 3 different spatio-temporal coupling cases (Writing Speed = 1mm/s). (a) Schematic diagram indicating orientation of PFT with respect to writing direction (black dashed arrows), depicting how lines are inscribed in the direction along and against the tilt. (b) Negative β (PFT = 0.6 fs/μm, pulse energy is 3.5 μJ). Directional dependence is observed with nanograting formation when moving along the tilt and damage-like modification transitioning to the nanograting state in the opposite direction. (c) β = PFT = 0 (2.5 μJ). No directional dependence is evident with non-uniform nanograting modification in both directions. (d) Positive β (PFT = -0.6 fs/μm, 3.5 μJ). The directional dependence of writing does not reverse with the change in PFT orientation, even though the quill-effect disappears when PFT = 0.

It is worth noting that both femto- and picosecond pulses induce comparable birefringence. However, the modified area created at longer pulse durations is noticeably darker when viewed under the optical microscope (Fig. 8.5b, d vs. Fig. 8.5c). Specifically, transmission measurements using a VIS microspectrometer at 546 nm revealed 90-95% and 28-39% transmission yielded from femto- and picosecond pulses, respectively. Such a remarkable difference originates from the scattering and the development of stress regions surrounding the lines incurred with picosecond pulses [168].

8.4 Discussion

The unexpected observation of the directional dependence not following the direction of PFT (Fig. 8.5) re-opens the discussion in what spatio-temporal couplings reside in the focus during laser-matter interaction. In previous studies reporting on the quill-effect, the sign of the PFT was changed either by hologram-based methods [166] or by adding an additional mirror to the beam path [5]. Both of these methods changed either the orientation of the spatial chirp, angular dispersion or simply flipped the entire beam with all associated spatio-temporal couplings, which would correspond to the positive β (PFT = 0.6 fs/µm) and β = PFT = 0 cases in experiment. In the one experiment that suggested that the quill-effect flipped with the sign of β, it becomes clear that the spatio-temporal couplings were much more complex than suggested [5] (Fig. 8.6). The PFT was thought to be flipped by simply tuning the compressor in the original experiment and by flipping the PFT sign. Upon further review, the pulse duration and SC were the same in both cases but the PFT doubled in magnitude. This suggests that an additional term (potentially AD) was added to the beam before focusing. Moreover, further review of the SC value quoted in the Yang et al. study [5] is unphysical. However, in our experimental conditions, the magnitude and direction of the PFT is controlled without affecting the SC. In this case, despite the strength of the quill-effect being proportional to PFT, its sign before the lens does not affect the nonreciprocal behaviour.

Figure 8.6: The quill-effect was thought to have flipped due to a change in sign of the TC. However, the PFT doubles in magnitude while the SC stayed constant. Upon further review, the SC value is unphysical, thus re-opening the discussion on what causes the quill-writing effect. Image source: Yang et al. [5]

In order to describe spatio-temporal couplings in the Gaussian laser pulse propagating along the z-axis, it is convenient to present the electric field in the following form [126]:

$$E(x,t) \propto \exp\{\tilde{Q}_{xx}x^2 + 2\tilde{Q}_{xt}xt - \tilde{Q}_{tt}t^2\} \tag{8.1}$$

where the y-dependence of the electric field is suppressed. The complex parameters $\tilde{Q}_{xx} = -1/a^2 - ik/2R$ and $\tilde{Q}_{tt} = 1/\tau^2 - i\beta$, where *a* is the beam spot size, *k* is the wavevector, *R* is the wavefront curvature, τ is the pulse duration, and β is the temporal chirp, describe the spatial and temporal characteristics of the beam, respectively. GDD is also determined by $\tilde{Q}_{tt}$, i. e.

$$GDD = \frac{1}{2}\mathrm{Im}\left[\frac{1}{\tilde{Q}_{tt}}\right] = \frac{\beta\tau^4}{2(\beta^2\tau^2+1)} \tag{8.2}$$

One can observe from Equation (8.2) that while GDD and β are representative of the same quantity for Gaussian pulses, conversion from one to the other requires the pulse length.

The spatio-temporal couplings are represented by the complex parameter $\tilde{Q}_{xt}$ in Equation (8.1). The experimental observables can then be presented as the following [120]:

$$AD = \mathrm{Re}\left[\frac{\tilde{Q}_{xt}}{\tilde{Q}_{tt}}\right] \tag{8.3}$$

$$FRG = \frac{2\mathrm{Im}[\tilde{Q}_{xt}.\tilde{Q}^*_{tt}]}{\mathrm{Re}[\tilde{Q}_{tt}]} \tag{8.4}$$

$$PFT = \frac{\mathrm{Re}[\tilde{Q}_{xt}]}{\mathrm{Re}[\tilde{Q}_{tt}]} \tag{8.5}$$

$$WFR = \mathrm{Im}[\tilde{Q}_{xt}] \tag{8.6}$$

It is worth noting that in the Gaussian pulse with spatial and temporal chirp, the experimentally observable parameters are dependent on one another. In particular, by combining Equation (8.2-8.6), the following relations can be found:

$$PFT = (FRG \times GDD) + AD \tag{8.7}$$

$$WFR = \frac{1}{2}FRG - \beta \times PFT \tag{8.8}$$

Thus, in order to control the propagation direction of the wavefront (i.e. WFR) and the intensity front (i.e. PFT) in the beam, it is necessary to suppress angular dispersion in the beam. At *AD = 0*, Equation (8.7) and (8.8) becomes:

$$PFT = \frac{FRG \times \beta\tau^4}{2(1+\beta^2\tau^4)} \tag{8.9}$$

$$WFR = \frac{FRG}{2(1+\beta^2\tau^4)} \tag{8.10}$$

Therefore, the direction of the WFR follows the FRG, while the sign of PFT depends on both FRG and β.

One can observe from Equation (8.9-8.10) that the PFT and WFR do not change sign under reversal of the writing direction because the spatial chirp (i.e. the value of FRG) remains unchanged [126]. However, the magnitude of WFR decreases with PFT. When β = 0, WFR = FRG/2 is at a maximum, but directional dependence of writing is not observed (Fig. 8.5c). In contrast, the directional dependence is observed when the WFR before the lens is slower (Fig. 8.5b, d). Specifically, when β ~ 1.1×10 6 fs^{-2} , FRG = 1 nm/mm and PFT = 0.6 fs/μm, the WFR over the beamspot is approximately 0.05 mrad/ps (7.85 × 10^7 revolutions per second). When β = 0, the WFR is approximately 0.3 mrad/ps (4.7 × 10^8 revolutions per second). The physical rotation of the wavefront during the pulse is 0.09 mrad and 0.165 mrad at β ~ 1.1×10 6 fs^{-2} and β = 0, respectively. These values are a few orders lower than the WFR being utilized in attosecond generation and streaking [123,124,148], by exploiting the lighthouse-based movement in plasma. It should be noted that in contrast to our experimental set-up (Fig. 8.1), in previous studies WFR was induced due to angular dispersion of a large bandwidth source before the lens, resulting in the direction and large magnitude of WFR to be only dependent on angular dispersion [124].

It is worth noting that WFR would still be dominated by FRG before the depth of focus making the direction of rotation unchanging in the focused beam. In order to illustrate this, simulations were performed for a 15 fs pulse (we considered a short pulse duration to enhance the effect) (Fig. 8.7). When plotting the contours of the phase along focusing, it can be seen that for large values of β (GDD = 700 fs^2), the arrival of the spectral components is sheared out in time similar to what would be observed for CW Gaussian beams (Fig. 8.7a). When β = 0 (GDD = 0), the curvature of the wavefronts is enhanced from the angular variation of the different spectral components (Fig. 8.7b). In the context of the experimental conditions, the enhancement would be much smaller at 400 fs and even smaller at 3 ps, effectively being sheared out in time. This allows us to conclude that in our experimental conditions, rotation of the wavefront during the pulse unlikely affects the inscription process in the bulk silica glass. Therefore, WFR cannot be the origin of the writing asymmetry effect making PFT the remaining spatio-temporal coupling, which could cause the directionally asymmetric writing.

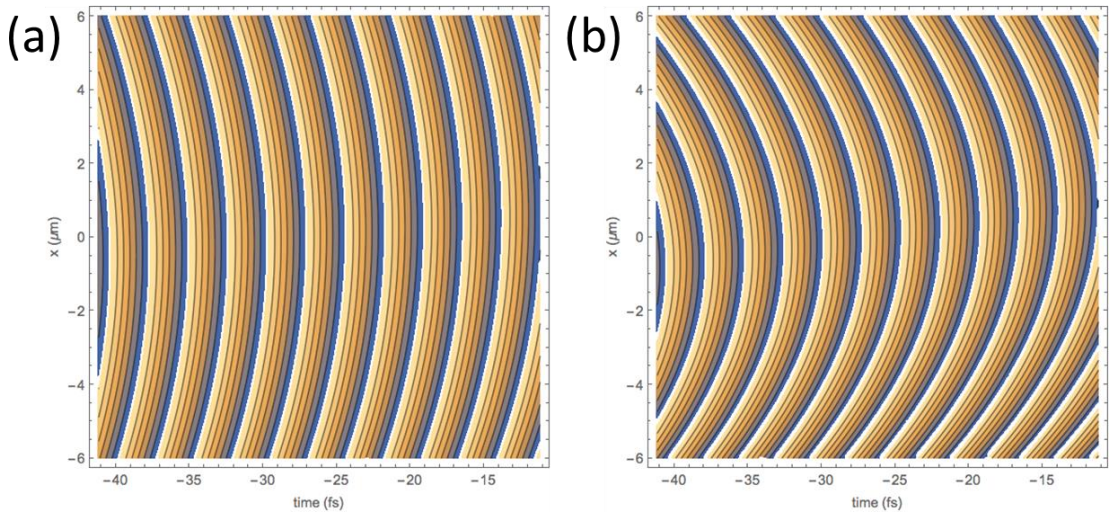

Figure 8.7: Contour plots of wavefronts (Im[log[E(x, t)]) at axial position $z = z_R/2$ (z_R is the Rayleigh range). (a) GDD = 700fs^2. Each frequency component arrives at a different time, so this curvature matches a Gaussian CW beam description. (b) GDD = 0. Frequency components are superimposed and the angular variation of the beam with SC enhances the wavefront curvature. Pulse duration is set to 15 fs for the sake of illustrating the wavefronts.

It is important to understand that PFT is affected by focusing [181,199,226]. Recently it has been shown that regardless of the state of a spatially chirped beam before the lens, the intensity front will always be tilted at the focus [171,200] and is dependent on the spatial chirp at the lens entrance and the focal beam waist [171]. Using the formalism developed in Ref. 171, we performed the analysis of the evolution of PFT along the propagation direction in and out of the focal plane, as a function of GDD (Fig. 8.8). One can observe from Fig. 8.8 that for when PFT > 0 before the lens (red line, GDD ~ 4.5×10^5 fs^2), PFT increases as a function of the axial position along focusing. To understand the non-monotonic dependence of the PFT on the axial position, one can recall that since AD = 0 before the lens, *PFT = FRG* × *GDD* (Equation (8.7)), i.e. tilt of the intensity front is due to the combination of spatial and temporal chirp. Focusing results in a finite AD and the spectral components begin to overlap as the beam spot shrinks. This increases the FRG and hence both terms in Equation (8.7) contribute to the PFT, which grows rapidly. However, once the beam reaches the Rayleigh range of the focusing optic (depth of focus), the beamspot no longer shrinks as the spatial components continue to overlap. At the focus, FRG = 0 and the second term in Equation (8.7) dominates resulting in *PFT* ≈ *AD* ≈ -200 fs/μm. For the PFT < 0 case (blue line, GDD ~ -4.5×10^5 fs^2), the evolution of PFT is flipped at the focal plane. When PFT is zero before the lens (green line, GDD = 0), it remains zero out of the Rayleigh range but at the focus the PFT due to angular dispersion becomes evident, maximizing in magnitude at the focus to the same value (*PFT* ≈ -200 fs/μm) as seen in the cases with non-zero GDD.

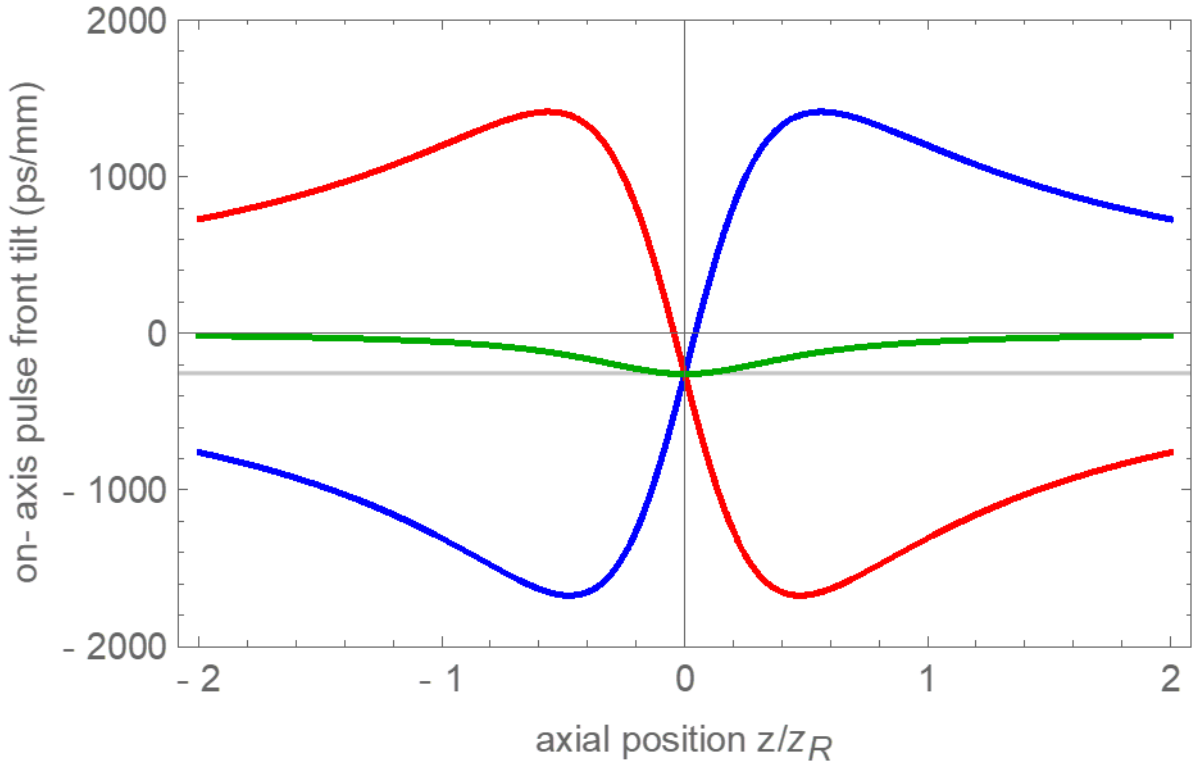

Figure 8.8: Evolution of PFT along focusing for the three different PFT cases. In the case of positive PFT before the lens (red line), the PFT maximizes as the beamspot shrinks making FRG maximum before the focal plane of the lens. At the focal plane, the spectral components overlap making FRG = 0. Angular dispersion dependent PFT dominates at the focus (PFT ≈ -200 fs/µm). In the case of zero GDD (and thus zero PFT before the lens, green line), the PFT remains small along the optical axis except near the focal plane where the PFT depends only on the AD. For the negative PFT before the lens case (blue line), the evolution is similar to the positive case but flipped along the focal plane.

Therefore in our experimental conditions, both the zero and non-zero PFT before the lens cases result in the same PFT in the focal area. The question arises why the asymmetry in laser writing was observed at non-zero PFT (Fig. 8.5b, d) and was not observed at zero PFT (Fig. 8.5c), alongside why the directional dependence does not flip when PFT changes sign. To explain this, one needs to take into account that in our experimental conditions, at the laser fluence in the focal plane of about ~10^2 J/cm^2, the maximum focal intensities are ~10^2 TW/cm^2 and ~10^3 TW/cm^2 at non-zero and zero PFT, respectively. This drastic difference in intensity indicates that modification of the silica at zero and non-zero PFT takes place at different distances from the focal plane. Comparing the relative intensities for the different PFT cases as a function of the square root of the pulse duration (Fig. 8.9), the PFT = 0 case (Fig. 8.9, green line) reaches the same intensity as the non-zero PFT cases (Fig. 8.9, red and blue lines) before the focal zone (~z_R). Thus, the beam with zero PFT before the lens enables ionization and material deformations at z_R where the PFT during

focusing remains close to zero (Fig. 8.9, green line). In this situation, the intensity front is perpendicular to the beam axis and no directional asymmetry in the laser writing may emerge when β = 0.

When PFT before the lens is non-zero, the modification would take plane near the focal plane (i.e. the picosecond pulses deposit energy closer to the focus [168]). One can observe from Fig. 8.8 that PFT in the focal plane is independent on the sign of β, being entirely due to the angular dispersion from the lens. Therefore, the inscription of the lines written within the bulk of the fused silica takes place at the same PFT ≈ -200 fs/µm. This explains why the asymmetric writing behavior does not flip when the sign of PFT before the lens changes.

It is worth noting that in order to observe directional dependence at β = 0, the intensity at the focal plane needs to be similar to that seen for the non-zero PFT cases (i.e. pulse energy decreased by a factor of 3). However at such low intensities, nanogratings may form provided the writing speeds are low but the damage-like modification would not occur, making it difficult to observe the asymmetrical writing behavior.

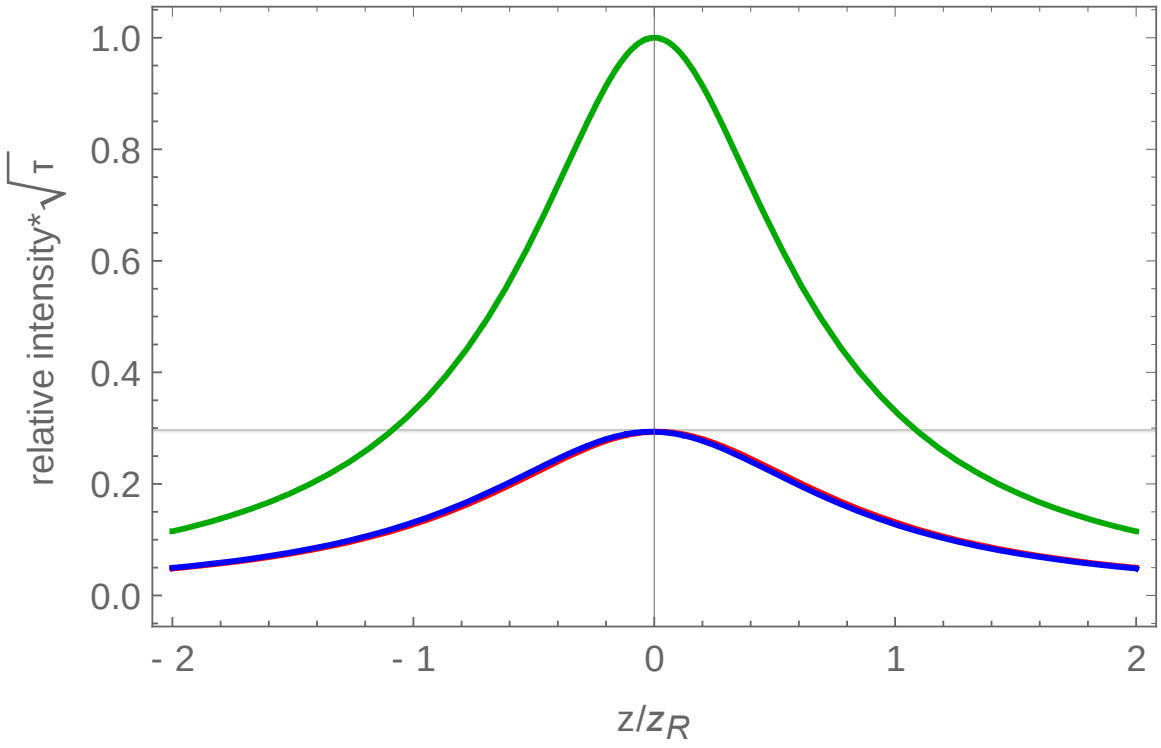

Figure 8.9: Relative intensity threshold evolution during focusing for the three PFT cases. The zero PFT case (green line) is larger by a factor of 3 than the non-zero PFT cases (PFT > 0 - red line, PFT < 0 – blue line). The grey line indicates where the non-zero PFT cases reach their max intensity and threshold for modification. The zero PFT case reaches that same threshold at zR in front of the focus where PFT is minimal. To reach the same threshold at the focus, the pulse energy for the zero PFT case must

be decreased by a factor of three. The location of maximum intensity for the non-zero PFT cases are slightly shifted from the focus, depending on the sign of the temporal chirp.

The observed switching of the modification regime from the formation of the isotropic damage to the formation of the nanograting when writing and tilt direction coincide (Fig. 8.5b, d) is a very interesting scientific finding. It can be thought of in terms of a first-order phase transition [227] (Fig. 8.10) where latent heat is needed to initiate the transfer from one material phase to another. Using this analogy, the switching of the modification regimes can be seen as a phase transition in the modified region between an isotropic damage-like state (Fig. 8.10, (1)) and a nanograting state (Fig. 8.10, (2)). Following the Landau theory, we can introduce the free energy of the modified region as the following:

$$F = a_1\eta^2 + a_2\eta^3 + a_3\eta^4 \tag{8.11}$$

Here $\eta > 0$ is the order parameter, which describes the form-birefringence in the modified region and a_1, a_2 and a_3 depend on the energy, writing speed and other beam parameters. In the experiment, it is natural to assume that the absorbed energy, W, of the laser pulse determines the state of the modification. In the framework of the Landau theory, we can assume that $a_1 = \alpha(W-W_0)$, where $\alpha > 0$ is constant and W_0 determines the absorbed energy that corresponds to the stable state with $\eta > 0$ (i.e. form birefringence in the modified region). The theory of the first-order phase transition states that at high intensities ($W \gg W_0$), $\eta = 0$ is the only solution that minimizes the free energy [227] (Equation (8.11)). Moreover, when $a_2 > 0$, there are no other positive η to satisfy the equation.

$$\frac{\partial F}{\partial \eta} = 2a_1\eta + 3a_2\eta^2 + a_3\eta^3 = 0 \tag{8.12}$$

When $a_2 < 0$, another solution of Equation (8.12) that corresponds to the minimum of the free energy is permitted:

$$\eta_1 = \frac{1}{8a_3}\left(3|a_2| + \sqrt{9{a_2}^2 - 32a_3\alpha(W - W_0)}\right) \tag{8.13}$$

This solution exists at $W < W_1$ where:

$$W_1 = W_0 + \frac{9{a_2}^2}{32a_3\alpha} \tag{8.14}$$

However, this solution, which represents the damage-like state, is unstable until the free energy is positive (i.e. the free energy exceeds the free energy of the damage-like state, $F(\eta_1) > F(\eta_0) = 0$). When the absorbed energy decreases down to:

$$W_2 = W_0 + \frac{{a_2}^2}{4a_3\alpha} \tag{8.15}$$

the free energy of the damage state eventually becomes equal to that of the nanograting state. In other words, the first order transition between the damage and birefringent state occurs. As intensity decreases further, the nanograting state becomes metastable and finally, at $W = W_0$, there is no local minimum of the free energy at η = 0 (damage-like state is forbidden).

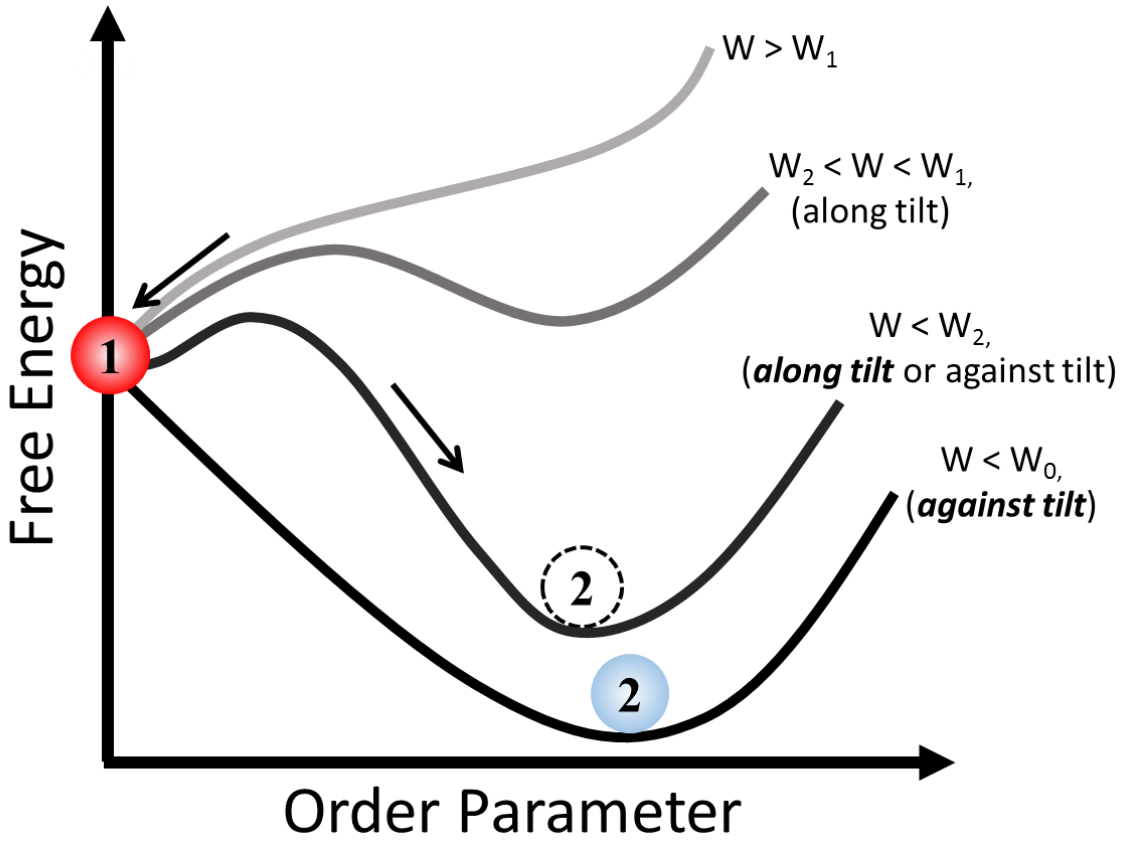

Figure 8.10: First-order phase transition interpretation for the switching of the modification regime from an isotropic damage-like state (1) to the nanograting state (2). When the absorbed energy, W, exceeds the damage like state threshold, W_1, the damage-like state corresponds to the absolute minimum of the free energy (i.e. the writing produces the damage-like modification of the substrate). When $W_2 < W < W_1$, the damage-like state at η = 0 is energetically favorable. However, there is a local minimum of the free energy at $\eta = \eta_1$, which is associated with the metastable nanograting state. When the absorbed energy decreases further $W < W_2$, the absolute minimum of the free energy corresponds to the grating state. In such a case, the damage-like state becomes metastable. That is a fluctuation in the writing

process can add an activation energy necessary to switch from the isotropic damage-like to the birefringent nanograting state. At $W<W_0$, the free energy has only a minimum, which corresponds to the formation of the nanograting.

In our phenomological phase transition model of the ultrashort pulse modification, the absorbed energy is equivalent to temperature in the Landau phase transition theory. For writing along the tilt, when the absorbed energy is higher than writing against the tilt, we observe the metastable damage-like state converted into the nanograting state when an activation energy is supplied to the system (i.e. via fluctuation in the incident fluence). Remarkably, the transition takes place without a change in the absorbed energy. This is similar to the freezing of supercooled water that is not accompanied with a change in temperature. By further exploring this analogy with respect to the damage-like to nanograting switching and the first order phase transition, there should be an analog of latent heat, which is released into the system similar to the water freezing process. This "latent heat" in the femtosecond laser writing process may be associated with the energy consumed in the formation of nanovoids in the damage-like state or released as potential energy of the electrons clustering in the formation of nanogratings. The latter is supported if one assumes that white light accompanying the modification originates from the thermal emission of electrons or Bremsstrahlung emission. Correspondingly, the drop in white-light emission observed in the nanograting regime may indicate that the kinetic energy of electrons is converted into potential energy associated with the charge separation (clustering) of the plasma producing the nanograting.

It is worth noting that the observed switching from the damage-like to nanograting modification is different from the transition and self-healing process of nanogratings that is dependent on the randomness of crack initiation in glass [228]. This transition can revert back from one state to another simply by continuing the writing process, while the transition observed in our experiment is irreversible.

The directional asymmetry in laser writing was originally interpreted based on an anisotropic trapping of electron plasma due to a ponderomotive force [4,5], when the pulse front is tilted in the writing direction. The issue with this explanation is the need of large intensities at the focal plane to observe an effective "snow-plow" displacement of electrons [84,229,230], which are thought to be difficult to reach in the material due to a laser induced plasma clamping effect [170]. However, it has been determined that in tight focusing regimes (NA > 0.4), voids appear within the first few pulses [101,231,232]. The voids eventually transition into self-assembled nanogratings after further irradiation [231]. Evidence in previous publications suggest that voids could be potentially created within the first few pulses and then trapped or constantly

collapsing and reforming during the writing process, resulting in a void at the end of an inscribed line [5,89,95,233] (Fig. 8.11). The formed void could interact with the intensity front differently depending on the orientation of the tilt. We suggest that two different forces govern the behavior of this void during laser writing. The first one is the gradient force in the tilted front that could push the void out of the region of high intensity. The second is a thermocapillary force, which pushes the void into the region of high temperature and intensity (Marangoni effect) [234]. When the laser writing is in the direction against the tilt (Fig. 8.11 left), the thermocapillary force traps the void in the horizontal direction, confining it in the high temperature region. As writing continues, the void could move towards the head of the structure, increasing the scattering and promoting nanograting growth. When the laser writing is in the direction along the tilt (Fig. 8.11 right), the void is again formed near the focus of the beam and is trapped in the horizontal direction by the thermocapillary force. As the writing continues, the gradient force from the tilted intensity front keeps the void from moving vertically (i.e. gradient force > thermocapillary force), forcing it to stay near the focus. This allows the following pulses to remain unperturbed, interacting with pristine material to ensure efficient energy deposition. Writing in this direction produces the damage-like modification, which results in a metastable, "supercooled" state of modification. As the writing length increases, an instantaneous transition from the damage-like to nanograting modification takes place. This indicates that the seed necessary for nanograting growth could be produced after a certain incubation length, as seen by the dependence of the transition point as a function of the writing speed (Fig. 8.3). In other words, writing along the tilt results in a continuous change of an unknown (or "dark") parameter, which is not revealed in the appearance of modification. It is possible to speculate that this "dark" parameter could be the result of the void increasing in size or a generated charge as the laser writing continues. The void could continue to grow as more pulses are deposited into the bulk while the void is trapped within the focal region. The void would reach a critical size where it could either overcome the forces trapping it and allowing the void to move towards the head of the structure or the void could explode/collapse. With respect to the charge scenario, the charge could be produced by diffusion of electrons from the region of high intensity in the focus of the beam [235,236] or dragging of the weakly trapped void similar to an electrostatic charge generated by flowing liquids [237]. The charge would accumulate to a critical value as writing length increases until it reaches the governed incubation length when it promotes the void and nanograting formation. These scenarios allow the critically sized void or generated charge to interfere with the laser irradiation where it would incur scattering and instigate the transition to nanograting formation. However, the noted incubation length associated with the transition and what causes and governs it is still up for debate.

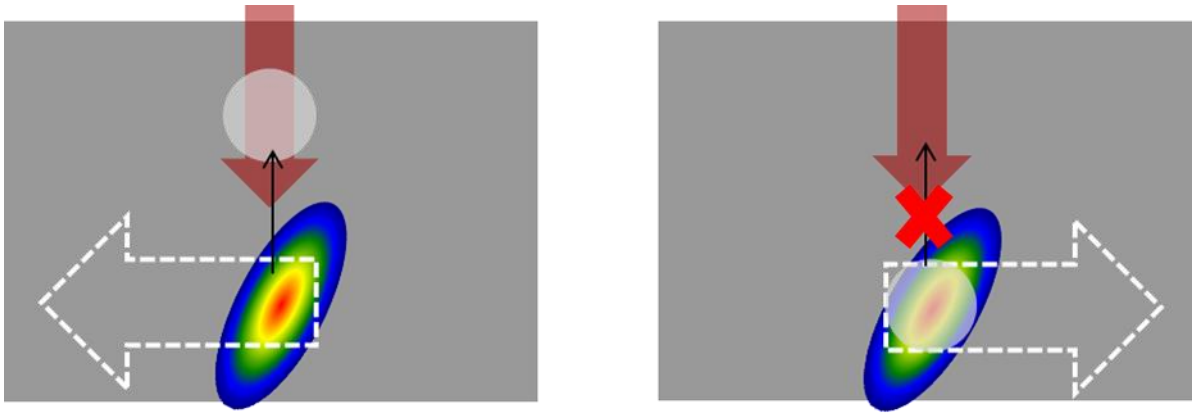

Figure 8.11: Schematic diagram of potential void-trapping mechanism for the directional asymmetric writing effect. During the writing process, voids are formed initially and are subsequently trapped by a combination of forces. If the beam translation is against the tilt (left), thermocapillary forces trap the void in the horizontal direction. However, the void could move towards the head of the structure limiting the energy deposition due to scattering and promoting nanograting growth. If the beam translation is along the tilt (right), the void is again trapped by thermocapillary forces but is also forced to stay near the focus by the gradient of the tilted intensity front. This allows the following pulses to interact with pristine material, allowing for stronger energy absorption. As writing continues, the instantaneous transition from the damage like state to the nanograting state occurs after a noted incubation length. This transition could be the result of the void growing to a critical size or a generated charge from dragging a trapped void where it would scatter the incoming laser light after the noted incubation length, triggering the transition.

Therefore, the conditions for strong energy absorption could be achieved by controlling the PFT of ultrashort laser pulses and writing in the direction along the tilt. Previous laser writing experiments have stated that typically 40-60% of the laser energy is consumed from absorption, reflection and scattering depending on the experimental conditons [168,232]. We speculate based on the thresholds for damage-like modification, writing along the tilt direction provides a 5-15% increase in energy absorption as opposed to writing against the tilt direction, which can be proven useful in the manufacturing of optical elements using ultrafast laser writing. However, it depends on the application whether it is advantageous to laser write with a tilted intensity front. If there were a need for uniform modification of the same strength/state regardless of direction, then it would be advantageous to laser write in a regime where there is zero PFT. One way to ensure this is by laser writing within the bulk where it is expected that PFT is zero by choosing the appropriate intensities, similar to the zero PFT case in experiment. Another way is to remove all spatio-temporal couplings of the beam before the focusing optic. While conceptually

straightforward, in practice it is difficult to work in a regime of zero PFT. Any laser that has a built-in chirped pulse amplification design can produce residual spatio-temporal couplings due to slight misalignments [238], which can lead to strong asymmetries in writing. In order to choose the appropriate laser intensity where PFT is zero, a thorough understanding of the spatio-temporal properties is necessary. Since the identity of these spatio-temporal couplings can be quite complicated (i.e. spatial chirp, angular dispersion, higher-order dispersion, etc.), it is difficult to characterize effectively. To correct for them, complicated diffractive element-based designs of SLM methods are necessary. Alongside that, the concept of SSTF in laser writing is to produce stronger modification closer to the focus, which would result in PFT at the focus [113,238]. Therefore, it might be advantageous to use PFT as an extra degree of freedom in direct laser writing. By understanding the mutual orientation of the PFT with respect to the writing direction, one can utilize the PFT inherent in their bare beam to create stronger modification by writing in the appropriate direction.

8.5 Conclusions

In conclusion, I demonstrated the unambiguous evidence that PFT is the origin of the non-reciprocal behaviour known as the “quill-writing effect.” The transformation from damage-like modification to self-assembled nanogratings is described in terms of the first-order phase transition. Furthermore, the transition point can be manipulated via the control of spatio-temporal couplings, leading to the manifestation of the quill-writing effect. I confirmed that the non-reciprocal laser writing follows the direction of the PFT. The directional dependence is then explained via polarization dependent optical scattering, originating from the interaction of the PFT with the interface of the modification front. Knowing SSTF is pivotal in creating highly localized modification, the same associated spatio-temporal couplings will lead to the manifestation of the “quill-writing effect,” which is vital to control and enhance ultrafast laser material processing.

Chapter 9: Symmetric On-Axis Simultaneous Spatio-Temporal Focusing With a Circular Grating

9.1 Introduction

Ultrafast laser pulses are characterized by short pulse durations and broad spectrum. The ability to control the spatial and temporal distribution of the spectrum led to a number of important developments, allowing high energy pulse amplification and few cycle pulse generation. Recently, several experiments demonstrate the importance of spatio-temporal properties in light-matter interactions [6,165] and attosecond pulse generation [148] alongside the work discussed earlier in this thesis (Chapter 6 and 8). SSTF has been developed for background-free, nonlinear microscopy [116,134,239]. The basic concept of the technique is to pre-chirp the laser pulse in space and time before the focusing optics. The focusing lens then acts as a pulse compressor, producing the shortest pulse duration and highest intensity only at the focus of the beam. SSTF is typically implemented using grating-lens combinations [115,118,240] or spatial light modulators [162] but these set-ups are intrinsically complicated in the sense of alignment and lead to unwanted spatio-temporal distortions [166]. There are physical limits however with SSTF designs. While SSTF gives the benefits of tight focusing, it is effectively reducing the NA of focusing in parallel. Large SC will make the beam highly elliptical and can easily be clipped by focusing optics, thus limiting the maximum SC allotted. This can be alleviated with the use of parabolic mirrors, which are currently being used in many SSTF designs [111,116,147,172,208] but are quite impractical for typical laser writing set-ups. Additionally, the area distribution of SSTF beams do not use large areas of the focusing optic. If large amounts of power are needed, it can potentially damage the optics. In order to introduce SC into the laser pulse without the use of typical prism or grating pairs, I employed a circular diffraction grating. In this chapter I report the potential design of a simple circular grating and axicon combination that can maintain a symmetric SSTF with variable spatio-temporal control, with the position of the axicon that can stretch the input beam in the region around the focus of a simple lens. In this case, the SC has cylindrical symmetry thus allowing for the potential of reaching the same SC as seen in typical grating-based SSTF designs but also work at higher NA and higher laser power since the beam is spread across the whole back pupil of a focusing lens. As a result, the directional dependence and photosensitive anisotropy observed in laser writing experiments could be effectively eliminated [4,6]. The results in this chapter are preliminary and the issues with the design of the circular grating for the potential of SSTF are discussed.

9.2 Methods

The circular grating is produced by periodically varying the birefringence and slow axis azimuth, which is dependent on the intensity and polarization of the laser beam, similar to the manufacturing process for optical converters [62,63,165,241]. By continually rotating linearly polarized light with a λ/2 waveplate, one can control the direction of the grating written (Fig. 9.1a). Since the circular grating is written with polarization dependence, light propagating through the circular grating has polarization and phase sensitivity as opposed to a typical grating, which only modulates phase and amplitude. A one inch diameter circular grating was written with NA = 0.55 at a writing speed of 200 µm/s at a pulse energy of 0.5 µJ at 300 fs to write a polarization grating with a 60 µm periodicity.

A regeneratively amplified, mode-locked Yb:KGW based femtosecond laser system (Pharos, Light Conversion Ltd.) operating at 1030 nm and delivering pulses of ~300 fs at varying repetition rates was used in the experiments. A NOPA was used to switch the input wavelength to 750 nm with a transform-limited pulse duration of 50 fs. The input laser propagates through a circular grating to create a symmetric ring of the laser which is then collimated with a matching axicon (Fig. 9.1b). As the beam propagates after the grating, SC is induced and thus increases the local pulse duration. The position of the axicon away from the grating controls the amount SC in the pulse. The circular grating also induces TC into the beam similarly to typical grating compressor designs, making it an on-axial grating compressor.

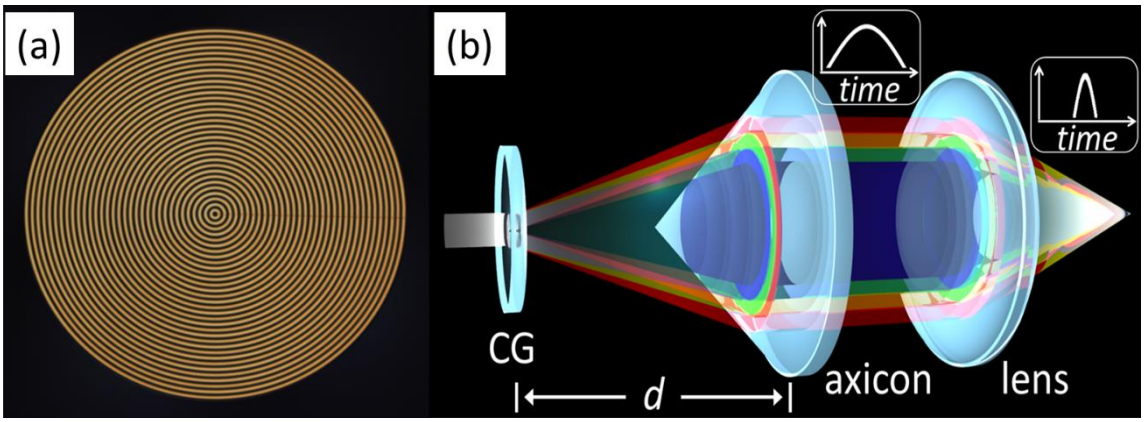

Figure 9.1: (a) Circular Grating Converter printed in the bulk of fused silica, observed under cross polarizers (Periodicity ≈ 60 µm). (b) Schematic of simultaneous spatial and temporal focusing technique with observed symmetry, splitting the wavelengths in symmetric rings. This symmetry ensures that all of the behavior observed is solely based on the spatio-temporal properties of the beam.

9.3 Theory

The basis of the circular grating is to essentially behave as an on-axial pulse compressor by spatially separating the spectral components of a beam in a cylindrical geometry and collimating it with a matching axicon or opposite signed grating for easy alignment and design. The separation between the two objects controls the pulse duration. Moreover, the spatial separation before focusing adds an additional level of control through SSTF. The issue with SSTF in ultrafast laser material modification is that it can lead to PFT in the focus which introduces directional dependence and polarization dependent modification during ultrafast laser writing. However, since the beam is symmetrically chirped in a radial geometry, it would effectively negate any directional or anisotropic behaviour since there is no defined direction to be dependent on. Assume a wavelength at 750 nm with a 30 nm bandwidth impinges on a circular grating of periodicity *d* (Fig. 9.2). From there it is simple to calculate the AD induced:

$$AD_\lambda = \frac{d\theta_D}{d\lambda} = \frac{m}{d\cos\theta_D} \tag{9.1}$$

where *m* is the diffracted order (typically *m = -1* for gratings) and θ_D is the angle of diffraction with respect to the central wavelength. In terms of frequency, Equation (9.1) is given by:

$$AD_\omega = \frac{d\theta_D}{d\omega} = \frac{2\pi c}{d\omega^2\cos\theta_D} \tag{9.2}$$

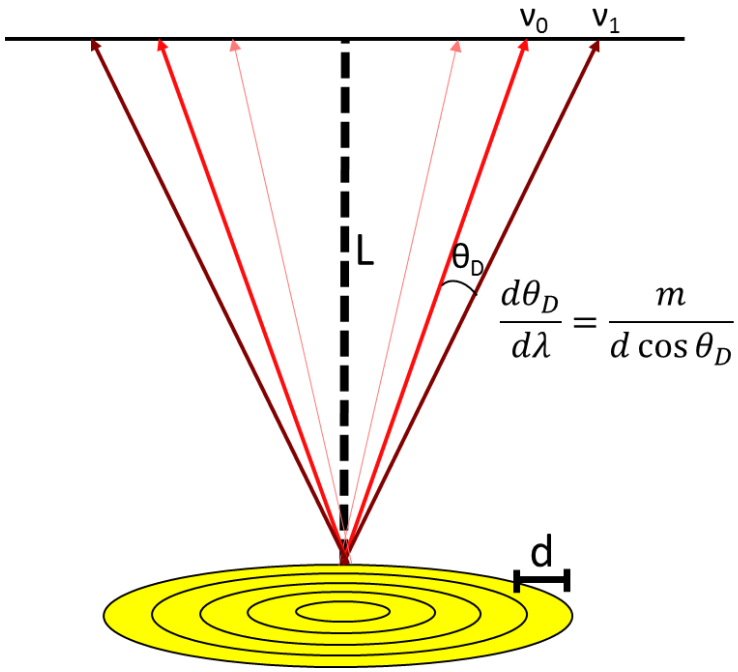

Figure 9.2: Schematic of diffraction from circular grating where d is the grating periodicity, θ_D is the diffraction angle, and L is the separation between the circular grating and the collimating axicon.

AD induces SC, which is easily quantified through SD. When a beam with AD propagates over a distance, *L*, the induced change in SD is:

$$SD = L * AD_{\omega} = \frac{2\pi cL}{d\omega^2 \cos\theta_D} \tag{9.3}$$

When adding SC to a laser beam, locally the beam is stretched due to the change in bandwidth of the respective beamlets in respect to the transform-limited laser pulse. The local pulse duration, τ', is given by [129]:

$$\tau' = \sqrt{{\tau_0}^2 + 4\frac{SD^2}{w^2}} \tag{9.4}$$

where τ_0 is the transform-limited pulse duration and *w* is the transform-limited beamspot. Additionally, the grating induces TC into the beam. The GDD of the grating is given by [180]:

$$GDD = \frac{m^2\lambda^3 L}{2\pi c^2 d^2 \cos^2\theta_D} \tag{9.5}$$

where the new stretched pulse duration (and thus global pulse duration), τ_{out}, is:

$$\tau_{out} = \frac{\sqrt{{\tau_0}^4 + 16(\ln 2)^2 GDD^2}}{\tau_0} \tag{9.6}$$

Depending on the periodicity of the grating and the length of propagation between the grating axicon, different pulse durations can be generated both locally and globally (Fig. 9.3 a, b).

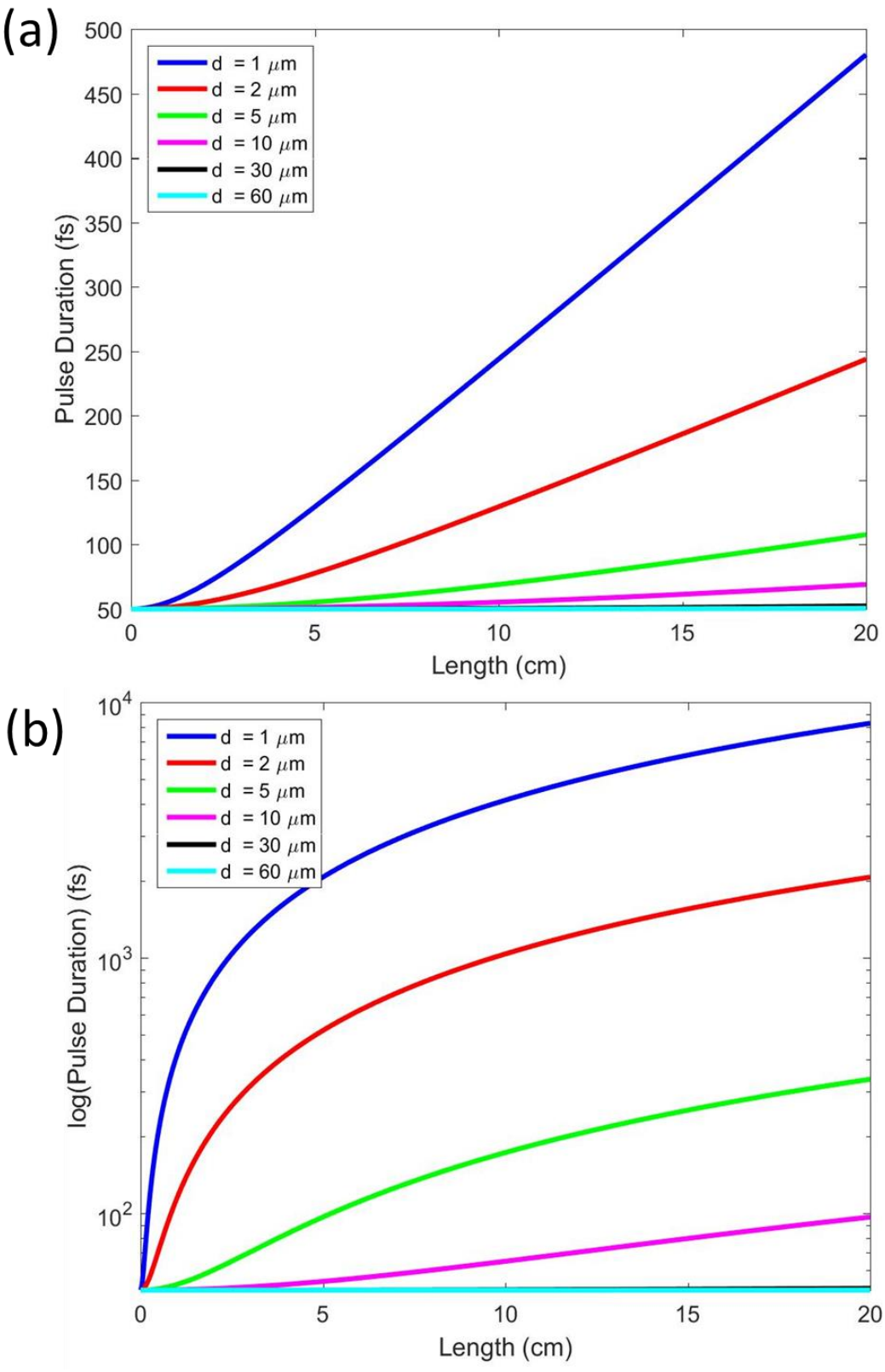

Figure 9.3: (a) Local and (b) Global pulse durations as a function of separation distance for varying grating periodicities at λ = 750 nm with Δλ = 30 nm.

9.4 Results

An initial circular grating was manufactured with a periodicity of 60 µm (17 lines/mm) and illuminated with a white-light source to validate its diffractive measure (Fig. 9.4). A rainbow ring beam is generated with the circular grating with each wavelength propagating at a different angle, thus validating the spatially chirped ring beam for the design. It can be noted that the radial nature of the rainbow beam (whether the red ring is on the outside or inside) is dependent on propagation distances after the grating, due to the angle of propagation for each wavelength.

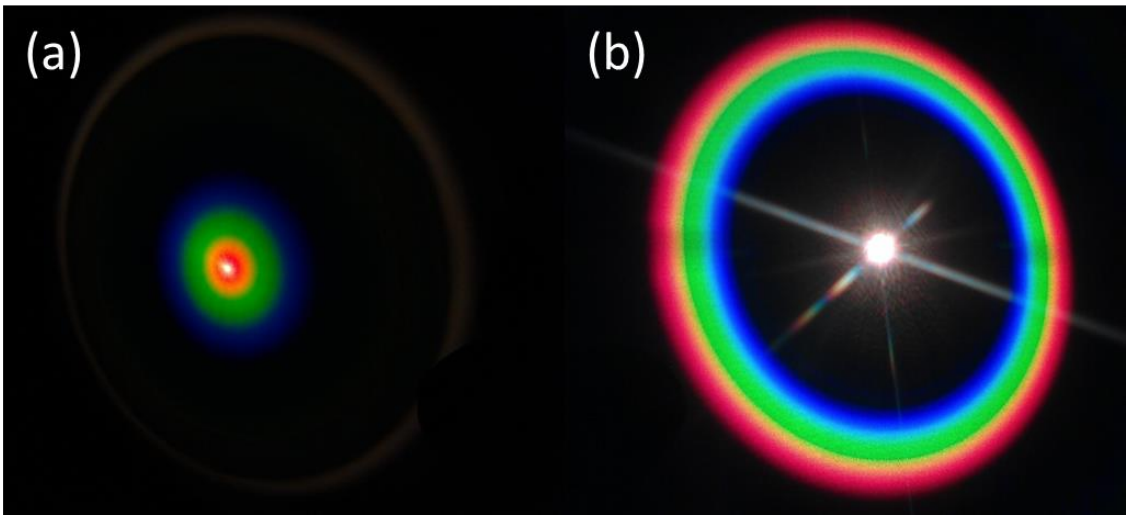

Figure 9.4: Diffraction ring pattern created by circular grating with a white light source (a) Near the circular grating and (b) Far from the circular grating. Depending on wavelength, the different components are separated into symmetric rings around the centre, spatially chirping the laser in a symmetric ring. Each wavelength propagates at a different angle depending on the grating period causing the red ring and blue ring to flip.

Effectively, this circular grating can be viewed as an axicon. Since the grating is birefringent, any polarization incident on it would be split into two circularly polarized beams. One circular polarization would see the grating as a positive axicon and the other would see it as a negative axicon. For negative axicons, a ring is generated which effectively grows in diameter. For positive axicons, the ring first collapses into a Bessel beam and then eventually turns into a ring. In both cases, the AD is the same but the positive axicon yields a smaller ring.

Based on the design (Fig. 9.1b), positioning the axicon at different positions from the circular grating controls the amount of stretching observed in the laser pulse (Fig. 9.5a). The focusing conditions contain multitude of different factors. One of the focusing factors is SSTF and the other is the focusing of a ring beam to create a point focus, approximating a Bessel beam. As the

grating-axicon separation increases, the strength of focusing effectively increases. The larger the separation, the larger the range of pulse stretching is seen in the area around the focus.

Due to the polarization nature of the circular grating, the strength of focusing can also be controlled simply by using polarization (Fig. 9.5b). By changing the input polarization to the grating from different states of circular polarization, the intensity profile of the laser is changed from an inner ring to an outer ring. This then adds an additional degree of freedom with the strength of focusing otherwise unachieved in current SSTF designs simply due to highlighting different diffractive orders.

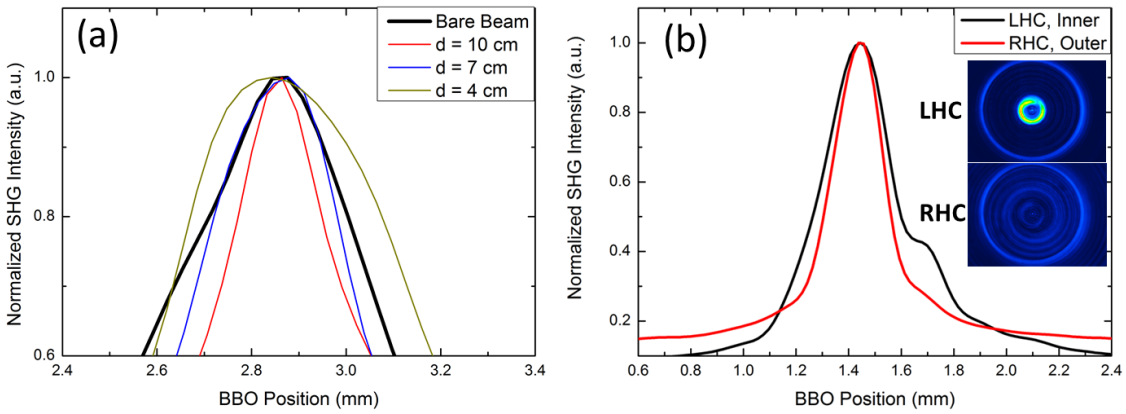

Figure 9.5: (a) Compression of pulse based on f = 2.5 cm lens dependent on grating-axicon separation over the focusing range in a 100 µm BBO. (B) Compression of pulse based on f = 2.5 cm lens dependent on input polarization with corresponding beam profiles over the focusing range.

9.5 Discussion

While the concept has the potential of simplifying otherwise complicated designs currently used for SSTF and pulse compression, the major issue lies in the manufacturing process of the circular grating. Typical gratings have dimensions of 600 to 1200 lines/mm, which results in a periodicity of roughly 1 µm. It is only at these periodicities that there is sufficient diffraction to allow for pulse stretching/compression, whereas for 60 µm periodicities, the pulse barely stretches and there barely is a benefit in stretching the local pulse duration due to SC (Fig. 9.3). In the manufacturing process of the circular grating, successive lines are written, separated by a specific distance. Each line is written with a changing polarization to create a polarization diffraction grating. The issue with this is to create small periodicities, the space between successive lines needs to small. In the original polarization diffraction grating study, each line was separated by 2 µm to ascertain a periodicity of 125 µm [241]. Once the track separation becomes smaller, successive lines are effectively overwritten by the next line since nanogratings can be rewritten.

This then degrades the quality of the polarization grating and makes it unusable. While tighter focusing can lead to better periodicities, there is the issue that the induced birefringence may not be strong enough due to the smaller Rayleigh range. The modification is effectively smaller so the overall strength of the grating would be smaller. This can be alleviated by writing several birefringent layers but would need extremely long writing times. The use of cylindrical and Bessel beams for the benefit of material modification is currently underway and showing promise in creating geometric phase elements that could reach the necessary periodicities for this concept to work.

The other issue is the PFT generated from the single pass geometry. As the beam passes the circular grating, the components are travelling at different angles introducing a PFT that increases as the laser light propagates based on the SC and TC induced. This can be alleviated by compensating the TC beforehand with an initial double-pass geometry compressor similar to the experiments conducted in Chapter 6 and 8. Another method would be to employ the on-axial SSTF design in a double pass geometry by using elements of opposite sign. However, it would all be in one optical line by using opposite phase elements where the separation between subsequent elements would control the TC. If a single pass-geometry is used, PFT will be generated upon focusing due to the AD of the focusing optic. Of particular interest is how the PFT is oriented. Since the beam has a ring distribution with SC radially distributed, the PFT is radial as well. It would create a conical intensity distribution upon focusing, either pointing towards or away from the focus (Fig. 9.6). The interaction this type of beam would have with matter is unknown and would be interesting to investigate.

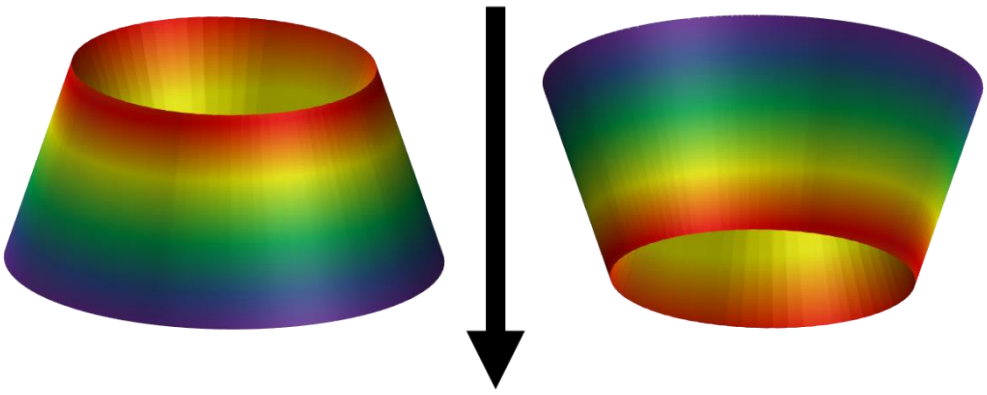

Figure 9.6: PFT orientation upon focusing when circular grating is used for SSTF. The arrow indicates the propagation direction for both orientations of PFT.

9.6 Conclusions

The circular grating-axicon concept has the potential of simplifying otherwise complicated set-ups currently used for SSTF. The on-axis design allows for easy alignment and straightforward installation in any optical set-ups. The robustness of the stretching of the pulse can also replace off-axis compression set-ups (ex. Prism pairs, gratings, etc.) or complicated pulse shapers. The design can easily be implemented into any imaging system and can be made to target specific wavelengths by writing the circular grating according to the wavelength. The simple on-axis set-up has the potential to revolutionize SSTF and provide a manner of observing the effect spatio-temporal couplings have, uninhibited, with complete control. This development will be beneficial not only for the laser material processing community but also to biology and medicine where nonlinear microscopy is a major characterization tool.

Chapter 10: Conclusions and Future Outlook

10.1 Summary and Discussion

In this thesis, I have reported the investigation of the ultrafast laser induced phenomena with respect to the spatio-temporal couplings of the laser pulse. Two of the major phenomena associated with ultrafast laser material modification, the non-reciprocal writing behaviour known as the quill-writing effect and the photosensitive anisotropic behaviour known as the blade effect, were investigated with a thorough characterization and control of the spatio-temporal couplings of the pulse. This work included the design of an experimental design that would facilitate the complete control of the spatio-temporal couplings with the use of two pulse compressors, in conjunction with one another to control the spatial and temporal properties of the pulse independently from one another. This was first conducted with a visible, large bandwidth laser source generated with NOPA and two prism compressors. Many difficulties arose in the design with this source due to beam spot distortions, power loss and the extreme sensitivity to dispersive elements like objective lenses, which made this design extremely difficult to use in controlling and properly characterizing the spatio-temporal couplings of the pulse. Two grating compressors used in conjunction with one another with the 1030 nm laser source provided the ability to control the parameters of the pulse without any major beamspot distortion or power loss. The small bandwidth associated with the source (~8 nm) made it insensitive to dispersive elements allowing for the control of the spatio-temporal couplings. This alongside theoretical models to be able to calculate the spatio-temporal couplings of the pulse before the lens through Kostenbauder matrices and characterization techniques such as SHG-FROG allow for a complete understanding of the electric field of an ultrafast laser pulse before focusing.

I demonstrate that spatio-temporal couplings are inherent for all ultrafast laser systems with chirped-pulse amplification. When conducting experiments with the bare beam and measuring the spatio-temporal properties of the pulse, residual SC and AD is evident in the beam, which simply arise from spatio-temporal manipulations involved in typical laser systems. I show that they accumulate in multi-pulse irradiation and lead to a strongly anisotropic light-matter interaction; known as the blade-effect. When controlling the spatio-temporal couplings of the pulse and generating PFT simply through SC and TC, it was observed that the blade effect is evident for any beam with spatial chirp regardless of PFT before the lens. The experimental results identify angular dispersion in the focus as the main cause for the polarization dependence in modification, yielding a 200% increase in modification strength. With tight focusing (NA ≥ ~0.4), this non-paraxial effect leads to an apparent manifestation of spatio-temporal couplings in

photo-induced modification. With control of the spatio-temporal properties of the pulse, I devise a practical way to control the polarization dependence and exploited it as a new degree of freedom in tailoring laser induced modification in transparent material. A non-paraxial field structure analysis of an optical beam near the focus was conducted and provides insight on the origin of the polarization dependent modification. However, single pulse non-paraxial corrected calculations are not sufficient to explain the phenomena confirming the experimental observations and exemplifying the need for multi-pulse analysis.

Based on the results of the blade-effect experiments, it reopened the debate as to what the cause of the quill-writing effect could be. During the initial experiments reporting the quill-writing effect, there were key errors in the characterization and identification of spatio-temporal couplings in the pulse during ultrafast laser material modification, which further raised questions. Through the control and characterization of the spatio-temporal couplings of the pulse, three states of PFT were examined: ±PFT and PFT = 0. It was observed that when PFT = 0, there is effectively no directional dependence in modification. When adding +PFT, the directional dependence was observed, inducing either an isotropic damage-like structure or a self-assembled nanostructure depending on the beam movement direction. When adding –PFT, the directional dependence was observed again but it did not flip directions alongside the PFT as originally explained [5]. A thorough investigation of both PFT and WFR in focusing was conducted to determine which major spatio-temporal coupling would be the cause of the non-reciprocity observed in writing. It was observed that spatially chirping a laser pulse before a focusing lens would lead to PFT in the focus due to AD, regardless of the magnitude and sign of TC. Since the cases with PFT are effectively picosecond pulses, the nonlinear ionization occurs closer to the focus, facilitating an environment where the PFT becomes a factor in material modification. For the case with PFT = 0, the pulse duration is in the femtosecond regime. The intensity is sufficiently high and instigates nonlinear ionization well outside the depth of focus of the focusing geometry, where PFT is effectively zero, leading to no observable non-reciprocity in writing.

While one direction provides stable modification, the other direction shows a switching of the modification regime from the formation of isotropic damage-like to anisotropic grating-like structures when the translation of the beam is in the direction of the tilt. This switching of modification regimes is qualitatively described in terms of the first order phase transition in the irradiated volume of a transparent dielectric. This sudden transition occurs either after a specific amount of translation of the sample, with respect to the beam depending on the writing speed, or in the regime of jitter or instability. The transition point can be manipulated via the control of spatio-temporal couplings leading to the manifestation of the quill-writing effect.

Another interesting observation through the blade-effect study was the formation of Type II nanograting formation after Type III void formation, which was thought to be a non-reversible path following the laser intensity regimes. Based on this observation, the structural evolution of void modification to self-assembled nanogratings in fused silica was investigated alongside simulations based on the nonlinear Schrödinger equation. It was clearly observed that a chain of voids can form within the first set of pulses under moderate focusing conditions (NA > 0.4) and after further irradiation, transitions to form birefringence at the top of the structures. The simulations conducted calculated the laser fluence, intensity and electron density in the regions of modification for the same laser parameters. Comparing the experiments with numerical calculations, the voids form in the regions where the electron density exceeds 10^{20} cm^{-3} but is below critical. In this scenario, the energy absorption is insufficient to reach the critical electron density that was once assumed to occur in the regime of void formation and, more importantly, nanograting formation. This observation provides insight on the potential formation mechanism of nanogratings that still, after 13 years since the initial finding, is left unexplained.

In an attempt to understand more about the formation mechanism of nanogratings based on the two-plasmon decay model, an *in-situ* measurement apparatus was developed to measure harmonic generation in the bulk of transparent materials during ultrafast laser writing. The observation of 2ω and 3ω were made and compared against nanograting formation with respect to pulse duration, pulse energy and laser irradiation times. While 2ω seemed to be independent of nanograting formation, subsequently generated due to plasma gradients during laser light-matter interaction, 3ω shows to be dependent on the nanograting process. 3ω is generated as two propeller-like lobes oriented along the incident light polarization. When measuring the angle of propagation of the lobes after the sample, it is observed to be propagating at 16.81°±0.2°. This angle correlates with the generation of 3ω based on the Cherenkov mechanism, which should propagate at 16.67° based on theoretical estimations. When looking at the harmonic generation dependence on polarization, 2ω counts were independent of the change of linear to circular polarization, indicating that it is not involved in the nanograting process, since nanogratings cannot form with circular polarization. 3ω on the other hand does not generate and maximizes in counts for linear polarization, indicating the processes are corollary of one another. Moreover, an enhancement in both harmonics is observed for elliptically polarized light, indicating a larger excitation for a mixture of circular and linear polarization induced absorption cross-sections. While the measurement of 3ω/2 was never made, the unusual enhancement and generation in 3ω could provide insight into the formation mechanism of self-assembled nanogratings. Moreover, the *in-situ* measurement technique could be used to probe any phenomena during ultrafast laser-light interactions.

The concept of an on-axial SSTF-pulse compressor design with the use of a circular polarization grating was discussed. The design entails a polarization grating that is printed by varying the birefringence and slow-axis azimuth in a circularly symmetric geometry and is collimated with an axicon of the opposite phase in one axis. This then creates an on-axial SSTF design where the beam is spatially chirped in a symmetric circle. Due to this unique beam shape, there would be no defined direction of spatio-temporal couplings to give rise to the non-reciprocal and photosensitive anisotropic behaviours observed during ultrafast laser writing. An analysis of the potential of the concept with typical grating periodicities was conducted, showing that both the local and global pulse durations can be stretched to large orders of magnitudes simply by controlling the separation distance between the grating and axicon. A 60 µm periodicity circular grating was printed and tested to show that the beam can be spatially chirped in a circular symmetric way. The grating itself is polarization dependent, adding an additional level of control in the strength of focusing. The current limitations of the design of a low periodicity element are discussed but the simple on-axis set-up has the potential to revolutionize SSTF and pulse compression techniques as well as ultrafast laser material modification.

10.2 Future Outlook

The work discussed in this thesis represents the advancement in the understanding of the light-matter interaction phenomena involved with ultrafast lasers. However, understanding one thing opens up questions and possibilities which need to be addressed in the future.

The understanding of how relevant spatio-temporal couplings are and how they affect ultrafast laser material modification is extensively shown. With respect to the photosensitive anisotropy observed in modification, multi-pulse simulations are necessary to fully understand how the material interacts with the electric field of a pulse with spatio-temporal couplings. These models are extremely hard to develop due to the complexity of plasma physics but a model is currently under development to address these issues.

Even though the understanding of how AD couples with polarization to induce the polarization dependent modification is still underway, the effect introduces a new degree of freedom when it comes to material modification. Being able to tune the modification simply by rotating the SC of a beam with respect to polarization can allow the tailoring of birefringent structures and can significantly reduce manufacturing times for application. The introduction of rotation optics, such as a dove prism, can be introduced into a writing system and the efficacy of it can be studied. For example in polarization multiplexed memory, this technique can reduce the writing speed by adding the extra degree of control. SSTF also shows great promise in inducing more efficient and

stronger modification closer to the focal zone, with shorter irradiation times. For applications where the modification resolution needs to be as small as possible, SSTF shows promise.

With respect to the non-reciprocal writing behaviour, one of the major questions remaining is what causes the sudden and abrupt phase transition. This unique observation shows that after a particular moment of time, something is collected causing a drop in intensity to occur. This drop in intensity then leads to the sudden transition from damage-like modification to nanogratings. One idea is that a collection of electrons occur during writing, which suddenly causes the intensity to drop after a threshold is met. This would then lead to the production of a space charge effect. The signature of space charge in dielectrics is the generation of 2ω. Using the *in-situ* measurement technique discussed in this thesis, I attempted to measure the harmonic signatures during the transition. While white light emission was observed to drop significantly at the point of transition, there was no enhancement in 2ω at any point during the writing process. Another hypothesis is that the transition is due to thermal effects. However, there is no signature of melting/boiling in the material and the transition does not occur gradually. The identification of the origin of the transition needs to be investigated. One idea of investigating it is viewing the transition through plasma imaging techniques. An ultrafast imaging of transient electronic plasmas can be conducted with the use of pump-probe experiments and *in-situ* plasma emission microscopy has been developed and used in the past to attempt to validate the ponderomotive force explanation of the quill-writing effect [169,194]. These techniques can be used in conjunction of one another, to better understand the phenomena observed with the quill-writing effect.

Another question that is introduced is what the origin of the white light emission is. White light emission is explained to be due to both a recombination of electrons and Bremsstrahlung radiation. There are two major observations that can be made about white light emission. The first is that the plasma emission is material independent. The second is that the generation of white light is due to optical breakdown in the material, leading to the formation of plasma. One of the observations from the phase transition seen in quill-writing is that the white light emission becomes darker immediately at the transition and remains dimmed for the rest of the writing. It is also seen in the blade-effect experiments that the orthogonal polarization state, with respect to SC, yields brighter white light emission as opposed to the parallel polarization state. The origin of the white light emission can provide clues behind what the underlying mechanics are. The argument that it is both could be correct. However if white light emission was due to a recombination of electrons, a few issues are introduced. Recombination would involve emitting energy, either through kinetic energy or through binding energy. Binding energy is material dependent. Kinetic energy is temperature dependent and thus wavelength dependent. Yet, white

light emission spectra seems to be independent of both. Therefore, it would be beneficial to understand ultrafast laser induced phenomena by correctly identifying the origin of the white light emission.

The polarization circular grating concept shows promise in potentially revolutionizing the ultrafast laser community. If smaller periodicities can be printed, the on-axial design can greatly benefit any pulse compression or SSTF-based experiment and design. Moreover, the additional degree in focusing through the Bessel Beam generated adds another degree of focusing, which could potentially benefit ultrafast laser machining. It is also interesting to see if the conical PFT that could potentially be generated in the focus has any benefit in ultrafast laser machining. The major obstacle to overcome is being able to print tracks closer together without overlapping and effectively writing over birefringent tracks. SSTF and tighter focusing could benefit this process in being able to deliver energy closer to the focal zone, thus improving the resolution. Currently, work is ongoing in creating better polarization gratings, but the potential for small periodicity polarization gratings are manifold.

The biggest outstanding problem that remains is the formation mechanism of self-assembled nanogratings. In my thesis, the generation of 3ω is dependent on nanograting formation. Based upon this observation, 3ω could yield a clue as to what forms nanogratings. The popular interference model used to explain the formation of nanogratings involves the interference of harmonics to create periodicity in the bulk of a material. Most interference models involve some fraction of critical plasma concentrations. Plasma concentrations in the bulk of transparent materials is dependent on the wavelength of the pump, where lower electron concentrations are sufficient to reach critical at lower wavelengths [201,218,242]. Potentially, the 3ω could be a signature of the process. One idea is to attempt to print nanogratings in the bulk of a transparent material with one wavelength and attempt to seed it with its respective 3ω. By changing the percentage of 3ω with respect to ω and observing an enhancement in the structures printed, it could be proven that the 3ω is part of the nanograting formation mechanism. One idea is to use a harmonic generator alongside the laser system and have the beams travel together in phase. Another idea is to place a χ^3 crystal in the main laser line and attempt to seed the modification process with the 3ω generated. The issues that arise in both cases is that it is near impossible to have an accurate measurement of how much 3ω there is with respect to the pump beam. When using a harmonic generator, it is difficult to know if there are other harmonics being generated as well since most harmonic generators and NOPA designs use 2ω to amplify signals. There is also the issue of focusing conditions being different since typical objective lenses are wavelength dependent. Another study could simply determine whether wavelengths can promote nanograting formation more efficiently. Currently, nanograting formation cannot occur with

single pulses. It would be beneficial to observe if the process is more efficient as a function of the incident wavelength. The model being created to understand multi-pulse effects in transparent materials could also be used to attempt to model nanograting formation. One way or another, a systematic study of how different harmonics affect nanograting formation needs to be conducted to better understand the formation mechanism. In order for the field of ultrafast laser material modification to move forward, the formation mechanism of self-assembled nanogratings needs to be resolved.

Appendices

Appendix A

Derivation of the Kostenbauder matrix for a prism pair

Consider a typical prism with the incident laser light, λ_0, at an angle ϑ_{in} and exiting out of the prism at an angle $\vartheta_{out.}$ This would then have the corresponding interior angles of ψ_{in} and ψ_{out} and an interior prism length of L (Fig. A1). The general Kostenbauder matrix for a general prism is:

$$\begin{bmatrix} m_{in}m_{out} & \frac{Lm_{out}}{nm_{in}} & 0 & -\frac{2\pi\frac{\mathrm{d}n}{\mathrm{d}\omega}Lm_{out}\tan\psi_{in}}{n} \\ 0 & \frac{1}{m_{in}m_{out}} & 0 & \frac{-2\pi\frac{\mathrm{d}n}{\mathrm{d}\omega}(\tan\psi_{in}+\tan\psi_{out})}{m_{out}} \\ -\frac{2\pi\frac{\mathrm{d}n}{\mathrm{d}\omega}m_{in}(\tan\psi_{in}+\tan\psi_{out})}{\lambda_0} & \frac{-2\pi\frac{\mathrm{d}n}{\mathrm{d}\omega}L\tan\psi_{out}}{nm_{in}\lambda_0} & 1 & \frac{4\pi^2\left(\frac{\mathrm{d}n}{\mathrm{d}\omega}\right)^2 L\tan\psi_{in}\tan\psi_{out})}{n\lambda_0+2\pi Lk''} \\ 0 & 0 & 0 & 1 \end{bmatrix} \quad \text{(A1)}$$

where $k'' = \frac{\mathrm{d}^2k}{\mathrm{d}\omega^2}|_{\omega_0}$ *is the GVD*, $m_{in} \equiv \frac{\cos\psi_{in}}{\cos\vartheta_{in}}$ *and* $m_{out} \equiv \frac{\cos\vartheta_{out}}{\cos\psi_{out}}$

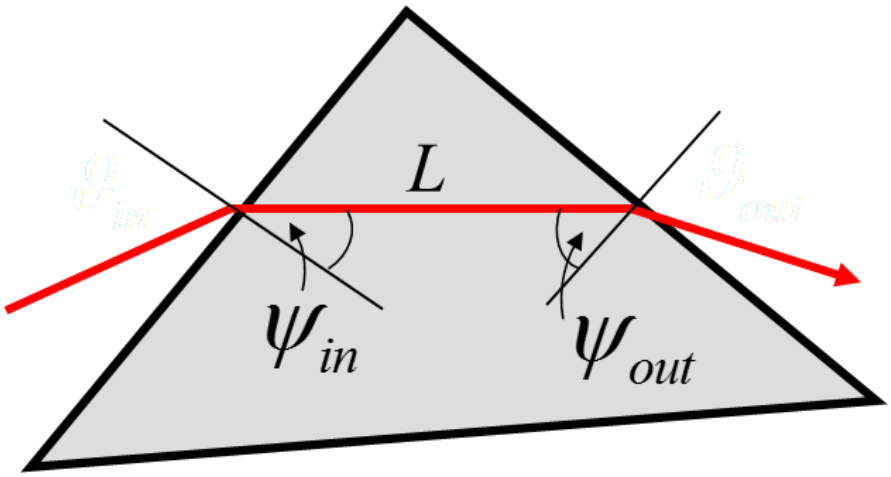

Figure A1: Diagram for Kostenbauder matrix for a general prism.

If the beam passes through the apex of the prism, *L = 0*. This can be further simplified using a Brewster prism. The angle of incidence and exit in this case would be the same, $\psi_{in} = \psi_{out} = \psi$. This yields a K-matrix of:

$$K_{prism} = \begin{bmatrix} 1 & 0 & 0 & 0 \\ 0 & 1 & 0 & \pm\mathcal{D} \\ \pm\frac{\mathcal{D}}{\lambda_0} & 0 & 1 & 0 \\ 0 & 0 & 0 & 1 \end{bmatrix} \quad \text{(A2)}$$

where $\mathcal{D} = -4\pi\left(\frac{\mathrm{d}n}{\mathrm{d}\omega}\right)\tan\psi/m_{out} = -4\pi m_{in}\left(\frac{\mathrm{d}n}{\mathrm{d}\omega}\right)\tan\psi$

Appendix A

The sign in front of the terms in the K-matrix is dependent on the orientation of the prism. To calculate the total K-matrix for a double-pass prism compressor geometry, the total propagation of the laser light needs to be accounted for. There will be a total of 7 matrices in the total matrix multiplication. 4 of them will be representative of the prisms and the other 3 are from the free-space propagation in between the prisms (Fig. A2). The K-matrix for free space propagation is:

$$K_{air} = \begin{bmatrix} 1 & L_i & 0 & 0 \\ 0 & 1 & 0 & 0 \\ 0 & 0 & 1 & 0 \\ 0 & 0 & 0 & 1 \end{bmatrix} \tag{A3}$$

where L_i is the distance between subsequent prisms.

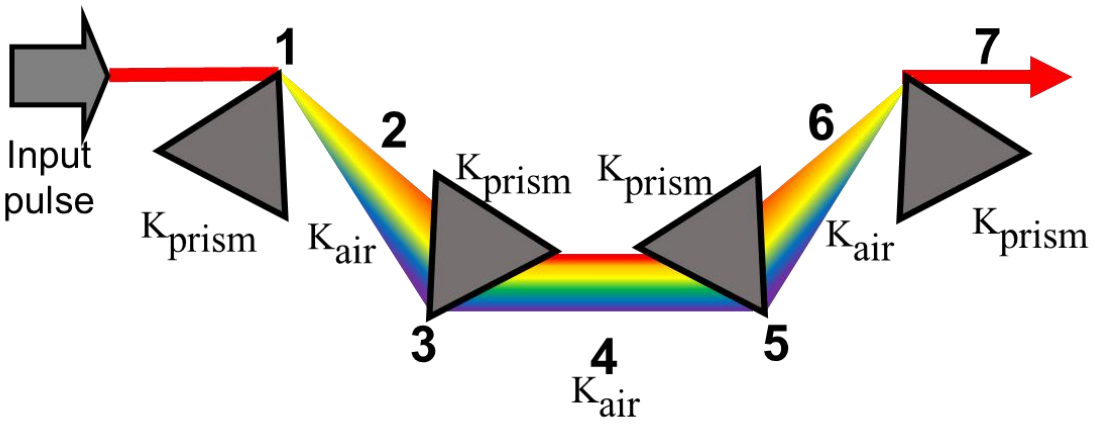

Figure A2: Modelling a prism pulse compressor using Kostenbauder matrices

Using Equation (A2) and (A3), the K-matrix for a prism compressor can then be derived by:

$$K = K_7 K_6 K_5 K_4 K_3 K_2 K_1 \tag{A4}$$

$$K = \begin{bmatrix} 1 & L_1 + L_2 + L_3 & 0 & \mathcal{D}(L_1 - L_3) \\ 0 & 1 & 0 & 0 \\ 0 & -\frac{\mathcal{D}}{\lambda_0}(L_1 - L_3) & 1 & -\frac{\mathcal{D}^2}{\lambda_0}(L_1 + L_3) \\ 0 & 0 & 0 & 1 \end{bmatrix}$$

There are a few key observations that can be made from Equation (A4). By looking at the terms with L_1 - L_3 terms, SC and WFR is evident in the beam unless $L_1 = L_3$. Also, by looking at the $L1 + L_3$ term, it is clear that prism compressors induce negative GDD to a laser pulse. This can be tuned however by changing the amount of extra glass in the beam (i.e. $L \neq 0$).

Appendix B

The MATLAB code for modelling the laser propagation through Kostenbauder Matrices

Here I present the basic MATLAB code which I have written for modelling the laser propagation through dispersive elements. The main function of the code is to know exactly what the spatio-temporal couplings are in the laser pulse for a defined geometry of dispersive elements, which are then used to compare against what is measured in experiment to ensure the true identification of the properties of the pulse. These values are then placed into another program to calculate the Q-coefficients for the definition of the electric field of the pulse. To ensure the Q-coefficients are correct, a number of parameters were calculated to ensure that the values matched what was calculated in the original K-matrix code as well as what is seen in experiment.

K-Matrix for Grating Compressor

```
% K-Matrix for Single Pass Grating Compressor
clear all
close all

Kmatrix = zeros(4);
Ktelmatrix = zeros(4);
Kmatrixfs = zeros(4);

L = 4E8; %length between gratings, nanometres
theta_i = 0; %incident angle, deg
theta_d = 50; %reflection angle, deg
lambda = 1030; %wavelength, nm
c = 299.792458; %speed of light, nm/fs
f = c/lambda;
d = 1E6/600; %grating period, nm

Kmatrixfs(1,1) = 1;
Kmatrixfs(1,2) = L*5; %Propagation from grating set-up to lens
Kmatrixfs(2,2) = 1;
Kmatrixfs(3,3) = 1;
Kmatrixfs(4,4) = 1;

%%  %K-Matrix for Grating Compressor From Kostenbauder, 1990

theta_i = 90;
Kgrating1 = zeros(4);
Kgrating2 = zeros(4);
Kmatrixfs2 = zeros(4);

Kmatrixfs2(1,1) = 1; %K-matrix for free-space propagation between the
grating
Kmatrixfs2(1,2) = L;
Kmatrixfs2(2,2) = 1;
Kmatrixfs2(3,3) = 1;
Kmatrixfs2(4,4) = 1;

Kgrating1(1,1) = -sind(theta_d)/sind(theta_i); %K-matrix for Grating 1
Kgrating1(2,2) = -sind(theta_i)/sind(theta_d);
```

```
Kgrating1(2,4) = (cosd(theta_d) - cosd(theta_i))/(f*(sind(theta_d)));
Kgrating1(3,1) = (cosd(theta_i) - cosd(theta_d))/(c*sind(theta_i));
Kgrating1(3,3) = 1;
Kgrating1(4,4) = 1;

Kgrating2(1,1) = -sind(theta_i)/sind(theta_d); %K-matrix for Grating 2
Kgrating2(2,2) = -sind(theta_d)/sind(theta_i);
Kgrating2(2,4) = (cosd(theta_i) - cosd(theta_d))/(f*sind(-theta_i));
Kgrating2(3,1) = (cosd(theta_d) - cosd(theta_i))/(c*sind(-theta_d));
Kgrating2(3,3) = 1;
Kgrating2(4,4) = 1;

Kmatrix2 = Kmatrixfs*Kgrating2*Kmatrixfs2*Kgrating1;

SCH2 = Kmatrix2(1,4);
FRG_Z2 = SCH2/(2*pi);
FRG_omega2 = 1000000/(FRG_Z2*(1+ ((320^2)/((400^2)-320^2)))); %Frequency
Gradient, d_omega/dx, rad/(mm*fs)
test = 1/FRG_omega2
FRG_lambda2 = FRG_omega2*((lambda)^2)/(2*pi*c); %Frequency gradient,
d_lambda/dx, nm/mm
GDD2 = Kmatrix2(3,4)/(2*pi); %Induced GDD
tau_new2 = sqrt(420^4 + (16*(log(2)^2)*GDD2^2))/420; %New Global Pulse
Duration
PFTtest = GDD2*FRG_omega2; %Value of PFT
```

Q-Coefficient Calculation for the Electric Field Definition

```
clear all
close all

% Q-Coefficient Calculation for Case 1 (With PFT) (For Case 2 (No PFT),
% make GDD = 0)

lambda = 1.03;  %wavelength, um
 GDD = -445344.005531139; %group delay dispersion measured at lens, fs^2
% GDD = 0; %Switch to do Case 2
tau = 300; %initial pulse duration, fs
w = 2300; %beam spot size at lens, um
c = 0.299792458; %speed of light, um/fs
FRG_lambda = -8E-7; %Frequency Gradient, um/um
FRG_omega = (FRG_lambda)*2*pi*(c)/((lambda)^2); %frequency gradient,
rad/(fs*um)
Z = 1/(FRG_omega*(1+(tau^2/(420^2 - tau^2)))); %spatial dispersion, um*fs

Qxx = (lambda/pi)*(2*GDD - j*(tau^2))/((4*(Z^2)) + ((w^2)*(tau^2))+
(j*2*GDD*(w^2))); %1/(um)
Qxt = (-2*lambda/pi)*(Z)/((4*(Z^2)) + ((w^2)*(tau^2))+
(j*2*GDD*(w^2))); %1/(fs)
Qtt = (j*lambda/pi)*(w^2)/((4*(Z^2)) + ((w^2)*(tau^2))+
(j*2*GDD*(w^2))); %um/(fs^2)

Qxx_tilda = -j*pi*Qxx/lambda %1/(um^2)
Qtt_tilda = -j*pi*Qtt/lambda %1/(fs^2)
Qxt_tilda = -j*pi*Qxt/lambda %1/(um*fs)

%% Testing of Coefficients

%Calculate R-Coefficients For FRG Test
Rxw_tilda = -j*(Qxt_tilda)/(2*Qtt_tilda);
Rww_tilda = 1/(4*Qtt_tilda);
Rxx_tilda = Qxx_tilda + (Qxt_tilda^2)/Qtt_tilda;
```

```
%Local Pulse Duration
localtau1 = 1/sqrt(pi/lambda*imag(Qtt)); %fs
localtau2 = sqrt(1/real(Qtt_tilda)); %fs
localtau3 = sqrt(tau^2 +((4*Z^2)/(w^2)) + (4*(GDD^2)/(tau^2 +
(4*(Z^2)/(w^2))))); %fs

%Local Beamspot Size
localw1 = 1/sqrt(-pi/lambda*imag(Qxx));  %um
localw2 = sqrt(-1/real(Qxx_tilda)) ; %um


%Global Beamspot Size
globalw1 = (1/(sqrt(-real(Qxx_tilda) -
(real(Qxt_tilda)^2)/real(Qtt_tilda)))); %um
globalw2 = (-real(Rww_tilda)/((real(Rxw_tilda^2)) +
(real(Rww_tilda)*real(Rxx_tilda))))^0.5; %um

%Global Pulse Duration
globaltau1 = (1/(sqrt(real(Qtt_tilda) +
(real(Qxt_tilda)^2)/real(Qxx_tilda)))); %fs
globaltau2 = sqrt(420^4 + (16*(log(2)^2)*GDD^2))/420; %fs

%Frequency Gradient
FRG_omegatest = real(Rxw_tilda)/(real(Rww_tilda)); %rad/(um*fs)
FRG_omegatest2 = 2*((imag(Qxt_tilda)*real(Qtt_tilda)) -
(real(Qxt_tilda)*imag(Qtt_tilda)))/real(Qtt_tilda);%rad/(um*fs)

%GDD
GDD2 = -imag(Qtt_tilda)/(2*(abs(Qtt_tilda)^2));

%PFT
PFT1 = FRG_omega*GDD; %fs/um
PFT2 = real(Qxt_tilda)/real(Qtt_tilda); %fs/um

%WFR
WFR1 = (FRG_omegatest/2) + ((PFT2)*imag(Qtt_tilda)); %rad/(fs*um)
WFR2 = imag(Qxt_tilda);

%TVA
TVA = (real(Qxt_tilda)*imag(Qxx_tilda) -
(imag(Qxt_tilda)*real(Qxx_tilda)))/((real(Qxx_tilda))^2 +
(imag(Qxx_tilda))^2)
```

List of Publications

Journal Publications

1. **A. Patel**, V. T. Tikhonchuk, J. Zhang, M. Beresna, P. G. Kazansky. “Non-Paraxial Polarization Spatio-Temporal Coupling: A New Degree of Freedom in Light Matter Interaction.” Laser and Photonics Reviews. 1600290 (2017)

2. **A. Patel**, Y. Svirko, C. Durfee, M. Beresna, P. G. Kazansky. “Pulse Front Tilt Induced Non-Reciprocity during Ultrafast Laser Direct Writing.” Scientific Reports. (2017)

3. Y. Dai, **A. Patel**, J. Song, M. Beresna, P. G. Kazansky. “Void-Nanograting Transition by Ultrashort Laser Pulse Irradiation in Silica Glass.” Optics Express, Vol. 24 (17), 19344-19353 (2016).

4. J. Zhang, A. Čerkauskaitė, R. Drevinskas, **A. Patel**, M. Beresna, P. G. Kazansky. “Eternal 5D Data Storage by Ultrafast Laser Writing in Glass.” SPIE Photonics West: Laser-Based Micro- and Nanoprocessing X, United States. p. 1-16 (13-18 Feb 2016)

5. P. G. Kazansky, A. Čerkauskaitė, M. Beresna, R. Drevinskas, **A. Patel**, J. Zhang, M. Gecevicius. “Eternal 5D Data Storage via Ultrafast-Laser Writing in Glass.” SPIE Optoelectronics and Communications (2016)

Conference Publications

1. P. G. Kazansky, **A. Patel**, A. Čerkauskaitė, R. Drevinskas, Y. Svirko, V. T. Tikhonchuk, C. Durfee. “Harnessing non-reciprocity and polarization spatio-temporal couplings in ultrafast laser material processing.” Nonlinear Optics (NLO) Waikoloa, Hawaii (2017). NTu2B.6

2. **A. Patel**, Y. Svirko, C. Durfee, R. Drevinskas, P. G. Kazansky. “Solving the puzzle of non-reciprocity in ultrafast laser writing.” Conference on Lasers and Electro-optics and European Quantum Electronics Conference, Presentation, Munich, Germany (2017). CM-5.3.

3. R. Drevinskas, **A. Patel**, A. Čerkauskaitė, C. Durfee, P. G. Kazansky. “Geometric phase circular gratings fabricated by ultrafast laser nanostructuring for symmetric simultaneous

spatio-temporal focusing." Conference of Lasers and Electro-Optics and European Quantum Electronics Conference, Munich, Germany (2017). CM-9.4.

4. J. Zhang, A. Čerkauskaitė, R. Drevinskas, **A. Patel**, M. Beresna, P. G. Kazansky. "Current Trends in Multi-Dimensional Optical Data Storage Technology." Asia Communications and Photonics Conference, Wuhan, China (2016). AF1J.4.

5. P. G. Kazansky, **A. Patel**, R. Drevinskas, A. Čerkauskaitė, F. Zhang. "Revealing the mystery of non-reciprocity and polarization spatio-temporal couplings in ultrafast laser direct writing." International Conference on Advanced Laser Technologies (ALT 2016), Invited Presentation, Galway, Ireland (2016). LM-1-1.

6. **A. Patel**, P.G. Kazansky, R. Drevinskas, A. Čerkauskaitė, M. Beresna, F. Zhang, S. Lotarev, A. Okhrimchuk, V. N. Sigaev. "Advancing the Art of Ultrafast Laser Writing in Glass." Glass and Optical Materials Division Meeting, Invited Presentation, Madison, Wisconsin (2016). GOMD-S3-015-2016.

7. R. Drevinskas, M. Beresna, J. Zhang, **A. Patel**, A. Čerkauskaitė, A. G. Kazanskii, P. G. Kazansky. "Geometric Phase Holograms Imprinted by Femtosecond Laser Nanostructuring." Conference of Lasers and Electro-Optics US (CLEO), Presentation, San Jose, California (2016). SW4L.2.

8. P. G. Kazansky, M. Beresna, M. Gecevicius, J. Zhang, R. Drevinskas, **A. Patel**, A. Čerkauskaitė, A. S. Lipatiev, A. G. Okhrimchuk, V. N. Sigaev. "Advances in Femtosecond Laser Nanostructuring in Glass: From Printed Geometrical Phase Optics to Eternal Data Storage." Advanced Solid State Lasers Conference, Presentation, Berlin (2015). AW1A.4.

9. **A. Patel**, M. Beresna, P. G. Kazansky. "Harnessing Polarization Spatio-Temporal Coupling: A New Degree of Freedom in Ultrafast Laser Material Processing." Conference of Lasers and Electro-Optics US (CLEO), Presentation, San Jose, California (2015). SW1K.7.

10. P.G. Kazansky, M. Beresna, M. Gecevicius, J. Zhang, **A. Patel**, R. Drevinskas, A. Kazanskii. "Recent Progress in Ultrafast Laser Nanostructuring from Two-Plasmon Decay to Longitudinal Field Puzzle." Nonlinear Optics Digest. Presentation (2013). NF2A.4.

11. **A. Patel**, M. Gecevicius, R. Drevinskas, M. Beresna, P. G. Kazansky. “3/2 Harmonic Generation – The Clue to the Mechanism of Ultrafast Laser Nanostructuring.” Conference of Lasers and Electro-Optics US (CLEO), Presentation, San Jose, California (2013). CM2M.2.

12. **A. Patel**, M. Gecevicius, R. Drevinskas, M. Beresna, P. G. Kazansky. “Unambiguous Evidence of Two Plasmon Decay During Ultrafast Laser Writing in Glass.” Conference of Lasers and Electro-Optics Europe (CLEO), Presentation, Munich, Germany (2013). CM_4_3.

Bibliography

1. P. Bado, W. Clark, and A. Said, "Ultrafast Laser Micromachining Handbook," http://www.cmxr.com/Education/Introduction.html.

2. Y. Shimotsuma, P. Kazansky, J. Qiu, and K. Hirao, "Self-Organized Nanogratings in Glass Irradiated by Ultrashort Light Pulses," Phys. Rev. Lett. **91**, 247405 (2003).

3. V. R. Bhardwaj, E. Simova, P. P. Rajeev, C. Hnatovsky, R. S. Taylor, D. M. Rayner, and P. B. Corkum, "Optically Produced Arrays of Planar Nanostructures inside Fused Silica," Phys. Rev. Lett. **96**, 1–4 (2006).

4. P. G. Kazansky, W. Yang, E. Bricchi, J. Bovatsek, A. Arai, Y. Shimotsuma, K. Miura, and K. Hirao, "“Quill” writing with ultrashort light pulses in transparent materials," Appl. Phys. Lett. **90**, 151120 (2007).

5. W. Yang, P. G. Kazansky, Y. Shimotsuma, M. Sakakura, K. Miura, and K. Hirao, "Ultrashort-pulse laser calligraphy," Appl. Phys. Lett. **93**, 171109 (2008).

6. P. G. Kazansky, Y. Shimotsuma, M. Sakakura, M. Beresna, M. Gecevičius, Y. Svirko, S. Akturk, J. Qiu, K. Miura, and K. Hirao, "Photosensitivity control of an isotropic medium through polarization of light pulses with tilted intensity front.," Opt. Express **19**, 20657–64 (2011).

7. E. Bricchi, B. G. Klappauf, and P. G. Kazansky, "Form birefringence and negative index change created by femtosecond direct writing in transparent materials," Opt. Lett. **29**, 119–121 (2004).

8. E. Bricchi and P. G. Kazansky, "Extraordinary stability of anisotropic femtosecond direct-written structures embedded in silica glass," Appl. Phys. Lett. **88**, 111119 (2006).

9. E. G. Gamaly, S. Juodkazis, K. Nishimura, H. Misawa, B. Luther-Davies, L. Hallo, P. Nicolai, and V. T. Tikhonchuk, "Laser-matter interaction in the bulk of a transparent solid: Confined microexplosion and void formation," Phys. Rev. B **73**, 214101 (2006).

10. S. Juodkazis, K. Nishimura, S. Tanaka, H. Misawa, E. G. Gamaly, B. Luther-Davies, L. Hallo, P. Nicolai, and V. T. Tikhonchuk, "Laser-induced microexplosion confined in the bulk of a sapphire cystal: Evidence of multimegabar pressures," Phys. Rev. Lett. **96**, 1–4 (2006).

11. S. Juodkazis, H. Misawa, T. Hashimoto, E. G. Gamaly, and B. Luther-Davies, "Laser-induced microexplosion confined in a bulk of silica: Formation of nanovoids," Appl. Phys. Lett. **88**,

152–155 (2006).

12. K. Miura, J. Qiu, H. Inouye, T. Mitsuyu, and K. Hirao, "Photowritten optical waveguides in various glasses with ultrashort pulse laser," Appl. Phys. Lett. **71**, 3329 (1997).

13. W. Cai, A. R. Libertun, and R. Piestun, "Polarization selective computer-generated holograms realized in glass by femtosecond laser induced nanogratings.," Opt. Express **14**, 3785–91 (2006).

14. M. Beresna, M. Gecevičius, P. G. Kazansky, and T. Gertus, "Radially polarized optical vortex converter created by femtosecond laser nanostructuring of glass," Appl. Phys. Lett. **98**, 1–4 (2011).

15. Y. Shimotsuma, M. Sakakura, P. G. Kazansky, M. Beresna, J. J. Qiu, J. J. Qiu, K. Miura, and K. Hirao, "Ultrafast manipulation of self-assembled form birefringence in glass.," Adv. Mater. **22**, 4039–43 (2010).

16. R. Gattass and E. Mazur, "Femtosecond laser micromachining in transparent materials," Nat. Photonics **2**, 219–225 (2008).

17. C. B. Schaffer, A. Brodeur, and E. Mazur, "Laser-induced breakdown and damage in bulk transparent materials induced by tightly focused femtosecond laser pulses," Meas. Sci. Technol. **12**, 1784–1794 (2001).

18. L. V. Keldysh, "Ionization in the field of a strong electromagnetic wave," Sov. Phys. JETP **20**, 1307–1314 (1965).

19. H. Misawa and S. Juodkazis, *3D Laser Microfabrication. Principles and Applications* (Wiley-VCH, 2006).

20. M. D. Perry, B. C. Stuart, P. S. Banks, M. D. Feit, V. Yanovsky, and A. M. Rubenchik, "Ultrashort-pulse laser machining of dielectric materials," J. Appl. Phys. **85**, 6803 (1999).

21. L. Sudrie, A. Couairon, M. Franco, B. Lamouroux, B. Prade, S. Tzortzakis, and A. Mysyrowicz, "Femtosecond laser-induced damage and filamentary propagation in fused silica.," Phys. Rev. Lett. **89**, 186601 (2002).

22. D. G. Papazoglou, I. Zergioti, and S. Tzortzakis, "Plasma strings from ultraviolet laser filaments drive permanent structural modifications in fused silica," Opt. Lett. **32**, 2055–2057 (2007).

23. J. W. Chan, T. Huser, S. Risbud, and D. M. Krol, "Structural changes in fused silica after

exposure to focused femtosecond laser pulses.," Opt. Lett. **26**, 1726–1728 (2001).

24. A. M. Streltsov and N. F. Borrelli, "Study of femtosecond-laser-written waveguides in glasses," J. Opt. Soc. Am. B **19**, 2496 (2002).

25. A. Zoubir, C. Rivero, R. Grodsky, K. Richardson, M. Richardson, T. Cardinal, and M. Couzi, "Laser-induced defects in fused silica by femtosecond IR irradiation," Phys. Rev. B - Condens. Matter Mater. Phys. **73**, 1–5 (2006).

26. V. R. Bhardwaj, P. B. Corkum, D. M. Rayner, C. Hnatovsky, E. Simova, and R. S. Taylor, "Stress in femtosecond-laser-written waveguides in fused silica.," Opt. Lett. **29**, 1312–1314 (2004).

27. D. Du, X. Liu, G. Korn, J. Squier, and G. Mourou, "Laser-induced breakdown by impact ionization in SiO2 with pulse widths from 7 ns to 150 fs," Appl. Phys. Lett. **64**, 3071–3073 (1994).

28. J. Qiu, K. Miura, and K. Hirao, "Femtosecond laser-induced microfeatures in glasses and their applications," J. Non. Cryst. Solids **354**, 1100–1111 (2008).

29. E. N. Glezer, M. Milosavljevic, L. Huang, R. J. Finlay, T. H. Her, J. P. Callan, and E. Mazur, "Three-dimensional optical storage inside transparent materials.," Opt. Lett. **21**, 2023–2025 (1996).

30. M. Birnbaum, "Semiconductor Surface Damage Produced by Ruby Lasers," J. Appl. Phys. **36**, 3688 (1965).

31. J. Bonse, J. Krüger, S. Höhm, and A. Rosenfeld, "Femtosecond laser-induced periodic surface structures," J. Laser Appl. **24**, 42006 (2012).

32. S. K. Das, H. Messaoudi, A. Debroy, E. McGlynn, and R. Grunwald, "Multiphoton excitation of surface plasmon-polaritons and scaling of nanoripple formation in large bandgap materials," Opt. Mater. Express **3**, 1705 (2013).

33. Y. Han, X. Zhao, and S. Qu, "Polarization dependent ripples induced by femtosecond laser on dense flint (ZF6) glass.," Opt. Express **19**, 19150–5 (2011).

34. X. Shi, L. Jiang, X. Li, S. Wang, Y. Yuan, and Y. Lu, "Femtosecond laser-induced periodic structure adjustments based on electron dynamics control: from subwavelength ripples to double-grating structures.," Opt. Lett. **38**, 3743–6 (2013).

35. M. Straub, B. Weigand, M. Afshar, D. Feili, H. Seidel, and K. König, "Periodic subwavelength

ripples on lithium niobate surfaces generated by tightly focused sub-15 femtosecond sub-nanojoule pulsed near-infrared laser light," J. Opt. **15**, 55601 (2013).

36. R. Buividas, L. Rosa, R. Sliupas, T. Kudrius, G. Slekys, V. Datsyuk, and S. Juodkazis, "Mechanism of fine ripple formation on surfaces of (semi)transparent materials via a half-wavelength cavity feedback.," Nanotechnology **22**, 55304 (2011).

37. A. E. Siegman and P. M. Fauchet, "Stimulated Wood's Anomalies on Laser-Illuminated Surfaces," IEEE J. Quantum Electron. **22**, 1384–1403 (1986).

38. Z. Guosheng, P. M. Fauchet, and A. E. Siegman, "Spontaneous Periodic Surface Structures on Solids During Laser Illumination," Phys. Rev. B **26**, 5366 (1982).

39. Y. Yuan, L. Jiang, X. Li, C. Wang, H. Xiao, Y. Lu, and H. Tsai, "Formation mechanisms of sub-wavelength ripples during femtosecond laser pulse train processing of dielectrics," J. Phys. D. Appl. Phys. **45**, 175301 (2012).

40. M. Huang, F. Zhao, Y. Cheng, N. Xu, and Z. Xu, "Origin of laser-induced near-subwavelength ripples: Interference between surface plasmons and incident laser," ACS Nano **3**, 4062–4070 (2009).

41. J. E. Sipe, J. F. Young, J. S. Preston, and H. M. Van Driel, "Laser-induced periodic surface structure. I. Theory," Phys. Rev. B **27**, 1141–1154 (1983).

42. D. Dufft, A. Rosenfeld, S. K. Das, R. Grunwald, and J. Bonse, "Femtosecond laser-induced periodic surface structures revisited: A comparative study on ZnO," J. Appl. Phys. **105**, (2009).

43. A. Rosenfeld, M. Rohloff, S. Höhm, J. Krüger, and J. Bonse, "Formation of laser-induced periodic surface structures on fused silica upon multiple parallel polarized double-femtosecond-laser-pulse irradiation sequences," Appl. Surf. Sci. **258**, 9233–9236 (2012).

44. F. Liang, R. Vallée, and S. L. Chin, "Mechanism of nanograting formation on the surface of fused silica," Opt. Express **20**, 4389 (2012).

45. J. Wang and C. Guo, "Formation of extraordinarily uniform periodic structures on metals induced by femtosecond laser pulses," J. Appl. Phys. **100**, 1–5 (2006).

46. P. G. Kazansky, H. Inouye, T. Mitsuyu, K. Miura, J. Qiu, K. Hirao, and F. Starrost, "Anomalous Anisotropic Light Scattering in Ge-Doped Silica Glass," Phys. Rev. Lett. **82**, 2199 (1999).

47. L. Sudrie, M. Franco, B. Prade, and A. Mysyrowicz, "Writing of permanent birefringent microlayers in bulk fused silica with femtosecond laser pulses," Opt. Commun. **171**, 279–284 (1999).

48. Y. Shimotsuma, K. Hirao, J. Qiu, and P. G. Kazansky, "Nano-Modification Inside Transparent Materials By Femtosecond Laser Single Beam," Mod. Phys. Lett. B **19**, 225–238 (2005).

49. Y. Shimotsuma, K. Hirao, J. Qiu, and K. Miura, "Nanofabrication in transparent materials with a femtosecond pulse laser," J. Non. Cryst. Solids **352**, 646–656 (2006).

50. S. Richter, C. Miese, S. Döring, F. Zimmermann, M. J. Withford, A. Tünnermann, and S. Nolte, "Laser induced nanogratings beyond fused silica - periodic nanostructures in borosilicate glasses and ULE^{TM}," Opt. Mater. Express **3**, 1161 (2013).

51. M. Lancry, F. Zimmerman, R. Desmarchelier, J. Tian, F. Brisset, S. Nolte, and B. Poumellec, "Nanogratings formation in multicomponent silicate glasses," Appl. Phys. B Lasers Opt. **122**, 1–8 (2016).

52. J. Cao, L. Mazerolles, M. Lancry, D. Solas, F. Brisset, and B. Poumellec, "Form birefringence induced in multicomponent glass by femtosecond laser direct writing," Opt. Lett. **41**, 2739 (2016).

53. D. Wortmann, J. Gottmann, N. Brandt, and H. Horn-Solle, "Micro- and nanostructures inside sapphire by fs-laser irradiation and selective etching," 2008 Conf. Quantum Electron. Laser Sci. Conf. Lasers Electro-Optics, CLEO/QELS **16**, 197–200 (2008).

54. J. Gottmann, D. Wortmann, and M. Hörstmann-Jungemann, "Fabrication of sub-wavelength surface ripples and in-volume nanostructures by fs-laser induced selective etching," Appl. Surf. Sci. **255**, 5641–5646 (2009).

55. W. Yang, E. Bricchi, P. G. Kazansky, J. Bovatsek, and A. Y. Arai, "Self-assembled periodic sub-wavelength structures by femtosecond laser direct writing.," Opt. Express **14**, 10117–24 (2006).

56. M. Lancry, B. Poumellec, J. Canning, K. Cook, J. C. Poulin, and F. Brisset, "Ultrafast nanoporous silica formation driven by femtosecond laser irradiation," Laser Photonics Rev. **7**, 953–962 (2013).

57. Y. Liao, J. Ni, L. Qiao, M. Huang, Y. Bellouard, K. Sugioka, and Y. Cheng, "High-fidelity visualization of formation of volume nanogratings in porous glass by femtosecond laser irradiation," Optica **2**, 329 (2015).

58. J. Zhang, M. Gecevičius, M. Beresna, and P. G. Kazansky, "Seemingly unlimited lifetime data storage in nanostructured glass," Phys. Rev. Lett. **112**, 1–5 (2014).

59. J. Zhang, A. Čerkauskaitė, R. Drevinskas, A. Patel, M. Beresna, and P. G. Kazansky, "Eternal 5D data storage by ultrafast laser writing in glass," Spie **9736**, 97360U (2016).

60. R. S. Taylor, C. Hnatovsky, E. Simova, P. P. Rajeev, D. M. Rayner, and P. B. Corkum, "Femtosecond laser erasing and rewriting of self-organized planar nanocracks in fused silica glass.," Opt. Lett. **32**, 2888–2890 (2007).

61. M. Beresna, M. Gecevičius, P. G. Kazansky, T. Taylor, and A. V. Kavokin, "Exciton mediated self-organization in glass driven by ultrashort light pulses," Appl. Phys. Lett. **101**, 53120 (2012).

62. M. Beresna, M. Gecevičius, and P. G. Kazansky, "Polarization sensitive elements fabricated by femtosecond laser nanostructuring of glass [Invited]," Opt. Mater. Express **1**, 783 (2011).

63. R. Drevinskas, M. Beresna, M. Gecevičius, M. Khenkin, A. G. Kazanskii, I. Matulaitienė, G. Niaura, O. I. Konkov, E. I. Terukov, Y. P. Svirko, and P. G. Kazansky, "Giant birefringence and dichroism induced by ultrafast laser pulses in hydrogenated amorphous silicon," Appl. Phys. Lett. **106**, 171106 (2015).

64. R. Taylor, C. Hnatovsky, and E. Simova, "Applications of femtosecond laser induced self-organized planar nanocracks inside fused silica glass," Laser Photonics Rev. **2**, 26–46 (2008).

65. E. Bricchi, J. D. Mills, P. G. Kazansky, B. G. Klappauf, and J. J. Baumberg, "Birefringent Fresnel zone plates in silica fabricated by femtosecond laser machining.," Opt. Lett. **27**, 2200–2 (2002).

66. S. J. Mihailov, D. Grobnic, C. W. Smelser, P. Lu, R. B. Walker, and H. Ding, "Bragg grating inscription in various optical fibers with femtosecond infrared lasers and a phase mask," Opt. Mater. Express **1**, 754 (2011).

67. J. D. Mills, P. G. Kazansky, E. Bricchi, and J. J. Baumberg, "Embedded anisotropic microreflectors by femtosecond-laser nanomachining," Appl. Phys. Lett. **81**, 196 (2002).

68. M. Gecevičius, M. Beresna, and P. G. Kazansky, "Polarization sensitive camera by femtosecond laser nanostructuring.," Opt. Lett. **38**, 4096–9 (2013).

69. M. Gecevičius, R. Drevinskas, M. Beresna, and P. G. Kazansky, "Single beam optical vortex tweezers with tunable orbital angular momentum," Appl. Phys. Lett. **104**, 1–5 (2014).

70. W. A. Clarkson, D. Lin, M. Beresna, P. G. Kazansky, and P. C. Shardlow, "High Power Fiber Lasers with Radially Polarized Output Beams," in *Conference on Lasers and Electro-Optics, OSA Technical Digest* (Optical Society of America, 2016).

71. M. Gecevičius, M. Beresna, R. Drevinskas, and P. G. Kazansky, "Airy beams generated by ultrafast laser-imprinted space-variant nanostructures in glass.," Opt. Lett. **39**, 6791–4 (2014).

72. D. H. Auston, K. P. Cheung, J. A. Valdmanis, and D. A. Kleinman, "Cherenkov radiation from femtosecond optical pulses in electro-optic media," Phys. Rev. Lett. **53**, 1555–1558 (1984).

73. E. N. Glezer and E. Mazur, "Ultrafast-laser driven micro-explosions in transparent materials," Appl. Phys. Lett. **71**, 882 (1997).

74. E. G. Gamaly, L. Rapp, V. Roppo, S. Juodkazis, and A. V. Rode, "Generation of high energy density by fs-laser-induced confined microexplosion," New J. Phys. **15**, (2013).

75. M. Lenzner, J. Krüger, S. Sartania, Z. Cheng, C. Spielmann, G. Mourou, W. Kautek, and F. Krausz, "Femtosecond optical breakdown in dielectrics," Phys. Rev. Lett. **80**, 4076–4079 (1998).

76. B. C. Stuart, M. D. Feit, S. Herman, A. M. Rubenchik, B. W. Shore, and M. D. Perry, "Nanosecond-to-femtosecond laser-induced breakdown in dielectrics.," Phys. Rev. B. Condens. Matter **53**, 1749–1761 (1996).

77. L. P. R. Ramirez, M. Heinrich, S. Richter, F. Dreisow, R. Keil, A. V. Korovin, U. Peschel, S. Nolte, and A. Tünnermann, "Tuning the structural properties of femtosecond-laser-induced nanogratings," Appl. Phys. A **100**, 1–6 (2010).

78. A. I. Avrov, V. Y. Bychenkov, N. Krokhin, V. V Pustovalov, A. A. Rupasov, V. P. Silin, G. V Sklizkov, V. T. Tikhonchuk, and A. S. Shikanov, "Generation of the (3/2)w harmonic of the neodymium-laser radiation during the heating of spherical targets," Zh. Eksp. Teor. Fiz., **72**, 970 (1977).

79. P. G. Kazansky, E. Bricchi, Y. Shimotsuma, and K. Hirao, "Self-Assembled Nanostructures and Two-Plasmon Decay in Femtosecond Processing of Transparent Materials," CLEO Sci. Innov. (2007).

80. M. Watanabe, S. Juodakis, J. Nishii, S. Matsuo, and H. Misawa, "Microfabrications by a High Fluence Femtosecond Exposure: Mechanism and Applications," SPIE **4637**, 159–168 (2002).

81. A. Simon, R. W. Short, E. A. Williams, and T. Dewandre, "On the inhomogeneous two-plasmon instability," Phys. Fluids **26**, 3107 (1983).

82. L. Veisz, W. Theobald, T. Feurer, H. Schillinger, P. Gibbon, R. Sauerbrey, and M. S. Jovanović, "Three-halves harmonic emission from femtosecond laser produced plasmas," Phys. Plasmas **9**, 3197 (2002).

83. L. Veisz, W. Theobald, T. Feurer, H. Schwoerer, I. Uschmann, O. Renner, and R. Sauerbrey, "Three-halves harmonic emission from femtosecond laser produced plasmas with steep density gradients," Phys. Plasmas **11**, 3311 (2004).

84. W. Kruer, "Simulations of electromagnetic wave plasma interactions," Radio Sci. **25**, 1351–1357 (1990).

85. C. Hnatovsky, R. S. Taylor, P. P. Rajeev, E. Simova, V. R. Bhardwaj, D. M. Rayner, and P. B. Corkum, "Pulse duration dependence of femtosecond-laser-fabricated nanogratings in fused silica," Appl. Phys. Lett. **87**, 14104 (2005).

86. R. Buschlinger, S. Nolte, and U. Peschel, "Self-organized pattern formation in laser-induced multiphoton ionization," Phys. Rev. B - Condens. Matter Mater. Phys. **89**, 1–10 (2014).

87. P. P. Rajeev, M. Gertsvolf, C. Hnatovsky, E. Simova, R. S. Taylor, P. B. Corkum, D. M. Rayner, and V. R. Bhardwaj, "Transient nanoplasmonics inside dielectrics," J. Phys. B At. Mol. Opt. Phys. **40**, S273–S282 (2007).

88. G. Malpuech, A. Kavokin, and G. Panzarini, "Propagation of exciton polaritons in inhomogeneous semiconductor films," Phys. Rev. B **60**, 16788–16798 (1999).

89. W. Watanabe and K. Itoh, "Motion of bubble in solid by femtosecond laser pulses," Opt. Express **10**, 603–608 (2002).

90. J. H. Marburger, "Self-focusing: Theory," Prog. Quantum Electron. **4**, 35–110 (1975).

91. S. Kanehira, J. Si, J. Qiu, K. Fujita, and K. Hirao, "Periodic nanovoid structures via femtosecond laser irradiation," Nano Lett. **5**, 1591–1595 (2005).

92. E. Toratani, M. Kamata, and M. Obara, "Self-fabrication of void array in fused silica by femtosecond laser processing," Appl. Phys. Lett. **87**, 1–3 (2005).

93. A. Vogel, N. Linz, S. Freidank, and G. Paltauf, "Femtosecond-laser-induced nanocavitation in water: Implications for optical breakdown threshold and cell surgery," Phys. Rev. Lett. **100**, 1–4 (2008).

94. C. Mauclair, A. Mermillod-Blondin, S. Landon, N. Huot, A. Rosenfeld, I. V Hertel, E. Audouard, I. Myiamoto, and R. Stoian, "Single-pulse ultrafast laser imprinting of axial dot arrays in bulk glasses," Opt. Lett. **36**, 325–327 (2011).

95. W. Watanabe, T. Toma, K. Yamada, J. Nishii, K. Hayashi, and K. Itoh, "Optical seizing and merging of voids in silica glass with infrared femtosecond laser pulses," Opt. Lett. **25**, 1669–1671 (2000).

96. H. Y. Sun, J. Song, C. B. Li, J. Xu, X. S. Wang, Y. Cheng, Z. Z. Xu, J. R. Qiu, and T. Q. Jia, "Standing electron plasma wave mechanism of void array formation inside glass by femtosecond laser irradiation," Appl. Phys. A-Materials Sci. Process. **88**, 285–288 (2007).

97. J. Song, X. Wang, X. Hu, Y. Dai, J. Qiu, Y. Cheng, and Z. Xu, "Formation mechanism of self-organized voids in dielectrics induced by tightly focused femtosecond laser pulses," Appl. Phys. Lett. **92**, 152–155 (2008).

98. M. Terakawa, E. Toratani, T. Shirakawa, and M. Obara, "Fabrication of a void array in dielectric materials by femtosecond laser micro-processing for compact photonic devices," Appl. Phys. A Mater. Sci. Process. **100**, 1041–1047 (2010).

99. E. Toratani, M. Kamata, and M. Obara, "Self-organization of nano-void array for photonic crystal device," Microelectron. Eng. **83**, 1782–1785 (2006).

100. M. Beresna, M. Gecevičius, N. M. Bulgakova, and P. G. Kazansky, "Twisting light with micro-spheres produced by ultrashort light pulses.," Opt. Express **19**, 18989–96 (2011).

101. K. Mishchik, C. D'Amico, P. K. Velpula, C. Mauclair, a. Boukenter, Y. Ouerdane, and R. Stoian, "Ultrafast laser induced electronic and structural modifications in bulk fused silica," J. Appl. Phys. **114**, (2013).

102. A.-C. Tien, S. Backus, H. Kapteyn, M. Murnane, and G. Mourou, "Short-Pulse Laser Damage in Transparent Materials as a Function of Pulse Duration," Phys. Rev. Lett. **82**, 3883–3886 (1999).

103. O. Gessner, A. M. D. Lee, J. P. Shaffer, H. Reisler, S. V. Levchenko, A. I. Krylov, J. G. Underwood, H. Shi, A. L. L. East, D. M. Wardlaw, E. t. H. Chrysostom, C. C. Hayden, and A. Stolow, "Femtosecond multidimensional imaging of a molecular dissociation," Science **311**,

219–222 (2006).

104. T. Brixner, N. H. Damrauer, P. Niklaus, and G. Gerber, "Photoselective adaptive femtosecond quantum control in the liquid phase.," Nature **414**, 57–60 (2001).

105. W. R. Zipfel, R. M. Williams, and W. W. Webb, "Nonlinear magic: multiphoton microscopy in the biosciences.," Nat. Biotechnol. **21**, 1369–1377 (2003).

106. S. H. Chung and E. Mazur, "Surgical applications of femtosecond lasers," J. Biophotonics **2**, 557–572 (2009).

107. D. Strickland and G. Mourou, "Compression of amplified chirped optical pulses," Opt. Commun. **55**, 447–449 (1985).

108. M. D. Perry and G. Mourou, "Terawatt to petawatt subpicosecond lasers.," Science **264**, 917–924 (1994).

109. F. He, H. Xu, Y. Cheng, J. Ni, H. Xiong, Z. Xu, K. Sugioka, and K. Midorikawa, "Fabrication of microfluidic channels with a circular cross section using spatiotemporally focused femtosecond laser pulses.," Opt. Lett. **35**, 1106–1108 (2010).

110. F. He, Z. Wang, B. Zeng, J. Ni, W. Chu, K. Sugioka, and Y. Cheng, "Three-dimensional patterning in transparent materials with spatiotemporally focused femtosecond laser pulses," in *Optoelectronic Imaging and Multimedia Technology III* (2014), Vol. 9273, p. 927316.

111. R. Kammel, R. Ackermann, J. Thomas, J. Götte, S. Skupin, A. Tünnermann, and S. Nolte, "Enhancing precision in fs-laser material processing by simultaneous spatial and temporal focusing," Light Sci. Appl. **3**, e169 (2014).

112. C. G. Durfee and J. A. Squier, "Breakthroughs in photonics 2014: Spatiotemporal focusing: Advances and applications," IEEE Photonics J. **7**, 1–6 (2015).

113. J. U. Thomas, E. Block, M. Greco, A. Meier, C. G. Durfee, J. A. Squier, S. Nolte, and A. Tünnermann, "Simultaneously spatially and temporally focusing light for tailored ultrafast micro-machining," Spie Lase **8972**, 897219 (2014).

114. O. Katz, Y. Bromberg, E. Small, and Y. Silberberg, "Focusing and Compression of Ultrashort Pulses through Scattering Media," Nat. Photonics **5**, 1–6 (2010).

115. M. E. Durst, G. Zhu, and C. Xu, "Simultaneous spatial and temporal focusing for axial scanning.," Opt. Express **14**, 12243–54 (2006).

116. M. E. Durst, G. Zhu, and C. Xu, "Simultaneous spatial and temporal focusing in nonlinear microscopy," Opt. Commun. **281**, 1796–1805 (2008).

117. E. Block, M. Greco, D. Vitek, O. Masihzadeh, D. A. Ammar, M. Y. Kahook, N. Mandava, C. Durfee, and J. Squier, "Simultaneous spatial and temporal focusing for tissue ablation.," Biomed. Opt. Express **4**, 831–41 (2013).

118. D. J. McCabe, A. Tajalli, D. R. Austin, P. Bondareff, I. A. Walmsley, S. Gigan, and B. Chatel, "Spatio-temporal focusing of an ultrafast pulse through a multiply scattering medium.," Nat. Commun. **2**, 447 (2011).

119. X. Gu, S. Akturk, and R. Trebino, "Spatial chirp in ultrafast optics," Opt. Commun. **242**, 599–604 (2004).

120. P. Gabolde, D. Lee, S. Akturk, and R. Trebino, "Describing first-order spatio-temporal distortions in ultrashort pulses using normalized parameters.," Opt. Express **15**, 242–51 (2007).

121. Z. Bor, B. Racz, G. Szabo, M. Hilbert, and H. A. Hazim, "Femtosecond pulse front tilt caused by angular dispersion," Opt. Eng. **32**, 2501–2504 (1993).

122. J. P. Torres, M. Hendrych, and A. Valencia, "Angular dispersion: an enabling tool in nonlinear and quantum optics," Adv. Opt. Photonics **2**, 319 (2010).

123. J. A. Wheeler, A. Borot, S. Monchocé, H. Vincenti, A. Ricci, A. Malvache, F. Quéré, and R. Lopez-Martens, "Attosecond lighthouses from plasma mirrors," Nat. Photonics **6**, 829–833 (2012).

124. H. Vincenti and F. Quéré, "Attosecond lighthouses: How to use spatiotemporally coupled light fields to generate isolated attosecond pulses," Phys. Rev. Lett. **108**, 1–5 (2012).

125. R. Trebino, P. Bowlan, P. Gabolde, X. Gu, S. Akturk, and M. Kimmel, "Simple devices for measuring complex ultrashort pulses," Laser Photonics Rev. **3**, 314–332 (2009).

126. S. Akturk, X. Gu, P. Gabolde, and R. Trebino, "The general theory of first-order spatio-temporal distortions of Gaussian pulses and beams.," Opt. Express **13**, 8642–61 (2005).

127. A. G. Kostenbauder, "Ray-Pulse Matrices: A Rational Treatment for Dispersive Optical Systems," IEEE J. Quantum Electron. **26**, 1148–1157 (1990).

128. I. Newton, "The Third Book of Opticks. Part I.," in *Opticks: Or, A Treatise of the Reflections, Refractions, Inflections and Colours of Light*, Opticks: Or, A Treatise of the Reflections,

Refractions, Inflections and Colours of Light (William Innys at the West-End of St. Paul's., 1730), p. Quest. 31.

129. S. Akturk, X. Gu, E. Zeek, and R. Trebino, "Pulse-front tilt caused by spatial and temporal chirp.," Opt. Express **12**, 4399–410 (2004).

130. J. P. Heritage, A. M. Weiner, and R. N. Thurston, "Picosecond pulse shaping by spectral phase and amplitude manipulation.," Opt. Lett. **10**, 609–611 (1985).

131. A. M. Weiner, J. P. Heritage, and E. M. Kirschner, "High-resolution femtosecond pulse shaping," J. Opt. Soc. Am. B **5**, 1563 (1988).

132. A. M. Weiner, "Ultrafast optical pulse shaping: A tutorial review," Opt. Commun. **284**, 3669–3692 (2011).

133. Y. Silberberg, "Quantum coherent control for nonlinear spectroscopy and microscopy.," Annu. Rev. Phys. Chem. **60**, 277–292 (2009).

134. G. Zhu, J. van Howe, M. Durst, W. Zipfel, and C. Xu, "Simultaneous spatial and temporal focusing of femtosecond pulses.," Opt. Express **13**, 2153–9 (2005).

135. D. Oron, E. Tal, and Y. Silberberg, "Scanningless depth-resolved microscopy.," Opt. Express **13**, 1468–1476 (2005).

136. D. N. Vitek, E. Block, Y. Bellouard, D. E. Adams, S. Backus, D. Kleinfeld, C. G. Durfee, and J. A. Squier, "Spatio-temporally focused femtosecond laser pulses for nonreciprocal writing in optically transparent materials," Opt. Express **18**, 24673–24678 (2010).

137. N. Gorunski, N. Dimitrov, A. Dreischuh, and G. G. Paulus, "Pulse-front tilt created in misaligned dispersionless optical systems and correct interferometric autocorrelation," Opt. Commun. **283**, 5192–5198 (2010).

138. J. Hebling, "Derivation of the pulse front tilt caused by angular dispersion," Opt. Quantum Electron. **28**, 1759–1763 (1996).

139. C. Dorrer, E. M. Kosik, and I. a. Walmsley, "Spatio-temporal characterization of the electric field of ultrashort optical pulses using two-dimensional shearing interferometry," Appl. Phys. B Lasers Opt. **74**, s209–s217 (2002).

140. T. R. Zhang, H. R. Choo, and M. C. Downer, "Phase and group velocity matching for second harmonic generation of femtosecond pulses.," Appl. Opt. **29**, 3927–3933 (1990).

141. A. Dubietis, G. Valiulis, G. Tamosauskas, R. Danielius, and A. Piskarskas, "Nonlinear second-harmonic pulse compression with tilted pulses.," Opt. Lett. **22**, 1071–1073 (1997).

142. R. Danielius, A. Piskarskas, P. Di Trapani, A. Andreoni, C. Solcia, and P. Foggi, "Matching of group velocities by spatial walk-off in collinear three-wave interaction with tilted pulses.," Opt. Lett. **21**, 973–5 (1996).

143. T. Kobayashi and A. Shirakawa, "Tunable visible and near-infrared pulse generator in a 5fs regime," Appl. Phys. B **70**, S239–S246 (2000).

144. J. Hebling, K.-L. Yeh, M. C. Hoffmann, B. Bartal, and K. A. Nelson, "Generation of high-power terahertz pulses by tilted-pulse-front excitation and their application possibilities," J. Opt. Soc. Am. B **25**, B6 (2008).

145. J. Hebling, G. Almasi, I. Kozma, and J. Kuhl, "Velocity matching by pulse front tilting for large area THz-pulse generation.," Opt. Express **10**, 1161–1166 (2002).

146. A. Stepanov, J. Kuhl, I. Kozma, E. Riedle, G. Almási, and J. Hebling, "Scaling up the energy of THz pulses created by optical rectification.," Opt. Express **13**, 5762–5768 (2005).

147. F. Quéré, H. Vincenti, A. Borot, S. Monchocé, T. J. Hammond, K. T. Kim, J. a Wheeler, C. Zhang, T. Ruchon, T. Auguste, J. F. Hergott, D. M. Villeneuve, P. B. Corkum, and R. Lopez-Martens, "Applications of ultrafast wavefront rotation in highly nonlinear optics," J. Phys. B At. Mol. Opt. Phys. **47**, 124004 (2014).

148. K. T. Kim, C. Zhang, T. Ruchon, J.-F. Hergott, T. Auguste, D. M. Villeneuve, P. B. Corkum, and F. Quéré, "Photonic streaking of attosecond pulse trains," Nat. Photonics **7**, 651–656 (2013).

149. X. Gu, S. Akturk, A. Shreenath, Q. Cao, and R. Trebino, "The Measurement of Ultrashort Light Pulses — Simple Devices , Complex Pulses," Opt. Rev. **11**, 141–152 (2004).

150. S. Akturk, X. Gu, P. Bowlan, and R. Trebino, "Spatio-temporal couplings in ultrashort laser pulses," J. Opt. **12**, 93001 (2010).

151. R. Trebino, *Frequency-Resolved Optical Gating: The Measurement of Ultrashort Laser Pulses* (Kluwer Academic Publishers, 2000).

152. O. E. Martinez, "Matrix Formalism for Pulse Compressors," IEEE J. Quantum Electron. **24**, 2530–2536 (1988).

153. D. J. Kane and R. Trebino, "Characterization of Arbitrary Femtosecond Pulses Using

Frequency -Resolved Optical Gating," Quantum Electron. IEEE J. **29**, 571–579 (1993).

154. S. Akturk, M. Kimmel, P. O'Shea, and R. Trebino, "Measuring pulse-front tilt in ultrashort pulses using GRENOUILLE.," Opt. Express **11**, 491–501 (2003).

155. S. Akturk, M. Kimmel, P. O'Shea, and R. Trebino, "Measuring spatial chirp in ultrashort pulses using single-shot Frequency-Resolved Optical Gating.," Opt. Express **11**, 68–78 (2003).

156. J. B. Ashcom, R. R. Gattass, C. B. Schaffer, and E. Mazur, "Numerical aperture dependence of damage and supercontinuum generation from femtosecond laser pulses in bulk fused silica," J. Opt. Soc. Am. B **23**, 2317 (2006).

157. A. Marcinkevičius, V. Mizeikis, S. Juodkazis, S. Matsuo, and H. Misawa, "Effect of refractive index-mismatch on laser microfabrication in silica glass," Appl. Phys. A Mater. Sci. Process. **76**, 257–260 (2003).

158. C. B. Schaffer, A. Brodeur, J. F. García, and E. Mazur, "Micromachining bulk glass by use of femtosecond laser pulses with nanojoule energy," Opt. Lett. **26**, 93–95 (2001).

159. S. V. Chekalin and V. P. Kandidov, "From self-focusing light beams to femtosecond laser pulse filamentation," Uspekhi Fiz. Nauk **183**, 133–152 (2013).

160. A. Couairon and A. Mysyrowicz, "Femtosecond filamentation in transparent media," Phys. Rep. **441**, 47–189 (2007).

161. A. Brodeur and S. L. Chin, "Ultrafast white-light continuum generation and self-focusing in transparent condensed media," J. Opt. Soc. Am. B **16**, 637 (1999).

162. E. Small, O. Katz, and Y. Silberberg, "Spatiotemporal focusing through a thin scattering layer.," Opt. Express **20**, 5189–95 (2012).

163. L.-C. Cheng, C.-Y. Chang, C.-Y. Lin, K.-C. Cho, W.-C. Yen, N.-S. Chang, C. Xu, C. Y. Dong, and S.-J. Chen, "Spatiotemporal focusing-based widefield multiphoton microscopy for fast optical sectioning," Opt. Express **20**, 8939 (2012).

164. D. N. Vitek, D. E. Adams, A. Johnson, P. S. Tsai, S. Backus, C. G. Durfee, D. Kleinfeld, and J. A. Squier, "Temporally focused femtosecond laser pulses for low numerical aperture micromachining through optically transparent materials.," Opt. Express **18**, 18086–94 (2010).

165. M. Gecevičius, M. Beresna, J. Zhang, W. Yang, H. Takebe, and P. G. Kazansky,

"Extraordinary anisotropy of ultrafast laser writing in glass.," Opt. Express **21**, 3959–68 (2013).

166. P. S. Salter and M. J. Booth, "Dynamic control of directional asymmetry observed in ultrafast laser direct writing," Appl. Phys. Lett. **101**, 141109 (2012).

167. P. Kazansky, M. Beresna, Y. Shimotsuma, M. Gecevicius, M. Sakakura, C. Corbari, K. Miura, K. Hirao, and Y. Bellouard, "Phase transitions induced by ultrafast laser writing in transparent materials," CLEO2011 - Laser Appl. to Photonic Appl. JTuI106 (2011).

168. C. Corbari, A. Champion, M. Gecevičius, M. Beresna, Y. Bellouard, and P. G. Kazansky, "Femtosecond versus picosecond laser machining of nano-gratings and micro-channels in silica glass.," Opt. Express **21**, 3946–58 (2013).

169. T. T. Fernandez, J. Siegel, J. Hoyo, B. Sotillo, P. Fernandez, and J. Solis, "Controlling plasma distributions as driving forces for ion migration during fs laser writing," J. Phys. D. Appl. Phys. **48**, 155101 (2015).

170. D. Rayner, A. Naumov, and P. Corkum, "Ultrashort pulse non-linear optical absorption in transparent media.," Opt. Express **13**, 3208–3217 (2005).

171. C. G. Durfee, M. Greco, E. Block, D. Vitek, and J. A. Squier, "Intuitive analysis of space-time focusing with double-ABCD calculation.," Opt. Express **20**, 14244–59 (2012).

172. S. Zhang, D. Asoubar, R. Kammel, S. Nolte, and F. Wyrowski, "Analysis of Pulse Front Tilt in Simultaneous Spatial and Temporal Focusing," JOSA A **31**, 2437–2446 (2014).

173. Y. Dai, G. Wu, X. Lin, G. Ma, and J. Qiu, "Femtosecond laser induced rotated 3D self-organized nanograting in fused silica," Opt. Express **20**, 18072 (2012).

174. Y. Dai, J. Ye, M. Gong, X. Ye, X. Yan, G. Ma, and J. Qiu, "Forced rotation of nanograting in glass by pulse-front tilted femtosecond laser direct writing.," Opt. Express **22**, 28500–5 (2014).

175. Z. Wang, B. Zeng, G. Li, H. Xie, W. Chu, F. He, Y. Liao, W. Liu, H. Gao, and Y. Cheng, "Time-resolved shadowgraphs of transient plasma induced by spatiotemporally focused femtosecond laser pulses in fused silica glass," Opt. Lett. **40**, 5726 (2015).

176. Thor Labs, *Pulse Characterization FROG Scanning Module User Guide* (2012).

177. G. Cerullo and S. De Silvestri, "Ultrafast optical parametric amplifiers," Rev. Sci. Instrum. **74**, 1–18 (2003).

178. A. Zaukevičius, V. Jukna, R. Antipenkov, V. Martinėnaitė, A. Varanavičius, A. P. Piskarskas, and G. Valiulis, "Manifestation of spatial chirp in femtosecond noncollinear optical parametric chirped-pulse amplifier," JOSA B **28**, 2902–2908 (2011).

179. J. Bromage, C. Dorrer, and J. D. Zuegel, "Angular-dispersion-induced spatiotemporal aberrations in noncollinear optical parametric amplifiers.," Opt. Lett. **35**, 2251–2253 (2010).

180. A. M. Weiner, *Ultrafast Optics* (John Wiley and Sons, 2009).

181. B. Sun, P. S. Salter, and M. J. Booth, "Effects of aberrations in spatiotemporal focusing of ultrashort laser pulses.," J. Opt. Soc. Am. A. Opt. Image Sci. Vis. **31**, 765–72 (2014).

182. J.-C. Diels and W. Rudolph, *Ultrashort Laser Pulse Phenomena: Fundamentals, Techniques, and Applications on a Femtosecond Time Scale* (2006).

183. M. Padgett and J. Lesso, "Dove prisms and polarized light," J. Mod. Opt. 37–41 (1999).

184. I. Moreno, "Jones matrix for image-rotation prisms.," Appl. Opt. **43**, 3373–81 (2004).

185. M. Shribak and R. Oldenbourg, "Techniques for fast and sensitive measurements of two-dimensional birefringence distributions.," Appl. Opt. **42**, 3009–3017 (2003).

186. A. Barty, K. A. Nugent, D. Paganin, and A. Roberts, "Quantitative optical phase microscopy.," Opt. Lett. **23**, 817–819 (1998).

187. D. Paganin and K. a. Nugent, "Noninterferometric phase imaging with partially coherent light," Phys. Rev. Lett. **80**, 2586–2589 (1998).

188. P. G. Kazansky, H. Inouye, T. Mitsuyu, J. Qui, K. Hirao, and F. Starrost, "Anisotropic Cherenkov light generation by intense ultrashort light pulses in glass," in *Quantum Electronics and Laser Science Conference, 2000.* (2000), pp. 138–139.

189. J. V. Jelley, *Cerenkov Radiation And Its Applications* (Pergammon Press Ltd., 1958).

190. M. Beresna, M. Gecevičius, and P. G. Kazansky, "Ultrafast laser direct writing and nanostructuring in transparent materials," Adv. Opt. Photonics **6**, 293–339 (2014).

191. R. Graf, A. Fernandez, M. Dubov, H. J. Brueckner, B. N. Chichkov, and A. Apolonski, "Pearl-chain waveguides written at megahertz repetition rate," Appl. Phys. B **87**, 21–27 (2006).

192. A. Srivastava and D. Goswami, "Control of supercontinuum generation with polarization of incident laser pulses," Appl. Phys. B Lasers Opt. **77**, 325–328 (2003).

193. V. V. Temnov, K. Sokolowski-Tinten, P. Zhou, A. El-Khamhawy, and D. von der Linde, "Multiphoton Ionization in Dielectrics: Comparison of Circular and Linear Polarization," Phys. Rev. Lett. **97**, 237403 (2006).

194. W. Gawelda, D. Puerto, J. Siegel, A. Ferrer, A. Ruiz de la Cruz, H. Fernández, and J. Solis, "Ultrafast imaging of transient electronic plasmas produced in conditions of femtosecond waveguide writing in dielectrics," Appl. Phys. Lett. **93**, 121109 (2008).

195. D. Liu, Y. Li, M. Liu, H. Yang, and Q. Gong, "The polarization-dependence of femtosecond laser damage threshold inside fused silica," Appl. Phys. B **91**, 597–599 (2008).

196. B. Poumellec, M. Lancry, A. Chahid-Erraji, and P. G. Kazansky, "Modification thresholds in femtosecond laser processing of pure silica: review of dependencies on laser parameters [Invited]," Opt. Mater. Express **1**, 766 (2011).

197. S. I. Kudryashov, V. D. Zvorykin, A. A. Ionin, V. Mizeikis, S. Juodkazis, and H. Misawa, "Acoustic monitoring of microplasma formation and filamentation of tightly focused femtosecond laser pulses in silica glass," Appl. Phys. Lett. **92**, 101916 (2008).

198. C. Hnatovsky, D. Grobnic, and S. J. Mihailov, "In Situ Monitoring of Fiber Bragg Grating Evolution During Femtosecond-laser Inscription Process," in *Photonics and Fiber Technology 2016 (ACOFT, BGPP, NP)* (Optical Society of America, 2016), p. BTh3B.2.

199. F. He, B. Zeng, W. Chu, J. Ni, K. Sugioka, Y. Cheng, and C. G. Durfee, "Characterization and control of peak intensity distribution at the focus of a spatiotemporally focused femtosecond laser beam.," Opt. Express **22**, 9734–48 (2014).

200. S. Zhang, F. Wyrowski, R. Kammel, S. Nolte, D. Asoubar, R. Kammel, S. Nolte, F. Wyrowski, R. Kammel, and S. Nolte, "Analysis of Pulse Front Tilt in Simultaneous Spatial and Temporal Focusing," JOSA A **9135**, 2437–2446 (2014).

201. N. M. Bulgakova, V. P. Zhukov, and Y. P. Meshcheryakov, "Theoretical treatments of ultrashort pulse laser processing of transparent materials: toward understanding the volume nanograting formation and “quill” writing effect," Appl. Phys. B **113**, 437–449 (2013).

202. M. Born and E. Wolf, *Principles of Optics* (Pergammon Press Ltd., 1980).

203. P. M. J. H. Wormell, "Advanced optical imaging theory," Opt. Lasers Eng. **33**, 237–238 (2000).

204. L. W. Davis, "Theory of electromagnetic beams," Phys. Rev. A **19**, 1177–1179 (1979).

205. Y. I. Salamin, "Fields of a Gaussian beam beyond the paraxial approximation," Appl. Phys. B Lasers Opt. **86**, 319–326 (2007).

206. J. Zhang, R. Drevinskas, M. Beresna, and P. G. Kazansky, "Polarization sensitive anisotropic structuring of silicon by ultrashort light pulses," Appl. Phys. Lett. **41114**, 2–6 (2015).

207. A. Rudenko, J. Colombier, and T. E. Itina, "From random inhomogeneities to periodic nanostructures induced in bulk silica by ultrashort laser," Phys. Rev. B **75427**, 1–13 (2016).

208. R. Kammel, K. Bergner, J. U. Thomas, R. Ackermann, S. Skupin, and S. Nolte, "Simultaneous spatial and temporal focusing: A route towards confined nonlinear materials processing," Proc. SPIE **9736**, 1–10 (2016).

209. K. Sugioka and Y. Cheng, "Ultrafast lasers—reliable tools for advanced materials processing," Light Sci. Appl. **3**, e149 (2014).

210. S. Richter, F. Jia, M. Heinrich, S. Döring, U. Peschel, A. Tünnermann, and S. Nolte, "The role of self-trapped excitons and defects in the formation of nanogratings in fused silica," Opt. Lett. **37**, 482 (2012).

211. Y. Liao, W. Pan, Y. Cui, L. Qiao, Y. Bellouard, K. Sugioka, and Y. Cheng, "Formation of in-volume nanogratings with sub-100-nm periods in glass by femtosecond laser irradiation," Opt. Lett. **40**, 3623 (2015).

212. R. Le Harzic, D. Dörr, D. Sauer, M. Neumeier, M. Epple, H. Zimmermann, and F. Stracke, "Large-area, uniform, high-spatial-frequency ripples generated on silicon using a nanojoule-femtosecond laser at high repetition rate.," Opt. Lett. **36**, 229–231 (2011).

213. M. S. Ahsan, Y. G. Kim, and M. S. Lee, "Formation mechanism of nanostructures in soda-lime glass using femtosecond laser," J. Non. Cryst. Solids **357**, 851–857 (2011).

214. A. P. Singh, A. Kapoor, K. N. Tripathi, and G. R. Kumar, "Laser damage studies of silicon surfaces using ultra-short laser pulses," Opt. Laser Technol. **34**, 37–43 (2002).

215. M. Beresna, M. Gecevičius, M. Lancry, B. Poumellec, and P. G. Kazansky, "Broadband anisotropy of femtosecond laser induced nanogratings in fused silica," Appl. Phys. Lett. **103**, (2013).

216. A. Okhrimchuk, V. Mezentsev, H. Schmitz, M. Dubov, and I. Bennion, "Cascaded nonlinear absorption of femtosecond laser pulses in dielectrics," Laser Phys. **19**, 1415–1422 (2009).

217. Z. Wu, H. Jiang, L. Luo, H. Guo, H. Yang, and Q. Gong, "Multiple foci and a long filament observed with focused femtosecond pulse propagation in fused silica.," Opt. Lett. **27**, 448–450 (2002).

218. I. M. Burakov, N. M. Bulgakova, R. Stoian, A. Mermillod-Blondin, E. Audouard, A. Rosenfeld, A. Husakou, and I. V. Hertel, "Spatial distribution of refractive index variations induced in bulk fused silica by single ultrashort and short laser pulses," J. Appl. Phys. **101**, (2007).

219. P. Török, P. Varga, A. Konkol, and G. R. Booker, "Electromagnetic diffraction of light focused through a planar interface between materials of mismatched refractive indices: structure of the electromagnetic field. II," J. Opt. Soc. Am. A **13**, 2232 (1996).

220. W. Liu, O. Kosareva, I. S. Golubtsov, A. Iwasaki, A. Becker, V. P. Kandidov, and S. L. Chin, "Femtosecond laser pulse filamentation versus optical breakdown in H2O," Appl. Phys. B Lasers Opt. **76**, 215–229 (2003).

221. A. Couairon, O. G. Kosareva, N. A. Panov, D. E. Shipilo, V. A. Andreeva, V. Jukna, and F. Nesa, "Propagation equation for tight-focusing by a parabolic mirror," Opt. Express **23**, 31240 (2015).

222. K. Mishchik, G. Cheng, G. Huo, I. M. Burakov, C. Mauclair, a Mermillod-Blondin, A. Rosenfeld, Y. Ouerdane, a Boukenter, O. Parriaux, and R. Stoian, "Nanosize structural modifications with polarization functions in ultrafast laser irradiated bulk fused silica.," Opt. Express **18**, 24809–24824 (2010).

223. P. Saeta and B. Greene, "Primary relaxation processes at the band edge of SiO2," Phys. Rev. Lett. **70**, 3588–3591 (1993).

224. D. G. Papazoglou and S. Tzortzakis, "Physical mechanisms of fused silica restructuring and densification after femtosecond laser excitation," Opt. Mater. Express **1**, 625–632 (2011).

225. S. Höhm, A. Rosenfeld, J. Krüger, and J. Bonse, "Femtosecond laser-induced periodic surface structures on silica," J. Appl. Phys. **112**, 14901 (2012).

226. P. Bowlan, P. Gabolde, and R. Trebino, "Directly measuring the spatio-temporal electric field of focusing ultrashort pulses.," Opt. Express **15**, 10219–30 (2007).

227. L. D. Landau and E. M. Lifshitz, *Statistical Physics Part 1*, 3rd ed. (Pergammon Press Ltd., 1980).

228. N. Groothoff, M.-O. Hongler, P. Kazansky, and Y. Bellouard, "Transition and self-healing

process between chaotic and self-organized patterns observed during femtosecond laser writing," Opt. Express **23**, 16993 (2015).

229. G. Shvets, N. J. Fisch, and A. Pukhov, "Acceleration and compression of charged particle bunches using counterpropagating laser beams," IEEE Trans. Plasma Sci. **28**, 1185–1192 (2000).

230. C. McKinstrie and E. Startsev, "Electron acceleration by a laser pulse in a plasma," Phys. Rev. E **54**, R1070–R1073 (1996).

231. Y. Dai, A. Patel, J. Song, M. Beresna, and P. G. Kazansky, "Void-nanograting transition by ultrashort laser pulse irradiation in silica glass," Opt. Express **24**, 19344 (2016).

232. A. Cerkauskaite, R. Drevinskas, A. O. Rybaltovskii, and P. G. Kazansky, "Ultrafast laser-induced birefringence in various porosity silica glasses: from fused silica to aerogel," Opt. Express **25**, 2199–2202 (2017).

233. F. Zimmermann, A. Plech, S. Richter, A. Tunnermann, and S. Nolte, "The onset of ultrashort pulse-induced nanogratings," Laser Photonics Rev. **10**, 327–334 (2016).

234. J. M. Wang, G. H. Liu, Y. L. Fang, and W. K. Li, "Marangoni effect in nonequilibrium multiphase system of material processing," Rev. Chem. Eng. **32**, 551–585 (2016).

235. K. Mishchik, Y. Petit, E. Brasselet, A. Royon, T. Cardinal, and L. Canioni, "Patterning linear and nonlinear optical properties of photosensitive glasses by femtosecond structured light," Opt. Lett. **40**, 201 (2015).

236. G. Papon, N. Marquestaut, Y. Petit, A. Royon, M. Dussauze, V. Rodriguez, T. Cardinal, and L. Canioni, "Femtosecond single-beam direct laser poling of stable and efficient second-order nonlinear optical properties in glass," J. Appl. Phys. **115**, (2014).

237. M. R. Shafer, D. W. Baker, and K. R. Benson, "Electric Currents and Potentials Resulting From the Flow of Charged Liquid Hydrocarbons Through Short Pipes," J. Res. Natl. Bur. Stand. - C, Eng. Instrum. **69C**, 307–317 (1965).

238. A. Patel, V. T. Tikhonchuk, J. Zhang, and P. G. Kazansky, "Non-paraxial polarization spatio-temporal coupling in ultrafast laser material processing," Laser Photon. Rev. **1600290**, 1600290 (2017).

239. J. Aulbach, A. Bretagne, M. Fink, M. Tanter, and A. Tourin, "Optimal spatiotemporal focusing through complex scattering media," Phys. Rev. E **85**, 16605 (2012).

240. M. Coughlan, M. Plewicki, and R. Levis, "Parametric spatio-temporal control of focusing laser pulses," Opt. Express **17**, 15808–15820 (2009).

241. M. Beresna and P. G. Kazansky, "Polarization diffraction grating produced by femtosecond laser nanostructuring in glass.," Opt. Lett. **35**, 1662–1664 (2010).

242. N. M. Bulgakova, V. P. Zhukov, S. V. Sonina, and Y. P. Meshcheryakov, "Modification of transparent materials with ultrashort laser pulses: What is energetically and mechanically meaningful?," J. Appl. Phys. **118**, (2015).